Non-linear Finite Element Analysis Oriented to Optimisation of Fibre Reinforced Concrete Structures

Thesis by publications

PhD Thesis by:

Alejandro Nogales Arroyo

Directed by:

Albert de la Fuente Antequera

Nikola Tošić

Barcelona, February 2022

PhD THESIS

Universitat Politècnica de Catalunya
Departament d'Enginyeria Civil i Ambiental

Acknowledgments

Siempre he pensado que este trabajo sólo ha sido posible gracias al apoyo que he tenido de todo mi entorno, han sido numerosos los momentos en los que he tenido que respaldarme en él para seguir adelante. A todos ellos, muchas gracias.

Por supuesto debo agradecer a Albert y Nikola por enseñarme tanto, por estar siempre atentos y nunca hacerme sentir que estaba solo ante tantas cosas que me abrumaban. Albert fue quien me animó a llevar a cabo esta tarea y un poco después llegó Nikola para insuflarme la energía suficiente para que la terminara. También agradecer a los compañeros del departamento, han sido una referencia y un apoyo fundamental. Y mientras escribo esto no quisiera olvidarme de Stas que ha sido mi compañero de fatigas, que espero que pueda terminar pronto, y de Carla, que espero que termine antes que yo, mucho ánimo.

Gracias a María por aguantarme, a Neska por sacarme a pasear y a toda mi familia y amigos por estar ahí en los momentos en los que se necesita desconectar.

Alejandro Nogales Arroyo

Summary

The construction industry is one of the industrial sectors with the largest output worldwide and, thus, of great economic interest. In this sector, reinforced concrete plays a significant role since it is one of the most used materials and particularly in the civil construction sector.

This situation presents the research on concrete as a necessity. In the last decades, the addition of fibres into concrete, for structural purpose, has been done for either partial or total substitution of conventional reinforcement (steel rebar). This material is called fibre reinforced concrete (FRC) and its main feature is its residual (post-cracking) strength, which means that traditional linear elastic analyses are not recommended for implementation since they are not able to take full advantage of the material's potential. In this sense, international and national codes and guidelines have included models to characterise the behaviour of this material.

Technological breakthroughs in computational tools allow the simulation of FRC aided by non-linear finite element models. In this PhD thesis, by means of these models, different structural elements comprised of FRC currently built in the industry are analysed: precast tunnel segments excavated with tunnel boring machines (TBMs), column–supported elevated flat slabs and simply supported and two-span continuous beams. To this end, by means of constitutive models implemented through a finite element software, the models are calibrated and validated comparing the results with the outcomes obtained from experimental tests. Once this is done, the use of computational tools allows performing broad parametrical analysis to assess the performance of FRC structural elements.

This thesis aims to deepen the knowledge of the behaviour of FRC and to contribute towards a better understanding of it in terms of research and structural design. The results derived from the conducted parametrical analyses are used for identifying which parameters have more influence on the structural performance of the different FRC members: evaluating the influence of the residual flexural strength classes, on members with fibres as unique reinforcement, and the combination of the latter with rebar reinforcement ratio on members with hybrid reinforcement. As a result, optimised reinforcement configurations of members made of FRC and code modifications are proposed.

The proposed method along with the results are meant to support designers and decision makers to optimise FRC structures. Less material consumption will benefit the construction industry productiveness, in terms of time and direct costs savings, whilst leading it towards a more sustainable production and improving the social perception associated with environmental factors.

Resumen

La industria de la construcción es uno de los sectores de mayor producción en el mundo y, por tanto, de mayor interés económico. En éste, el hormigón armado tiene un papel fundamental ya que es uno, si no el que más, de los materiales más empleados y de particular importancia para la construcción de obra civil.

Este escenario sitúa la necesidad de investigación en este tipo de material en un primer plano. Desde hace varias décadas la incorporación de fibras al hormigón, para el uso estructural, se ha venido practicando ya sea para sustituir parcial o totalmente la armadura de acero convencional. A este material se le denomina hormigón reforzado con fibras (HRF) y su principal característica radica en su resistencia residual (resistencia después de la fisuración) y, por tanto, los tradicionales análisis lineales elásticos no son recomendables ya que no son capaces de sacar todo su potencial. A este respecto, distintas normativas y guías de diseño, nacionales e internacionales, ya han incorporado modelos para su caracterización.

Avances en el desarrollo de herramientas computacionales permiten la simulación del HRF con la ayuda de modelos no-lineales de elementos finitos. En esta tesis doctoral, mediante estos modelos, se simulan distintos elementos estructurales compuestos de HRF de actual aplicación industrial: dovelas prefabricadas para túneles excavados con tuneladora, forjados de loza maciza para edificación y vigas simples y continuas. Para ello, mediante los modelos constitutivos del material implementados en un programa de elementos finitos, se calibran y validan los modelos comparándolos con los resultados de ensayos experimentales. Una vez hecho esto, el uso de las herramientas computacionales permite llevar a cabo amplios análisis paramétricos para evaluar el comportamiento estructural de elementos compuestos de HRF.

El propósisto de esta tesis es profundizar en el conocimiento en torno al comportamiento del HRF y contribuir a un mayor entendimiento del mismo tanto a nivel de investigación como de diseño estructural. Los resultados de los análisis paramétricos son usados para identificar aquellos parámetros que tiene una mayor influencia en el comportamiento estructural de los distintos elementos compuestos de HRF: analizar la influencia de las distintas clases de resistencias residuales, en miembros con fibras como único armado, y la combinación de ésta con la ratio de armado convencional en elementos con armado híbrido. Como resultado, se proponen configuraciones de armado optimizadas para los elementos estudiados y modificaciones en los distintos códigos estructurales.

El método propuesto junto con los resultados está pensado como apoyo para diseñadores para optimizar el armado de estructuras compuestas de HRF. Un menor consumo del material ayudará a la industria a tener una mayor productividad, en cuestiones de ahorro de tiempo y costes directos,

Alejandro Nogales Arroyo

mientras la guía hacia una producción más sostenible y mejorando la percepción social asociada a factores medioambientales.

Table of contents

Alejandro Nogales Arroyo

1. GENERAL INTRODUCTION

This chapter presents a general introduction of fibre reinforced concrete, its applications in the current industry and the research necessity regarding this area. Moreover, this chapter describes the general and specific objectives of this thesis. Additionally, it includes the list of publications derived from this work and the structure of the document.

1.1. GENERAL INTRODUCTION

In 2017, the global construction industry was evaluated at a 12.5% of the global world gross domestic product (GDP) and its growth was higher than the global GDP [1]. Civil engineering is 20% of the construction market and, as an example of its growth, the tunnel construction industry growth rate was 2.5 times higher than the global GDP. Within this framework, it is necessary to invest in research on this industry in order to drive it towards more optimised structures with stricter sustainability requirements: less material consumption, lower maintenance costs and longer service life.

In this sense, over the last decades, the use of fibre reinforced concrete (FRC) for structural purposes has grown noticeably [2,3]. As it is depicted in Figure 1.1 (literature research made in the online database Scopus [4]), research on this topic started gaining interest in the early 2000s and in the 2010s this interest boosted research of and publication on FRC. Figure 1 also shows the trend for some specific FRC structural elements currently built in the construction industry.
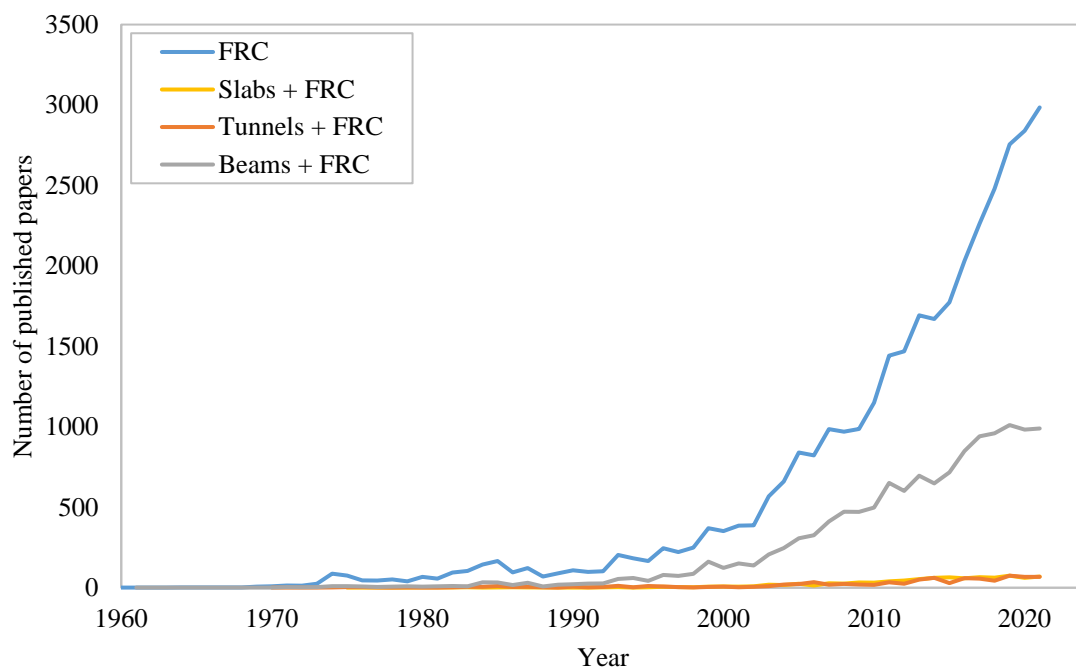
Figure 1 – Number of published papers per year on FRC [4].

The research and the widespread use of the material have given rise to questions on the necessity of codes and guidelines for engineers and practitioners. As a reaction, several international and national codes and guidelines have included design-oriented models for FRC structural elements, e.g., DBV [5], RILEM TC 162-TDF [6], CNR-DT 204/2006 [7], EHE-08 [8], *fib* Model Code [9] and ACI 544 [10].

These codes allow the partial (hybrid reinforcement) or even the total substitution of steel bars (conventional reinforcement) and taking into consideration that more than 50% of concrete produced in developed countries is used for structural applications [11,12], this leads to a lower consumption of steel and therefore towards a more sustainable industry.

Nowadays, among the applications of FRC in the building sector are: concrete pavements (ground supported slabs) [13–17], sewer pipes [18,19], shotcrete [20,21], precast tunnel segments [22–27], foundation slabs [28] and other building elements [29,30].

These applications show an increasing use in structural elements subjected to bending and long-term loads. The presence of fibres in the concrete matrix enhances the mechanical behaviour: improves toughness [31], structural performance under tensile and flexural actions (the material is able to sustain tensile stresses after cracking) [32–34], higher impact resistance and fatigue [35], cracking control (generating a distributed crack pattern and reducing crack width) [36,37] and reduces deflections [38–41].

However, despite all the research carried out and the existence of general guidelines, even oriented to specific structural elements (e.g., FRC flat slabs [42], FRC tunnel linings [43,44]), its straightforward implementation is far from being consolidated and there is still some reluctance to use this material in some areas. The traditional linear elastic design approach does not take full advantage of the material post-cracking mechanical performance and non-linear analyses are recommended in cases where complex phenomena take place, such as stress redistribution in highly statically redundant structures (statically indeterminate structures) or triaxial stress states (high concentrated loads in concrete blocks).

To take into account the full mechanical performance of FRC it is necessary to implement its material model (through its constitutive equations) carrying out non-linear numerical analysis as the post-cracking mechanical performance of FRC is non-linear. To this end, a common approach is by means of finite element (FE) methods. In Annex I of the present thesis, a brief overview is provided of the different FE models used for concrete (and FRC) simulation. In this research work, the implementation of the FRC constitutive curves is made through a FE software.

The use of non-linear analysis by means of FE has proven to be a reliable tool in FRC simulation as it can be observed by the increasing number of publications in the literature (see Figure 2). In the graph it is also indicated the percentage (in 2021) out of the total of papers published on the main topic.

Despite all the literature available regarding FRC, there are still few research focus on the optimisation of the reinforcement of FRC structural members, either reinforced only with fibres or with a combination of fibres and conventional reinforcement (hybrid reinforcement), and this

seems to be beyond the scope of the already published codes and guidelines. The optimisation of these structural members will drive the construction industry towards a reduction in material consumption and, as a consequence, to a time and costs reduction that will boost the productiveness. Apart from direct economic aspects, reinforcement optimisation also affects indirect costs or social and environmental factors which must be taken into account by project planners for leading the way towards a more sustainable industry.
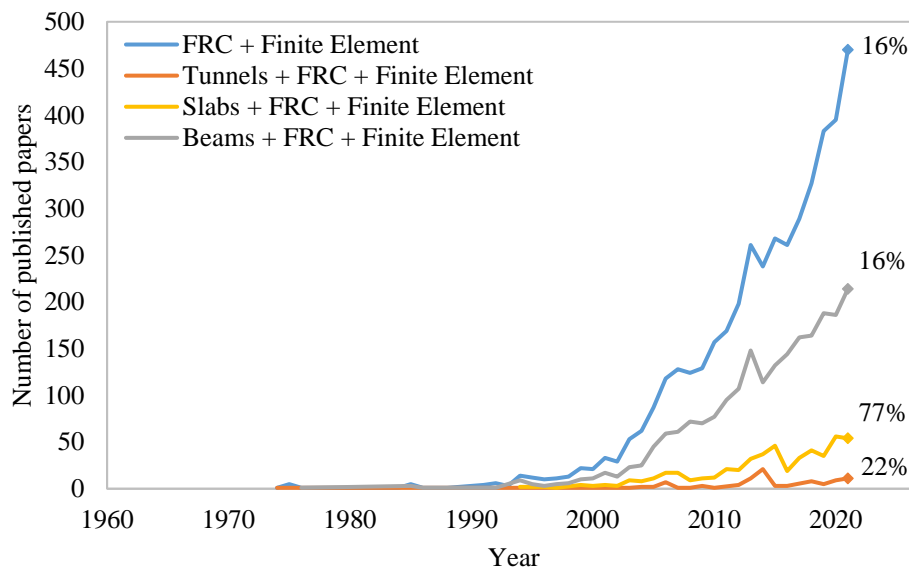
Figure 2 – Number of published papers per year on FRC and FE [4]

Based on the aforementioned aspects, the aim of this thesis is to deepen the knowledge of FRC structural performance and to propose methods to optimise the reinforcement of FRC structural members, with both fibres as unique reinforcement and hybrid reinforcement. To this end, parametrical analyses are carried out by means of non-linear FE simulations in order to identify those parameters with major influence on the structural performance. The outcomes are used for proposing code modifications realted to FRC member's design, modification of the material constitutive equations in order to improve the simulation accuracy of the post-cracking response and meant to support designers and decision makers to optimise FRC structural members.

1.2.   OBJECTIVES

1.2.1. GENERAL OBJECTIVES

The main objective of this thesis is to propose numerical approaches and guidance to optimise the reinforcement of FRC structural members with direct applications in the construction industry: segment linings for tunnel construction and elevated flat slabs and beams for residental and office buildings. To guarantee the achievement of the main objective, it is necessary to carry out non-linear parametric analyses after the calibration and validation of the models based on experimental

tests. The outcomes derived from these analysis are used to propose optimised reinforcement ratios, optimise residual strength values and code modifications for a better characterisation of FRC. The approaches and recommendations outcoming from this research are extendable to other structural typologies and could be the first step towards a more reliable and sustainable design of FRC elements.

1.2.2. SPECIFIC OBJECTIVES

The specific objectives are gathered in the three main areas of research of the thesis:

1. Tunnel Linings

    -   Develop a model for simulating the Tunnel Boring Machine (TBM) thrust on precast segments during the excavation stage.

    -   Assess the global and local (splitting and bursting) mechanical performance.

    -   Carry out a parametrical analysis taking into account different FRC classes, combining traditional reinforcing bars and fibres and different factors that may occur during the TBM thrust stage.

    -   Identify the most influential phenomenon that takes place during this stage and the most influent residual flexural parameter for tunnel lining design.

    -   Propose the optimal reinforcement and the most optimal class in terms of economic and technical points of view.

2. Pile-supported elevated flat slab

    -   Carry out a parametric analysis on a real-scale elevated flat slab comprised of different reinforcement configurations: FRC and hybrid-reinforcement.

    -   To identify and quantify the influence of the different reinforcement configuration to fulfil both SLS and ULS requirements.

    -   Design a real-scale elevated flat slab to test experimentally and propose a lower amount of fibres compared with previous experimental tests on real-scale structures.

    -   Propose a method to derive the safety factors to be applied to the global resistance of the structure.

3. Two-span continuous beams

- Literature research of rotational capacity of beams reinforced with fibres for both unique and combined reinforcement.

- Undertake a parametric analysis for both simply supported and two-span continuous beams comprised of different HRC and hybrid-reinforced configurations.

- Assess the deformation and rotational capacity of FRC simply supported beams.

- Quantify the moment redistribution capacity on two-span continuous and identify the governing parameters in this phenomenon for FRC or hybrid-reinforcement.

- Propose and recommend minimum reinforcement ratios to guarantee adequate to rotation and redistribution capacity of HRC members.

4. FRC characterization

- Compare the beam flexural post-cracking strength test with the experimental one (comparing the results with the non-linear analysis using the constitutive equations of the model code).

- Assess the material models of the codes and identify possible flaws of the method and the differences between the different types of fibres: polypropylene FRC (PPFRC) and steel FRC (SFRC).

- Propose recommendations and changes in the model for properly reproduce the post-cracking behaviour of fibre reinforced concrete.

1.3. METHODOLOGY

This PhD thesis is comprised of publications as provided in the PhD regulations of the Doctoral Program in Construction Engineering (UPC). All publications derived from this thesis are listed below. The publications are grouped into published and submitted papers.

Published Papers

Journal Paper I

Alejandro Nogales and Albert de la Fuente, "Crack width design approach for fibre reinforced concrete tunnel segments for TBM thrust loads", Tunnelling and Underground Space Technology, Volume 98, 2020, 103342, Impact Factor: 6.53, Q1. DOI: 10.1016/j.tust.2020.103342.

Journal Paper II

Alejandro Nogales and Albert de la Fuente, "Numerical-aided flexural-based design of fibre reinforced concrete column-supported flat slabs", Engineering Structures, Volume 232, 2021, Impact Factor: 4.77, Q1. DOI: 10.1016/j.engstruct.2020.111745.

Journal Paper III

Alejandro Nogales, Nikola Tošić and Albert de la Fuente, "Rotation and moment redistribution capacity of fiber-reinforced concrete beams: Parametric analysis and code compliance", Structural Concrete, 2021, Impact Factor: 2.72, Q1. DOI: 10.1002/suco.202100350.

Research contribution for conference I

Alejandro Nogales and Albert de la Fuente, "TBM Thrust on Fibre Reinforced Concrete Precast Segment Simulation". In: Serna P., Llano-Torre A., Martí-Vargas J.R., Navarro-Gregori J. (eds) Fibre Reinforced Concrete: Improvements and Innovations II. BEFIB 2021. RILEM Bookseries, vol 36. Springer, Cham., 2022, DOI: 10.1007/978-3-030-83719-8_58.

Research contribution for conference II

Alejandro Nogales and Albert de la Fuente, "Elevated Flat Slab of Fibre Reinforced Concrete Non-linear Simulation up to Failure", In: Serna P., Llano-Torre A., Martí-Vargas J.R., Navarro-Gregori J. (eds) Fibre Reinforced Concrete: Improvements and Innovations II. BEFIB 2021. RILEM Bookseries, vol 36. Springer, Cham., 2022, DOI: 10.1007/978-3-030-83719-8_57.

Research contribution for conference III

Alejandro Nogales, Eduardo Galeote and Albert de la Fuente, "Finite element analysis characterization of macro synthetic fibre reinforced concrete constitutive equation" In: 75th RILEM WEEK Proceedings, 2021.

Research contribution for conference IV

Eduardo Galeote, Alejandro Nogales and Albert de la Fuente, "Analysis of design constitutive model for plastic fibre reinforced concrete through inverse analysis" In: 75th RILEM WEEK Proceedings, 2021.

Journal Paper IV

Stanislav Aidarov, Alejandro Nogales, Igor Reynvart, Nikola Tošić and Albert de la Fuente "Effects of Low Temperature on Flexural Strength of Macro-Synthetic Fiber Reinforced Concrete: Experimental and Numerical Investigation". Materials, 2022. Impact Factor: 3.6. DOI: 10.3390/ma15031153.

Submitted Papers

Journal Paper Submitted for Publication I

Nikola Tošić, Marc Sanabra, Alejandro Nogales and Albert de la Fuente, "Effective Moment of Inertia and Slenderness Limits of RC and FRC Slabs", Submitted to ACI Structural and Materials Journal in September, 2021.

1.4.   STRUCTURE OF THE DOCUMENT

Aiming at presenting the results derived from in this research work, this document gathers a compilation of scientific contributions (scientific papers and research contributions) written during the PhD. The thesis is divided in four chapters (as it is shown in Figure 3), which are gathered in four parts: Introduction (Chapter I), Body of the Thesis (Chapter II and Chapter III) and Conclusions (Chapter VI). Two annexes are presented in the last part of the document for a better understanding of the thesis.

Chapter I: Presents a brief description of the state of art of FRC: its different applications in the current building industry, the material models available in codes and guidelines, current research areas and future perspectives.

Chapter II: Contains a full version of the published journal papers for the official compendium of publications.

Chapter III: Contains a full version of the presented and published research contributions for conferences.

Chapter IV: General discussion of the contributions made are summarised general and specific conclusions.

Annex I: Theoretical background of the non-linear modelling of FRC.

Annex II: Contains a full version of the complementary co-authored research derived from the thesis, excluded from the official compendium of publications: research contributions, publications and publications submitted under revision.
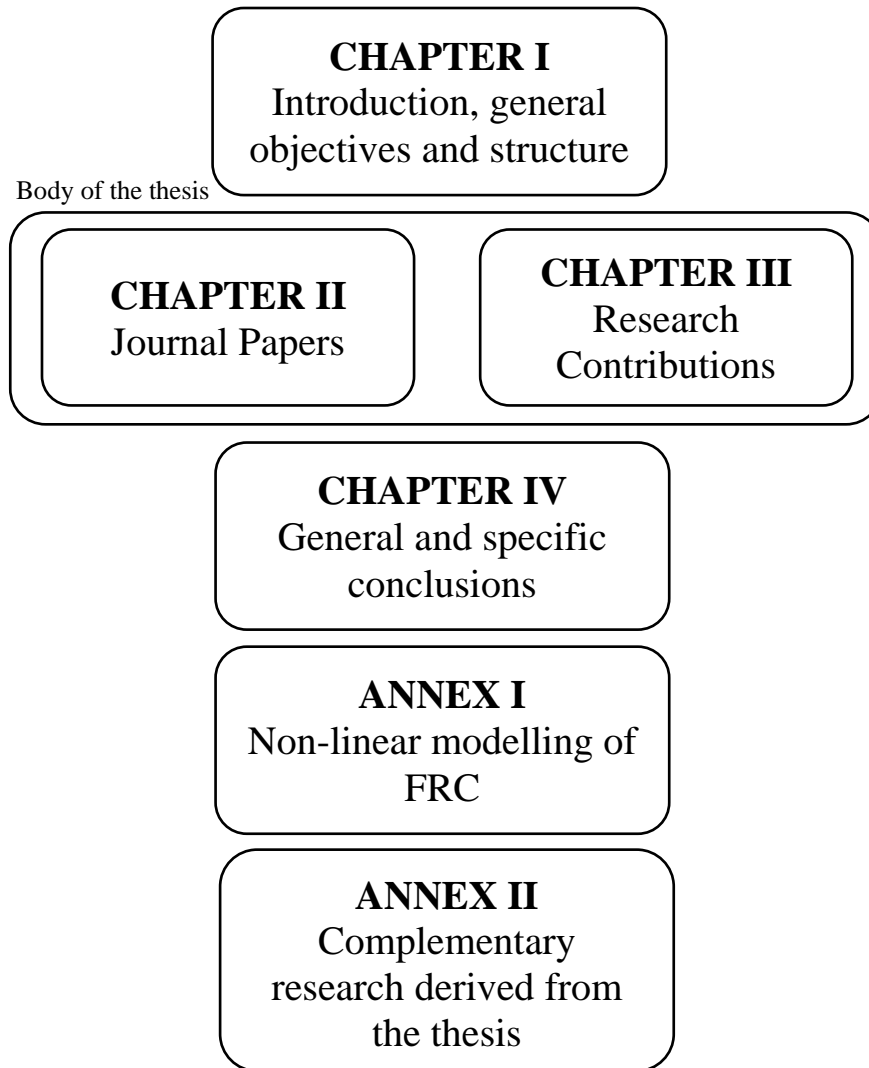
Figure 3 – PhD document outline

1.5. REFERENCES

[1] International Tunnelling and Underground Space Association. ITA-AITES 2021. https://www.ita-aites.org (accessed December 1, 2021).

[2] di Prisco M, Toniolo G. Structural applications of steel fibre reinforced concrete. Proc Int Work Milan, Italy 2000.

[3] di Prisco M, Plizzari G, Vandewalle L. Fibre reinforced concrete : new design perspectives. Mater Struct 2009:1261–81. https://doi.org/10.1617/s11527-009-9529-4.

[4] Science Direct Scopus. Scopus 2021. https://www.scopus.com/home.uri (accessed December 1, 2021).

[5] DBV. Guide to Good Practice: Steel Fibre Concrete. Ger Soc Concr Constr Technol (DBV), Berlin, Ger 2001.

[6] RILEM TC 162-TDF. Test and design methods for steel fibre reinforced concrete. Design with σ-ε method. Mater Struct 2003;35:262–78. https://doi.org/10.1617/13837.

[7] CNR. CNR-DT 204/2006 - Guide for the Design and Construction of Fibre-Reinforced Concrete Structures. vol. 75. 2007. https://doi.org/10.14359/10516.

[8] Comisión Permanente del Hormigón. Instrucción de Hormigón Estructual (EHE-08), Ministerio de Fomento. 2008.

[9] International Federation for Structural Concrete (fib). fib-Model Code for Concrete Structures 2010. Lausanne: 2010. https://doi.org/10.1002/9783433604090.

[10] ACI 544. Fibre-Reinforced Concrete: Design and Construction of Steel Fibre- Reinforced Precast Concrete Tunnel Segments. 2014.

[11] Scrivener KL, Vanderley JM, Gartner EM. Eco-Efficient Cements: Potential, Economically Viable Solutions for a Low-CO2, Cement Based Materials Industry. Paris, France: 2016.

[12] Tošić N, Aidarov S, de la Fuente A. Systematic Review on the Creep of Fiber-Reinforced Concrete. Materials (Basel) 2020;13:5098. https://doi.org/10.3390/ma13225098.

[13] Meda A, Plizzari GA, Riva P. Fracture behavior of SFRC slabs on grade. Mater Struct Constr 2004;37:405–11. https://doi.org/10.1617/14093.

[14] Meda A, Plizzari G. New design approach for steel fiber-reinforced concrete slabs-on-ground based on fracture mechanics. ACI Struct J 2004;101 (3):298–303.

[15] Sorelli L, Meda A, Plizzari G. Steel fiber concrete slabs on ground: A structural matter. ACI Struct J 2006;103:551–8.

[16] Roesler JR, Altoubat SA, Lange DA, Rieder KA, Ulreich GR. Effect of synthetic fibers on structural behavior of concrete slabs-on-ground. ACI Mater J 2006;103:3–10.

[17] Alani AM, Beckett D. Mechanical properties of a large scale synthetic fibre reinforced concrete ground slab. Constr Build Mater 2012;41:335–44. https://doi.org/10.1016/j.conbuildmat.2012.11.043.

[18] de la Fuente A, Escariz RC, de Figueiredo AD, Molins C, Aguado A. A new design method for steel fibre reinforced concrete pipes. Constr Build Mater 2012;30:547–55. https://doi.org/10.1016/j.conbuildmat.2011.12.015.

[19] de la Fuente A, Escariz RC, de Figueiredo AD, Aguado A. Design of macro-synthetic fibre reinforced concrete pipes. Constr Build Mater 2013;43:523–32. https://doi.org/10.1016/j.conbuildmat.2013.02.036.

[20] Banthia N, Trottier J, Beaupré D. Steel-fiber-reinforced wet-mix shotcrete: Comparisons with cast concrete. J Mater Civ Eng 1994;6:430–7.

[21] Cengiz O, Turanli L. Comparative evaluation of steel mesh, steel fibre and high-performance polypropylene fibre reinforced shotcrete in panel test. Cem Concr Res 2004;34:1357–64. https://doi.org/10.1016/j.cemconres.2003.12.024.

[22] Caratelli A, Meda A, Rinaldi Z, Romualdi P. Structural behaviour of precast tunnel segments in fiber reinforced concrete. Tunn Undergr Sp Technol 2011;26:284–91. https://doi.org/10.1016/j.tust.2010.10.003.

[23] Meda A, Rinaldi Z, Caratelli A, Cignitti F. Experimental investigation on precast tunnel segments under TBM thrust action. Eng Struct 2016;119:174–85. https://doi.org/10.1016/j.engstruct.2016.03.049.

[24] Plizzari GA, Tiberti G. Steel fibers as reinforcement for precast tunnel segments. Tunn Undergr Sp Technol 2006;21:438–9. https://doi.org/10.1016/j.tust.2005.12.079.

[25] Liao L, de la Fuente A, Cavalaro SHP, Aguado A. Design of FRC tunnel segments considering the ductility requirements of the fib Model Code 2010: Application to the Barcelona Metro line 9. Tunn Undergr Sp Technol 2015;47:200–10.

[26] de la Fuente A, Pujadas P, Blanco A, Aguado A. Experiences in Barcelona with the use of fibres in segmental linings. Tunn Undergr Sp Technol 2012;27:60–71. https://doi.org/10.1016/j.tust.2011.07.001.

[27] Jamshidi M, Hoseini A, Vahdani S, de Santos C, de la Fuente A. Seismic fragility curves for vulnerability assessment of steel fiber reinforced concrete segmental tunnel linings. Tunn Undergr Sp Technol 2018;78:259–74. https://doi.org/10.1016/j.tust.2018.04.032.

[28] Buchta V, Mynarcik P. Experimental testing of fibre-concrete foundation slab model. Appl Mech Mater 2004;504–504:291–4. https://doi.org/10.1016/j.compstruct.2018.01.094.

[29] de la Fuente A, Aguado A, Molins C, Armengou J. Innovations on components and testing for precast panels to be used in reinforced earth retaining walls. Constr Build Mater 2011;25:2198–205. https://doi.org/10.1016/j.conbuildmat.2010.11.003.

[30] di Prisco M, Dozio D, Belletti B. On the fracture behaviour of thin-walled SFRC roof elements. Mater Struct Constr 2013;46:803–29. https://doi.org/10.1617/s11527-012-9935-x.

[31] Bencardino F, Rizzuti L, Spadea G, Swamy RN. Stress-strain behavior of steel fiber-reinforced concrete in compression. J Mater Civ Eng 2008;20:255–63. https://doi.org/10.1061/(ASCE)0899-1561(2008)20:3(255).

[32] Barros J, Figueiras JA. Flexuaral behaviour of SFRC: testing and modeling. J Mater Civ Eng 1999:331–9.

[33] Barros J, Cunha VMCF, Ribeiro AF, Antunes JAB. Post-cracking behaviour of steel fibre reinforced concrete. Mater Struct Constr 2005;38:47–56. https://doi.org/10.1617/14058.

[34] Jones PA, Austin SA, Robins PJ. Predicting the flexural load-deflection response of steel fibre reinforced concrete from strain, crack-width, fibre pull-out and distribution data. Mater Struct Constr 2008;41:449–63. https://doi.org/10.1617/s11527-007-9327-9.

[35] Bindiganavile V, Banthia N. Impact response of the fiber-matrix bond in concrete. Can J Civ Eng 2005;32:924–33. https://doi.org/10.1139/l05-039.

[36] Chiaia B, Fantilli AP, Vallini P. Evaluation of crack width in FRC structures and application to tunnel linings. Mater Struct Constr 2008;42:339–51. https://doi.org/10.1617/s11527-008-9385-7.

[37] Vandewalle L. Cracking behaviour of concrete beams reinforced with a combination of ordinary reinforcement and steel fibers. Mater Struct Constr 2000;33:164–70.

[38] Pfyl T, Marti P. Behaviour of reinforced steel fibre concrete members in bending and tensions. Proc. 3rd Int. PhD Symp. Civ. Eng., vol. 2, 2000, p. 47–55.

[39] Meda A, Minelli F, Plizzari GA. Flexural behaviour of RC beams in fibre reinforced concrete. Compos Part B Eng 2012;43:2930–7. https://doi.org/10.1016/j.compositesb.2012.06.003.

[40] Conforti A, Minelli F, Plizzari GA. Wide-shallow beams with and without steel fibres: A peculiar behaviour in shear and flexure. Compos Part B Eng 2013;51:282–90. https://doi.org/10.1016/j.compositesb.2013.03.033.

[41] Pujadas P, Blanco A, de la Fuente A, Aguado A. Cracking behavior of FRC slabs with traditional reinforcement. Mater Struct Constr 2012;45:707–25. https://doi.org/10.1617/s11527-011-9791-0.

[42] ACI 544.6R-15. Report on Design and Construction of Steel Fiber-Reinforced Concrete Elevated Slabs 2015.

[43] ACI 544.7R-16. Report on Design and Construction of Fiber-Reinforced Precast Concrete Tunnel Segments. ACI Comm Rep 2016:1–36.

[44] FIB – Task Group 1.4.1. Precast Tunnel Segments in Fibre-Reinforced Concrete. Lausanne: Federation internationale du béton; 2017.

2. PUBLICATIONS: JOURNAL PAPERS

This chapter reproduces the published journal and conference papers derived from this thesis. Each paper follows its own numbering of sections, figures, equations and references.

2.1. JOURNAL PAPER I: CRACK WIDTH DESIGN APPROACH FOR FIBRE REINFORCED CONCRETE TUNNEL SEGMENTS FOR TBM THRUST LOADS

Alejandro Nogales[a,b,*] and Albert de la Fuente[b]

[a]Smart Engineering Ltd., UPC Spin-Off, Jordi Girona 1-3, 08034 Barcelona, Spain

[b]Civil and Environmental Engineering Deparment, Universitat Politècnica de Catalunya (UPC), Jordi Girona 1-3, 08034 Barcelona, Spain

*Corresponding author

ABSTRACT

Concentrated loads induced during the excavation stage by Tunnel Boring Machines (TBMs) is still a matter of discussion into the tunnelling construction field, this having a strong impact from both the technical (e.g., durability and service conditions) and the economic perspectives. Fiber reinforced concrete (FRC) has been gaining acceptance as a structural material for producing precast segments as this has proven to lead to various advantages respect to the traditional reinforced concrete, especially for improving the crack control during transient loading situations. In this sense, several experimental programs and numerical studies were previously carried out in which the different geometric and mechanical governing variables were analyzed and, from the results, valuable conclusions were derived. Nonetheless, there are still observed lacks and gaps related with the optimum reinforcement design (FRC strength class and/or amount of traditional steel bar reinforcement) which is often hindering the use of fibers as main reinforcement for concrete segments. The main purpose of the research consist in developing a parametric analysis related with the TBM-thrust effects on FRC segments by means of using a non-linear 3D FEM, previously calibrated with full-scale tests. The results are used to determine the range of FRC strength classes suitable for controlling the crack with during the TBM thrust phase. The results and conclusions are expected to be useful for tunnels designers when establishing the FRC mechanical requirements.

KEYWORDS: Fibre reinforced concrete, TBM thrust, concentrated load, crack width, numerical simulation

Nomenclature		h	segment height
List of symbols		P_{acc}	Accidental load
$A_{s,min}$	minimum reinforced area	P_{cr}	Cracking load
b	segment width	P_{spall}	Spalling cracking load
d	segment effective depth	P_{sp}	Splitting cracking load
$CMOD$	crack mouth opening displacement	w	crack opening in mm
E_{cm}	modulus of elasticity for concrete	w_k	Characteristic value crack opening
E_{ci}	tangent modulus of elasticity of concrete at a stress σ_i	w_m	Mean value crack opening
		w_s	crack opening for f_{Fts}
E_{c1}	secant modulus from the origin to the peak compressive stress	w_{spall}	Spalling crack opening
		w_{sp}	Spalling crack opening
f_{cm}	mean value of the cylindrical compressive concrete	w_t	crack opening when $\sigma_j = 0$
f_{ctm}	mean value of the tensile concrete strength	w_u	crack opening for f_{Ftu}
f_{Fts}	serviceability residual strength (post-cracking strength for serviceability crack opening)	ε_1	concrete strain for f_{ctm}
f_{Ftu}	ultimate residual strength (post-cracking strength for ultimate crack opening)	ε_c	concrete compression strain
$f_{R,j}$	value of the residual flexural strength corresponding to $CMOD = CMODj$	$\rho_{s,min}$	longitudinal reinforcement ratio
f_{yk}	yield strength of steel bar reinforcement	σ_c	concrete compression stress
G_F	fracture energy of concrete	σ_j	stress point for concrete tensile constitutive curve

1. INTRODUCTION

Over the last decades, the addition of fibres in concrete mixes has noticeable grown for structural purpose [1–5]. Among the structural applications where FRC is used is tunnelling, precast tunnel segments are used to be suitable when using the Tunnel Boring Machines (TBM) excavation method [6,7], even from the sustainability point of view [8]. The use of fibres in concrete mix has been proven as a potential solution and tunnel linings were made up with this material: "Barcelona Metro Line 9" [9–12], "Monte Lirio Tunnel" in Panamá [13,14]; and the "Prague Metro Line" [15,16] are examples, among others (in the fib Bulletin 83 [17] more than 70 examples are gathered).

Experiences on tunnel design and researches have proven that in terms of loading and concrete cracking, the most demanding scenarios may not occur during the operational stage [18,19]. Actions on tunnel construction can be classified in: (1) Primary loads due to soil-structure interactions and water pressure and (2) Secondary loads, which occurs during construction called transient phases, which include demoulding, storage, transportation, handling, placing and TMB jack's thrust. Primary loads induce compressive forces combined with low shear forces and bending moments on the ring that can be resisted by the concrete matrix and a combination of fibre and conventional reinforcement in linings with large diameters [20–22]; this situation is particularly frequent in case of predominance of soil homogeneity (e.g., no geologic faults existence), low probability and magnitude of seismic actions and/or no high internal water pressure (e.g. sewage-storage tunnels). However, in hydraulic or metro tunnels (less than 6.0 m diameter) mainly subjected to compression in service stage, it is during transient phases where tensile stresses appear either due to bending moments (during stacking, transport, handling and placing) or thrust phase where high concentrated loads lead to tensile stresses (splitting and spalling).

During excavation, high concentrated loads are exerted on the last placed ring by TBM jacks. The application of concentrated loads induces to a complex state of stresses, which both magnitude and distribution are difficult to be assessed due to the existence of a disturbance zone beneath the load transfer along a certain length called "D region". This subject has been deeply studied and discussed by Leonhardt [23] and Iyengar [24] for transfer zones for pre-stressed structures. Compressive stresses trajectories in the region results in a tri-axial state of stresses where a principal tensile component of stresses (splitting stresses) acts orthogonally to the paths of compressions. In addition, on precast tunnel segments as a result of compatibility demand with respect to deformed cross section tensile stresses (spalling stresses) appear [7].

These state of stresses and the bended shape of the elements lead to the use of conventional reinforcement with complex detailing, which may leave uncovered areas where spalling and splitting stresses take place. Alternatively (or complimentary), FRC can deal with this matter due to the random distribution nature of the fibres within the whole segment. This FRC property is particularly interesting for covering those stresses derived from the TBM jacks' thrust and those due to the interaction of longitudinal joints, especially when seismic forces are expected to occur during the service live [25,26].

It is worthwhile noticing that the magnitude of these forces depend on several factor such as surrounding ground type and friction forces between shield and soil, also the force exerted for each jack depends on the number of jacks used per segment, the loading plate area and its distribution [27]. Furthermore, some of the cracks may appear by imperfect placing of the

segments or wrong TBM operation which generates load eccentricities and imperfect contact between adjacent rings [9,28].

Fibres of different materials (mainly metallic and synthetic) and geometries (length, thickness) are used in fibre reinforced concrete. While steel fibre reinforced concrete (SFRC) is the most used in tunnel lining constructions, there is a growing interest in synthetic fibres and several and extensive research has been developed on polypropylene fibres reinforced concrete (PFRC) in the last years [29–31]. Tests on specimens cast with PFRC, PC (plain concrete) and PFRC+RC (reinforced concrete) were carried out, combining loading situations (line and point load) and geometries (prismatic and plane specimens and tunnel segments).

Test results indicate that synthetic fibres can be a reinforcement solution for precast segments. Point load tests made on prismatic specimens (250x250x750 mm) with a total amount of $10kg/m^3$ for evaluating the local splitting behaviour concluded that, taking PC as reference, synthetic fibres enhances the ductility and the bearing capacity up to +40%, the casting direction having a great influence on it. Tests on actual precast segments, using the same volume of fibres ($10kg/m^3$), demonstrated that polypropylene fibres can be used as flexural, splitting and minimum shear reinforcement. Furthermore, results pointed out that PFRC can be used as spalling reinforcement combined with conventional rebar and guarantees a better cracking control.

A remarkable advantage of synthetic reinforcement (either fibres or rebar) is in terms of corrosion resistance against aggressive environment especially for hydraulic tunnels [32]. Experimental campaigns using glass fibre reinforced polymer (GFRP) rebar [32–34] concluded that there were no significant differences with steel rebar reinforcement on the flexural behaviour point of view and exhibited a better performance in terms of cracking reduction under concentrated loads. When a better flexural performance is required, GRFP rebar can be combined with SFRC [35].

Table 1 gathers several numerical and experimental programs related to FRC precast segments subjected to concentrated loads.

Table 1 – Previous research focused on FRC elements subjected to concentrated loads

Elements	f_c [MPa]	Dimensions [mm]	Material	C_f [kg/m³]	Φ_f/λ_f	Tests	Load	Numerical Simulation	Ref.
PS (RP)	60	300 x 3000 x 1000 (panels)	RC SFRC	- 35 60	- 0.65/60 0.65/60 0.92/65	4	Centred jack	3D-FE (ANSYS)	[36]
B (RP)	60	350 x 350 x 700	SFRC	35 60	0.65/60 0.92/60	12	Centred line and point load	3D-FE (ANSYS) and strut-tie models	[37]

PS (MT)	50	900 x 520 x 175 (panels)	RC+SFRC SFRC	30 60	1.00/65	4	Centred and eccentric jack	3D-FE elastic model (ANSYS)	[11]
PS (RP)	75-100	3150 x 1420 x 300	RC SFRC	- 60	- 1.00/50	5	Centred jack	3D-FE (ABAQUS) and strut-tie models	[38]
PS (HT)	35	1840 x 1200 x 250	SFRC	40	0.75/80	1	Centred jack	None	[13]
PS (RP)	60	2539 x 1400 x 350	PC SPFRC	- 30+1 40+1	- 0.75/80+ PP fibres	9	Centred Jack on cantilever supported segment	None	[39]
PS (RT)	50	3400 x 1500 x 200	RC SFRC	- 40	- 0.35/85	2	Centred jack	None	[14]
PT (HT)	35	1840 x 1200 x 250	SFRC	40	0.35/85 0.60/50 0.75/40	3	Centred jack	Design with MC2010	[40]
PT (MT)	60	2570 x 1500 x 250	SFRC	40 50	0.75/80	15	Centred jack on uniformly and cantilevered supported segment	2D-FE (ATENA) and 3D-FE for the full-scale tests on precast segments	[15,41]
B (RP)	75-95	300 x 150 x 150	PC SFRC	- 40 60 80 60	- 0.75/80 0.90/65 0.71/85 0.55/55	96	Different loaded-area ratios with varying positions of the concentrated load	3D-FE (MSC-Marc)	[42]
PS (RP)	150-170	1000 x 500 x 100 (reduced scale)	UHPC UHSFRC	- 236	- 0.20/80	2	Centred TBM jack simulation	None	[43]
B (RP)	50	250 x 250 x 750	PC PFRC	- 10	- 0.81/54	18	Centred line and point load	None	[31]
B (RP-MT)	40-50	(200-750) x 150 x 300	PC SFRC	- 40	0.75/60	32	Centred TBM jack simulation	None	[22]
PS (RP)	80	3000 x 1400 x 300	RC		-	31	Centred TBM jack simulations on uniformly and cantilevered supported segment	3D-FE (Diana TNO)	[44]
B (RP)	50-60	250 x 250 x 750	SFRC	10	0.66/55 0.8/75	6	Centred line load	None	[31]
PS (RP)	50-60	1000 x 750 x 150 (reduced scale)	PFRC PC RC+PFRC	10 - 10	0.80/67	8	Centred line and point load	None	[29]
PS (RP-MT)	60	1920 x 1200 x 250	RC PFRC RC+PFRC	- 10 10	0.81/67	3	Centred TBM jack simulation	None	[30]

Alejandro Nogales Arroyo

PS (RP)	50	4150 x 1483 x 250	GFRP	-	-	2	Centred TBM jack simulation	None	[32]
PS (RP)	60	3000 x 1400 x 300	GFRP+ SFRC SFRC	40	0.75/60	2	Centred TBM jack simulation	None	[35]
PS (RP-MT)	40	3020 x 1420 x 300	RC RC+PRFC	10	0.81/55	2	Centred TBM jack simulation	None	[45]

PS: precast concrete segment;	**MT**: metro tunnel;	**RC**: reinforced concrete	**C**$_f$: amount of fibres
B: concrete block;	**HT**: hydraulic tunnel;	**SFRC**: steel fibre reinforced concrete	**Φ**$_f$: diameter of the fibre
RP: research project;	**RT**: road tunnel	**PC**: plain concrete;	**λ**$_f$: slenderness ratio of the fibre
UHPSFRC: Ultra high performance steel fibre reinforced concrete	**UHPC**: Ultra high performance reinforced concrete	**PFRC**: Polypropylene fibre reinforced concrete	**GFRP**: Glass fiber reinforced polymer rebar

Comprehensive parametric studies have been done in these programs. As can be seen in Table 1, steel fibres amounts ranged from 35 to 80 kg/m^3 and 10 kg/m^3 in case of synthetic fibres are commonly used. [43]) tested a segment with 236 kg/m^3 of micro steel fibres in order to evaluate the structural benefits of using ultra-high performance steel fibre reinforced concrete (UHPSFRC). Fibre orientation influence on FRC performance was considered in [38,42] and [31]. Most of the analysed tests applied a centred load, either line or point load, except for [11] and [42] which also studied the influence of eccentric loads. In order to simulate an imperfect support between adjacent rings, several researchers have set tests with a cantilever configuration support [15,39,41,44]. Furthermore, the loading area is a topic of concern, [29,42] analysed the influence of the contact area on the response.

Numerical analysis were made using finite element (FE) packages. Those most commonly used for simulating the TBM thrust jack were: ANSYS [46], ATENA [47], ABAQUS [48], DIANA [49] and MSC-Marc [50]. These FE softwares are capable of reproducing the nonlinear response due to cracking of concrete and FRC after reaching tensile strength. The post-cracking response modelling can be done in several ways: smeared crack, discrete cracking and damaged models. The numerical analysis results compared to those obtained in experimental campaigns showed that the response of the model were in good agreement with the nonlinear behaviour and cracking of the tested FRC segments.

Furthermore, it must be highlighted that several guidelines have included FRC design recommendations such as DBV, RILEM TC 162-TDF [51], *fib* Model Code 2010 [52], CNR-DT 204/2006 [53], EHE-08 [54], and ACI 544 [55] and specific documents have been published recently for supporting the design of precast tunnel segments *fib* Bulletin 83 [17] and ACI 544.7R-16 [56] to the practitioners.

In regard to thrust phase, despite being a temporary stage, can influence the design of precast tunnel segments. This phase is the most frequent source of cracking cause during tunnel construction and lifetime [19]. The thrust phase can jeopardize costs, structural durability and the serviceability of the tunnel: the corrosion arising from cracks in aggressive environments due to carbonization and chloride ions undermine reinforcement and in case of sewage and water supply tunnels a completely watertightness is required.

The response of the segment under concentrated loads is difficult to evaluate and analyse, in particular for FRC when some cracking is permitted. The evaluation of fibres benefits under concentrated loads in a design process can be done experimentally, either by local experimental tests (splitting tests) or global experimental tests (full-scale tests), or by means of a non-linear numerical analyses of FRC tunnel segments [17]. Knowing how the segment subjected to concentrated loads performs is of great interest since compromises designing (segment geometry, amount and reinforcement distribution) and therefore costs.

Despite many experimental and numerical research can be found in the literature, most of them are focused on studying the benefits of using fibres as partial (or total) reinforcement for splitting stresses under concentrated loads. Spalling phenomena has barely been studied [29,30,44] although these is the most common crack pattern reported for thrust phase [19]. FRC results are commonly compared with PC or RC and a lack of research is found when comparing between FRC classes. These latter have been introduced in the *fib* MC-2010 in order to classify the post cracking strengths of FRC. The effect of using different FRC and its mechanical response, cracking and ultimate load has not been yet studied and many questions arise when dealing with precast FRC segments, how affect using different FRC classes and until where improving the FRC strength (higher FRC class) affects the cracking and structural response of the whole segment.

The aim of this paper is to evaluate the structural performance of TBM constructed tunnels with FRC precast segmental linings under thrust jack forces. The main goal consists in analysing the effects of precast segments cast with different classes of FRC according to *fib* MC-2010 and provide a range of classes that can be the more advantageous reinforcement solution for future tunnel designing. The FRC results are to be compared also with PC, RC and hybrid reinforcement (FRC+RC). A comprehensive non-linear numerical simulation campaign was carried out using a finite element software package ABAQUS [48]; the model being previously calibrated by using results derived from other experimental programs. Both the results and conclusions achieved are of interest in terms of structural and economic optimization in those cases for which the TBM thrust is the design governing phase.

2. NUMERICAL MODELLING OF FRC

According to *fib* Bulletin 83 [17], the design of FRC tunnel segments subjected to concentrated loads can be carried out by non-linear FE analysis. Regarding the modelling of the FRC mechanical response, according to *fib* MC-2010, the FRC strength class can be ranged by the characteristic values of the flexural residual strength (f_{Rk}) obtained from the three point bending test on notched-beams according to EN 14651:2005 [57]. Two parameters are used for classifying: f_{R1k} that represents the residual strength for a crack mouth opening displacement (CMOD) of 0.5 mm and a letter (a, b, c, d or e) that represents the f_{R3k}/f_{R1k} ratio, where f_{R3k} stands for a COMD of 2.5 mm.

To establish the compressive stress-strain (σ-ε) and tensile stress-crack opening (σ-w) constitutive relationships from *fib* MC-2010 are used, see Figure 1. Mean values of each of the involved mechanical variables are considered for the numerical simulations.
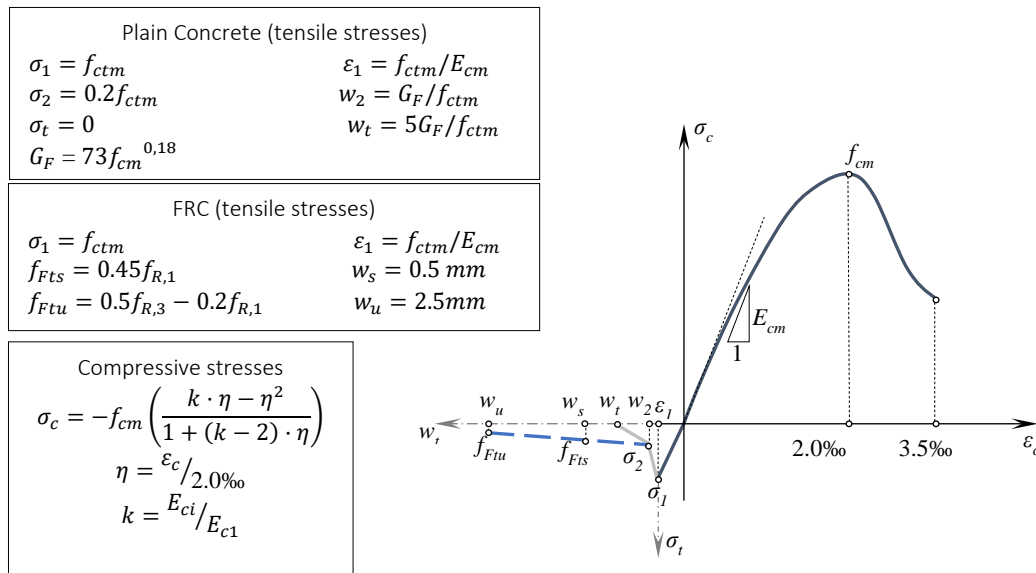

Plain Concrete (tensile stresses)

$\sigma_1 = f_{ctm}$ $\varepsilon_1 = f_{ctm}/E_{cm}$
$\sigma_2 = 0.2 f_{ctm}$ $w_2 = G_F/f_{ctm}$
$\sigma_t = 0$ $w_t = 5 G_F/f_{ctm}$
$G_F = 73 f_{cm}^{0,18}$

FRC (tensile stresses)

$\sigma_1 = f_{ctm}$ $\varepsilon_1 = f_{ctm}/E_{cm}$
$f_{Fts} = 0.45 f_{R,1}$ $w_s = 0.5\ mm$
$f_{Ftu} = 0.5 f_{R,3} - 0.2 f_{R,1}$ $w_u = 2.5 mm$

Compressive stresses

$$\sigma_c = -f_{cm}\left(\frac{k \cdot \eta - \eta^2}{1 + (k-2)\cdot\eta}\right)$$

$$\eta = \frac{\varepsilon_c}{2.0‰}$$

$$k = \frac{E_{ci}}{E_{c1}}$$

Figure 1 – Constitutive equations for concrete; σ-ε for compression and σ-w for tensile

With the purpose of implementing the FRC post-cracking response in the software, the Concrete Damage Plasticity (CDP) model [48] available in the software is used. The CDP model is a continuum, smeared crack, plasticity-based, damage model for concrete. In smeared crack models the damage zone coincides with the element dimensions. The model assumes that the main two failure mechanisms are tensile cracking and compressive crushing of the concrete material. In order to reproduce the concrete behaviour the input data required are uniaxial σ-ε curves for compression and tension. It is worth noticing that to overcome mesh dependence the σ-w tensile curve is used instead. In this regard, the σ-w tensile and σ-ε compression curves proposed by the *fib* MC-2010 are used for the analysis, the characteristic length (L_{ch}), to turn crack opening into strain, implemented by default by the software is the size of the element. The CDP

parameters adopted in all the simulations of this research work are the default ones proposed in ABAQUS User's Manual [48] for plain concrete.

3. EXPERIMENTAL MODEL VALIDATION

3.1. SMALL-SCALE BLOCKS (SCHNÜTGEN AND ERDEM, 2001)

Small-scale experimental tests carried out by Schnütgen and Erdem [37] which consisted in SFRC anchor blocks subjected to concentrated loads oriented to assess the response against splitting [58] is taken as reference for calibrating the model. This campaign has previously been used for other model validations [9]. To this end, twelve blocks (350 x 350 mm in cross-section, 700 mm high) cast with three different SFRC mixes and subjected to line loads (Figure 2a). LVDT transducers were placed on the frontal face, perpendicular to the load, to measure displacements (horizontal) produced by splitting stresses. 35 kg/m^3 (SFRC-A) and 60 kg/m^3 (SFRC-B) of hooked-end steel fibres (0.75 mm in diameter and 60 mm in length) were used for produce the SFRC mixes. The average compressive concrete strength (f_{cm}) was 58.2 N/mm^2 and 50.2 N/mm^2 for SFRC-A and SFRC-B, respectively. The average equivalent flexural residual strengths (f_{eqm}) measured according the NBN-B-15-238:1992 [59] were 5.41 N/mm^2 ($f_{eqm,1}$) and 4.81 N/mm^2 ($f_{eqm,3}$) for SFRC-A and 6.49 N/mm^2 and 5.96 N/mm^2 for SFRC-B.
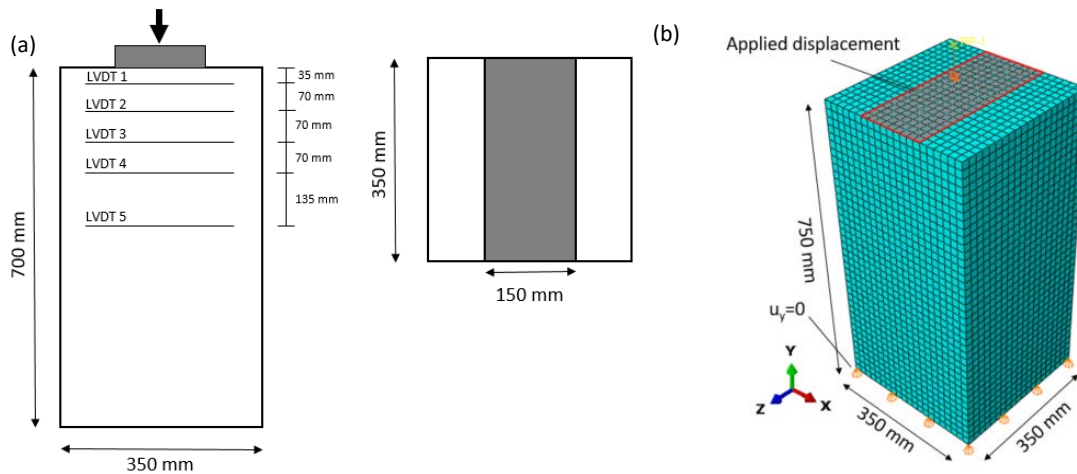

Figure 2 – Splitting Line Load test (a) Lab test configuration and (b) FE model meshed considered

A non-linear 3D model was implemented (Figure 2b) to simulate both the geometry and loading conditions presented in Figure 2a. The mesh consists of 8-noded solid linear hexahedral elements (C3D8R) used for modelling concrete, this leading to an amount of 16,800 elements. Vertical displacement is restricted ($u_y=0$) at the bottom face and the load is applied by displacement control, in order to guarantee a better convergence, on a 350 x 150 mm surface on the top according to the test configuration (Figure 2a).

Figure 3a and 3b present the stress pattern on the block for a load $P = P_{sp}$ (Splitting load) /2 (1030 kN), where S11 stands for stress in x direction (MPa). In Figure 3c for the same load level, together with the numerical model stress data, obtained from integration points throught a straigth vertical line in the mid section (Figure 3b), is presented the elastic solution according to the abacus for concentrated loads proposed by Iyengar [24], later corroborated [23]. It can be noticed that the model reproduces accurately the behaviour at this pre-cracked regime. The splitting load measured averaged 2500 kN for the four specimens tested and it resulted to be 17.6% lower according to the numerical model (2060 kN).
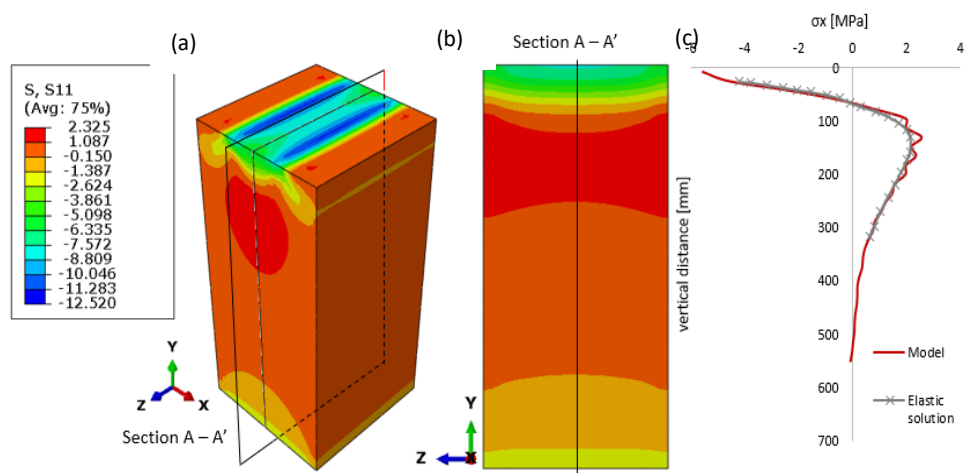

Figure 3 – Stress state in N/mm² for P=1030 kN (a) full specimen (b) mid-section (c) along straight line

Figure 4a and 4b presents both the experimental and numerical results for the SFRC-A and SFRC-B respectively, in terms of load-horizontal displacement at a distance of 175 mm from the top (LVDT 3) where the maximum tensile stresses appear due to splitting (see Figure 3c).

The specimen with SFRC-A (Figure 4a) presented maximum experimental loads of 3,200 kN (1A) and 2,870 kN (2A) while the numerical results reached a maximum load of 2,880 kN. SFRC-B specimens (Figure 4b) reached a maximum load up to 2,830 kN (1B) and 2,650 kN (2B), whereas the numerical model presented a magnitude of 2,815 kN.
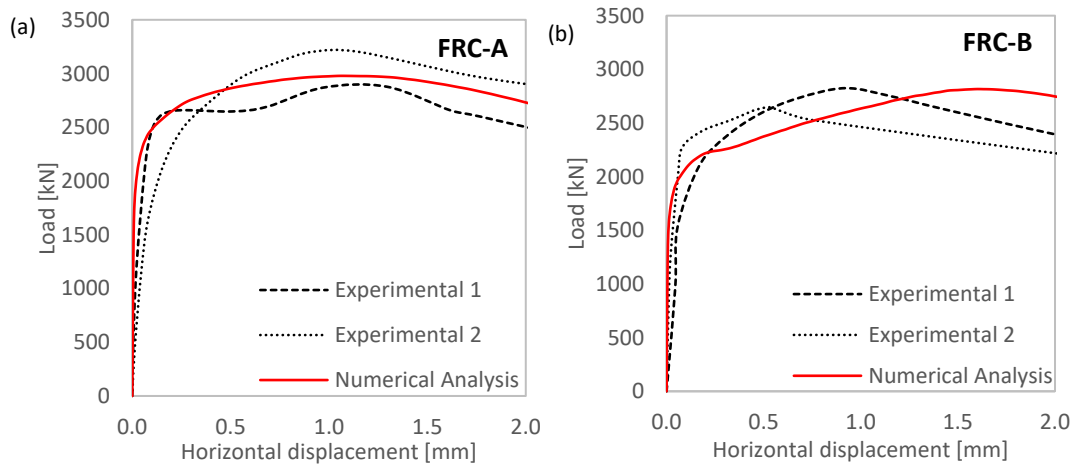
Figure 4 – Experimental and numerical load-horizontal displacement curves –(a) Concrete A and (b) Concrete B

Finally, Figure 5 includes the crack pattern reported and the one obtained numerically. The first crack is vertical and appears at the center of the specimen and progressively grows downwards while another cracks appear in the region under the loading pad, these growing until the merge with the former.
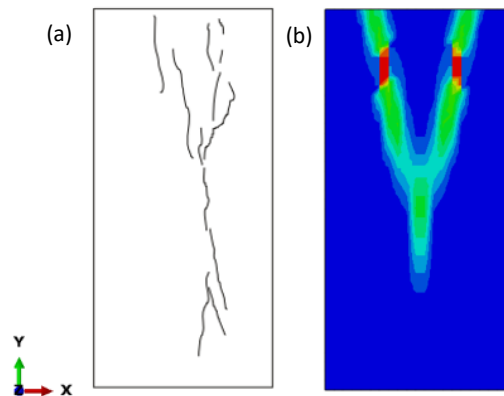

Figure 5 – Crack pattern (a) experimental test (b) model

Thus, according to the results presented in Figures 4-5, it can be remarked that the model can reproduce properly the mechanical response of SFRC short blocks subjected to concentrated line loads that generate splitting stresses and capture the resistant mechanism up to failure.

3.2. FULL-SCALE NON-CURVED SEGMENTS (CONFORTI ET AL., 2016)

Experimental program carried out by Conforti et al. [29] to evaluate the contribution of polypropylene fibres in controlling both the splitting and spalling phenomena in tunnel segments is the second experimental campaign used for the model calibration. Test were done on 8 non-curved 150 x 1000 mm in cross-section and 750 mm high specimens, combining different reinforcement configurations: PFRC and RC. Loads were applied through pads considering

centred loads with different widths of loading area (100 and 150 mm) on full-supported segments. Figure 6a presents the test set up, reinforcement configuration and the position of the measure devices for detecting and measuring the crack opening: potentiometric transducers (PTs) for splitting and linear differential transformers (LVDTs) for spalling cracks. 150 mm width loading area tests are used to compare. The segment were cast using three different reinforcement and concrete configurations: (1) PFRC with 10 kg/m^3 fibre amount, 48.3 N/mm^2 f_{cm} and 2.4 and 3.6 N/mm^2 for f_{R1m} and f_{R3m} respectively, according to EN-14651:2005, (2) same PFRC mix combining fibre and conventional reinforcement: top and bottom 4Ø8 chord were placed at a 120 mm depth and two-leg Ø6 stirrups at a distance of 150 mm in each chord with 552 N/mm^2 yield stress for steel rebar (RC+PFRC) and (3) PC with 57.2 N/mm^2 compressive strength.
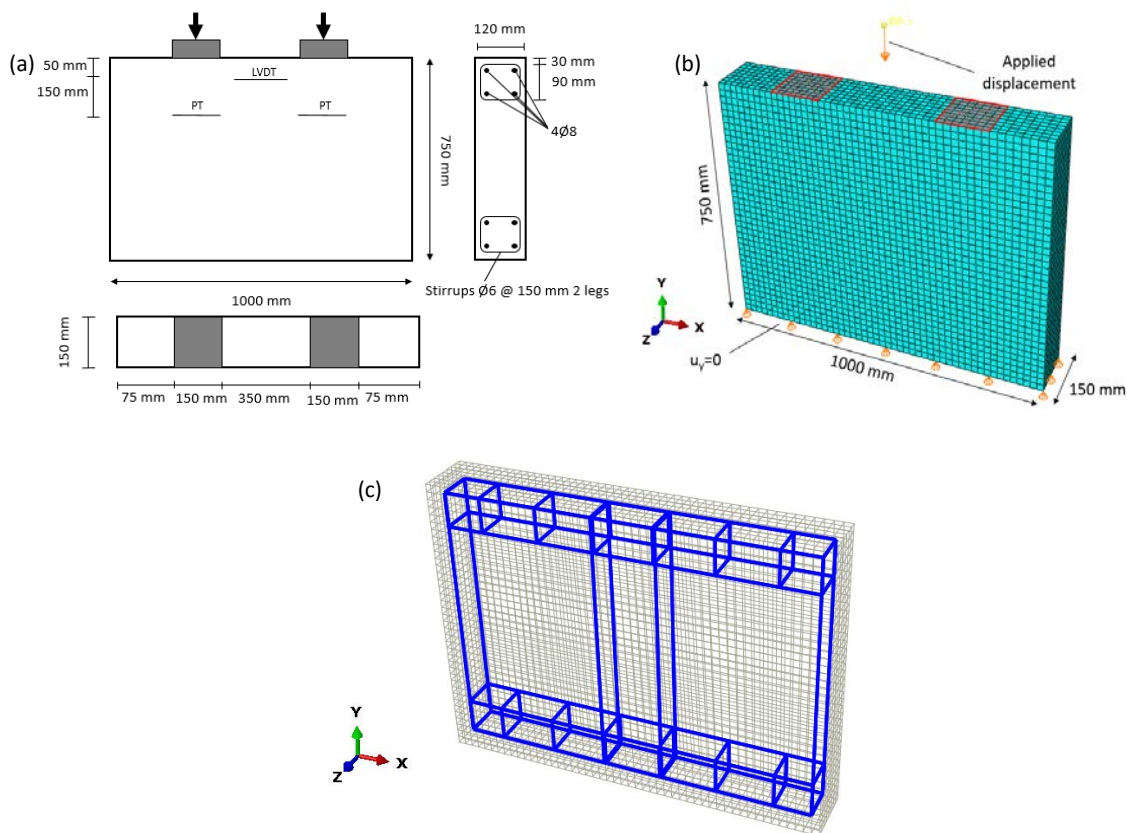

Figure 6 – Segment test (a) Test set up (b) meshed model and boundary conditions (c) meshed model reinforcement

The non-linear model is set by 20,000 elements, the concrete is modelled using C3D8R hexahedral elements and the steel rebar are reproduced with 2-noded 3D linear truss elements (T3D2) embedded into the solid elements. The embedded region constraint method available in ABAQUS is used to join the reinforcement with concrete. In Figure 6b is shown the meshed model and the boundary conditions: displacement is restricted at the bottom face (u_y=0). For the

sake of convergence, the load is applied by displacement control on a top 150 x 150 mm surface. In Figure 6c the meshed model showing the reinforcement distribution is presented.

The cracking loads due to spalling (P_{spall}) and splitting stresses (P_{sp}) as well as maximum load (P_{max}) are presented in Table 2. Besides, the maximum crack opening for spalling (w_{spall}) and splitting (w_{sp}) obtained experimentally and numerically are gathered. In the numerical model, spalling cracks, which appear between the load pads, and splitting cracks, which are produced under the load pads, were measured as the relative separation between two adjacent nodes in the element in which the plastic strain is detected.

Table 2 – Numerical loads and crack opening (relative error respect to the experimental results, negative values indicate that the numerical model overestimates the experimental result)

Type	P_{spall} [kN]	w_{spall} [mm]	P_{sp} [kN]	w_{sp} [mm]	P_{max} [kN]
PC	725 *(-3.1%)*	1.60 (7.0%)	1901 (-13.2%)	-	1901 (-13.2%)
PFRC	692 *(-10.2%)*	0.26 (7.1%)	1476 (8.0%)	0.84 (6.7%)	1995 (-0.7%)
PFRC+RC	695 *(-32.4%)*	0.36 (12.5%)	1610 (-1.9%)	0.62 (13.9%)	1895 (-2.1%)

Crack pattern at failure for PFRC are shown in Figure 7. The results reported in Table 2 confirm that the model tends to overestimate load capacities (from 0.7% to a maximum of 32.4%) whilst the crack widths resulted to be estimated from the safe side (with a maximum relative difference of 13.9%); these differences are properly covered in design stage by considering the proper safety factors. Therefore, the agreement between experimental and numerical results is acceptable from designing perspective. In this sense, it should be remarked that damage level of the left side of Figure 7a, particularly the splitting area, is more severe than that observed in the right side; latter being more aligned with that obtained in the numerical simulation. This asymmetrical response might be due to a non-desired (technically unavoidable though) imperfections at the support contact are and/or slight deviations of the load position. It should be also highlighted that the damage pattern depicted in Figure 7a corresponds to a post-failure loading regime, whose simulation is challenging and out of the scope of this research. In this regard, loads and cracking patterns expected at pre-failure stage are those interesting from the design point of view.

The results presented in this section show that the model can reproduce the global response of the segment when induced by concentrated loads, reproducing splitting and spalling stresses properly.
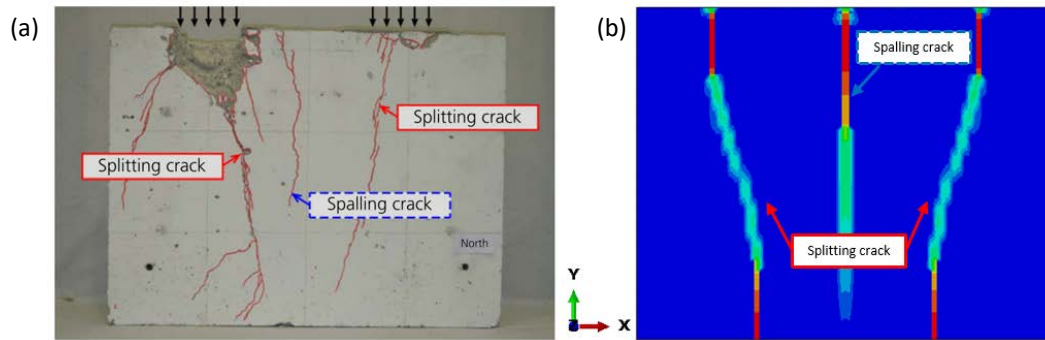
Figure 7 – Crack pattern (a) experimental test (b) model

3.3.   FULL SCALE CURVED SEGMENT CONFORTI ET AL., 2016)

In order to evaluate the model with a curved segment subjected to concentrated loads another experimental research work carried out by Conforti et al. [30] was used. Again, the contribution of polypropylene fibres in controlling the spalling is evaluated. To this end, a test is performed on a curved segment of 1810 mm length (internal diameter of 3200 mm), 1200 mm height and 250 thick subjected to concentrated loads by means of two loading shoes (500 x 250 mm). The segment is cast with 10 kg/m^3 polypropylene fibres, 49.9 N/mm^2 f_{cm} and 2.97 and 4.61 N/mm^2 for f_{R1m} and f_{R3m} respectively, according to EN-14651:2005. Figure 8a presents the test configuration, geometry and the position of the measure devices for detecting and measuring the crack opening: potentiometric transducers (PTs) for segment shortening in vertical direction and linear differential transformers (LVDTs) for spalling cracks.
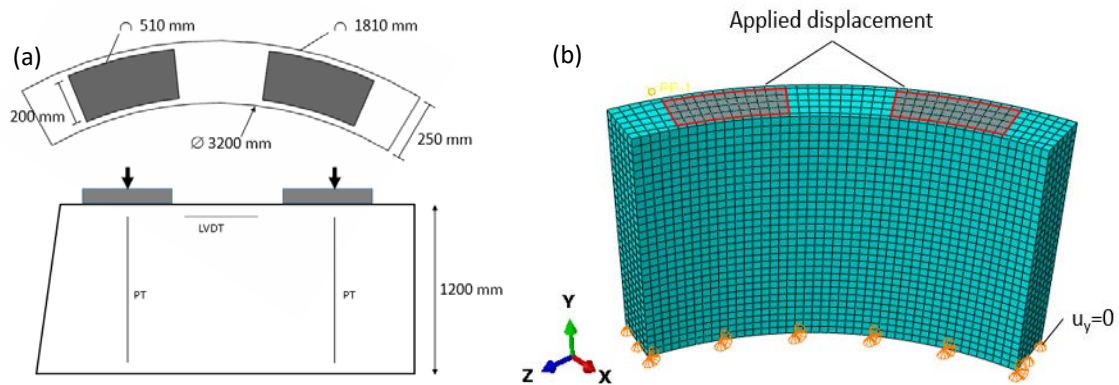

Figure 8 – Segment test (a) Test set up (b) meshed model and boundary conditions

8,100 C3D8R hexahedral elements were used for modelling concrete (Figure 8b). For the sake of simplicity and to obtain a regular mesh, the original geometry was changed and a regular geometry is used. This simplification has negligible influence on local behaviour which do not affect the results of splitting and spalling phenomena that are produced under the loading zone and between pads. In order to reproduce the experimental test conditions the only boundary conditions adopted is zero displacement at the segment bottom layer (u_y=0). The load is apply by

displacement control on top surfaces, representing the shoes, in order to guarantee a proper convergence (Figure 9b).

In Figure 9a the load - vertical displacement is presented. It is worth noticing that the model performs similarly to the experimental one up to 1200 kN, the P_{spall} is 995 kN and 979 kN for both experimental and numerical (-1.60%) and the P_{sp} was 1600 kN in the experimental test whereas 1585 kN is registered in the model (-0.93%). In the actual project the operational load (P_{nom}) and the accidental load (P_{acc}) were 785 kN and 1130 kN respectively. The spalling crack is measured and depicted in Figure 9b. In the numerical model, spalling cracks, which appear between the load pads (Figure 10b), was measured as the relative separation between two adjacent nodes in the element in which the plastic strain is detected. The spalling crack at P_{acc} (1130 kN) is 0.05 mm and the registered in the numerical model is 0.034 mm. Figure 10 shows the crack pattern obtained in the experimental and numerical test.
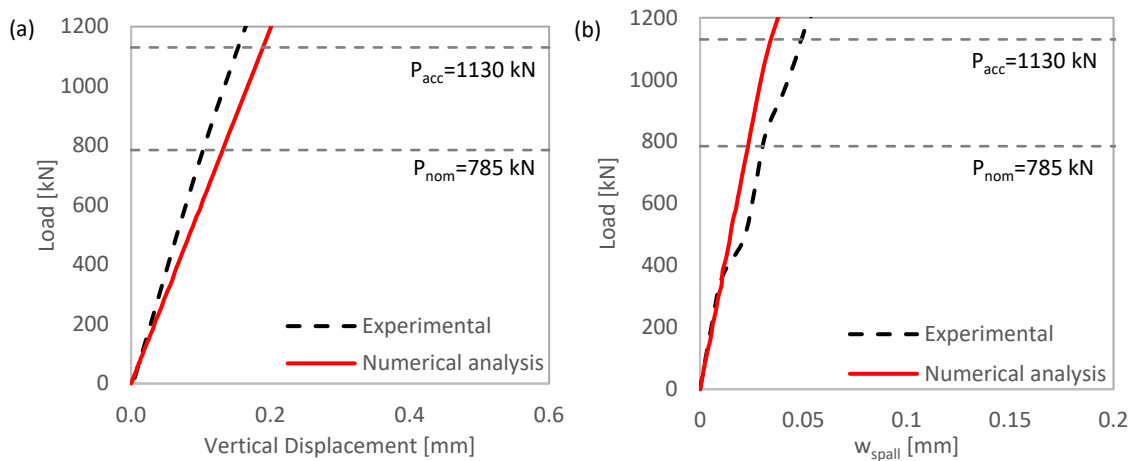

Figure 9 – Experimental and Numerical comparison (a) Load-vertical displacement (b) Load-spalling crack opening
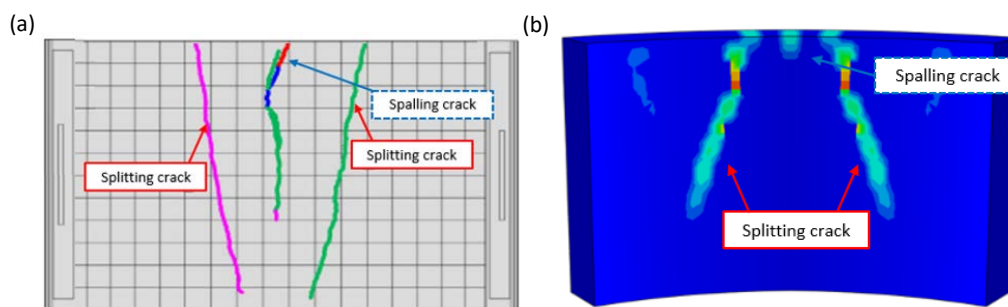

Figure 10 – Crack pattern (a) experimental test (b) model

According to the results presented in Figures 9-10, it can be remarked that the model can reproduce properly the mechanical response of FRC curved tunnel segment and the crack pattern that is developed when are subjected to concentrated loads.

Alejandro Nogales Arroyo

4. NUMERICAL PARAMETRIC STUDY ON FRC AND RC/FRC SEGMENTS SUBJECTED TO CONCENTRATED LOADS

4.1. SEGMENT GEOMETRY

The segment geometry and jack configuration are both taken from precast segment of an actual metro tunnel lining under construction. Since there are no point load tests conducted on the actual segment the results presented in Section 3 allow to validate FE model for precast segments under concentrated loads. The segment has 4075 mm inner radius, is 1500 mm width (tunnelling direction), 350mm thick and 4010 mm of arc-length (see Figure 11). The Japanese configuration [27] has been used for the TBM jacks distribution, this consisting in four 222 x 500 mm rectangular pads placed at 42 mm from the internal edge.
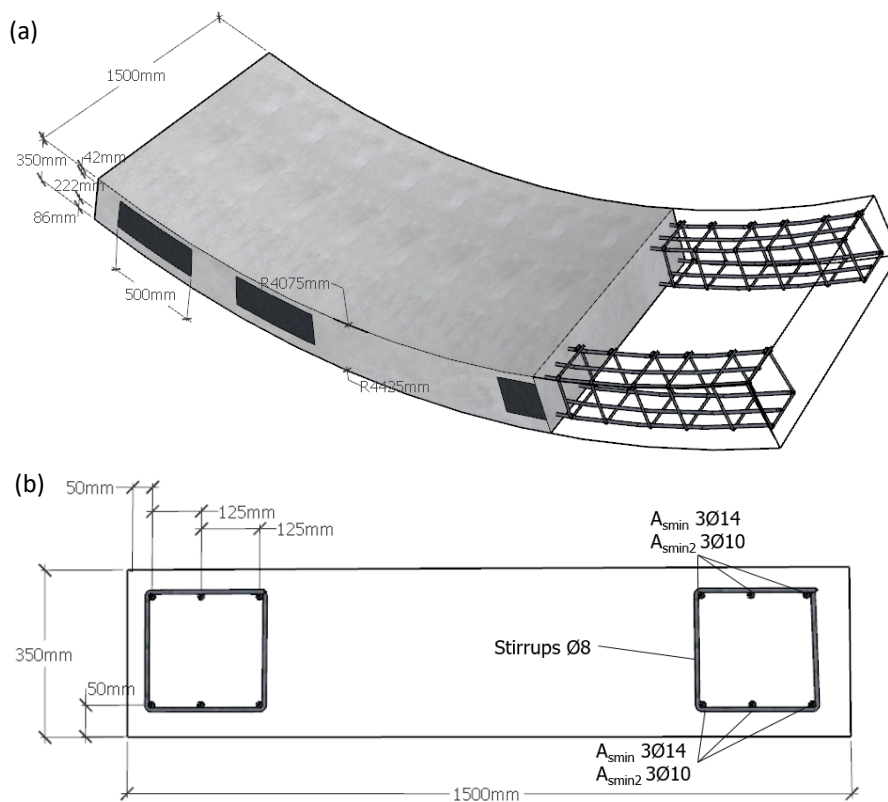

Figure 11 – Geometrical properties of the segment (a) general layout and (b) cross section and reinforcement distribution

4.2. MATERIALS

A C50/60 concrete has been used for the production of these segments; thus, according to the *fib* MC-2010, the values $f_{ctm} = 4.07$ N/mm^2, f_{cm} 58 N/mm^2 and $E_{cm} = 32900$ were assumed. The FRC strength classes 1, 3 and 5 (related to f_{R1k}) with f_{R3k}/f_{R1k} ratios a, b, c, d and e (see *fib* MC-2010) were considered for simulating different FRC performances (see Figure 12), these resulting in a total of 16 different concretes (15 FRC + 1 PC). The commonly accepted ratio $f_{Rk}/f_{Rm} = 0.7$ was used to estimate f_{Rm}. Thus, mean values of the crack widths (w_m) were obtained from the

numerical simulations. For design checks, if required, the characteristic value of w (w_k) could be estimated as $w_k = \beta \cdot w_m$, β being 1.7.
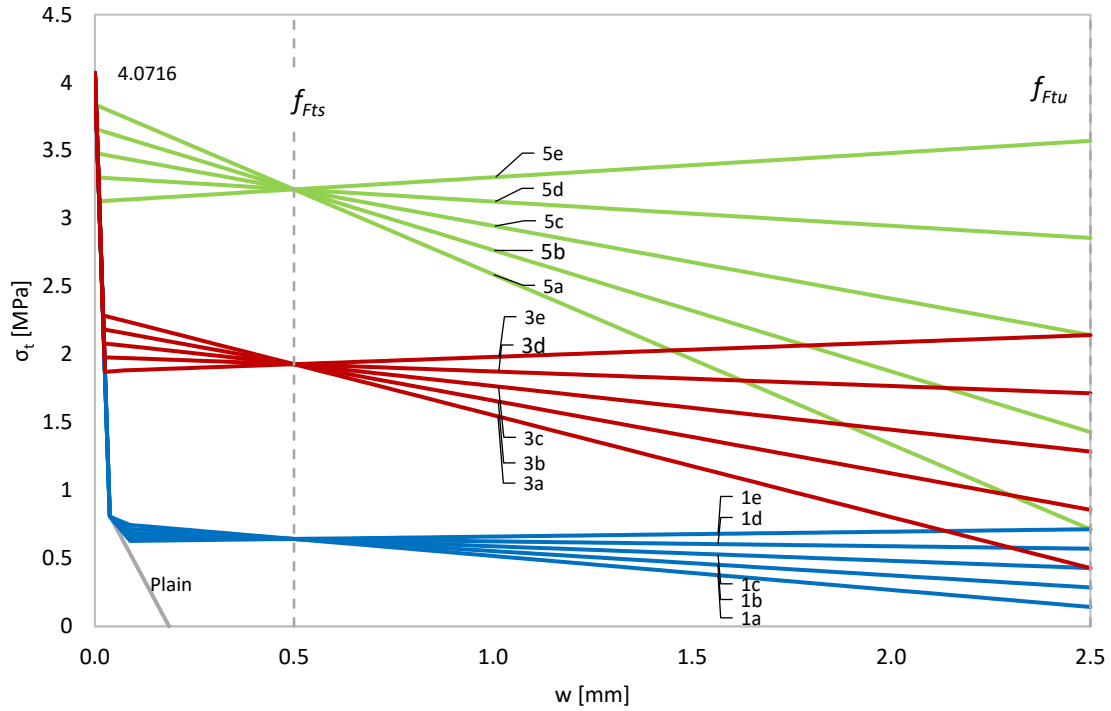

Figure 12 – Tensile constitutive equations of concrete mixes

Furthermore, aiming at optimising the reinforcement configuration, the hybrid reinforcement (RC+FRC) is also considered. Figure 11 b shows the segment rebar configuration, this being composed by two chords made by 2x3Ø14 curved rebar with Ø8@200mm stirrups, with a clear cover of 50mm. This amount (per face) corresponds to the minimum amount ($A_{s,min}$) required by *fib* MC-2010 to guarantee the ductile response. This minimum amount is computed with Equation 1, *b* being the segment width (1500 mm), *d* the effective depth and f_{yk} = 500 MPa is the characteristic value of the steel yielding stress. The reinforcement ratio, ρ_s, is calculated as Equation 2, where *h* corresponds to the segment height. It must be highlighted that the contribution of the fibres has been disregarded when computing the minimum amount of steel rebars (notice that Equation 1 do not account for the post-cracking strength of the FRC). In this sense, Liao [60,61] proposed a method for assessing the minimum reinforcement of hybrid segments that could be used if an optimized value of $A_{s,min}$ was to be required. Additionally, a ratio of $\rho_{s,min}/2$ (2x3Ø10 each face) has also been included into the analysis.

$$A_{s,min} = 0.26 \cdot b \cdot d \cdot \frac{f_{ctm}}{f_{yk}} \tag{1}$$

$$\rho_{s,min} = \frac{A_{s,min}}{b \cdot h} \tag{2}$$

4.3. MODEL DESCRIPTION

Figure 11 shows a general view of the mesh and boundary conditions of the segment model. Simplifications must be taken in order to guarantee a robust model with a non-dependent mesh able to reduce computational calculation time while giving accurate results. Only a single segment is modelled, the interactions with the surrounding segments at longitudinal and radial joints are not taken into account, these interactions has negligible influence on local behaviour which do not affect the results of splitting and spalling phenomena that are produced under the loading zone and between pads, besides this assumption helps to avoid convergence problems and reduce computational time. For the same reason, in spite of setting a regular mesh, bolt and gasket holes are not modelled.

In order to apply concentrated loads, thrust loads can be modelled as contact between packers and segment, which can produce convergence problems. Instead, using a quasi-static solver, the load is applied by means of displacement control loading on top surfaces representing the bearing pads.

Boundary conditions applied on the segment are: (1) vertical displacement restricted (u_y=0) at the bottom, (2) vertical displacement on top 222 x 500 mm surfaces (see Figure 13).
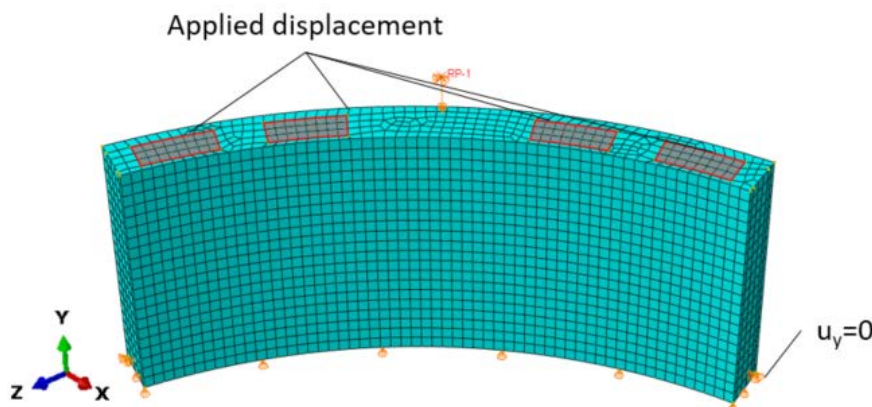

Figure 13 – Meshed model and boundary conditions

The concrete is modelled using C3D8R hexahedral solid elements and the 2 nodes 3D linear truss elements T3D2 are chosen for reinforcement, embedded constraint is used for join linear and solid elements. The embedded constraint creates a perfect bond between concrete and steel. After a mesh convergence analysis using the explicit solver implemented in ABAQUS (quasi-static analysis), a 70 mm size element has resulted to be suitable in terms of computational costs and preciseness.

5. NUMERICAL RESULTS AND DISCUSSION

5.1. CENTRED THRUST

The first crack is due to spalling stresses between the two inner load pads, this cracking load ($P_{cr} = P_{spall}$) is 1975 kN for each pad and this is taken as reference load for all cases of analysis since this is independent of the reinforcement configuration. The so called nominal load (P_{nom}) is the TBM work load, which is 480 kN for each pad in the actual project, and should be lower than the cracking load so that the integrity of the segment can be guaranteed. Within the context of this analysis, the ratio P_{cr}/P_{nom} has been established to be 1.0. In this sense, although P_{nom} is far below P_{cr}, it must be remarked that the same ring geometry and segment configuration could be used in other tunnels with more demanding TBM thrust conditions. Figure 14 shows the non-dimensional load ($P/P_{spalling}$) - axial displacement of the jack (δ). The *c* class has been taken as reference ($0.9 \leq f_{R3}/f_{R1} < 1.1$) since, according to the *fib* bulletin 83, this allows guaranteeing that FRC segments to show a ductile response in case of cracking due to bending.

As it can be noticed in Figure 14, P_{spall} is far from the maximum bearing load, which ranges between 2.5 and 3.2 times depending on the fibre content. The accidental thrust (P_{acc}) depends on the TBM type and equipment installed; the ratio P_{acc}/P_{nom} use to range between 1.2 up to 2.0. The higher ratio ($P_{acc} = 2 \cdot P_{nom} = 3950$ kN) has been considered in this analysis. The P/P_{spall} - δ resulted to be identical for all mixes up to $P/P_{spall} = 2.5$.
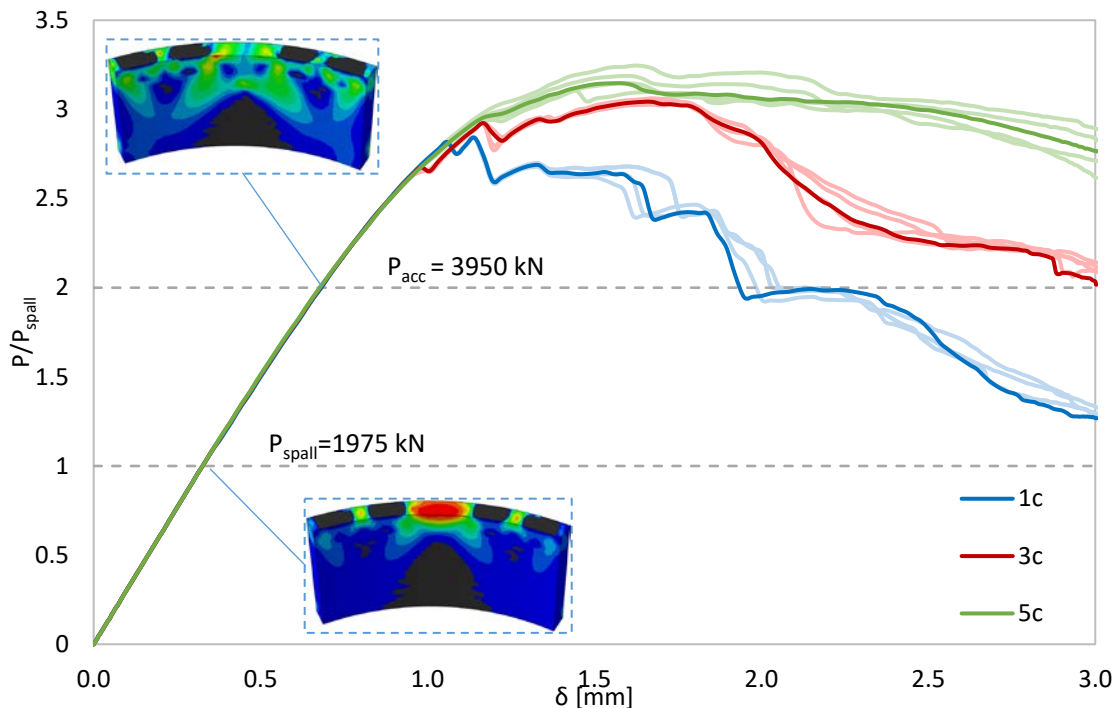

Figure 14 – Non-dimensional load-displacement curve for FRC. Stress pattern for P_{spall} and P_{acc}

The deformed shape of the segment is depicted for P_{spall} for stresses in tangential direction (S22 in MPa) and the crack pattern (plastic strain in tangential direction) in Figure 15a and 15b respectively, as aforementioned the region between the inner thrust pads is where spalling stresses

concentrate and once it exceeds the tensile strength of the concrete the crack appears. In this case, the concrete is able to reach the tensile strength (4.07 MPa) because the tangential direction is the only prevented from displacement (symmetry) while the radial and the axial are both free, all the stress is born in tangential direction.
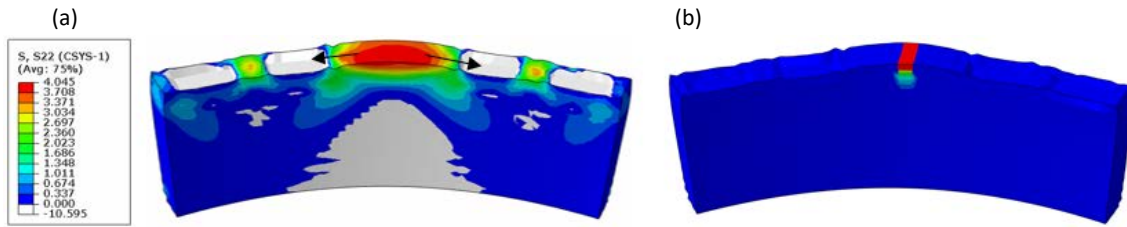

Figure 15 – Segment deformed shape for P_{spall} (a) Tangential tensile stresses (b) plastic strain - crack pattern

Figure 16 gathers the (P/P_{spall}) - spalling crack opening (w_{spall}). The crack opening is based on the assumption that only one spalling crack occurs, which is measured as the tangential relative separation between two adjacent nodes (separated 60 mm) of the element for which the plastic strain is first detected. This means that the concrete tensile strength has been exceeded and concrete cracked thereof [9,12].
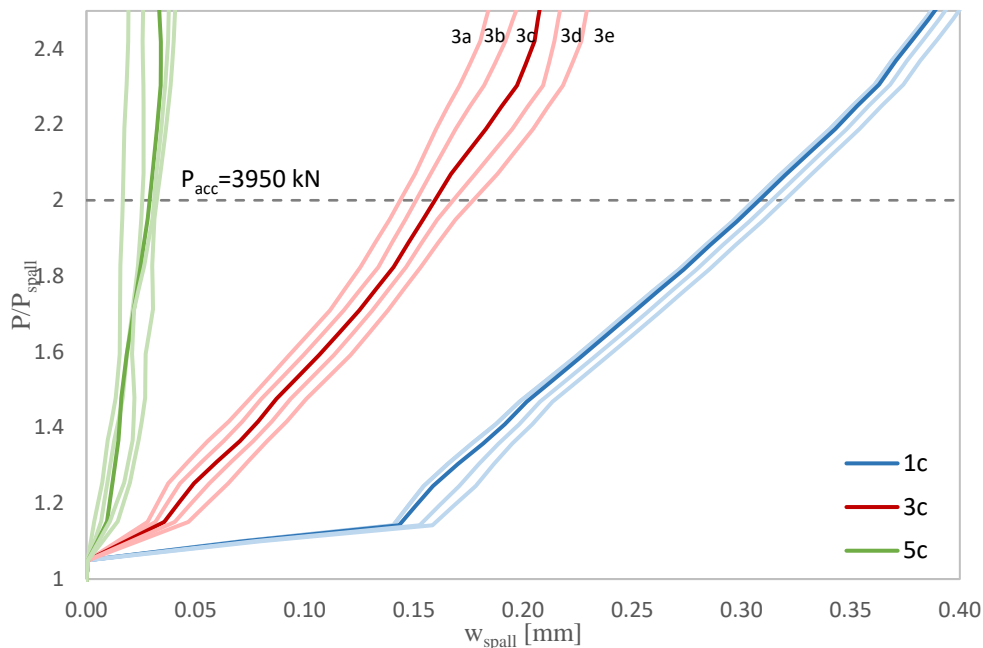

Figure 16 – Non-dimensional load – spalling crack opening

The results presented in Figure 16 allows confirming that f_{R1} has a great influence in cracking control while the strength ratios f_{R3}/f_{R1} do not play a significant role (once f_{R1} is defined). This was expectable since f_{R3} is a strength parameter associated to a 2.5 mm crack width and, therefore, beyond the range accepted for service conditions (w ≤ 0.5 mm). In this regard, the maximum w_{spall} detected for P_{acc} are 0.38, 0.30, 0.16, and 0.03 mm for Plain, 1c, 3c, and 5c, respectively.

In view of these results, the 3c FRC class can be the more advantageous reinforcement solution for this segment from both economic and technical points of view, as: (1) a crack with of 0.16 mm is acceptable for an exceptional load (unless very strict durability and waterproof requirements are established) and (2) a near 50% of crack width reduction respect to the 1c FRC class represents a great efficiency of the reinforcement for a low increment of the amount fibres necessary to reach the 3c FRC strength class. In view of this, the *c* type is fixed throughout the remaining analysis. This is aligned with the preference of the *fib* Bulletin 83 towards this FRC performance class for tunnel segments.

Splitting cracks under the inner thrust pads are detected for P_{sp} = 2173 kN (1.1P_{nom}). Because of the tri-axial state of stresses the cracking is produced before reaching the tensile strength in any direction. In Figure 17 a S11 stands for stress in radial direction (MPa). In this case, the splitting crack opening (w_{sp}) is calculated as the radial relative displacement between nodes placed in inner and outer faces where splitting cracks appear [3] (see Figure 17b).
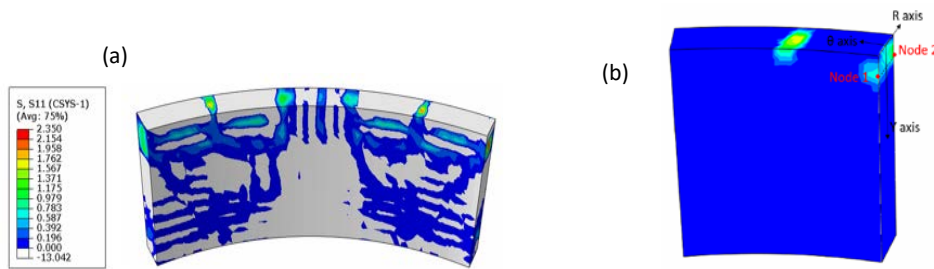
Figure 17 – Segment deformed shape for P_{sp} (a) Radial tensile stresses (b) Radial plastic strain and crack measurement scheme.

The P/P_{sp} - w_{sp} curves are represented in Figure 18. The maximum w_{sp} numerically detected for P_{acc} is lower than 0.05 mm and no significant differences are noticed between FRC strength classes. Hence, the spalling cracks appear to be those governing the post-cracking tensile strength requirements.

Figure 18 – Non-dimensional load – splitting crack opening

Alejandro Nogales Arroyo

5.2. ECCENTRIC THRUST

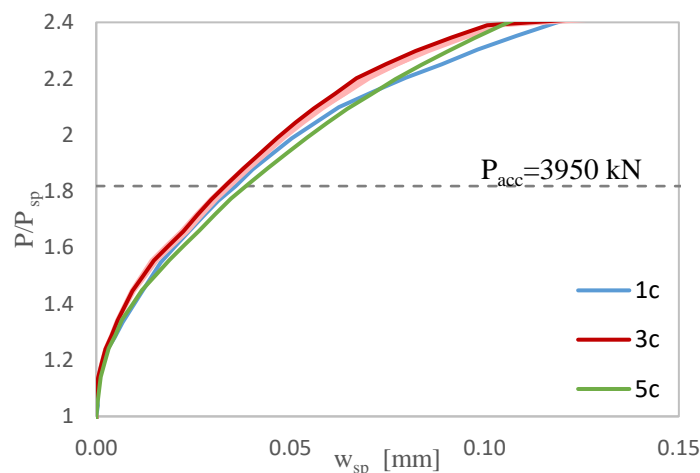Thrust has been simulated by considering an eccentricity (e) of 30 mm inwards (e=-30 mm) and outwards (e=+30mm) as Figure 19 shows. Both spalling and splitting cracks have been compared to centred thrust situation. Figure 20 depicts the relation of $P_{cr}/P_{spall,e=0}$ with the eccentricity for FRC.
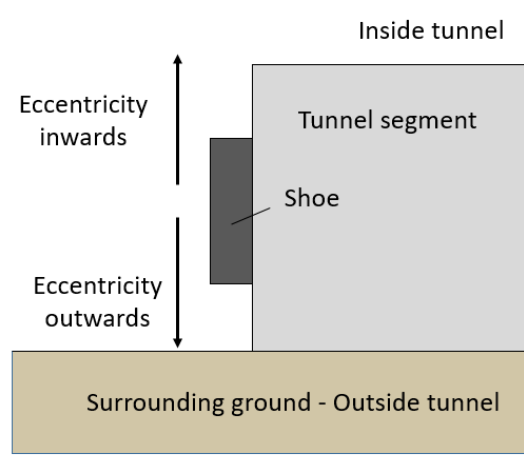

Figure 19 –Side view tunnel segment. Eccentricity scheme.
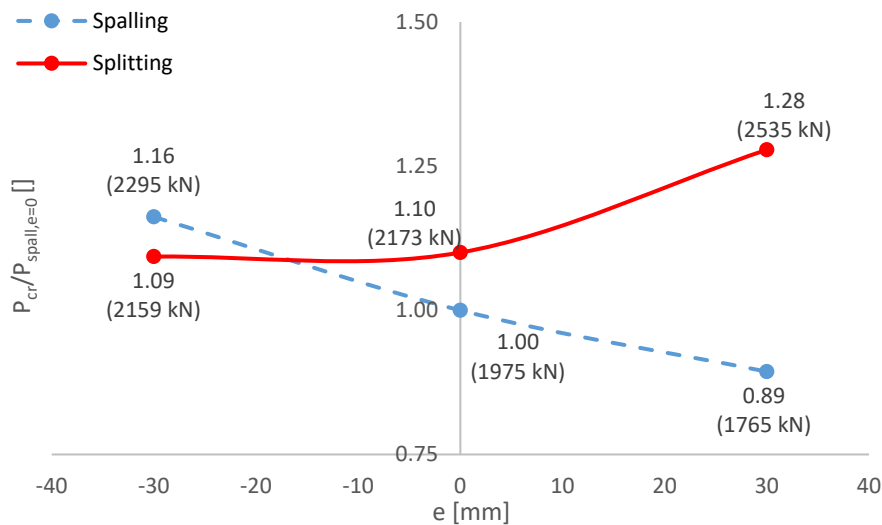
Figure 20 –Cracking load/spalling cracking load for e = 0 – eccentricity relationship for FRC.

As it occurred for centred loading ($P_{spall,e=0}$ = 1975 kN), according to Figure 20, for e > 0 the first crack is due to spalling stresses ($P_{spall}/P_{spall,e=0}$ = 0.89; e = +30 mm) and the second is due to splitting ($P_{sp}/P_{sp,e=0}$ = 1.28; e = 30 mm), whilst for e < 0 the crack appears firstly due to splitting stresses ($P_{sp}/P_{sp,e=0}$ = 1.09; e = -30 mm) followed by a spalling crack ($P_{spall}/P_{spall,e=0}$ = 1.16; e = -30 mm). It must be noticed that for e < 0 the cracking resistance increases respect to the centred thrust; this, nonetheless, must be taken with precaution since the existence of the gasket could slightly modify these results.

Figure 21 gathers $P/P_{spall,e=0}$ – spalling crack width relationship for the different values of the eccentricity analysed. Likewise, Table 3 gathers the P_{spall} loads and the spalling crack widths for P_{acc} ($w_{spall,acc}$) compared to those obtained for the centred thrust ($P_{spall,e=0}$ and $w_{spall,acc,e=0}$, respectively).

According to the results presented in Figure 21, it is remarkable that higher FRC strength classes have the ability to reduce the eccentricity effect on the crack openings. For instance, the 5c FRC class has a $w_{spall,acc}/w_{spall,acc,e=0}$ ratio of 1.06 and 1.00 for both e=+30mm and e=-30mm, which means that the effect of the eccentricity is controlled due to the great tensile residual strength of the FRC. Contrarily, the effect of eccentricity on the crack width is less effective as the FRC class is reduced.
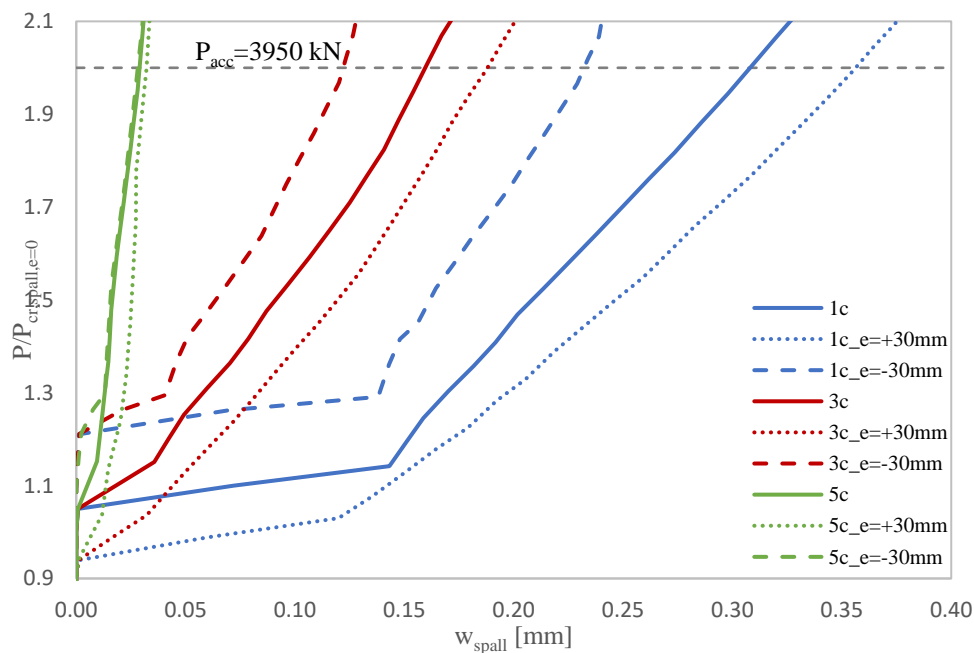
Figure 21 – Load/spalling cracking load for e = 0 – spalling crack width relationship

Table 3 – Spalling cracking Load and maximum crack width for eccentric loading

		P_{spall} [kN]	$P_{spall}/P_{spall,e=0}$	$w_{spall,acc}$ [mm]	$w_{spall,acc}/w_{spall,acc,e=0}$
e=+30 mm	1c	1765	0.89	0.35	1.16
	3c			0.18	1.12
	5c			0.04	1.06
e=-30 mm	1c	2160	1.09	0.23	0.76
	3c			0.12	0.75
	5c			0.03	1.00

Based on the results presented in Figure 21 and Table 3, it can be noticed that as the FRC strength class increases the spalling crack width is reduced drastically. The 3c FRC (see Figure 22) results to be the most suitable for controlling the crack width (while optimizing the amount of fibres) since the crack widths ranges between 0.12 mm (e = -30 mm) and 0.18 mm (e =+ 30

mm), which is an acceptable range (w < 0.20 mm) for dealing with the posterior service conditions; this considering that the probability of reaching P_{acc} must be, by definition, very low.

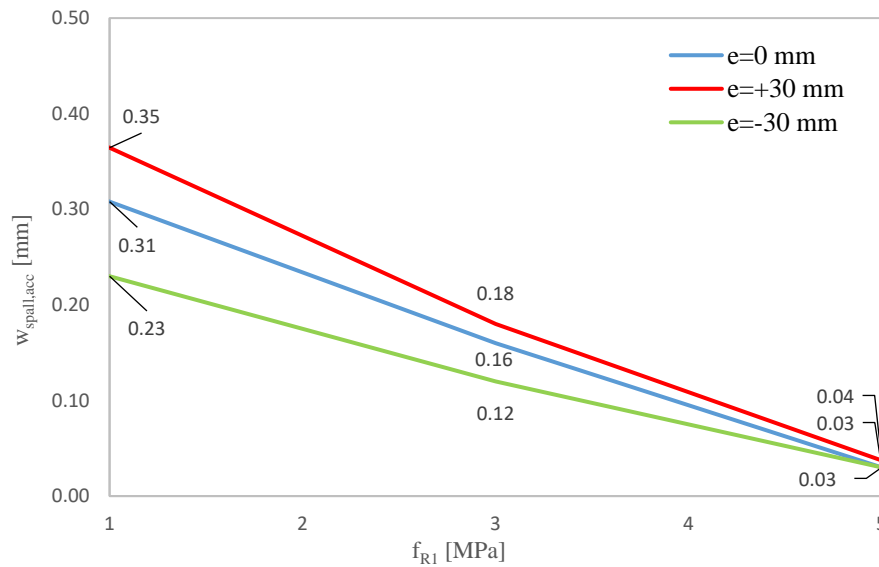*Figure 22 – Relation between f_{R1} and $w_{spall,acc}$ for P_{acc} considering different eccentricities*

Table 4 gathers the P_{sp} loads and the splitting crack widths for P_{acc} ($w_{sp,acc}$) compared to those obtained for the centred thrust ($P_{sp,e=0}$ and $w_{sp,acc,e=0}$, respectively). Figure 20 shows the non-dimensional $P/P_{sp,e=0} - w_{sp}$ relationship for the different values of the eccentricity considered.

The results shown in both Figure 23 and Table 4 reveal that eccentric thrust has a relevant influence on splitting cracks width whilst the FRC strength class influence barely affects the response (except for the 5c FRC and e=-30mm, which allows a better control of $w_{sp,acc}$). In this regard, $w_{sp,acc}$ increases up to 3.3 and 6.0 times $w_{sp,acc,e=0}$, for e=+30mm and e=-30mm respectively. Although $P_{sp,e=+30}$ is higher than $P_{sp,e=0}$, the former reaches higher values of crack width. For e<0, the splitting crack is produced at the same load level ($P_{sp,e=-30}/P_{sp,e=0} = 1.00$); however, e>0 thrust lead to a greater crack growth in comparison to centred thrust.
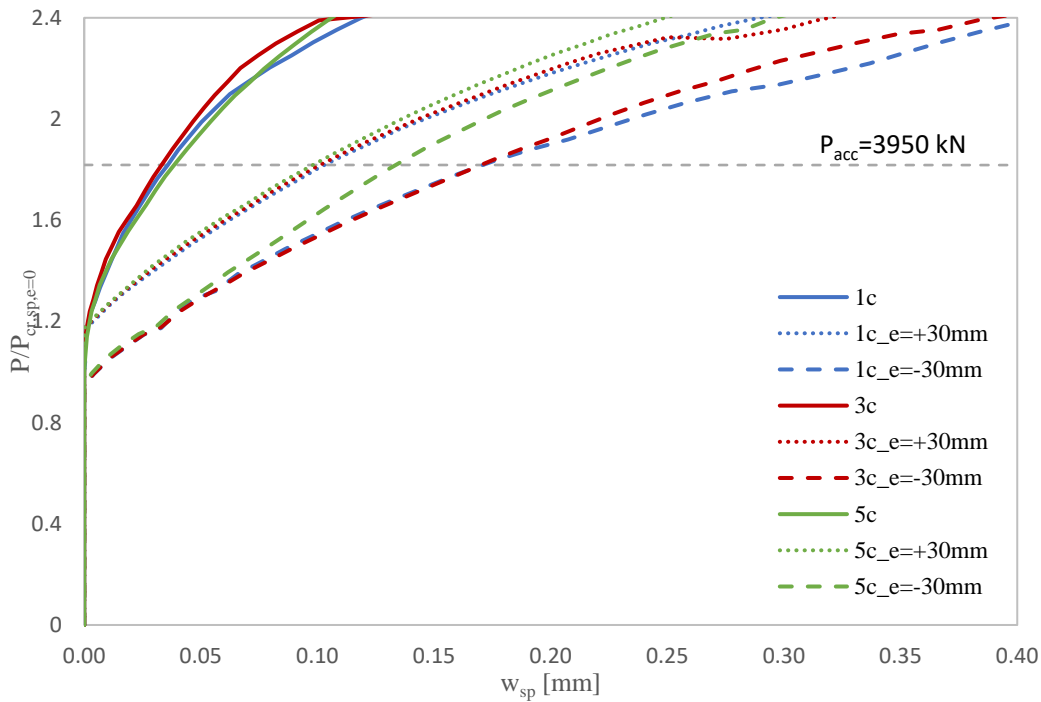
Figure 23 – Non-dimensional load – splitting crack opening for different eccentricities

Table 4 – Splitting cracking load and maximum crack width for eccentric loading

		P_{sp} [kN]	$P_{sp}/P_{sp,e=0}$	$w_{sp,acc}$ [mm]	$w_{sp,acc}/w_{sp,acc,e=0}$
	1c			0.10	3.33
e=+30mm	3c	2535	1.16	0.10	3.33
	5c			0.10	3.33
	1c			0.18	6.00
e=-30mm	3c	2159	1.00	0.18	6.00
	5c			0.13	4.33

5.3. HYBRID REINFORCED SEGMENT

Spalling cracks have proven to be the most concerning (wider) cracks during thrust phase for this segment geometry and thrust transfer configuration. In order to reduce these cracks while maintaining a competitive reinforcement configuration from both economical and time-saving perspectives, hybrid reinforcement (R/FRC) can be an optimal solution. Segments cast with plain, 1c, 3c and 5c FRC classes combined with two rebar configurations $\rho_{s,min}$ and $\rho_{s,min}/2$ (see Figure 11) are simulated with centred and eccentric thrust (e=±30mm).

Figure 25 gathers the spalling crack loads of hybrid configurations for centred and e=±30mm. The R/FRC solutions are able to increase P_{spall} compared to FRC in the centred configuration (2067 kN), in case of e=+30mm the cracking load for hybrid solution with $\rho_{s,min}$ (FRC+ $\rho_{s,min}$) is less affected by the eccentric thrust than the other solutions. Regarding to e < 0, it is worth noticing

that the cracking load remains the same for hybrid solutions respect to the centred thrust and, as aforementioned, must be taken with precaution since the existence of the gasket could slightly modify these results.
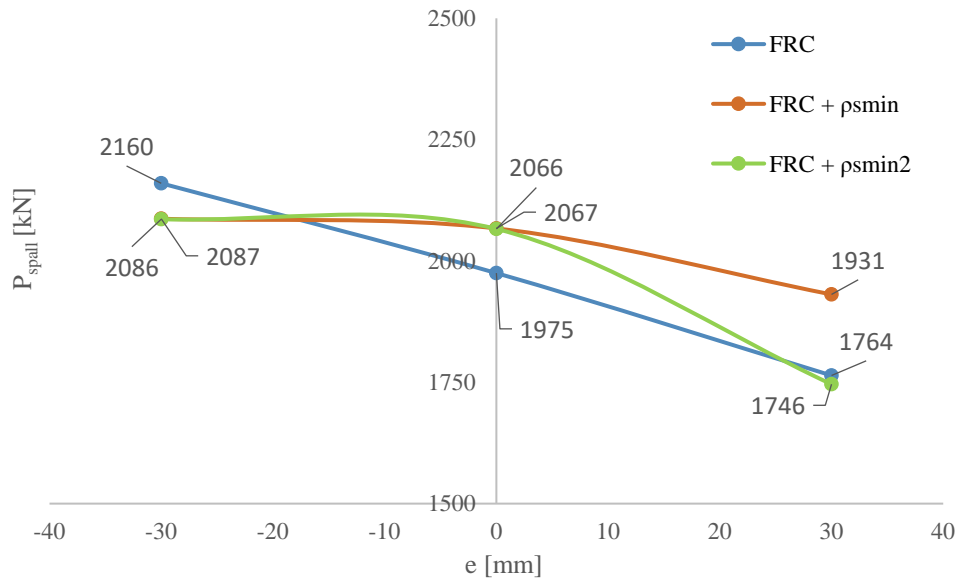

Figure 25 – Spalling cracking load for FRC and R/FRC segments for different eccentricities

Figure 26 depicts the $P/P_{spall,e=0} - w_{spall}$ relationship for centred thrust for all types of FRC. It can be noticed that the hybrid reinforcement is able to control better the crack width if this is compared to the FRC configuration for all reinforcement and eccentricity configurations; particularly. Figure 27 present the spalling crack width for P_{acc} for the whole range of eccentricities. As for the results presented in Figure 16, the spalling crack opening is based on the assumption that only one crack occurs in the spalling cracked regions and measured as the tangential relative separation between two adjacent nodes. In this sense, in case of hybrid reinforcement the assumption is conservative since multiple cracks are expected as a result of the collaboration between fibres and rebar.

The results of Figure 26 and Figure 27 allow confirming that the rebar reinforcement has impact in reducing the crack width for low FRC strength classes (1c); contrarily, the rebar reinforcement has less efficiency for higher FRC strength classes (3c and 5c) since the crack width is already well-controlled ($w_{spall} \leq 0.20$ mm) by solely the fibre reinforcement (FRC). Nonetheless, the R/FRC solution for medium and high FRC strength classes is a suitable solution when either very strict crack width limitations are imposed (e.g., $w \leq 0.15$ mm) and/or when traditional steel reinforcement is also required to resist bending moments superior to the cracking bending moment (M_{cr}); for which, the FRC as unique reinforcement can be an uneconomical alternative [60].
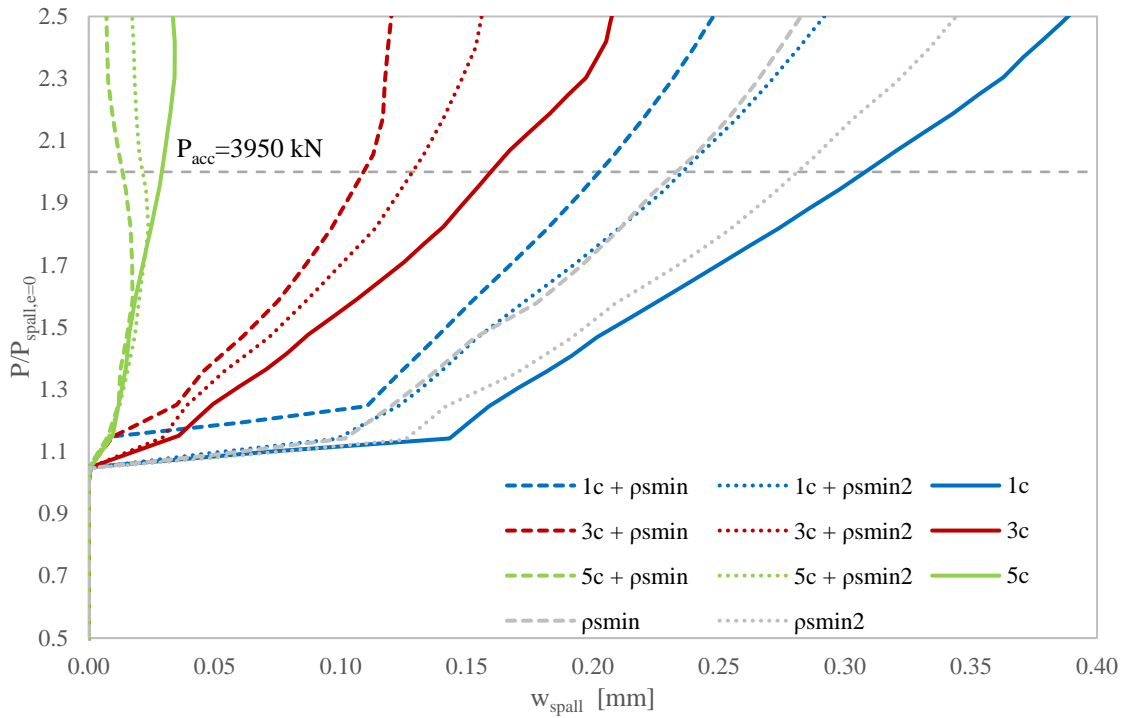
Figure 26 – Non-dimensional load – spalling crack opening for RC and R/FRC segments (for e = 0)
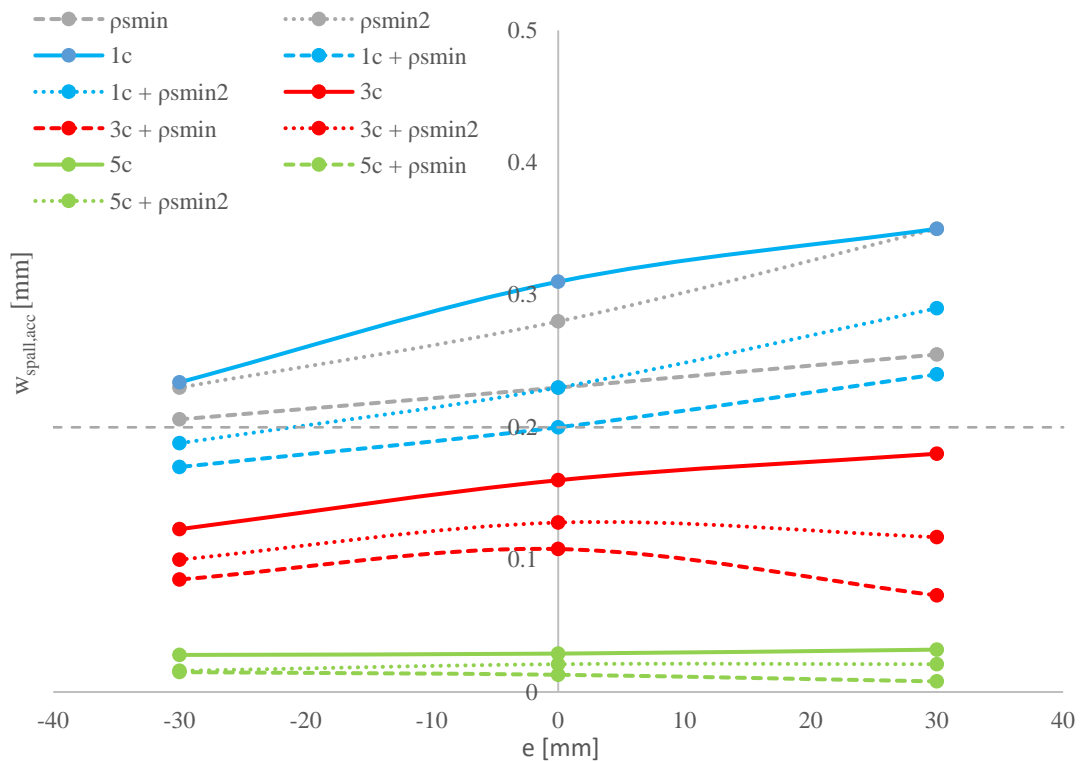

Figure 27 – Spalling crack opening – eccentricity for, 1c, 3c and 5c hybrid solutions

6.   CONCLUSIONS

The thrust phase of TBM-bored tunnels supported with segmental linings considering different FRC strength classes and hybrid solutions (R/FRC) is investigated from a numerical point of view by means of a 3D non-linear FE model contrasted with experimental results. By using this model, spalling and splitting cracks for a range of thrust eccentricities are estimated and compared according to the different reinforcement configurations.

Based on a particular segment geometry and a thrust transfer configuration, the following conclusions can be drawn:

- The residual flexural strength for a crack width of 0.5 mm (f_{R1}) has resulted to have a great influence in cracking control whilst the ratio f_{R3}/f_{R1} seems not play a significant role. This is of relevant importance when deciding the type of fibre (material and geometry) to be used since those that lead to higher f_{R1} would be more appropriate than those that perform better for larger crack widths.
- The spalling cracks appear to be those governing the FRC post-cracking tensile strength requirements. Eccentric thrust has a relevant influence on cracking performance; in this sense, attention must be paid for both cracking phenomena, specially, for splitting cracks for which cracks up to 6.0 times wider respect to the perfectly centred thrust have registered.
- Hybrid reinforcement leads to crack reduction and this can be considered as a suitable solution when severe crack width limitations are stablished for service.

It is worth noticing that the numerical simulations were carried out on a fixed segment geometry and bearing pads configuration; however, the abovementioned conclusions are also extendable to tunnels linings with other internal diameters and thicknesses and similar pads configurations considered.

ACKNOWLEDGEMENTS

REFERENCES

[1]   di Prisco, M, Plizzari G, Vandewalle L. Fibre reinforced concrete : new design perspectives. Mater Struct 2009:1261–81. https://doi.org/10.1617/s11527-009-9529-4.

[2] di Prisco M, Toniolo G. Structural applications of steel fibre reinforced concrete. Proc Int Work Milan, Italy 2000.

[3] Burgers R, Walraven J, Plizzari GA, Tiberti G. Structural behaviour of SFRC tunnel segments during TBM operations. Undergr Sp - 4th Dimens Metropolises 2007:1461–8.

[4] de la Fuente A, Blanco A, Pujadas P, Aguado A. Diseño óptimo de dovelas de hormigón reforzado con fibras para el revestimiento de túneles. Hormigón y Acero 2015;65:267–79. https://doi.org/10.1016/j.hya.2014.11.002.

[5] Chiaia B, Fantilli AP, Vallini P. Evaluation of crack width in FRC structures and application to tunnel linings. Mater Struct Constr 2008;42:339–51. https://doi.org/10.1617/s11527-008-9385-7.

[6] Blom CB. Design philosophy of concrete linings in soft soils 2002:70.

[7] de Waal RGA. Steel fibres reinforced tunnel segments for the application in shield driven tunnel linings. Technische Universiteit Delft, 2000.

[8] de la Fuente A, Blanco A, Armengou J, Aguado A. Sustainability based-approach to determine the concrete type and reinforcement configuration of TBM tunnels linings. Case study: Extension line to Barcelona Airport T1. Tunn Undergr Sp Technol 2017;61:179–88. https://doi.org/10.1016/j.tust.2016.10.008.

[9] Burgers R. Non-linear FEM modelling of steel fibre reinforced concrete. 2006.

[10] de la Fuente A, Pujadas P, Blanco A, Aguado A. Experiences in Barcelona with the use of fibres in segmental linings. Tunn Undergr Sp Technol 2012;27:60–71. https://doi.org/10.1016/j.tust.2011.07.001.

[11] Gettu R, Ramos G, Aguado A, García T, Barragán B. Steel Fiber Reinforced Concrete for the Barcelona Metro Line 9 Tunnel Lining. BEFIB 2004, Proc 6th RILEM Symp FRC 2004;RILEM Symp:1–46.

[12] Tiberti G. Conci prefabbricati in calcestruzzo fibrorinforzato per la realizzazione di gallerie. Università degli studi di Brescia, 2004.

[13] de Rivaz B, Meda A, Perruzza P, Rinaldi Z, Roumaldi P. Full scale tests on precast tunnel segment made in concrete reinforced with high strength steel fibres 2009.

[14] Caratelli A, Meda A, Rinaldi Z, Romualdi P. Structural behaviour of precast tunnel segments in fiber reinforced concrete. Tunn Undergr Sp Technol 2011;26:284–91. https://doi.org/10.1016/j.tust.2010.10.003.

[15] Beňo J, Hilar M. Steel fibre reinforced concrete for tunnel lining - Verification by extensive laboratory testing and numerical Modelling. Acta Polytech 2013;53:329–37. https://doi.org/1049 [pii].

[16] Hilar M, Vítek J, Vítek P, Pukl R. Load testing and numerical modelling of SFRC segments 2012:1–10.

[17] FIB - Working party 1.4.1. Precast Tunnel Segments in Fibre-Reinforced Concrete. Lausanne: Federation internationale du béton; 2017.

[18] Cavalaro SHP, Blom CB., Walraven J, Aguado A. Structural analysis of contact deficiencies in segmented lining. Packer behaviour under simple and coupled stresses. Tunn Undergr Sp Technol 2011;26:734–49.

[19] Sugimoto M. Causes of Shield Segment Damages During Construction. Int Symp Undergr Excav Tunn 2006:67–74.

[20] Plizzari GA, Tiberti G. Steel fibers as reinforcement for precast tunnel segments. Tunn Undergr Sp Technol 2006;21:438–9. https://doi.org/10.1016/j.tust.2005.12.079.

[21] Tiberti G, Plizzari GA, Walraven JC, Blom CBM. Concrete Tunnel Segments with Combined Traditional and Fibre Reinforcement. Tailor Made Concr Struct Solut Our Soc (FIB Symp 2008:605–10. https://doi.org/10.1201/9781439828410.ch37.

[22] Liao L, de la Fuente A, Cavalaro SHP, Aguado A, Carbonari G. Experimental and analytical study of concrete blocks subjected to concentrated loads with an application to TBM-constructed tunnels. Tunn Undergr Sp Technol 2015;49:295–306. https://doi.org/10.1016/j.tust.2015.04.020.

[23] Leonhardt F, Mönnig E. Berlin: Springer-Verlag; 1973 (Italian version: Leonhardt F, Mönnig E (1986) Casi speciali di dimensionamento nlle costruzioni in c.a. e c.a.p., vol. 2, Edizioni di Scienza e Tecnica, Milano). Tailor Made Concr Struct 1973:66–66. https://doi.org/10.1201/9781439828410.ch37.

[24] Iyengar K. Two-dimensional theories in anchorage zone stresses in Post- Tensioned prestressed beams. Heron 1962;32:45–56.

[25] Jamshidi M, Hoseini A, Vahdani S, de la Fuente A. Numerical-aided design of fiber reinforced concrete tunnel segment joints subjected to seismic loads. Constr Build Matreials 2018;170:40–54.

[26] Jamshidi M, Hoseini A, Vahdani S, de Santos C, de la Fuente A. Seismic fragility curves for vulnerability assessment of steel fiber reinforced concrete segmental tunnel linings. Tunn Undergr Sp Technol 2018;78:259–74. https://doi.org/10.1016/j.tust.2018.04.032.

[27] Slenders BMA. Modellering can boortunels (Dutch). Delft University of Technology and Projectorganisatie HSL-Zuid, 2002.

[28] Cavalaro SHP, Blom CB., Walraven J, Aguado A. Formation and accumulation of contact deficiencies in a tunnel segmented lining. Appl Math Model 2012;36(9):4422–4438.

[29] Conforti A, Tiberti G, Plizzari G. Combined effect of high concentrated loads exerted by TBM hydraulic jacks. Mag Concr Res 2016;68:1122–32. https://doi.org/10.1680/jmacr.15.00430.

[30] Conforti A, Tiberti G, Plizzari G, Caratelli A, Meda A. Precast tunnel segments reinforced by macro-synthetic fibers. Tunn Undergr Sp Technol 2016;63:1–11. https://doi.org/10.1016/j.tust.2016.12.005.

[31] Tiberti G, Conforti A, Plizzari GA. Precast segments under TBM hydraulic jacks: Experimental investigation on the local splitting behavior. Tunn Undergr Sp Technol 2015;50:438–50. https://doi.org/10.1016/j.tust.2015.08.013.

[32] Caratelli A, Meda A, Rinaldi Z, Spagnuolo S. Precast Concrete Tunnel Segments with GFRP Reinforcement. Tunn Undergr Sp Technol 2016;60:10–20. https://doi.org/10.1061/(asce)cc.1943-5614.0000803.

[33] Caratelli A, Meda A, Rinaldi Z, Spagnuolo S, Maddaluno G. Optimization of GFRP reinforcement in precast segments for metro tunnel lining. Compos Struct 2017. https://doi.org/10.1016/j.compstruct.2017.08.083.

[34] Spagnuolo S, Meda A, Rinaldi Z, Nanni A. Precast concrete tunnel segments with GFRP reinforcement. vol. 21. 2017. https://doi.org/10.1590/1679-78251783.

[35] Meda A, Rinaldi Z, Spagnuolo S, de Rivaz B. Precast concrete tunnel segments with GFRP reinforcement. ACI-Fib-RILEM Int Work 2018.

[36] Hemmy O. Sub-task 4.4 - Splitting of SFRC induced by local forces - Annex C Investigation of tunnel segments without curvature 2001:1–32.

[37] Schnütgen B, Erdem E. Sub-task 4.4 - Splitting of SFRC induced by local forces - Annex A 2001.

[38] Sorelli LG, Toutlemonde F. On the Design of Steel Fibre Reinforced Concrete Tunnel Lining Segments. 11th Int Conf Fract 2005:3–8.

[39] Pohn J, Tan KH, Peterson GL, Wen D. Structural testing of steel fibre reinforced concrete (SFRC) tunnel lining segments in Singapore. WTC 2009, Budapest, Hungary 2009.

[40] Caratelli A, Meda A, Rinaldi Z. Design according to MC2010 of a fibre-reinforced concrete tunnel in Monte Lirio, Panama. Struct Concr 2012;13:166–73. https://doi.org/10.1002/suco.201100034.

[41] Hilar M, Vítek J, Vítek P, Pukl R. Load testing and numerical modelling of SFRC segments 2012.

[42] Breitenbücher R, Meschke G, Song F, Hofman M, Zhan Y. Experimental and numerical study on the load-bearing behaviour of steel fibre reinforced concrete for precast tunnel lining segments under concentrated loads. FRC 2014 Jt ACI-Fib Int Work Fibre Reinf Concr Appl 2014:417–29.

[43] Abbas S, Soliman A, Nehdi M. Structural behaviour of ultra-high performance fibre reinforced concrete tunnel lining segments. FRC 2014 Jt ACI-Fib Int Work Fibre Reinf Concr Appl 2014:532–43.

[44] Meda A, Rinaldi Z, Caratelli A, Cignitti F. Experimental investigation on precast tunnel segments under TBM thrust action. Eng Struct 2016;119:174–85. https://doi.org/10.1016/j.engstruct.2016.03.049.

[45] Conforti A, Trabucchi I, Tiberti G, Plizzari GA, Caratelli A, Meda A. Precast tunnel segments for metro tunnel lining: A hybrid reinforcement solution using macro-synthetic fibers. Eng Struct 2019;199:149–296. https://doi.org/10.1016/j.engstruct.2019.109628.

[46] Swanson Analysis Systems. ANSYS User Manual 2013.

[47] Červenka Consulting Ltd. ATENA Program Documentation. Prague: 2013.

[48] Dassault Systèmes Simulia. Abaqus CAE User's Manual (6.12). Providence: Dassault Systèmes; 2012.

[49] TNO - DIANA FEA BV. Analysis procedures DIANA - Finite Element Analysis. User's Manual 2008.

[50] MSC Software Corporation. MSC-Marc Manual. 2008.

[51] RILEM TC 162-TDF. Test and design methods for steel fibre reinforced concrete. Design with σ-ε method. Mater Struct 2003;35:262–78. https://doi.org/10.1617/13837.

[52] International Federation for Structural Concrete (fib). fib-Model Code for Concrete Structures 2010. Lausanne: 2010. https://doi.org/10.1002/9783433604090.

[53] CNR. CNR-DT 204/2006 - Guide for the Design and Construction of Fibre-Reinforced Concrete Structures. vol. 75. 2007. https://doi.org/10.14359/10516.

[54] EHE-08. Instrucción de Hormigón Estructrural (EHE-08). Madrid: Ministerio de Fomento; 2008.

[55] ACI 544. Fibre-Reinforced Concrete: Design and Construction of Steel Fibre- Reinforced Precast Concrete Tunnel Segments. 2014.

[56] ACI 544.7R-16. Report on Design and Construction of Fiber-Reinforced Precast Concrete Tunnel Segments. ACI Comm Rep 2016:1–36.

[57] European Commitee for Standardization. Precast concrete products - test method for metallic fibre concrete- Measuring the flexural tensile strength. Br Stand Inst 2005. https://doi.org/9780580610523.

[58] Dupont D, Vandewalle L, Erdem E, Hemmy O, Schnütgen B, Steffen SH. Sub-task 4.4 - Splitting of SFRC induced by local forces 2001:1–12.

[59] NBN-B-15-238:1992. Essai des betons renforces des fibres. Essai de Flexion sur eprouvettes prismatiques (Testing of fiber reinforced concrete. Bending test on prismatic specimens) . Belgian Code - In French. 1992.

[60] Liao L, de la Fuente A, Cavalaro SHP, Aguado A. Design of FRC tunnel segments considering the ductility requirements of the fib Model Code 2010: Application to the Barcelona Metro line 9. Tunn Undergr Sp Technol 2015;47:200–10.

[61] Liao L, de la Fuente A, Cavalaro SHP, Aguado A. Design procedure and experimental study on fibre reinforced concrete segmental rings for vertical shafts. Mater Des 2016;92:590–601. https://doi.org/10.1016/j.matdes.2015.12.061.

2.2. JOURNAL PAPER II: NUMERICAL-AIDED FLEXURAL-BASED DESIGN OF FIBRE REINFORCED CONCRETE COLUMN-SUPPORTED FLAT SLAB

Alejandro Nogales[a,b,*] and Albert de la Fuente[b]

[a]Smart Engineering Ltd., UPC Spin-Off, Jordi Girona 1-3, 08034 Barcelona, Spain

[b]Civil and Environmental Engineering Deparment, Universitat Politècnica de Catalunya (UPC), Jordi Girona 1-3, 08034 Barcelona, Spain

*Corresponding author

ABSTRACT

The growing use of fibre reinforced concrete (FRC) for structural purposes has led several guidelines to include design-oriented models that allow the partial (and even total) substitution of the steel reinforcing bars. Among those, fibres as concrete reinforcement for elevated concrete flat slabs is gaining interest due to the identified technical and benefits and quantified sustainability enhancements. However, although this technology has already been used in buildings and its sufficient bearing capacity confirmed by real-scale experimental programs, its straightforward implementation is far from being consolidated. The latter is owing to the existence of several paramount aspects to be answered. One of those is the influence of the *fib* MC-2010 FRC post-cracking strength classification, including the combination of steel bars, on the mechanical response of these elements at ULS and SLS. In this context, a non-linear finite element model was implemented and validated by means of results from existing real-scale tests. Posteriorly, the model was used to design a new real-scale test to be performed within the context of the research project eFIB (from the Spanish, Optimization of Construction Processes of Structural Elements by using Fibre Reinforced Concretes). To this end, a parametric study was developed by considering several FRC post-cracking strength classes, using fibres as unique reinforcement or combined with steel meshes, to determine an optimum solution for flexure (which governs the main reinforcement requirements) based on the structural reliability index targeted for building construction. The model results and analysis permitted to derive relevant conclusions from the material design optimization point of view, which can be a reference for future similar experiences.

KEYWORDS: Fibre reinforced concrete; non-linear analysis; elevated flat slabs; hybrid reinforcement; structural safety.

Nomenclature

List of symbols

$A_{s,min}$	Minimum steel reinforcing area	q_Q	Live (variable) load
$CMOD$	Crack mouth opening displacement	$q_R; q_u$	Global structural bearing capacity (resistance) associated to a flexural limit state
E_c	Modulus of elasticity of concrete	q_S	Combination of acting loads
E_{ci}	Tangent modulus of elasticity of concrete at a stress σ_i	q_{SLS}	Combination of loads for service limit state
E_{c1}	Secant modulus of concrete from the origin to the peak compressive stress	q_{SW}	Self-weight load
E_S	Modulus of elasticity of steel	q_y	Yielding load
f_c	Compressive concrete strength	w	Crack opening in mm
f_{ct}	Tensile concrete strength	w_s	Crack opening for f_{Fts}
f_{Fts}	Residual tensile strength of FRC for service limit state	w_t	Crack opening when $\sigma_j = 0$
f_{Ftu}	Residual tensile strength of FRC for ultimate limit state	w_u	Crack opening for f_{Ftu}
$f_{R,j}$	Residual flexural strength of FRC corresponding to a $CMODj$	γ_R	Global resistance safety factor
f_y	Yield strength of steel bar reinforcement	γ_{Rd}	Model uncertainty factor
G_F	Fracture energy of concrete	δ_{SLS}	Deflection for q_{SLS}
h	Slab thickness	δ_u	Deflection for q_u
L	Slab clear span	ε_1	Concrete strain for f_{ctm}
P_{cr}	Cracking load (concentrated)	ε_{cc}	Concrete compression strain
P_{peak}	Peak Load (concentrated)	ε_{Fu}	Concrete strain for f_{Ftu}
P_u	Ultimate load (concentrated)	ε_{su}	Steel tensile strain at ultimate limit state
q	Uniformly distributed load	σ_{cc}	Concrete compressive stress
q_{cr}	Cracking load (uniformly distributed)	$\sigma_{ct,j}$	Stress point for concrete tensile constitutive curve
q_G	Permanent load		General subscripts
q_{peak}	Permanent load	d	Design value of the variable
		m	Mean value of the variable
		k	Characteristic value of the variable

1. INTRODUCTION

Over the last decades, the use of fibres for structural concrete reinforcement has noticeably grown [1,2]. The use of fibre reinforced concrete (FRC) is so far applied in concrete pavements (slabs on ground) [3–8], sewerage pipes [9,10], shotcrete [11,12], precast tunnel segments [13–18], foundation slabs [19] and other building elements [20,21]. It is known that structural fibres can partially substitute and be combined with conventional steel rebar, called hybrid reinforcement (HRC) in order to optimize rebar reinforcement [22–25].

As a reaction, several codes and guidelines such as DBV [26], RILEM TC 162-TDF [27], CNR-DT 204/2006, EHE-08 [28], *fib* Model Code [29] and ACI 544 [30] have included models for designing FRC structural elements. In this sense, *fib* MC-2010 has introduced the concept of FRC post-cracking (or residual) strength class to classify the post-cracking performance of the material. These codes are based on the limit states structural safety format and propose cross-sectional design-oriented constitutive equations to reproduce the full tensile response of FRC. In this regard, the publication of design codes for FRC has boosted the use of FRC in the construction industry.

Within the building sector, FRC has been used for slabs supported on pile foundation [31–33] and on columns [34,35]. These elements are designed considering that cracking occurs in service conditions and, hence, that post-cracking tensile strength of FRC is activated. This, together with the high degree of redundancy of these elements, allow reducing (even eliminating) the reinforcing steel bars. Nevertheless, despite of the existence of design guidelines specifically oriented to FRC flat slabs [36], experimental and existing buildings that prove its technical feasibility and even research [35] that identified and quantified positive outcomes from the sustainability perspective, there is still controversy and barriers to its implementation. Respect the latter, it is important to emphasize that the decision-making process of using FRC or RC technology is driven by direct costs, while indirect costs and environmental and social aspects are disregarded in the analysis [35].

Apart from the abovementioned, there are still some particular technical aspects for which further research and practical design rules should be provided, such as: (1) the influence of the FRC post-cracking strength class on the SLS and ULS response, including the addition of traditional reinforcement and (2) global safety factors to be considered when dealing with numerical-aided design to guarantee the equivalent structural reliability levels established in the standards.

In view of this, the objective of this research paper is two-fold: (1) to identify and quantify the influence of different reinforcement configurations on both the SLS (cracking and deformability) and ULS response of a pile-supported flat slab to be designed within the context of an extensive

research project, and (2) to calibrate and propose tentative safety factors to be applied to the global resistance of the structure. For these purposes, first, a non-linear FE model was implemented and validated by comparison with experimental results obtained from a real-scale tests of FRC column-supported flats slab, and secondly, the model was used to perform a parametric analysis (FRC post-cracking strength class considering hybridization with steel bars) and to calibrate safety factors. The results allowed drawing conclusions of interest from the flexural design point of view, these with direct economical positive outcomes as the in-plane reinforcement governs the concrete reinforcement costs.

2.   STATE-OF-ART ON FRC COLUMN-SUPPORTED FLAT SLABS

The interest of using FRC in elevated slabs has resulted in several experimental and numerical programs oriented to assess and characterise its mechanical response (see Table 1).

Based on the data presented in Table 1, the maximum span reached for FRC column-supported flat slabs (FRCFSs, hereinafter) was 8.00 m (slenderness of 26.6). Most of the studies were focused on the use of steel fibre reinforced concrete (SFRC) and the comparison between hybrid reinforced concrete (HRC) or traditional RC elements [37–40]. To the authors' best knowledge, only Salehian [41] compared the response of slabs cast with different volume of fibres. In these studies, fibres proved to be efficient in reducing spacing between cracks and deflections. Furthermore, HRC permitted to reach the same load level as RC while reducing the total steel content [39]. Regarding reinforcement optimization, Facconi [42] (column-supported slabs) and Taheri [43] (statically determinate elements) numerically proved the existence of an optimum amount of fibres in HRC elements.

Regarding the influence of different parameters in full scale elevated slabs, Salehian [41] conducted a parametric analysis on the load-carrying capacity of elevated slabs by assessing the influence of fibres segregation, volume of fibres, concrete compressive strength and the span length by resorting to the yield line theory. The analysis was performed under different loading conditions (quasi-point load and uniformly distributed load) and different bay positions (interior and corners). Likewise, the softening and hardening response of FRC (and HRC) elements failing in bending was assessed numerically by Taheri et al. [43].

While SFRC is the most used, there is a growing interest in polymeric fibres, not only due to durability aspects but also due to the constant enhancement that these fibres are experiencing. In this regard, extensive research has been developed on the use polymeric fibre reinforced concrete (PPFRC) in slabs [7,8,37,44,45]. However, to the authors' best knowledge, only Pujadas [44,45] carried out full-scale tests on PPFRC slabs in statically indeterminate configuration. The results evidenced that PPFRC slabs exhibited a ductile behaviour and a remarkable bending moment redistribution capacity. Flexural creep under permanent loads in PPFRC cracked sections is still

a topic under research and caution is required when designing this structural typology [46,47]; the combined use of traditional reinforcement is recommended to control tensile stress due to creep and relaxation (if expected) in cracked sections.

Di Prisco [40] pointed out the efficiency of fibres in redundant structural schemes respect to statically determinate tests on beams performed by Pujadas [37]. In this regard, both stress and bending moment redistribution capacity in FRCFSs were investigated by several authors [38,40,44,48,49]. The redistribution capacity is affected by the slab geometry [50], the increase of the span between supports leading to secondary cracking and greater deformability respect to those slabs with lower aspect ratio. Pujadas [44] remarked the stress redistribution capacity provided by the fibres on PPFRC slabs (under hyperstatic conditions), this inexistent for the same PPFRC material under statically determinate test configurations (beam tests). The last conclusion was corroborated by [51,52] by means of the two-span FRC and HRC beams tested under statically indeterminate conditions to investigate the flexural and moment redistribution.

Table 1 – Previous research focused on FRC slabs elements

Slab	f_c [MPa]	Dimensions in [mm] and (slenderness)	Support	Material	C_f [kg/m^3]	Φ_f/λ_f	Tests	Load	Reference
FS	35	2000^2 x 200 (10)	9 column grid	HRC	40 60	0.75/60	1	Point Load	[53]
FS	45	2000^2 x 160 (12.5)	9 column grid	SFRC	45	1.0/60	1	Point Load	[54]
CS	45	1500 x 150 (10) 2000 x 200 (10)	perimeter	SFRC	45 60 80 120	1.15/45 1.3/50 1.0/60	6	Point Load	[55]
FS	43.7	6000^2 x 200 (30)	16 column grid	SFRC	100	1.35/50	2	Surface load Point Load	[56]
FS	45	3000^{2}x 150 (20)	4 sided	SFRC HRC	62	1.0/60	2	Point Load	[57]
FS	43.7	5000^{2}x 160 (31.25)	16 column grid	SFRC	45	1.3/50	2	Surface load Point Load	[31]
CS	43.7	1500^2 x 150 (10)	perimeter	SFRC	80 100	1.35/50	2	Point Load	[58]
RS	60 40	3000 x 700 x 160 (18.75)	4 sided	SFRC	100 60	1.3/50 1.0/60	9	Point Load	[48]
FS	35	6000^2 x 250 (24)	Column grid	SFRC	100	1.3/50	1	Surfaces Load	[59]
RS	30	3000 x 1000 x 200 (15)	4 sided	SFRC HRC	22 (PFRC)	0.55/35 (SFRC)	18	Four point bending test	[37]

				PFRC	45 (SFRC)	0.75/60 (SFRC) 0.8/55 (PFRC) 0.44/40 (PFRC)			
FS	30	8000 x 7600 x 300 (26.6)	Column grid	HRC	100	1.3/50	-	Surface load	[60]
FS	40	3000 x 3000 x 130 (23.07)	25 column grid	SFRC HRC	40 60	0.9/60	16	Point Load	[38]
RS	50	3000 x 1500 x 200 (15) 3000 x 2000 x 200 (15) 3000 x 3000 x 200 (15)	4 sided	PFRC	9	0.8/48	6	Point Load	[44]
FS	43.7	6000^2 x 200 (30)	16 column grid	SFRC	70	1.0/60	2	Surface load Point Load	[32]
RS	50	3000 x 1500 x 200 (15) 3000 x 2000 x 200 (15) 3000 x 3000 x 200 (15)	4 sided	SFRC	40	0.75/50	6	Point Load	[50]
FS	65	1200 x 1000 x 75 (16)	Column grid	SFRC	90	0.5/70	3	Surface load Point Load	[34]
RS	50	4200 x 2500 x 80 (52.5)	4 sided	HRF RC	20 25	0.9/60 0.4/32	11	Point Load	[39]
RS	50	2000 x 2000 x 150 (13.3)	4 square columns	SFRC HRC RC	35	0.9/60	6	Point Load	[40]

CS: circular slab; **C$_f$**: amount of fibres; ; **FS**: full-scale slab; **HRC**: hybrid reinforced concrete; **PFRC**: Polypropylene fibre reinforced concrete; **RC**: rebar reinforced concrete; **RS**: rectangular slab; **SFRC**: steel fibre reinforced concrete; **λ$_f$**: slenderness ratio of the fibre; **Φ$_f$**: diameter of the fibre.

To quantify redistribution capacity at design level, *fib* MC-2010 presents the K_{Rd} factor that indirectly allows considering favourable effects due to redistribution. In the literature, different methods were proposed to compute this factor [61] and research was carried out to study this topic by means of non-linear numerical [61] or the yield-line theory [62].

Finally, the influence of the fibre orientation in flat slabs was investigated by Abrishambaf [63], Blanco [50], Døssland [57] and Pujadas [44]; moreover, favourable or unfavourable fibre orientations are identified by *fib* Model Code, 2010.

Apart from experimental tests on slabs, numerical analyses were carried out using finite element (FE) packages. Those most commonly used for simulating the flexural behaviour of elevated slabs are: ANSYS [64] [53], ATENA [65] [66,67], ABAQUS [68] [58,69] and DIANA

[70] [42,57]. These FE packages can reproduce the FRC non-linear response due to cracking. The FRC post-cracking response modelling can be performed in several ways: smeared crack and discrete crack. The comparison of both numerical and experimental results showed that the simulations are in good agreement with those experimental for the whole range of loading configurations for slabs. Nonetheless, the collapse mode (bending, punching or a combination) identification can be a challenge unless the proper failure criteria are imposed or experimental test results are available as reference.

3. MODEL VALIDATION

3.1. NUMERICAL MODELLING OF FRC

The compressive stress-strain (σ-ε) and tensile stress-crack opening (σ-w) constitutive relationships from *fib* MC-2010, for both FRC and PC, were considered (see Figure 1). Flexural residual strengths (f_R) can be obtained from three point bending tests notched-beams according to EN 14651:2005. f_{R1} stands for the residual strength for a crack mouth opening displacement (CMOD) of 0.5 mm and f_{R3k} for a COMD of 2.5 mm. In this sense, it must be remarked that the use of this multi-linear post-cracking strength model could lead to overestimations of the bearing capacity according to [43,72,73], particularly in statically indeterminate structural systems.

The Concrete Damage Plasticity (CDP) model [68] available in the software is used. The CDP model is a continuum, smeared crack, plasticity-based, damage model for concrete. In smeared crack models, the damage zone coincides with the finite element dimensions. The model assumes that the main two failure mechanisms for concrete are tensile cracking and compressive crushing. To reproduce the concrete behaviour, the input data required are uniaxial σ-ε curves for compression and tension. It is worth noticing that in order to overcome mesh dependence, the σ-w tensile curve is used instead. In this regard, the characteristic length (L_{ch}) magnitude, to convert crack opening into strain, implemented by default by the software is the cubic root of the element volume (equal to the size of the element for hexahedral elements). The CDP parameters adopted in all the simulations of this research are the default ones proposed in ABAQUS User's Manual [68] for plain concrete.
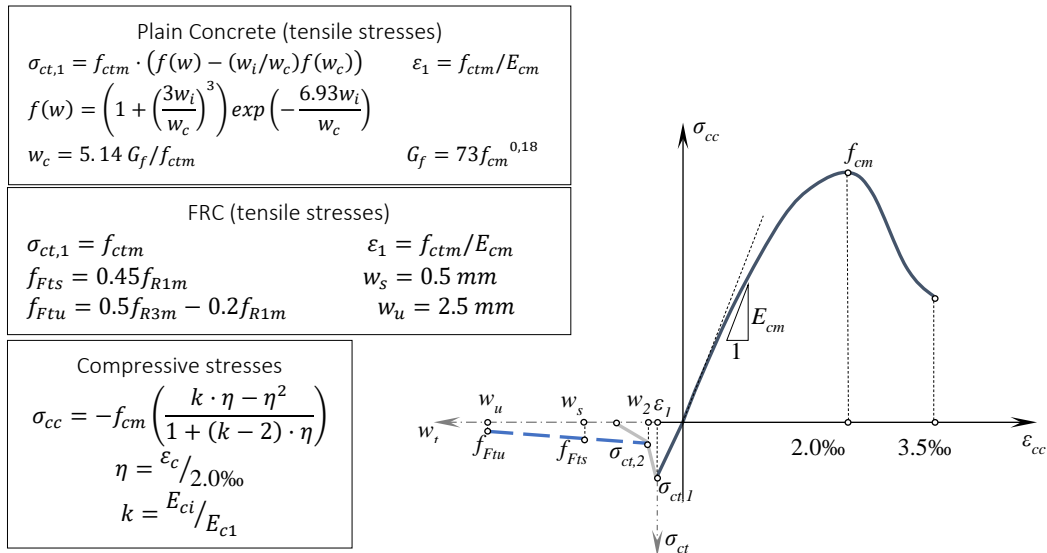
Plain Concrete (tensile stresses)

$$\sigma_{ct,1} = f_{ctm} \cdot \left(f(w) - (w_i/w_c) f(w_c) \right) \qquad \varepsilon_1 = f_{ctm}/E_{cm}$$

$$f(w) = \left(1 + \left(\frac{3w_i}{w_c} \right)^3 \right) exp \left(-\frac{6.93 w_i}{w_c} \right)$$

$$w_c = 5.14 \, G_f/f_{ctm} \qquad\qquad G_f = 73 f_{cm}^{0,18}$$

FRC (tensile stresses)

$$\sigma_{ct,1} = f_{ctm} \qquad\qquad \varepsilon_1 = f_{ctm}/E_{cm}$$

$$f_{Fts} = 0.45 f_{R1m} \qquad\qquad w_s = 0.5 \, mm$$

$$f_{Ftu} = 0.5 f_{R3m} - 0.2 f_{R1m} \qquad w_u = 2.5 \, mm$$

Compressive stresses

$$\sigma_{cc} = -f_{cm} \left(\frac{k \cdot \eta - \eta^2}{1 + (k-2) \cdot \eta} \right)$$

$$\eta = \frac{\varepsilon_c}{2.0‰}$$

$$k = \frac{E_{ci}}{E_{c1}}$$

Figure 1 – Constitutive equations for concrete; σ-ε for compression and σ-w for tensile

It must be remarked that mean values of each of the involved mechanical variables are considered for the numerical simulations.

3.2. ELEVATED SLABS: GOSSLA [56] AND PARMENTIER ET AL. [32]

The results from these tests were also considered for other models validation [42]. Both FRCFS composed by nine 6 x 6 m^2 span, 0.2 m slab thickness resting on a grid of sixteen 0.3 x 0.3 m^2 square columns in case of Gossla's (named Bissen slab) and 0.3 m-diameter circular columns for Parmentier's (named Limelette slab). The slabs were tested up to failure applying a punctual load at the centre of the slab (see Figure 2). The Bissen slab fibre dosage was 100 kg/m^3 of an undulated commercial steel fibre (1.3 mm in diameter and 50 mm in length). On the other hand, Limelette slab contained 60 kg/m^3 of hooked-end steel fibres (1.0 mm in diameter and 60 mm length). Complimentary, an anti-progressive collapse (APC) reinforcement was placed; this reinforcement has minor contribution in the structural performance for the level of deformations accepted in the simulations carried out herein and, therefore, this APC reinforcement was not modelled.

The f_{cm} were reported to be 42.0 N/mm^2 and 43.7 N/mm^2 for Bissen and Limelette respectively. The Bissen concrete post-cracking properties were obtained (by means of an inverse analysis) and reported by Soranakom [58] ($\sigma_{ct,1}$=2.5, $\sigma_{ct,2}$=1.75, $\sigma_{ct,3}$=1.06, $\sigma_{ct,4}$=0 MPa and w_1=0, w_2=0.25, w_3=1.25, w_4=2 mm). di Prisco [33] derived and reported the properties of Limelette slab's concrete ($\sigma_{ct,1}$=2.2, $\sigma_{ct,2}$=1.20, $\sigma_{ct,3}$=1.20 $\sigma_{ct,4}$=0 MPa and w_1=0, w_2=0.05, w_3=1.5, w_4=6 mm).

The non-linear 3D model was implemented (Figure 2b) to simulate both the geometry and loading conditions presented in Figure 2a. Due to the existence of a double-plane symmetry, only a quarter of the slab was modelled. For this purpose, displacement was fixed in both symmetry

planes (see Figure 2b); the columns were modelled as simple supports where vertical displacement were restricted ($U_y=0$), detailed in Figure 2c for Bissen slab and 2d for Limelette. The analysis was performed by first applying the self-weight (4.8 kN/m^2) and then the point load was applied on a circular steel plate of 20 mm of diameter (Figure 2d) by means of displacement control to guarantee numerical convergence. The mesh consists of 8-noded solid linear hexahedral elements (C3D8R) used for modelling concrete, this leading to an amount of 44,720 elements.
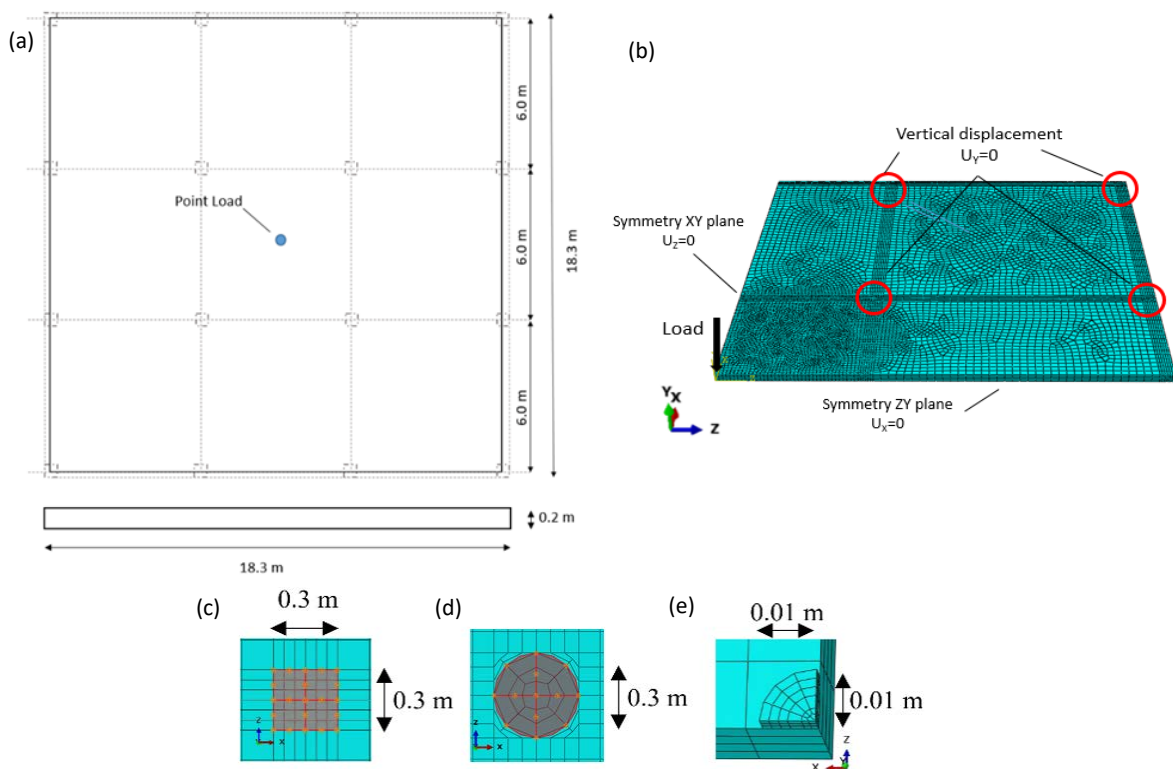
Figure 2 – Point load test (a) Experimental test configuration (b) FE meshed model considered (c) Bissen square columns simplified as simply supports (d) Limette circular columns as simply supports and (e) loading plate used in the model

Figure 3 presents both the numerical and experimental load-deflection relationships. It can be noticed that the model captured with suitable accuracy the pre- and post-cracking response (with a maximum load deviation of 40 kN for Bissen slab and 39 kN for Limelette slab, which correspond to 9% and 13% of error respectively). On the one hand, Bissen slab experimental cracking load ($P_{cr,exp}$), first crack detected at the top face onto the central column and the second at the bottom face of the mid span (see Figure 4)- were 140 kN and 200 kN, respectively, whereas the numerical cracking loads ($P_{cr,num}$) were 108 kN (22.8%) and 185 kN (7.5%), both from the safe side. On the other hand, in Limelette slab $P_{cr,exp}$ was not reported, instead a major crack initiation was spotted based on a change in slope at ±85 kN. This change in stiffness could also be seen in the numerical load-deflection curve in Figure 3.

Both numerical models detected a punching failure mode in the vicinities of the applied load similar to other authors that tested SFRC flat slabs subjected to punctual loads [74,75]. Nevertheless, the descending branch was not noticeable since a secondary stress redistribution was activated, which was found to be misaligned with the experimental observation. For this reason, the FRC tensile strain $\varepsilon_{Fu} = 0.02$ failure criterion stablished in the *fib* MC-2010 was considered to set P_u, this leading to a $P_{u,num} = 464$ kN (< 1% of error respect to $P_{peak} = 463$ kN achieved experimentally) in case of Bissen slab and $P_{u,num} = 341$ kN for Limelette slab (< 4% of error respect to $P_{peak} = 328$ kN achieved experimentally) . The maximum principal strain component at the centre of the slab bottom face, integration point beneath the loading plate, is plotted in Figure 3. Regarding deformation, the slab deflections were 51.0 mm for P_{peak} and 57.8 mm (13% higher) for $P_{u,num}$ and 64.6 mm for P_{peak} and 61.7 mm (4% lower) for Bissen slab and Limelette slab respectively. The former representing a L/120 (L being the span) that can also be assumed as a failure criterion for designing purposes. The $\varepsilon_{Fu} = 0.02$ failure criterion for FRC was also used for the design process presented in the following sections.

Considering the crack pattern similarities of both slabs only the results reported in the Bissen slab is reported. The model can provide crack widths assessed by means of the approach proposed in [76,77]. Neverthess, as only crack patterns at failure state were provided in Bissen slab [56], the damage levels obtained numerically for $P_{u,num} = 464$ kN were compared with those reported for $P_{peak} = 463$ kN to verify the capability of the model for reproducing these patterns. In Figure 4 the maximum principle plastic strain are plotted. Like both experimental tests showed, the slab was already cracked in some parts due to its self-weight. The firsts cracks appeared on top centre columns and progressively grew along the alignments of the inner columns (see Figure 4a). Like the experimental pattern, the numerical FE model capture the crack formation from the inner to the outer columns. At the bottom side, cracks appeared due to postive bending moments and bifurqued into two directions paralel to the slab edges, as observed experimentally (Figure 4b). The numerical crack pattern sequence coincided with that reported from the experiments; however, longer cracks were observed in the field tests.
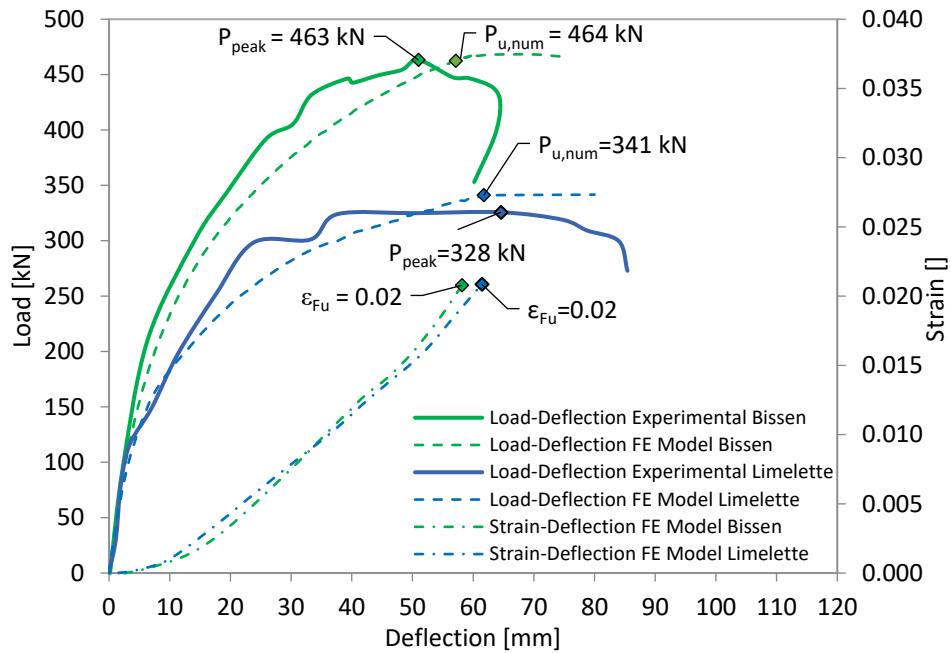
Figure 3 – Experimental and numerical load-deflection and curves and FRC tensile strain – deflection at midspan

Therefore, it can be stated that the model is capable of reproducing properly the mechanical response of the FRCFSs in terms of load bearing capacity as well as to identify the areas in which the damage caused by cracking is expected to occur. Both features are sufficient for design purposes, taking the proper safety measures, and to deal with parametric studies.
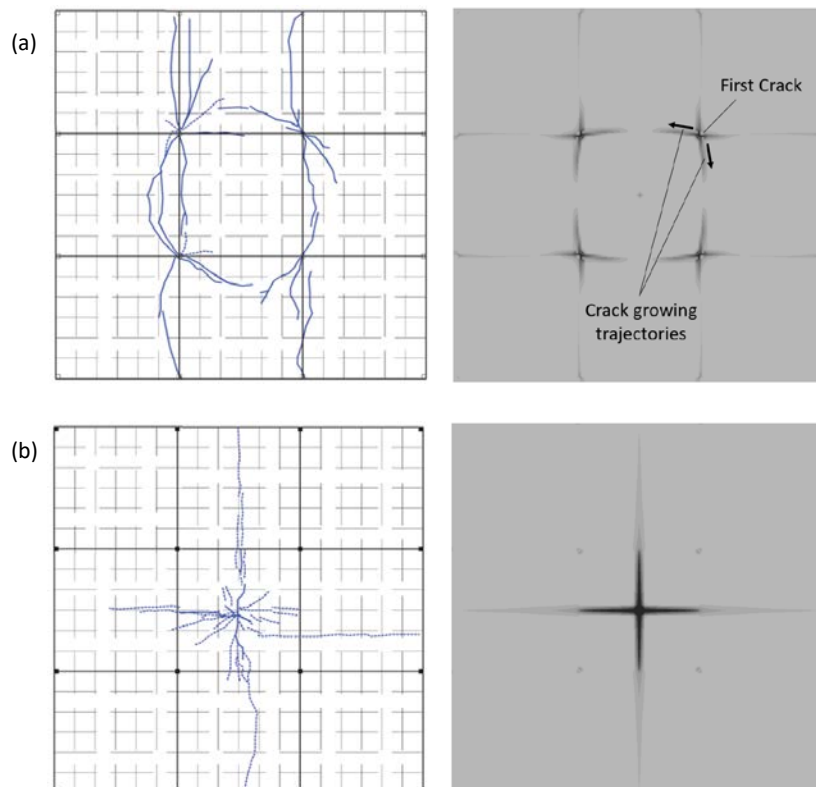

Non-linear Finite Element Analysis Oriented to Optimisation of Fiber Reinforced Concrete Structures

Figure 4 – Crack patterns (experimental) and contour of maximum principal plastic strains

(numerical) at P$_{max}$ for: (a) Top and (b) bottom faces

4. NUMERICAL-AIDED DESIGN OF THE ELEVATED SLAB REPORTED IN AIDAROV [78]

4.1. DESCRIPTION OF THE PROTOTYPE

Within the context of the research project eFIB, a 12.00 m x 10.00 m and 0.2 m in thickness FRCF supported by a grid of nine square columns (0.25 m) of 3.0 m in height , forming four bays 6.00 x 5.00 m meters each (Figure 5) was designed as a prototype of SFRC elevated flat slab. The target loads to be resisted where those established in the Spanish Building Code [79] for offices' buildings: self-weight (q$_{sw}$) of 4.8 kN/m^2, dead load (q$_G$) of 2.0 kN/m^2 and a variable load (q$_Q$) of 3.0 kN/m^2.
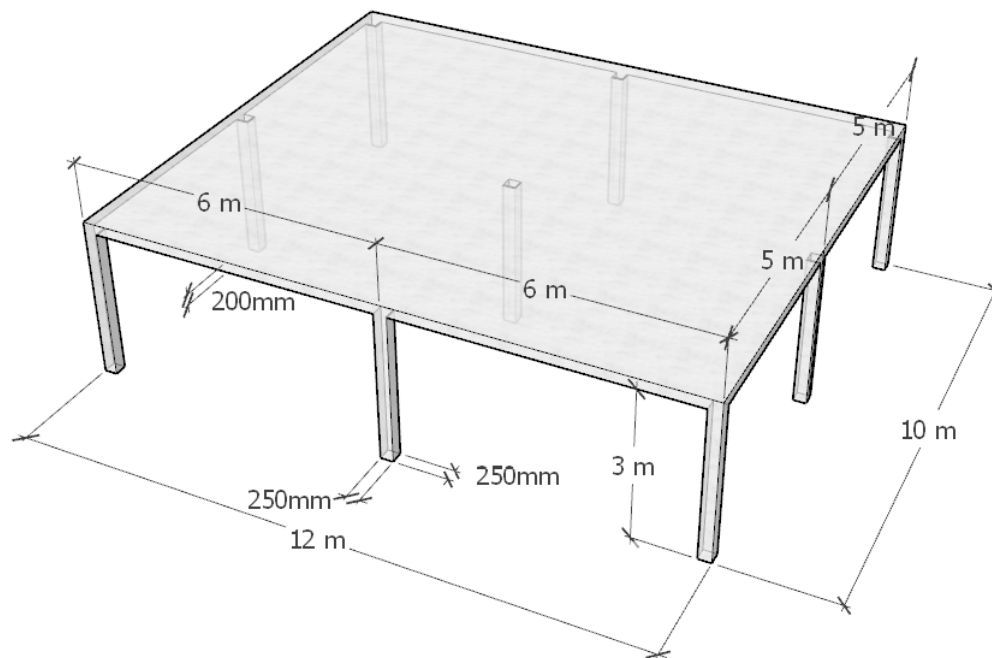

Figure 5 – Geometrical properties of the slab.

One of the main goals was of this industrial-oriented research was to prove the technical feasibility of reducing by a 30% the total amount of reinforcement used in previous similar experiences. In view of the boundary conditions (geometry and loads), this objective was found to be challenging from the structural point of view as well as a breakthrough that could make this technology more appealing from the economic perspective.

To this end, the structural design was performed considering steel macrofibres as unique reinforcement (except three 12 mm steel bars placed along the columns alignment, in both directions, as ACP reinforcement). The mechanical properties of the self-compacting concrete

were established by means of the numerical model and parametric analyses presented in the following sections. From the design process, a C50/60 ($f_{ck,28}$ = 50 N/mm^2 in cylinders) 6c self-compacting steel fibre-reinforced concrete (f_{R1k} = 6.0 N/mm^2 and $0.9 \leq f_{R3k}/f_{R1k} < 1.1$) post-cracking strength class according to the *fib* MC-2010 was fixed for the production and the quality control.

The prototype was tested under uniformly distributed loads considering permanent and variable loading patterns (see Figure 6). The prototype was loaded up to 16.0 kN/m^2 without collapsing and evidencing signs of significantly further load bearing capacity; the results can be found in [78]. It is worth to be mentioned that the mechanical performance proved to be sufficient to consider this solution as technically feasible.
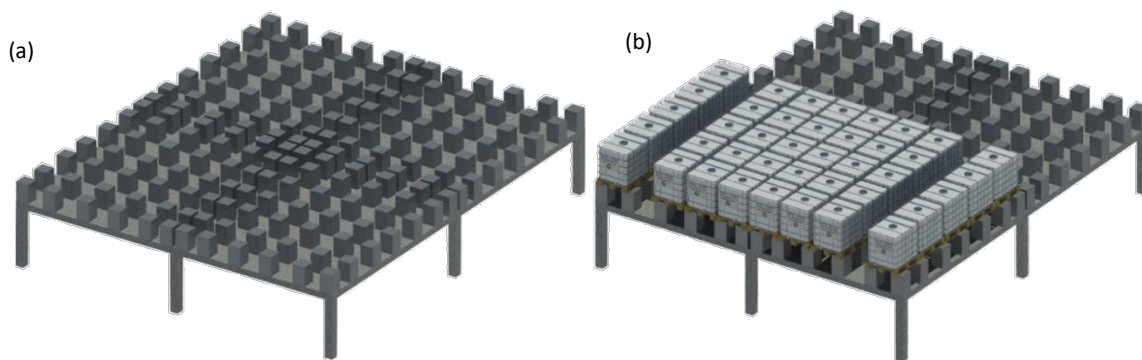

Figure 6 – Loading stages: (a) permanent loading with concrete cubes (0.3 kN/each) and (b) test up to failure with water tanks.

4.2. CONCRETE REINFORCEMENT ALTERNATIVES ANALYSED

Three different FRC performances were considered, these represented by f_{R1m} = 4.0, 6.0 and 8.0 N/mm^2 and f_{R3m}/f_{R1m} = 1.0 and the f_{FTsm} and f_{Ftum} gathered in Table 2. These properties and the respective σ_{ctm} - w design-oriented constitutive equations (see Figure 7) were computed according to *fib* MC-2010. Plain concrete (PC) curve is also computed according to *fib* MC-2010 and plotted in Figure 7.

Table 2 – FRC tensile properties in N/mm^2

Concrete	$f_{R1m}= f_{R3m}$	f_{Ftsm}	f_{Ftum}
FRC-4	4.0	1.8	1.2
FRC-6	6.0	2.7	1.8
FRC-8	8.0	3.6	2.4

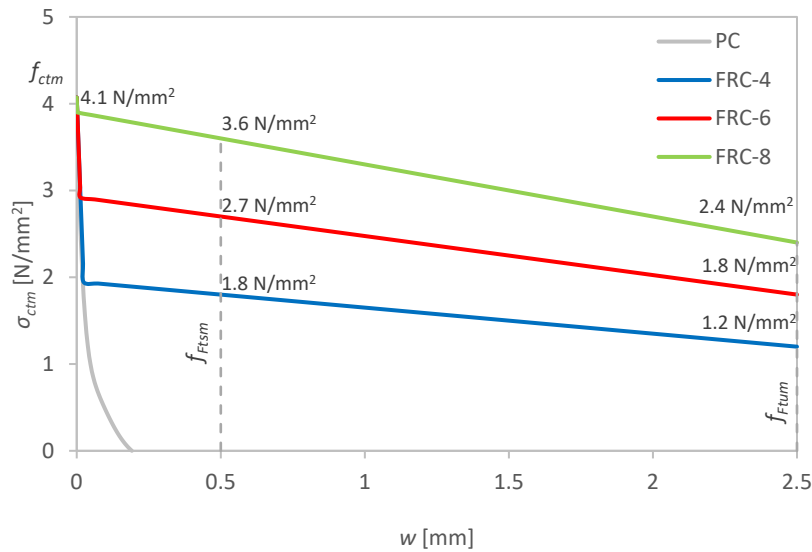*Non-linear Finite Element Analysis Oriented to Optimisation of Fiber Reinforced Concrete Structures*

Figure 7 – Tensile constitutive equations of the concrete mixes

The hybrid reinforcement alternatives (HRC-28/19-4, HRC-28/19-6 and HRC-28/19-8) consisted in the FRCs defined in Table 2 combined with a bottom steel mesh of Ø8@200 mm (28 kg/m^3) and an upper mesh of Ø12@150 (covering a 1/3 of the bay length, 19 kg/m^3), thus, longitudinal reinforcement ratios (ρ_s) of 0.13% and 0.38%, respectively. A clear concrete cover of 25 mm was established and a steel with $f_{ym} = 600$ N/mm^2 for the reinforcing bars. Figure 8 depicts the steel mesh configuration defined for the HRC solutions.
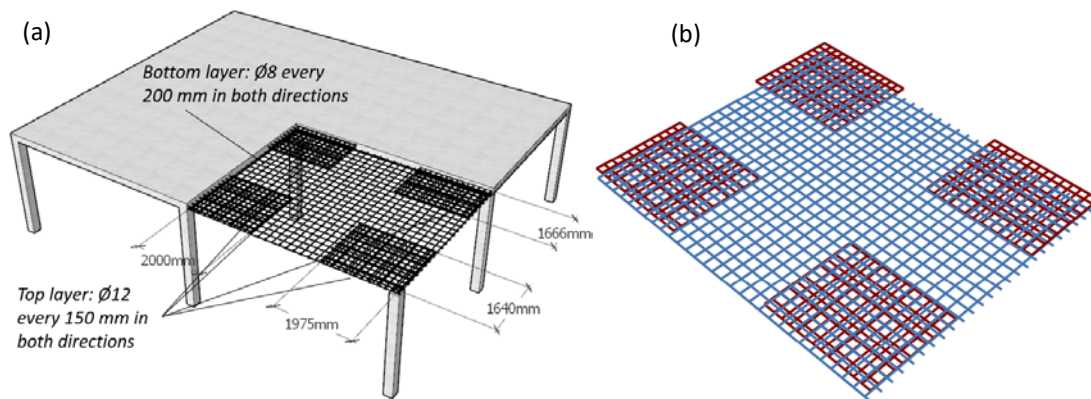

Figure 8 – Reinforced slab for hybrid solutions (a) rebar configuration (b) model meshed reinforcement.

It should be remarked that the $\rho_s = 0.38\%$ considered for the sections above columns is superior (> 50%) to the minimum longitudinal reinforcement ratio ($\rho_{s,min} = 0.26 \cdot f_{ctm}/f_{yk} = 0.18\%$; $f_{ctm} = 4.0$ N/mm^2 and $f_{yk} = 580$ N/mm^2) recommended in the *fib* MC-2010. This ρ_s was meant to resist the major part of the bending moment (M < 0) peaks and to optimize the magnitudes of f_R since the reinforcement requirements are governed by these sections. Likewise, the bending moment redistribution capacity is limited by these sections and, hence, it is advisable to avoid low

reinforcement ratios in order to prevent these sections from crack localization and fragile failures. In this regard, several authors [80–87] reported these undesirable phenomena from experimental full-scale bending tests where in which ρ_s and FRCs with marked strain-softening responses were combined.

4.3. NUMERICAL MODELLING OF THE TEST

The same modelling approach presented in section 3.2 was assumed to simulate this FRCFS. In this sense, Figure 9 presents the 18,000 C3D8R hexahedral solid 80 mm size finite elements' and constrictions established to simulate a quarter of the slab.
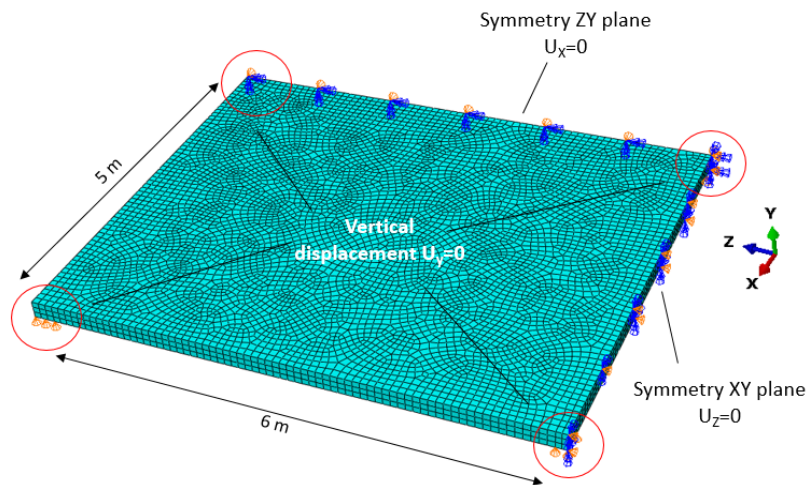

Figure 9 – Finite element mesh with boundary conditions considered for the FRCFS tested by Aidarov[78]

Additionally, 2-noded 3D linear truss elements T3D2 were chosen for simulating the steel bars. Full embedment constraint was imposed to simulate perfect bond between the concrete and steel bars. It must be highlighted that the reinforcement ratio adopted is considered for a hybrid solution (combining rebar and fibres) and not to withstand the design loads only with the steel meshed.

A mesh convergence analysis using the explicit solver implemented in ABAQUS (quasi-static analysis) was carried out, where 25 mm, 50 mm and 80 mm (which correspond to 1 [88], 2 and >3 times the maximum aggregate size) were adopted (see Figure 10). The simulation using 80 mm led to 14.9 kN/m^2 maximum capacity whereas 25 and 50 mm resulted in 5.5 and 3.7 % higher loads, respectively. 80 mm size element resulted to be suitable in terms of computational costs and accuracy in loads and crack distribution. Precaution must be taken with the dilation angle parameter set in the CDP, especially for cases where shear/punching failure mode can be the governing situation. In this sense, a dilation angle sensitivity analysis was carried out using different values and no difference was found, this meaning that the slab presented a flexural

failure mode (as the experimental tests confirmed) and the dilation angle magnitude was irrelevant. A 30° value was adopted for all simulations.

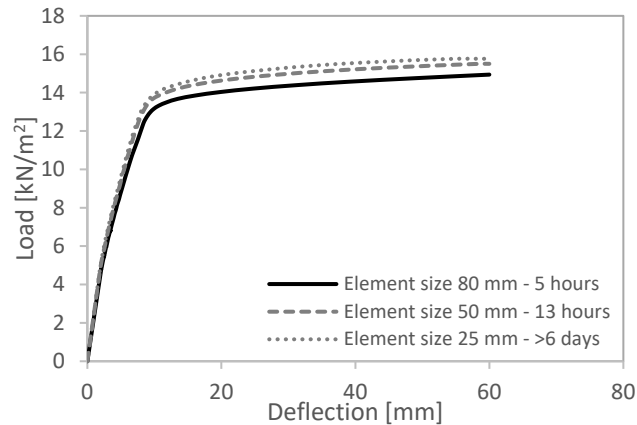*Figure 10 – Mesh sensitivity analysis for FRC-4*

4.4. RESULTS

4.4.1. ULTIMATE BENDING CAPACITY AND GLOBAL SAFETY FACTORS

The structure was subjected to an increasing uniformly distributed load applied onto the upper slab surface up to reach the failure criterion ($\varepsilon_{Fu} = 0.02$ for FRC and $\varepsilon_{su} = 0.01$ for HRC and reinforced concrete, RC). The $q - \delta$ relationships obtained for reinforced concrete RC-28/19 (reinforced concrete), FRC and HRC alternatives are presented in Figure 11.

According to the results shown in Figure 11, on one hand, the FRC solutions reached the mean yielding load (q_{ym}) for deflections comprised between 10 mm (FRC-4) and 25 mm (FRC-8), the magnitude of q_{ym} depending on the f_R of the FRC (Figure 12).For the FRC solutions, the plastic mechanism takes place through the quasi-horizontal plateau detected in the load-displacement relationships (represented as a square in Figure 11). The yielding load (q_{ym}) is identified as the onset load of this plateau. The plastic mechanism was equivalent in all cases (Figure 13) and permitted deflections from 61.2 mm (FRC-4) to 65.5 mm (FRC-8) for the mean ultimate load bearing capacity (q_{um}), which increased less than 10% respect to q_{ym}. On the other hand, the HRC solutions (HRC-28/19-4, HRC-28/19-6 and HRC-28/19-8) presented a higher q_{um} respect to those with only FRC (see Figure 11) owing to the contribution of the steel meshes. The plastic mechanism (Figure 14) was governed also by major cracks (yielding lines) with a greater number of secondary cracks respect to those FRC solutions. It was assumed that q_{ym} is achieved when the bottom steel mesh at the midspan yields ($\varepsilon_{sym} = f_{ym}/E_s = 0.00285$), the upper mesh at the central column being already yielded.
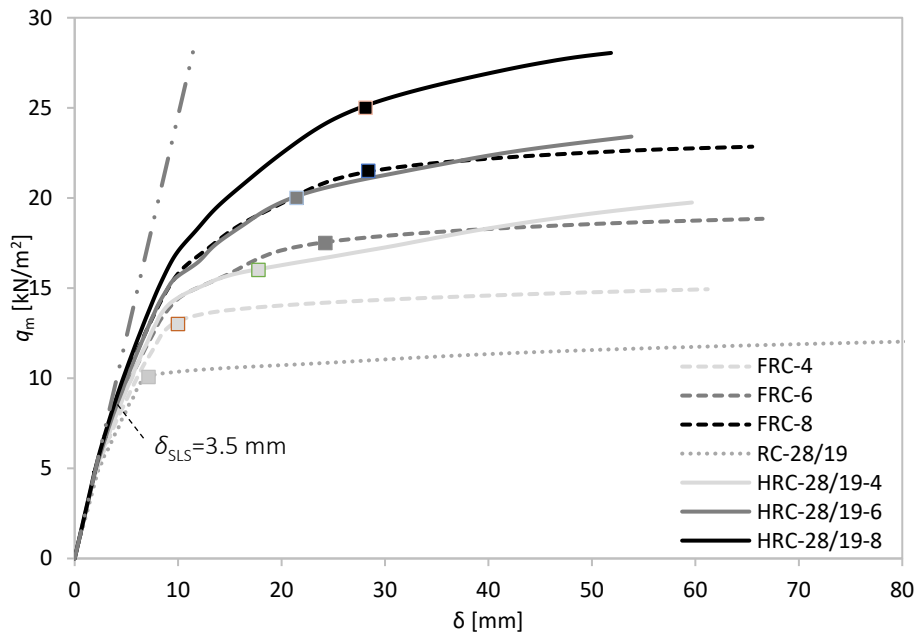
Figure 11 – Numerical load – deflection relationship for each reinforcement alternative.
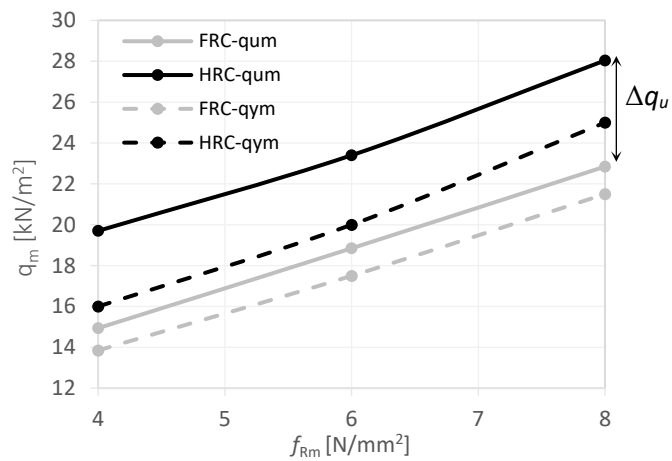

Figure 12 – $q_{um} – f_{Rm}$ and $q_{ym} – f_{Rm}$ relationships for FRC and HRC solutions.
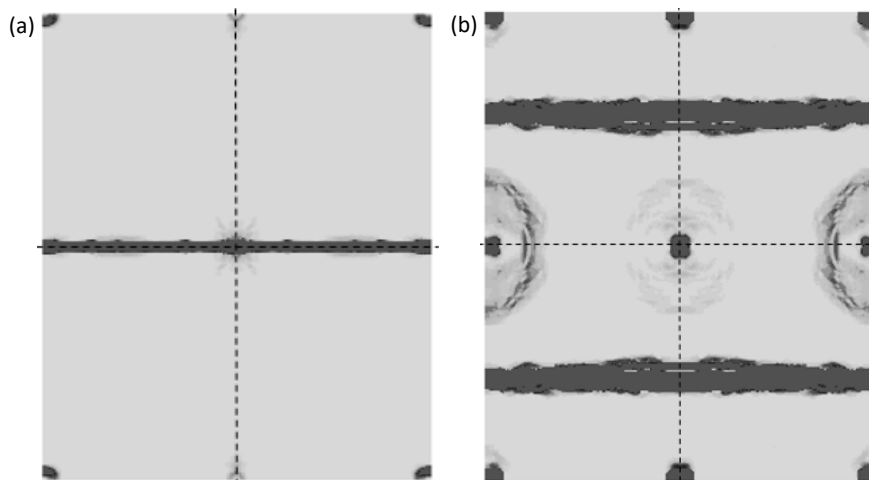
Figure 13 – Plastic mechanism for the FRC-8 with (a) negative yielding line on top face and (b) positive yielding lines on bottom face for q_{um} = 22.8 kN
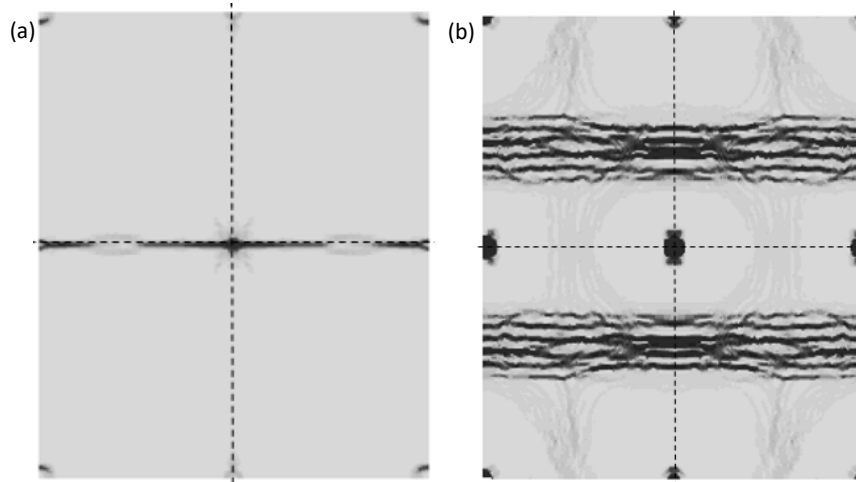

Figure 14 – Plastic mechanism for the HRC-28/19-8 with (a) negative yielding line on top face and (b) positive yielding lines on bottom face for q_{um} = 28.04 kN

A synergetic effect resulted from the combination of both types of reinforcement. This was quantified with the ratio $\Delta q_u / q_{u,HRC} = (q_{u,HRC} - q_{u,FRC}) / q_{u,HRC}$, which achieved values of 22.4% (HRC-28/19-8), 24.7% (HRC-28/19-6) and 32.2% (HRC-28/19-4). These results evidenced that the efficiency of the hybrid combination increases as the FRC performance decrease.

The fulfilment of the ULS of bending requires the satisfaction of the relation $q_{Rd} \geq q_{Sd}$. On the one hand, q_{Sd} is the design load combination for persistent situations assessed by means of using the partial safety coefficients (Υ) for loads recommended in the *fib* MC-2010. Hence, $q_{Sd} = \Upsilon_G \cdot (q_{SW} + q_G) + \Upsilon_Q \cdot q_Q = 13.7$ kN/m^2 (14.0 kN/m^2 for safe-side design purposes), $\Upsilon_G = 1.35$ and $\Upsilon_Q = 1.50$. On the other hand, q_{Rd} is the bearing capacity of the structure (global resistance of the structure) accounting for the uncertainties (geometric and mechanical) that can affect to the structural behaviour computed according to the Global Resistance Format proposed in the *fib* MC-2010 for non-linear analyses (sub-clause 4.6).

In this sense, the Equation 1 presents the relation between q_{Rd}, q_{Rm} (equivalent to q_{um}) and the global resistance safety factor (Υ_R) and the model uncertainty factor (Υ_{Rd}).

$$q_{Rd} = \frac{q_{Rm}}{\gamma_R \gamma_{Rd}} \tag{1}$$

γ_R can be calculated by computing Equation 2, where V_R is the resistance coefficient of variation and α_R and β stands to the resistance sensitivity factor and reliability index, respectively. Values of α_R=0.8 and β=3.8 (service life of 50 years) were considered as appropriate (failure probability $P_f \approx 1 \cdot 10^{-4}$) for residential/office buildings with medium consequences in case of

failure [89]. $\varUpsilon_{Rd} = 1.06$ (model validated in section 3.2 and with low and controlled uncertainties) was assumed following the recommendation of the *fib* MC-2010. In this sense, it should be remarked that the model proved to provide good accuracy respect to experimental values (see section 3.2) and that the governing uncertainties associated to the material (ex., variability of the flexural residual strength) are quantified, controlled and taken into account in the simulations.

$$\gamma_R = e^{(\alpha_R \cdot \beta \cdot V_R)} \tag{2}$$

The ECOV method proposed by Cervenka [90] allows estimating V_R by means of a logarithmic ratio between q_{Rm} and q_{Rk}, q_{Rk} being the characteristic resistance value of q_R obtained from considering characteristic values of all those mechanical variables involved in the non-linear analysis. Nominal values were assumed for the geometric variables.

$$V_R = \frac{1}{1,65} ln\left(\frac{q_{Rm}}{q_{Rk}}\right) \tag{3}$$

With the purpose of calibrating γ_R, numerical simulations considering characteristic values of each of the involved mechanical variables were carried out. To this end, the values of f_{Rk} for each FRC were established by assuming normal distribution of f_R [91] and imposing values of the coefficient of variation for f_R (CoV$_{fR}$). In this regard, based on the results extracted from a large FRC mechanical characterization program [92] and values of CoV$_{fR}$ derived from a numerical study on the intrinsic scatter of FRCs presented in [93], values of CoV$_{fR}$ of 10.0, 17.5 and 25.0% were found representative for FRC-8, FRC-6, and FRC-4, respectively. This assumption is aligned with the fact that the greater the f_{Rm} is, the lower the CoV$_{fR}$ is expected since the amount of fibres necessary to rise f_{Rm} also increases (and the number of fibres in the cracked region). The main characteristic properties and the respective σ_{ctk} - w design-oriented constitutive equations are gathered in Figure 15.
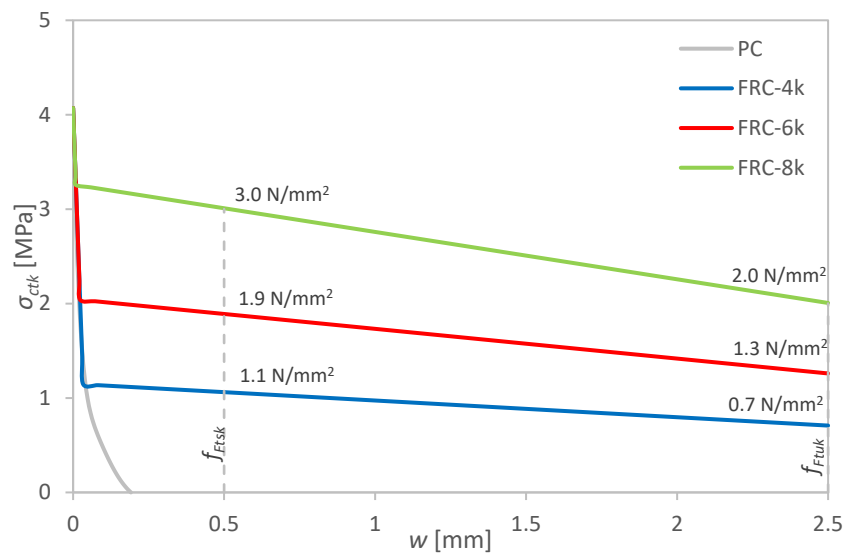

Figure 15 – Tensile constitutive equations of the concrete mixes using characteristic values.

Non-linear Finite Element Analysis Oriented to Optimisation of Fiber Reinforced Concrete Structures

Table 3 and Figure 16 gathers the values of q_{Rm} (q_{um} in Figures 11 and 12), q_{Rk} (computed with characteristic values of the mechanical variables), q_{Rd} (Equation 1) and Υ_R for the different FRC and HRC alternatives considered.

Table 3 – Mean, characteristic and design values of q_R and global resistance safety factor Υ_R

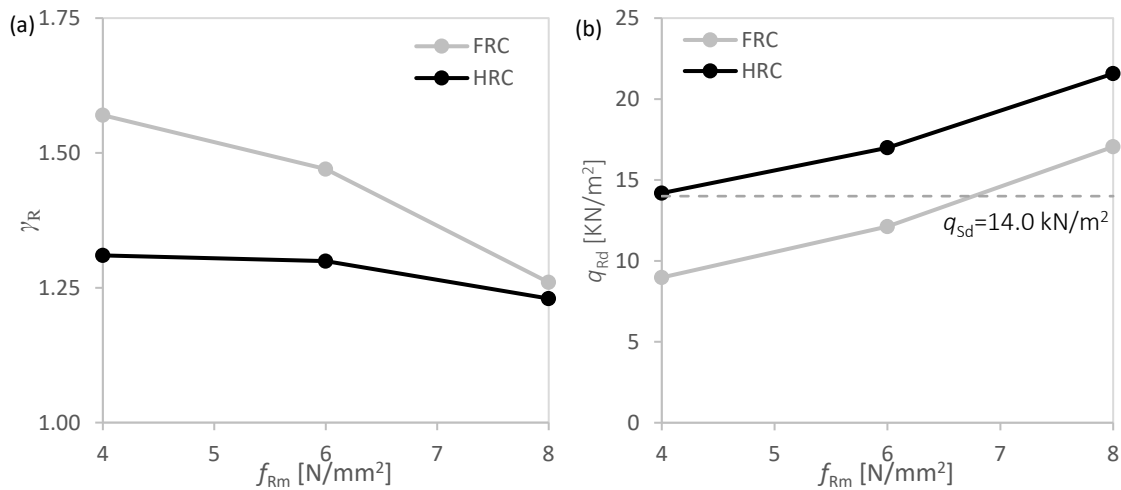| Type	$f_{R1m} = f_{R3m}$ [N/mm²]	CoV$_{fR}$ [%]	$f_{R1k} = f_{R3k}$ [N/mm²]	q_{Rm} [kN/m²]	q_{Rk} [kN/m²]	γ_R [-]	q_{Rd} [kN/m²]
FRC-4	4.0	25.0	2.4	14.9	11.6	1.57	9.0
FRC-6	6.0	17.5	4.3	18.8	15.31	1.47	12.1
FRC-8	8.0	10.0	6.6	22.8	20.1	1.26	17.0
HRC-28/19-4	4.0	25.0	2.4	19.7	17.0	1.31	14.2
HRC-28/19-6	6.0	17.5	4.3	23.4	20.30	1.30	16.7
HRC-28/19-8	8.0	10.0	6.6	28.04	25.1	1.23	21.6

Figure 16 – FRC and HRc curves for (a) global safety coefficient and (b) Design resistance - residual strength.

As this research prototype was meant to prove that a FRC solution could be technically feasible to withstand the established load requirements, the FRC-8 ($f_{R1m} = f_{R3m} = 8$ N/mm²) was selected. Considering the CoV$_{fR} = 10\%$, a $f_{R1k} = f_{R3k} = 6.6$ N/mm² was required; nevertheless, since a FRC-8 led to a ratio $q_{Rd}/q_{Sd} = 17.0/14.0 = 1.2$, a C50/60 compressive strength class 6c ($f_{R1k} = 6.0$ N/mm² and $0.9 \leq f_{R3k}/f_{R1k} < 1.1$) self-compacting SFRC was established for the concrete production.

The amount of steel macro-fibres to be used was assessed by means of the Equation (4) [94], where $f_{cm,cube}$ (68 N/mm²) is the mean compressive strength on cube specimens; V$_f$ (to be determined) is the fibre volume fraction; λ_f (80) the fibre aspect ratio and f_{fu} (1200 N/mm²) is the tensile strength of the steel fibre.

$$V_f = \frac{f_{R3m}}{1.430\sqrt{f_{cm,cube}}\lambda_f f_{fu}} \quad (4)$$

A $V_f = 0.8\%$ resulted from applying the Equation (4), and thus, and amount of steel fibres C_f = $V_f \cdot \delta_f$ = 63 kg/m^3 (δ_f = 7850 kg/m^3, the density of the steel fibre). This amount was increased up to 70 kg/m^3 for production purposes, and from the safety-side. It must be remarked that the amount of the steel mesh for the RC solution for this flat slab was 109 kg/m^3; therefore, a 36% of steel reduction was proposed. The hybrid solution HRC-28/19-4 represented a total amount of steel of 77 kg/m^3 (30 kg/m^3 of steel fibres), which could have also been an attractive solution from the economic point of view; nonetheless, those advantages related with the time savings due to the elimination of the steel mesh manipulation and placing were lost.

4.4.2. STRUCTURAL DUCTILITY REQUIREMENTS

As per *fib* MC 2010, a FRC structure shall fulfil the following conditions: (1) $q_u \geq q_{cr}$ (cracking load) and $q_u \geq q_{SLS}$; (2) $\delta_u \geq 20 \cdot \delta_{SLS}$, δ_{SLS} computed assuming a linear elastic response of the structure; and (3), $\delta_{peak} \geq 5 \cdot \delta_{SLS}$, δ_{peak} estimated for q_{peak}. These conditions, based on the $q - \delta$ relationships (Figure 11), are oriented to avoid a fragile response when cracking occurs and to guarantee both a ductile response through the failure regime and bending moment redistribution capacity in statically indeterminate structures.

Table 4 gathers the magnitudes of all those variables involved in the ductility checks. The characteristic load combination ($q_k = q_{SW} + q_G + \Psi_o \cdot q_Q = 8.9$ kN/m^2; $\Psi_o = 0.7$) was assumed as representative of the SLS load combination (q_{SLS}).

Table 4 – Magnitudes of the parameters involved in the ductility checks according to the fib MC-2010

	FRC-4	FRC-6	FRC-8	HRC-28/19-4	HRC-28/19-4	HRC-28/19-4
q_{cr} [kN]	4.8	4.8	4.8	4.8	4.8	4.8
q_u [kN]	14.9	18.8	22.8	19.7	23.4	28.04
q_u/q_{cr} [-]	3.10 > 1	3.92 > 1	4.75 > 1	4.10 > 1	4.88 > 1	5.84 > 1
q_u/q_{SLS} [-]	1.80 > 1	2.27 > 1	2.75 > 1	2.37 > 1	2.82 > 1	3.38 > 1
δ_{SLS} [mm]	3.5	3.5	3.5	3.5	3.5	3.5
δ_u [mm]	61.2	66.5	65.5	59.7	53.8	51.8
δ_u/δ_{SLS} [-]	**17.3 < 20**	**18.7 < 20**	**18.5 < 20**	**17.1 < 20**	**15.4 < 20**	**14.8 < 20**

The results presented in Table 4 allowed confirming that the strength requirements q_u/q_{cr} and q_u/q_{SLS} were fulfilled with ratios superior to 1.50 for all cases. Contrarily, none of the reinforcement alternatives considered achieved the ratio $\delta_u/\delta_{SLS} \geq 20$. This, however, was omitted since the ultimate conditions imposed were very restrictive and it was known beforehand that this structural typology is able to redistribute forces with high levels of ductility associated and

sufficient post-cracking strength is provided to the concrete. Consequently, the FRC-8 (with $\delta_u/\delta_{SLS} < 20$) was considered to be suitable and the results obtained from the real-scale tests [78] confirmed the goodness of this decision.

It must be remarked that it was assumed q_{peak} and δ_{peak} were assumed to be equal to q_u and δ_u, respectively, as the ultimate limit state condition was reached before the numerical model detected the peak load (see Figure 11); consequently, based on the results presented in Table 4, the relation $\delta_{peak} \geq 5 \cdot \delta_{SLS}$ is satisfied for all of the reinforcement alternatives analysed.

4.4.3. SERVICE LIMIT STATE OF CRACKING

The quasi-permanent load combination ($q_{qp} = q_{SW} + q_G + \Psi_2 \cdot q_Q = 7.4$ kN/m^2; $\Psi_2 = 0.2$) was considered according to [79]. For this load combination the cracks are mainly concentrated in the vicinities of the columns. Numerical models have been developed and recently published regarding this issue [95,96]. For FEM analysis, to provide an approximation of the mean value of the crack width associated to q_{qp} (w_{qp}), the approach proposed by Tiberti [76] and later used by Nogales [77] was applied, this consisting in multiplying the plastic strain by the L_{ch} (80 mm). According to those authors, this assumption uses to lead to conservative results, particularly for the HRC, as it assumes that plastic strains are concentrated in a single crack. Precaution must be taken since the FE simulations presented did not take into consideration any creep deformation or cracking resulting from long-term effects. Figure 17 presents the relationships $w_{qp} - f_R$ derived numerically.
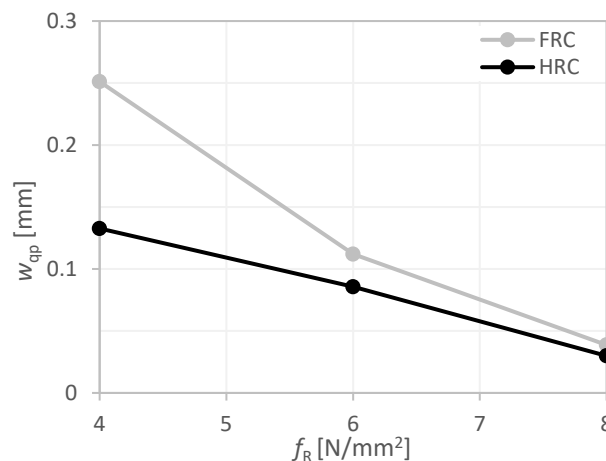

Figure 17 –Crack width – flexural residual strength ($f_{R1} = f_{R3}$) for the quasi-permanent load combination ($q_{qp} = 7.4$ kN/m^2).

In the light of the results presented in Figure 17, it can be stated that:

- HRCs confirmed to lead to a better crack width control respect to the FRC alternatives, particularly when comparing with FRCs with $f_R < 6.0$ N/mm^2.

- $w_{\mathrm{cp}} < 0.25$ mm for reinforcement alternatives studied and $w_{\mathrm{cp}} < 0.15$ mm for the HRC and those FRCs solutions with $f_R \geq 6.0$ N/mm^2.

Additionally, relationship between the tensile stress (σ_s) of the top steel-mesh (central column) and the applied load (q_m) is depicted in Figure 18.

The results gathered in Figure 18 allow confirming that the increase the FRC post-cracking strength capacity leads to a reduction of σ_s, and, hence, a reduction of the crack width. Particularly, for q_{cp}, σ_s decreases a 27% when comparing the HRC-28/19-8 ($\sigma_s = 54$ N/mm^2) and HRC-28/19-4 ($\sigma_s = 74$ N/mm^2). This reduction is of 38% ($\sigma_s = 189$ N/mm^2 and $\sigma_s = 307$ N/mm^2 for HRC-28/19-8 and HRC-28/19-4, respectively) when q_{Sd} is considered. Therefore, it seems that the efficiency of the FRC in controlling the tensile stresses of the bars, and consequently the crack width, increases with the load level.
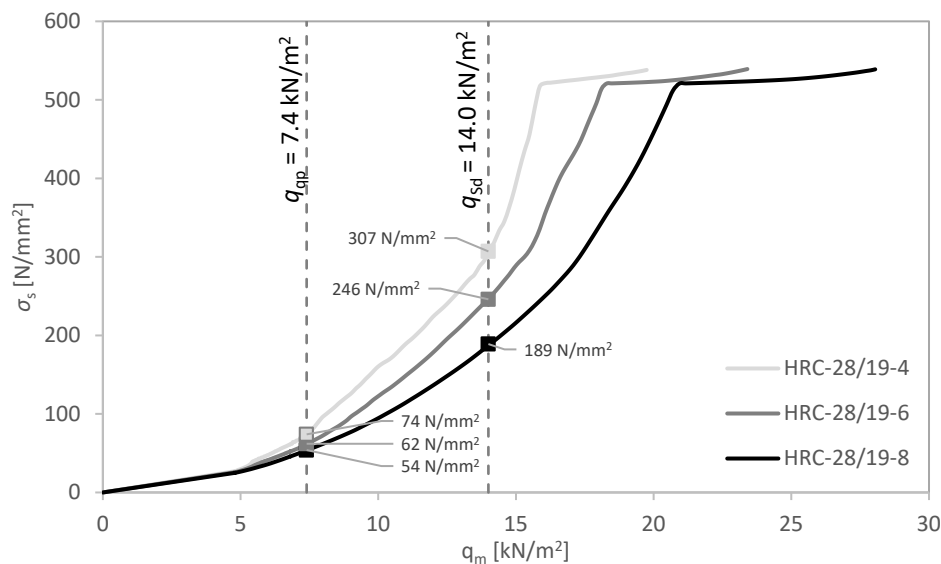

Figure 18 – σ_s – q_m relationship for the HRC alternatives (σs measured at the upper steel mesh of the central column)

5.   CONCLUSIONS

In this research paper, a four 6.0 x 5.0 m^2 bays column-supported SFRC flat slab with 0.2 m in thickness was designed by means of a 3D non-linear FE model previously validated considering results from an experimental program [56] and considering the provisions gathered in the fib MC-2010 for FRC structures. The main objective the industrial-oriented research consisted in reaching a valid design for flexure capable of reducing by 30% the amount of steel reinforcement respect to the existing traditional solutions (even those using fibres). To this end, the numerical model was used to perform a parametric analysis for which different reinforcement alternatives were analysed (including hybrid solutions). Moreover, the safety factor to be applied to global resistance of the structure was computed.

Based on the result obtained, the following conclusions can be drawn:

- The results derived from the validated numerical model allowed confirming that FRC and HRC solutions can lead to optimized amounts of steel reinforcement (for flexure) for column-supported flat slabs respect to the traditional RC alternatives. In the studied case, a reduction in 30% of the steel fibre amount was achieved respect the previous reported cases.

- The HRC solutions analyzed proved to provide a better structural performance than those with only FRC. In this sense, the structural efficiency of the HRC alternatives is more noticeable when low FRC residual strength classes are considered. Nevertheless, precautions should be taken when low reinforcement ratios and strain-softening FRCs are combined since crack localization and reductions of the sectional ductility were reported by other researchers [80–87]. To avoid these phenomena, the minimum reinforcement ratio should be assessed considering the residual tensile strength performance of the FRC.

- Hybrid configurations led to global resistance reduction safety factors lower than those obtained for the FRC solutions analysed. However, a convergence of this safety factor to 1.25 was detected for HRC and FRC with $f_{Rm} \geq 8.0$ N/mm^2.

- The numerical model together with the safety format presented in the *fib* Model Code for non-linear analysis proved to be a reliable tool for safely design of real-scale slab constructed, even from the safe side, according to the experimental results reported by Aidarov [78].

It is worth noticing that the numerical simulations were carried out on a fixed slab geometry and loading configuration; nevertheless, the abovementioned conclusions could be extended to slabs with similar slenderness ratio. The rebar amount and distribution were stablished for flexural loading and further research is needed for other loading situations such as punching and torsion.

ACKNOWLEDGEMENTS

REFERENCES

Alejandro Nogales Arroyo

[1] di Prisco M, Toniolo G. Structural applications of steel fibre reinforced concrete. Proc Int Work Milan, Italy 2000.

[2] di Prisco M, Plizzari G, Vandewalle L. Fibre reinforced concrete : new design perspectives. Mater Struct 2009:1261–81. https://doi.org/10.1617/s11527-009-9529-4.

[3] Barros J, Figueiras JA. Experimental behaviour of fibre concrete slabs on soil. Mech Cohesive-Frictional Mater 1998;3:277.

[4] Meda A, Plizzari GA, Riva P. Fracture behavior of SFRC slabs on grade. Mater Struct Constr 2004;37:405–11. https://doi.org/10.1617/14093.

[5] Meda A, Plizzari G. New design approach for steel fiber-reinforced concrete slabs-on-ground based on fracture mechanics. ACI Struct J 2004;101 (3):298–303.

[6] Sorelli L, Meda A, Plizzari G. Steel fiber concrete slabs on ground: A structural matter. ACI Struct J 2006;103:551–8.

[7] Roesler JR, Altoubat SA, Lange DA, Rieder KA, Ulreich GR. Effect of synthetic fibers on structural behavior of concrete slabs-on-ground. ACI Mater J 2006;103:3–10.

[8] Alani AM, Beckett D. Mechanical properties of a large scale synthetic fibre reinforced concrete ground slab. Constr Build Mater 2012;41:335–44. https://doi.org/10.1016/j.conbuildmat.2012.11.043.

[9] de la Fuente A, Escariz RC, de Figueiredo AD, Molins C, Aguado A. A new design method for steel fibre reinforced concrete pipes. Constr Build Mater 2012;30:547–55. https://doi.org/10.1016/j.conbuildmat.2011.12.015.

[10] de la Fuente A, Escariz RC, de Figueiredo AD, Aguado A. Design of macro-synthetic fibre reinforced concrete pipes. Constr Build Mater 2013;43:523–32. https://doi.org/10.1016/j.conbuildmat.2013.02.036.

[11] Banthia N, Trottier J, Beaupré D. Steel-fiber-reinforced wet-mix shotcrete: Comparisons with cast concrete. J Mater Civ Eng 1994;6:430–7.

[12] Cengiz O, Turanli L. Comparative evaluation of steel mesh, steel fibre and high-performance polypropylene fibre reinforced shotcrete in panel test. Cem Concr Res 2004;34:1357–64. https://doi.org/10.1016/j.cemconres.2003.12.024.

[13] Caratelli A, Meda A, Rinaldi Z, Romualdi P. Structural behaviour of precast tunnel segments in fiber reinforced concrete. Tunn Undergr Sp Technol 2011;26:284–91. https://doi.org/10.1016/j.tust.2010.10.003.

[14] Meda A, Rinaldi Z, Caratelli A, Cignitti F. Experimental investigation on precast tunnel segments under TBM thrust action. Eng Struct 2016;119:174–85. https://doi.org/10.1016/j.engstruct.2016.03.049.

[15] Plizzari GA, Tiberti G. Steel fibers as reinforcement for precast tunnel segments. Tunn Undergr Sp Technol 2006;21:438–9. https://doi.org/10.1016/j.tust.2005.12.079.

[16] Liao L, de la Fuente A, Cavalaro SHP, Aguado A. Design of FRC tunnel segments considering the ductility requirements of the fib Model Code 2010: Application to the Barcelona Metro line 9. Tunn Undergr Sp Technol 2015;47:200–10.

[17] de la Fuente A, Pujadas P, Blanco A, Aguado A. Experiences in Barcelona with the use of fibres in segmental linings. Tunn Undergr Sp Technol 2012;27:60–71. https://doi.org/10.1016/j.tust.2011.07.001.

[18] Jamshidi M, Hoseini A, Vahdani S, de Santos C, de la Fuente A. Seismic fragility curves for vulnerability assessment of steel fiber reinforced concrete segmental tunnel linings. Tunn Undergr Sp Technol 2018;78:259–74. https://doi.org/10.1016/j.tust.2018.04.032.

[19] Buchta V, Mynarcik P. Experimental testing of fibre-concrete foundation slab model. Appl Mech Mater 2004;504–504:291–4. https://doi.org/10.1016/j.compstruct.2018.01.094.

[20] de la Fuente A, Aguado A, Molins C, Armengou J. Innovations on components and testing for precast panels to be used in reinforced earth retaining walls. Constr Build Mater 2011;25:2198–205. https://doi.org/10.1016/j.conbuildmat.2010.11.003.

[21] di Prisco M, Dozio D, Belletti B. On the fracture behaviour of thin-walled SFRC roof elements. Mater Struct Constr 2013;46:803–29. https://doi.org/10.1617/s11527-012-9935-x.

[22] Gettu R, Ramos G, Aguado A, García T, Barragán B. Steel Fiber Reinforced Concrete for the Barcelona Metro Line 9 Tunnel Lining. BEFIB 2004, Proc 6th RILEM Symp FRC 2004;RILEM Symp:1–46.

[23] Chiaia B, Fantilli AP, Vallini P. Evaluation of minimum reinforcement ratio in FRC members and application to tunnel linings. Mater Struct Constr 2006;40:593–604. https://doi.org/10.1617/s11527-006-9166-0.

[24] Chiaia B, Fantilli AP, Vallini P. Combining fiber-reinforced concrete with traditional reinforcement in tunnel linings. Eng Struct 2009;31:1600–6. https://doi.org/10.1016/j.engstruct.2009.02.037.

[25] Tiberti G, Minelli F, Plizzari G. Reinforcement optimization of fiber reinforced concrete linings for conventional tunnels. Compos Part B Eng 2014;58:199–207. https://doi.org/10.1016/j.compositesb.2013.10.012.

[26] DBV. Guide to Good Practice: Steel Fibre Concrete. Ger Soc Concr Constr Technol (DBV), Berlin, Ger 2001.

[27] RILEM TC 162-TDF. Test and design methods for steel fibre reinforced concrete. Design with σ-ε method. Mater Struct 2003;35:262–78. https://doi.org/10.1617/13837.

[28] Comisión Permanente del Hormigón. Instrucción de Hormigón Estructual (EHE-08), Ministerio de Fomento. 2008.

[29] International Federation for Structural Concrete (fib). fib-Model Code for Concrete Structures 2010. Lausanne: 2010. https://doi.org/10.1002/9783433604090.

[30] ACI 544. Fibre-Reinforced Concrete: Design and Construction of Steel Fibre- Reinforced Precast Concrete Tunnel Segments. 2014.

[31] Destrée X, Mandl J. Steel fibre only reinforced concrete in free suspended elevated slabs: Case studies, design assisted by testing route, comparison to the latest SFRC standard documents. Tailor Made Concr Struct 2008:437–43. https://doi.org/10.1016/j.jhydrol.2010.04.024.

[32] Parmentier B, Van Itterbeeck P, Skowron A. The behaviour of SFRC flat slabs: The limelette full-scale experiments to support design model codes. Am Concr Institute, ACI Spec Publ 2014;2014-July:213–22. https://doi.org/10.35789/fib.bull.0079.ch21.

[33] di Prisco M, Martinelli P, Parmentier B. On the reliability of the design approach for FRC structures according to fib Model Code 2010: the case of elevated slabs. Struct Concr 2016;17:588–602. https://doi.org/10.1002/suco.201500151.

[34] Salehian H, Barros J. Assessment of the performance of steel fibre reinforced self-compacting concrete in elevated slabs. Cem Concr Compos 2015;55:268–80. https://doi.org/10.1016/j.cemconcomp.2014.09.016.

[35] de la Fuente A, Casanovas-Rubio MDM, Pons O, Armengou J. Sustainability of Column-Supported RC Slabs: Fiber Reinforcement as an Alternative. J Constr Eng Manag 2019;145:1–12. https://doi.org/10.1061/(ASCE)CO.1943-7862.0001667.

[36] ACI 544.6R-15. Report on Design and Construction of Steel Fiber-Reinforced Concrete Elevated Slabs 2015.

[37] Pujadas P, Blanco A, de la Fuente A, Aguado A. Cracking behavior of FRC slabs with traditional reinforcement. Mater Struct Constr 2012;45:707–25. https://doi.org/10.1617/s11527-011-9791-0.

[38] Hedebratt J, Silfwerbrand J. Full-scale test of a pile supported steel fibre concrete slab. Mater Struct Constr 2013;47:647–66. https://doi.org/10.1617/s11527-013-0086-5.

[39] Facconi L, Minelli F, Plizzari G. Steel fiber reinforced self-compacting concrete thin slabs – Experimental study and verification against Model Code 2010 provisions. Eng Struct 2016;122:226–37. https://doi.org/10.1016/j.engstruct.2016.04.030.

[40] di Prisco M, Colombo M, Pourzarabi A. Biaxial bending of SFRC slabs : Is conventional reinforcement necessary ? Mater Struct 2018;52:1–15. https://doi.org/10.1617/s11527-018-1302-0.

[41] Salehian H, Barros J. Prediction of the load carrying capacity of elevated steel fibre reinforced concrete slabs. Compos Struct 2017;170:169–91. https://doi.org/10.1016/j.compstruct.2017.03.002.

[42] Facconi L, Plizzari G, Minelli F. Elevated slabs made of hybrid reinforced concrete: Proposal of a new design approach in flexure. Struct Concr 2018:1–16. https://doi.org/10.1002/suco.201700278.

[43] Taheri M, Barros J, Salehian H. Parametric Study of the Use of Strain Softening/Hardening FRC for RC Elements Failing in Bending. J Mater Civ Eng 2012;24:259–74. https://doi.org/10.1061/(ASCE)MT.1943-5533.0000373.

[44] Pujadas P, Blanco A, Cavalaro SHP, Aguado A. Plastic fibres as the only reinforcement for flat suspended slabs: Experimental investigation and numerical simulation. Constr Build Mater 2014;57:92–104. https://doi.org/10.1016/j.conbuildmat.2014.01.082.

[45] Pujadas P, Blanco A, Cavalaro SHP, Aguado A, Grünewald S, Blom K, et al. Plastic fibres as the only reinforcement for flat suspended slabs: Parametric study and design considerations. Constr Build Mater 2014;70:88–96. https://doi.org/10.1016/j.conbuildmat.2014.07.091.

[46] Pujadas P, Blanco A, Cavalaro SHP, de la Fuente A, Aguado A. The need to consider flexural post-cracking creep behavior of macro-synthetic fiber reinforced concrete. Constr Build Mater 2017;149:790–800. https://doi.org/10.1016/j.conbuildmat.2017.05.166.

[47] Plizzari G, Serna P. Structural effects of FRC creep. Mater Struct 2018;51:1–11. https://doi.org/10.1617/s11527-018-1290-0.

[48] Ackermann FP, Schnell J. Steel Fibre Reinforced Continuous Composite Slabs. Int Conf Compos Constr Steel Concr 2008 Compos Constr Steel Concr VI 2008:125–37.

[49] Schumacher P. Rotation capacity of self-compacting steel fiber reinforced concrete. 2006.

[50] Blanco A, Pujadas P, de la Fuente A, Cavalaro SHP, Aguado A. Assessment of the fibre orientation factor in SFRC slabs. Compos Part B Eng 2015;68:343–54. https://doi.org/10.1016/j.compositesb.2014.09.001.

[51] Mahmood SMF, Agarwal A, Foster SJ, Valipour H. Flexural performance of steel fibre reinforced concrete beams designed for moment redistribution. Eng Struct 2018;177:695–706. https://doi.org/10.1016/j.engstruct.2018.10.007.

[52] Küsel F, Kearsley E. Effect of steel fibres in combination with different reinforcing ratios on the performance of continuous beams. Constr Build Mater 2019;227. https://doi.org/10.1016/j.conbuildmat.2019.07.279.

[53] Falkner H, Gossla U. Pile Supported Reinforced or Prestessed SFRC Ground Slabs. PRO 6 3rd Int RILEM Work High Perform Fiber Reinf Cem Compos (HPFRCC 3) 1999;38:595–602.

[54] Destrée X. Steel Fiber-Reinforced Concrete in Free Suspended-Elevated Slabs 2001:155–64.

[55] Destrée X. Structural application of steel fibres as only reinforcing in free suspended elevated slabs: conditions–Design examples. 6th Int RILEM Symp Fibre Reinf Concr 2004:1073–82.

[56] Gossla U. Development of SFRC Free Suspended Elevated Flat Slabs, research report for Arcelor Mittal 2005.

[57] Døssland AL. Fibre Reinforcement in Load Carrying Concrete Structures. Norwegian University of Science and Technology, 2008.

[58] Soranakom C, Mobasher B, Destree X. Numerical simulation of FRC round panel tests and full-scale elevated slabs. ACI Spec Publ 2007;248:31–40.

[59] Ošlejs J. New Frontiers for Steel Fiber - Reinforced Concrete - Experience from the Baltics and Scandinavia 2008:45–50.

[60] Maturana A. Estudio teórico-experimental de la aplicabilidad del hormigón reforzado con fibras de acero a losas de forjado multidireccionales. 2013.

[61] di Prisco M, Martinelli P, Dozio D. The structural redistribution coefficient KRd: a numerical approach to its evaluation. Struct Concr 2016;17:390–407. https://doi.org/10.1002/suco.201500118.

[62] Colombo M, Martinelli P, di Prisco M. On the evaluation of the structural redistribution factor in FRC design: a yield line approach. Mater Struct Constr 2017;50:1–18. https://doi.org/10.1617/s11527-016-0969-3.

[63] Abrishambaf A, Barros J, Cunha V. Relation between fibre distribution and post-cracking behaviour in steel fibre reinforced self-compacting concrete panels. Cem Concr Res 2013;51:57–66. https://doi.org/10.1016/j.cemconres.2013.04.009.

[64] Swanson Analysis Systems. ANSYS User Manual 2013.

[65] Červenka Consulting Ltd. ATENA Program Documentation. Prague: 2013.

[66] Pujadas Alvarez P. Caracterización y diseño del homigón reforzado con fibras plásticas. 2013.

[67] Blanco A, Cavalaro SHP, de la Fuente A, Grünewald S, Blom CBM, Walraven JC. Application of FRC constitutive models to modelling of slabs. Mater Struct Constr 2015;48:2943–59. https://doi.org/10.1617/s11527-014-0369-5.

[68] Dassault Systèmes Simulia. Abaqus CAE User's Manual (6.12). Providence: Dassault Systèmes; 2012.

[69] Oikonomou-Mpegetis S. Behavior and Design of steel fibres reinforced concrete slabs. 2012.

[70] TNO - DIANA FEA BV. Analysis procedures DIANA - Finite Element Analysis. User's Manual 2008.

[71] European Commitee for Standardization. Precast concrete products - test method for metallic fibre concrete- Measuring the flexural tensile strength. Br Stand Inst 2005. https://doi.org/9780580610523.

[72] Blanco A, Pujadas P, De La Fuente A, Cavalaro SHP, Aguado A. Application of constitutive models in European codes to RC-FRC. Constr Build Mater 2013;40:246–59. https://doi.org/10.1016/j.conbuildmat.2012.09.096.

[73] Blanco A, Pujadas P, Cavalaro SHP, De La Fuente A, Aguado A. Constitutive model for fibre reinforced concrete based on the Barcelona test. Cem Concr Compos 2014;53:327–40. https://doi.org/10.1016/j.cemconcomp.2014.07.017.

[74] Higashiyama H, Ota A, Mizukoshi M. Design Equation for Punching Shear Capacity of SFRC Slabs. Int J Concr Struct Mater 2011;5:35–42. https://doi.org/10.4334/ijcsm.2011.5.1.035.

[75] Maya LF, Fernández Ruiz M, Muttoni A, Foster SJ. Punching shear strength of steel fibre reinforced concrete slabs. Eng Struct 2012;40:83–94. https://doi.org/10.1016/j.engstruct.2012.02.009.

[76] Tiberti G. Conci prefabbricati in calcestruzzo fibrorinforzato per la realizzazione di gallerie. Università degli studi di Brescia, 2004.

[77] Nogales A, de la Fuente A. Crack width design approach for fibre reinforced concrete tunnel segments for TBM thrust loads. Tunn Undergr Sp Technol 2020;98. https://doi.org/10.1016/j.tust.2020.103342.

[78] Aidarov S, De La Fuente A, Mena F, Ángel S. Campaña experimental de un forjado de hormigón reforzado con fibras a escala real. III Congr. Consult. Estructuras - ACE - Barcelona 2019, 2019, p. 1–10.

[79] Gobierno de España. Código Técnico de la Edificación (CTE) Documento básico: Seguridad estructural. Apartado de "Acciones en la Edificación." 2009.

[80] Conforti A, Zerbino R, Plizzari GA. Assessing the influence of fibres on the flexural behaviour of RC beams with different longitudinal reinforcement ratios. Struct Concr 2020. https://doi.org/10.1093/comnet/xxx000.

[81] Markić T, Amin A, Kaufmann W, Pfyl T. Strength and Deformation Capacity of Tension and Flexural RC Members Containing Steel Fibers. J Struct Eng (United States) 2020;146:1–17. https://doi.org/10.1061/(ASCE)ST.1943-541X.0002614.

[82] Dancygier AN. Effect of cracking localization on the structural ductility of normal strength and high strength reinforced concrete beams with steel fibers. Int J Prot Struct 2019;10:457.

[83] Yoo DY, Moon DY. Effect of steel fibers on the flexural behavior of RC beams with very low reinforcement ratios. Constr Build Mater 2018;188:237–54. https://doi.org/10.1016/j.conbuildmat.2018.08.099.

[84] Dancygier AN, Berkover E. Cracking localization and reduced ductility in fiber-reinforced concrete beams with low reinforcement ratios. Eng Struct 2016;111:411–24. https://doi.org/10.1016/j.engstruct.2015.11.046.

[85] Dancygier AN, Savir Z. Flexural behavior of HSFRC with low reinforcement ratios. Eng Struct 2006;28:1503–12. https://doi.org/10.1016/j.engstruct.2006.02.005.

[86] Mertol HC, Baran E, Bello HJ. Flexural behavior of lightly and heavily reinforced steel fiber concrete beams. Constr Build Mater 2015;98:185–93. https://doi.org/10.1016/j.conbuildmat.2015.08.032.

[87] Meda A, Minelli F, Plizzari GA. Flexural behaviour of RC beams in fibre reinforced concrete. Compos Part B Eng 2012;43:2930–7. https://doi.org/10.1016/j.compositesb.2012.06.003.

[88] Červenka J, Červenka V, Laserna S. On crack band model in finite element analysis of concrete fracture in engineering practice. Eng Fract Mech 2018;197:27–47. https://doi.org/10.1016/j.engfracmech.2018.04.010.

[89] European Commitee for Standardization. EN 1990 2006. https://doi.org/10.2514/2.2772.

[90] Cervenka V. Global safety formats in fib Model Code 2010 for design of concrete structures. 11th Int Probabilistic Work 2013:31–40.

[91] Bernard E, Xu G. Normality of Post-Crack Performance Data for Fiber-Reinforced Concrete. Adv Civ Eng Mater 2019;8:145–57. https://doi.org/10.1520/ACEM20180054.

[92] Galeote E, Blanco A, Cavalaro SHP, de la Fuente A. Correlation between the Barcelona test and the bending test in fibre reinforced concrete. Constr Build Mater 2017;152:529–38. https://doi.org/10.1016/j.conbuildmat.2017.07.028.

[93] Cavalaro SHP, Aguado A. Intrinsic scatter of FRC: an alternative philosophy to estimate characteristic values. Mater Struct Constr 2015;48:3537–55. https://doi.org/10.1617/s11527-014-0420-6.

[94] Tiberti G, Germano F, Mudadu A, Plizzari GA. An overview of the flexural post-cracking behavior of steel fiber reinforced concrete. Struct Concr 2018;19:695–718. https://doi.org/10.1002/suco.201700068.

[95] Chiaia B, Fantilli AP, Vallini P. Evaluation of crack width in FRC structures and application to tunnel linings. Mater Struct Constr 2008;42:339–51. https://doi.org/10.1617/s11527-008-9385-7.

[96] Taheri M, Barros J, Salehian H. Integrated approach for the prediction of crack width and spacing in flexural FRC members with hybrid reinforcement. Eng Struct 2020;209:110208. https://doi.org/10.1016/j.engstruct.2020.110208.

2.3. JOURNAL PAPER III: ROTATION AND MOMENT REDISTRIBUTION CAPACITY OF FIBRE-REINFORCED CONCRETE BEAMS: PARAMETRIC ANALYSIS AND CODE COMPLIANCE

Alejandro Nogales[a,b,*], Nikola Tošić[b] and Albert de la Fuente[b],

[a]Smart Engineering Ltd., UPC Spin-Off, Jordi Girona 1-3, 08034 Barcelona, Spain

[b]Civil and Environmental Engineering Deparment, Universitat Politècnica de Catalunya (UPC), Jordi Girona 1-3, 08034 Barcelona, Spain

*Corresponding author

ABSTRACT

Fibre-reinforced concrete (FRC) has been proved to be a competitive solution for structural purposes. Extensive research has highlighted the benefits of adding fibers on the post-cracking strength, reduced crack spacing and crack width, and improved durability, among others. However, these aspects are related to serviceability limit states, and significant work remains to be done in terms of ultimate limit state behavior of FRC members. As recent publications have emphasized, reinforced concrete beams with low reinforcement ratios may result in a reduction of deformation capacity and, hence, to a loss of duc- tility. To further investigate this topic, this paper presents the results of a numerical parametric study of simply and continuous supported hybrid-reinforced concrete (HRC) beams made with different amounts of fibers and reinforcement ratios. The deformation, rotational, and moment redistribution capacity of those were assessed by means of a finite-element model previously calibrated using experimental results available in the literature. The results showed that there is a significant reduction of rotation capacity and moment redistribution for lightly reinforced (hybrid) members. Finally, the paper con- tains practical recommendations in terms of minimum reinforcement ratios that guarantee adequate rotation and redistribution capacity of HRC members. As such, the results of this study can provide a contribution toward more reli- able structural designs of HRC members.

KEYWORDS: Deformation capacity, ductility, fiber-reinforced concrete, ultimate limit state

Notation

List of symbols

		w	crack opening in mm
$CMOD$	crack mouth opening displacement	w_s	crack opening for f_{Fts}
E_c	modulus of elasticity for concrete	w_t	crack opening when $\sigma_j = 0$
E_{ci}	tangent modulus of elasticity of concrete at a stress σ_i	w	crack opening in mm
E_{c1}	secant modulus from the origin to the peak compressive stress	w_s	crack opening for f_{Fts}
f_c	mean value of the cylindrical compressive concrete	w_t	crack opening when $\sigma_j = 0$
f_{ct}	tensile concrete strength	w_u	crack opening for f_{Ftu}
f_{Fts}	serviceability residual strength (post-cracking strength for serviceability crack opening)	ε_1	concrete strain for f_{ctm}
f_{Ftu}	ultimate residual strength (post-cracking strength for ultimate crack opening)	ε_c	concrete compression strain
$f_{R,j}$	value of the residual flexural strength corresponding to $CMOD = CMODj$	ε_{botton}	strain at the bottom layer of the beam
f_y	yield strength of steel reinforcement	ε_{top}	strain at the top layer of the beam
f_u	ultimate strength of steel reinforcement		
f_{max}	maximum strength of steel reinforcement	ρ_s	longitudinal reinforcement ratio
G_F	fracture energy of concrete	σ_c	concrete compression stress
h	beam height	σ_j	stress point for concrete tensile constitutive curve, j being the point numbering
KMR	moment redistribution ratio	$\theta_{elastic}$	plastic rotation
M_{el}	theoretical elastic moment	$\theta_{plastic}$	elastic rotation
M_{exp}	moment measured experimentally	χ	Curvature
V_f	fibre volume fraction	χ_y	Curvature at steel yield strength

1. INTRODUCTION

The increasing use of fibre reinforced concrete (FRC) in those structural members for which flexure is the governing design condition has given rise to questions regarding the deformation capacity of such elements. As it has been previously shown, the addition of structural fibres tends

to reduce crack spacing, crack widths, and deflections, while at the same time it increases stiffness and the load-bearing capacity of flexural members [1–4]. Therefore, the improvements are mostly related to serviceability limit state (SLS) performance. These aspects allow engineers to use optimal combinations of fibres and longitudinal reinforcement that can maintain the same load-bearing capacity as reinforced concrete (RC), but with lower reinforcement ratios (ρ_s) minimizing cracks and deflections while reducing building time and costs. Nevertheless, as it has been outlined in [5–8] that the combination of fibres and conventional reinforcement (known as hybrid reinforced concrete, HRC hereinafter) may lead to failure at lower deformations compared with those corresponding to elements without fibres, hence, this compromising both the bearing capacity and degree of ductility at the ultimate limit state (ULS).

Experimental research carried out on simply supported beams combining different values of ρ_s and fibre volume fraction (V_f) [5,9–12] provided results that confirm this loss of deformation capacity, relating it directly to rotational capacity. The reported loss of rotation capacity was caused by crack localisation, resulting in failure of the conventional steel rebars at lower deformations, particularly for low values of ρ_s (i.e. <0.5%) that are close to the minimum reinforcement ratio necessary for avoiding brittle failure. Other tests conducted on simply supported beams with $\rho_s \geq 0.5\%$ showed that the beam deformation capacity was unaltered, without any crack localisation [13,14]. These outcomes are of paramount importance, as the combination of structural fibres with low amounts of conventional reinforcement is frequently used in several structural typologies (i.e., industrial flooring [15,16], precast concrete segments for tunnel linings [17], sewerage pipes [18,19]) and this embrittlement effect could jeopardize the ductile response expected in case of failure. In this regard, the previous experimental research has been focused on specific magnitudes of ρ_s and FRC strength classes and, consequently, the conclusions and recommendations derived from the results should be limited accordingly.

Of particular importance in this regard is the ability of statically indeterminate structures to redistribute moments. It allows the structure to transfer forces away from critical sections, this allowing to reach higher loads and eventually leading to more ductile failure; a feature of special importance in seismically active regions [20]. Comprehensive research have been carried out regarding this topic, since the capacity of the non-critical sections can be used allowing the designer to optimise reinforcement requirements and therefore costs [21]. Moment redistribution occurs at all limit states due to the longitudinal variation in stiffness, the most rigid sections tend to absorb more forces than less rigid [22]. When a section cracks, its stiffness is affected and it takes smaller moments under increasing loads than it would have if it had not cracked, the moment redistribution results in a change in the distribution of bending moments obtained from a theoretical linear elastic analysis [23–27]. At ultimate limit state, moment redistribution occurs

due to the formation and gradual rotation of plastic hinge regions, and has also been shown to be highly dependent on the stiffness or flexural rigidity of the non-hinge regions [24,28,29].

The large number of experimental results regarding this topic has allowed the incorporation of moment redistribution in design guidelines and codes. The margin of moment redistribution allowed in national and international codes [30–34] depends primarily, apart from the structure typology, on the rotation capacity of plastic hinge regions. For continuous beams, the maximum moment redistribution allowed is 30% for Eurocode 2 (EC2) [30], the *fib* Model Code 2010 (MC2010) [32] and the Australian code AS 3600-2009 [34], whereas it is limited to 15% for the Spanish code EHE-08 [31] and 20% for American Concrete Institute's Building Code ACI 318-14 [33].

Regarding moment redistribution in HRC members, experimental tests conducted on statically indeterminate HRC/FRC two-span continuous beams are gathered in Table 1. Küsel and Kearsley [35] found that the addition of fibres led to crack localisation, this reducing the deformation capacity and leading to less moment redistribution, this being more evident in FRC element with strain-softening response at the post-cracking regime. Contrarily, Mahmood et al. [36] observed no signs of crack localisation when comparing RC and HRC beams with ρ_s of 0.69% and 1.38%. Finally, Visintin et al. [37] tested ultra-high performance fibre reinforced concrete (UHPFRC) with large fibre contents. The results showed that fibres provided enough ductility to the concrete compressive behaviour that shifted the failure mode from concrete crushing to reinforcement rupture, this allowing the beam to reach larger deformation and, thus, no significant change in moment redistribution was reported.

Table 1 – Previous research focused on HRC and FRC two-span continuous beams

Material	f_{cm} [MPa]	Cross section [mm^2]	Span length [mm]	V_f [%]	ρ_s [%]	Tests	Distance of load from central support	Ref.
UHPFRC	156	200×220	2×2500	2.08	1.28–1.94	4	$0.5 \cdot L$	[37]
HRC	40	250×400	2×4000	0.38 / 0.76	0.69 / 1.38	6	$0.5 \cdot L$	[36]
HRC RC* FRC	80	200×100	2×2250	0.00 / 0.76 / 1.51 / 2.20	0.7 / 1.4 / 2.2	15	$0.44 \cdot L$	[35]

*RC – Reinforced concrete

In view of the results of the studies presented in this section, further study is required for HRC flexural members at ULS since there is uncertainty of its dependence on different values of ρ_s and FRC residual strength [38]. Hence, there is a pressing need to evaluate the influence of the use of fibres in the deformation capacity (plastic rotation) that could compromise the moment

redistribution phenomenon in HRC elements. Particularly, it is of paramount importance to investigate members with $\rho_s < 0.5\%$ since the addition of fibres to RC members is typically viewed as a way of optimizing (eventually reducing) longitudinal reinforcement.

In order to achieve this goal, a parametric analysis on simply supported beams and on statically indeterminate continuous beams with varying FRC residual strength classes, according to MC2010 [32], and varying longitudinal reinforcement ratios was performed in this study. The specific objectives of this study are twofold: (1) to evaluate the deformation and rotational capacity of simply supported HRC beams and (2) to quantify the moment redistribution for two-span continuous HRC beams. To this end, a finite element model (FEM) was calibrated and validated by using results from experimental programs reported in the literature and then applied to two comprehensive parametric studies. The obtained results were analysed, and design-oriented recommendations are provided to be potentially taken into consideration for future revisions of the MC2010 [32] and other national/international guidelines.

2.   CALIBRATION AND VALIDATION OF THE NUMERICAL MODEL FOR HRC BEAMS

The FEM was first calibrated on real-scale continuous beams reported in [36]. To verify the adequacy of the model to measure the moment redistribution phenomenon, two additional experimental programs were simulated [35,37]. Finally, the FEM was applied to simply supported beams tested by Bosco and Debernardi [39] to compare the results in terms of deformation capacity and plastic rotation.

2.1.   SELECTION OF CONSTITUTIVE MODELS

The compressive stress–strain (σ–ε) and tensile stress–crack opening (σ–w) relationships were established according to *fib* MC2010 [32] are used (see Figure 1). Flexural residual strengths (f_R) can be obtained from the three point bending test on notched-beams according to EN 14651 [40], where, f_{R1} and f_{R3} stand for the residual strengths for a crack mouth opening displacement (CMOD) of 0.5 and 2.5 mm, respectively. Mean values of each of the involved mechanical variables are considered for the numerical simulations.

The Concrete Damage Plasticity (CDP) model available in ABAQUS [41] is used. This software presents a versatile tool to successfully model a wide range phenomena of concrete structure behaviour, as evidenced by numerous published studies [42–45]. The CDP model is a continuum, smeared crack, plasticity-based, damage model for concrete. In smeared crack models, the damage zone is assumed to coincide with the FE dimensions. The model assumes that the main two failure mechanisms for concrete are tensile cracking and compressive crushing. To model the concrete behaviour, the input data required are uniaxial σ–ε curves for compression and tension, see Figure 1. However, to overcome mesh dependence, the σ–w tensile curve was used

instead. In this regard, the characteristic length (L_{ch}) was assumed to be the size of the FE. The CDP magnitude of the parameters adopted for all the simulations were those proposed in ABAQUS User's Manual [41] for plain concrete, except those for the dilation angle, which was determined by means of a sensitivity analysis.
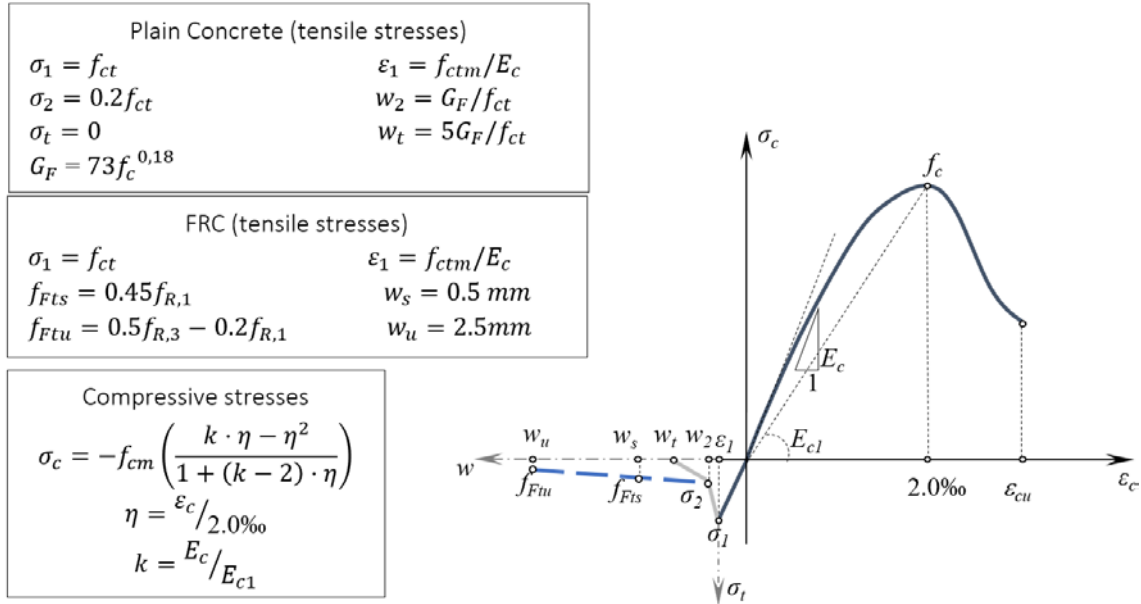

Figure 1 – Constitutive equations for concrete; σ–ε for compression and σ–w for tension

2.2.   HRC MODEL CALIBRATION

The experimental study carried out by Mahmood et al. [36] on flexural performance of steel fibre reinforced (SFRC) concrete beams was used for the model calibration. Full-scale two-span continuous reinforced concrete beams were tested using steel reinforcement ratios (ρ_s) of 0.69% and 1.38%, and 0, 30, and 60 kg/m^3 of steel fibres (corresponding to V_f of 0.38% and 0.76%), the combination of the parameters leading to a total of six beams. The steel fibres had a length and diameter of 60 and 0.9 mm, respectively. The tested beams had a clear span of 4000 mm, with a cross-section height and width of 400 and 250, respectively, as shown in Figure 2, with load evenly applied to both mid-spans.

The mean compressive concrete strength (f_{cm}) was 60 MPa. Furthermore, three point bending tests according to EN 14651 [40] were conducted to measure the tensile post-cracking behaviour of SFRC; for the purposes of this study, the flexural strength test results were used to derive the stress-crack width (σ–w) tensile constitutive curves according to MC2010 [32]. The uniaxial stress-strain (σ–ε) curves of the steel bars were also provided in [36] with a yield strength (f_y) equal to 540, a ultimate strength (f_u) and ultimate strain (ε_{su}) equal to 400 MPa and 0.18, respectively, and a maximum strength (f_{max}) of 613 MPa (at a strain of 0.11).

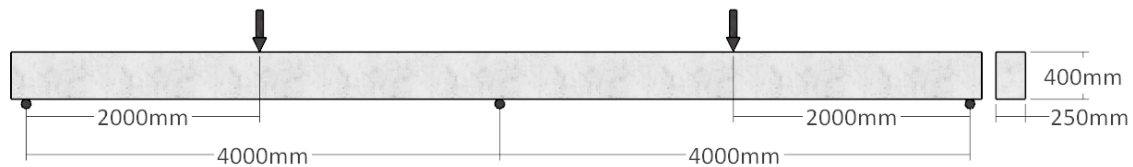*Figure 2 – Mahmood et al.[36] continuous beam experimental test set up.*

Two beams were used for the model calibration: B00(–30) and B30(–30) at [36], hereafter referred to as B0 and B30. Beam B0 is a RC and beam B30 is an HRC beam with V_f equal to 0.38% (30 kg/m^3 of steel fibres). For both beams, the reinforcement arrangement consisted of two 20-mm diameter bars at the top and bottom layer (with a concrete cover of 30 mm) along the beam length and an additional bar at the mid-spans (1250 mm at either side of the mid-span) which corresponded to ρ_s = 1.05%, as shown in Figure 3. The reinforcement configuration was adopted by the authors so a 30% moment redistribution was produced from the hogging to the sagging region (from the support to the mid-span region). Additionally, 10-mm diameter stirrups placed every 200 mm as transversal reinforcement. The FE mesh considered for the numerical analysis and the boundary conditions can be seen in Figure 3a. The mesh is comprised by 7800 elements: 6500 50-mm size 8-noded solid linear hexahedral solid elements (C3D8R) were used for modelling concrete, whereas the steel bars were modelled with 1300 linear T3D2 elements assuming a perfect bond between steel and concrete, using an embedded condition. The middle support was fixed in both x and y directions ($u_x = u_y = 0$) and the external supports were fixed only in the vertical direction ($u_y = 0$), both constraints applied along a line. The analysis was performed by first applying self-weight and then an increasing load applied by deflection control, which was applied on surfaces equal to the loading plates utilised in the actual test. Aiming at guaranteeing convergence, a quasi-static solver (Dynamic, Explicit) available in the software [41] was activated. The mesh representing the reinforcement of B0 and B30 specimens are plotted in Figure 3b. The σ–w curve for 0.38% V_f SFRC was determined by the following parameters: σ_1, σ_2, and σ_3 equal to 4.01, 0.98, and 3.01 MPa and w_1, w_2, and w_3 equal to 0.00, 0.035, and 2.50 mm.
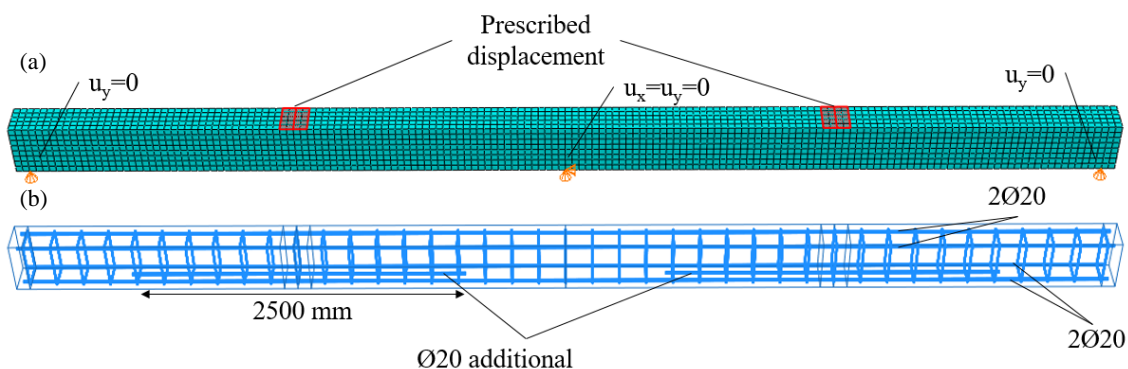

Figure 3 – FEM for B0 and B30 (a) mesh and boundary conditions (b) reinforcement arrangement.

In order to calibrate the model, a sensitivity analysis of finite element size and dilation angle were carried out. On the one hand, the model showed robustness in terms of the size of the element and a 50-mm finite element size was found suitable for the analysis in terms of runtime and preciseness (see Figure 4a). On the other hand, precaution must be taken with the dilation angle parameter, which governs the nonlinear volumetric strain of the model, set in the CDP model, especially for cases where shear failure mode can be the governing situation. In this sense, a dilation angle sensitivity analysis covering a wide range of values, from 16° up to 42°, was carried out, see Figure 4b. The curves are plotted up to 50 mm since it was the data reported by the authors. A significant influence in the model response was found for this parameter, whereby models with values under 42° failed to reach larger values of deformation without losing load bearing capacity. Hence, a dilation angle of 42° was chosen for this research work.
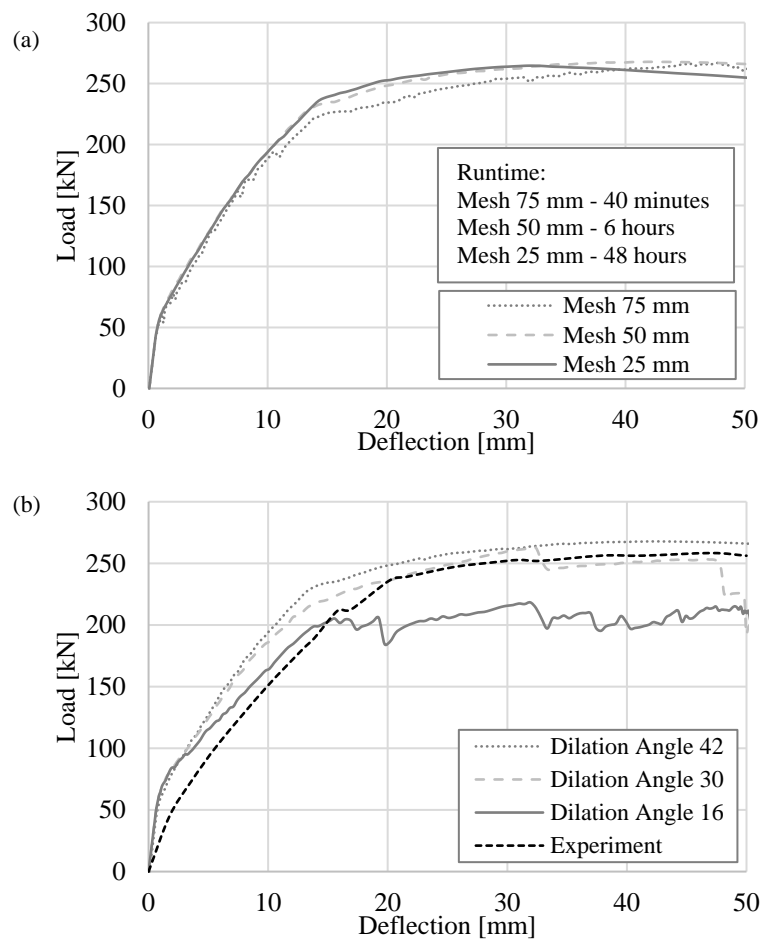

Figure 4 – Sensitivity analysis for beam B0 (a) Mesh (b) Dilation angle

In Figures 5a and 5b the load–deflection graphs for beams B0 and B30 along with the key points (cracking load, first yield, first hinge, second yield and second hinge) are plotted, where the load corresponds to the load applied in each span. Key point values are reported in Table 2. In all cases, the first crack occurred at the intermediate support, and cracking continued for both the support and in the mid-span regions of the beams up to first yield that occurred at the

intermediate support, the first hinge was formed shortly before the yield at the mid-span reinforcement for B0 whilst for B30 was produced immediately after. The final event was the formation of the second hinge in the vicinity of the mid-span in the critical member. In both charts, three expected stages for this sort of tests can be clearly identified: linear behaviour up to beam cracking, non-linear behaviour until the second hinge was developed, which generates the collapse mechanism, and finally a horizontal trend, which ends up in collapsing. Cracking and yielding loads have been identified when tensile strength (f_{ct}) and yield strength (f_y) were reached for concrete and steel reinforcement, respectively. The sequence of the plastic hinge formation is evident from the moment–curvature diagrams (M–χ) [36], where the onset of the hinge was detected when a change in slope was spotted (see Figure 6). It is worth noticing that cracking and yield loads can also be detected in these diagrams when a loss of stiffness (minor slope) is detected.

The graph presented in Figure 5 shows a suitable agreement between the numerical and experimental results. In case of beam B0, the key points were well captured in terms of loading; the maximum deviations found were 7.6% and 3.9% for second yield and the onset of the first hinge, respectively. For beam B30 slightly higher differences were observed for first yield (16.2%) and first hinge (9.8%), but the differences decreased for higher loading stages where the second hinge and the maximum load had a 2.2% and 3.5% of deviation, respectively. The results showed that both B0 and B30 models were able to withstand the load up to over 50 mm without collapsing, showing a good rotational plastic response.
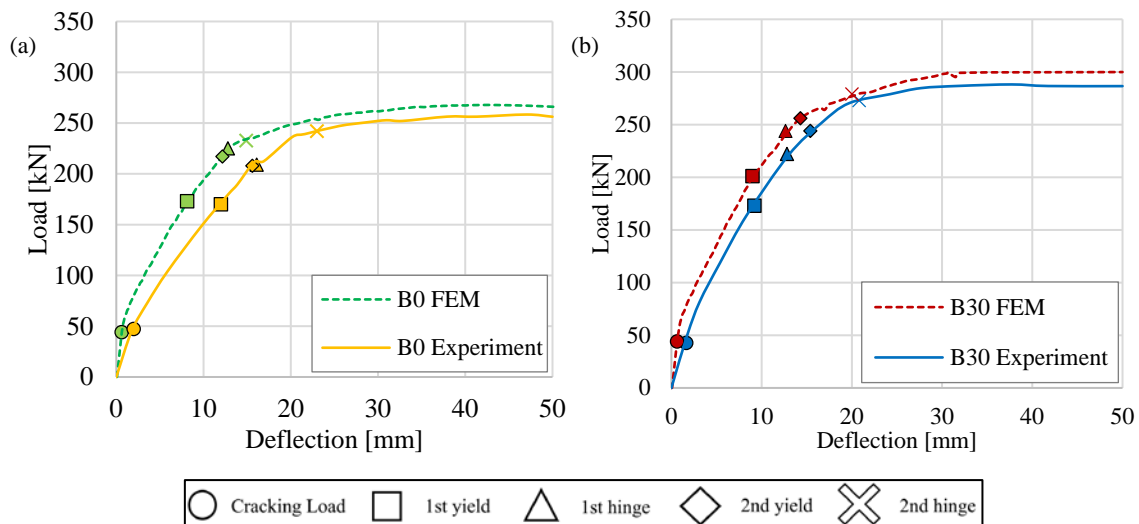

Figure 5 – Load-Deflection and key points for (a) B0 and (b) B30.

Table 2 – Key points loads for Mahmood et al.[36] *beams: experimental and numerical results*

		Cracking load [kN]	First yield [kN]	First hinge [kN]	Second yield [kN]	Second hinge [kN]	Maximum load [kN]
B0	Experiment	47.2	170.0	209.0	208.0	242.0	258.0

	FEM	44.0	173.0	225.0	216.0	237.0	266.0
B30	Experiment	42.7	173.0	222.2	244.0	273.0	289.0
	FEM	44.0	201.0	244.0	256.0	279.0	299.0

Figures 6a and 6b present the M–χ diagrams; curvature was calculated as the relative difference of top and bottom strain, ε_{top} and ε_{bot}, respectively, divided by the height of the beam h (Equation 1). ε_{top} and ε_{bot} were measured as the node relative difference of displacement, at a distance of 50 mm on either side of the centre, divided by the distance between them (100 mm).

$$\chi = \frac{\varepsilon_{bot} - \varepsilon_{top}}{h} \qquad (1)$$

As it can be seen, the model results are in good agreement with the data reported in [36]. While for beam B0, the cracking, yield and hinge loads were well captured, for beam B30, it can be observed that the first yield was reached at a higher moment, as reported in Table 2. Notably, higher numerical curvatures were obtained for both cases; likewise, the mid-span experimental curves stopped at lower moment values, the reason for this being that in the test the gauges were removed after reaching 24 mm of deflection for safety reasons.
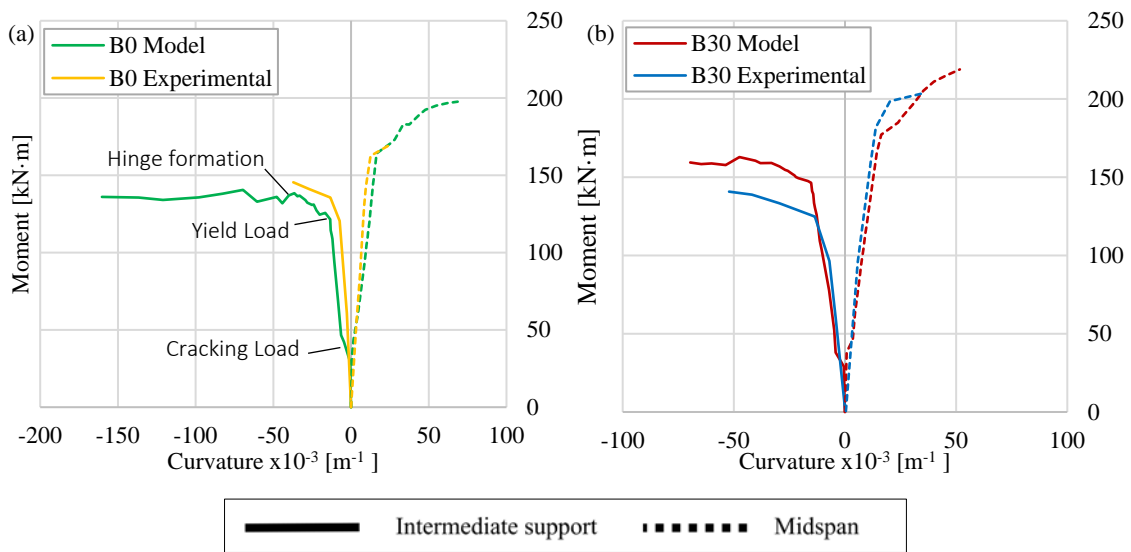

Figure 6 – Moment-Curvature for midspan and intermediate support for (a) B0 and (b) B30.

Table 3 gathers the moment redistribution (K_{MR}) values for the key points after cracking. The percentage of moment redistribution was calculated as in Equation 2, where M_{el} is the theoretical elastic moment and M_{exp} is the experimental moment that includes the contribution of the plastic behaviour. The redistribution values obtained were aligned with the ones obtained by means of the experimental test reaching 30%, as per design.

$$K_{MR} = \frac{M_{el} - M_{exp}}{M_{el}} \qquad (2)$$

Table 3 – Percentage of redistribution

		First hinge [kN]	Second yield [kN]	Second hinge [kN]	Maximum Load [kN]
B0	Experimental	13.9%	14.9%	23.6%	24.7%
	Numerical model	16.2%	17.3%	24.6%	31.0%
B30	Experimental	23.7%	28.2%	32.0%	31.0%
	Numerical model	3.36%	14.0%	27.0%	29.0%

2.3. MODEL VALIDATION

2.3.1. MOMENT REDISTRIBUTION CAPACITY

Experimental programs carried out by Küsel and Kearsley [35] and Visintin et al. [37] were used to validate the moment redistribution modelling capacities of the calibrated FEM.

First, the study by Küsel and Kearsley [35] was used to evaluate the moment redistribution of two-span continuous beams. To this end, two-span continuous beams cast with four batches of FRC (with V_f equal to 0%, 1.01%, 1.51% and 2.02%) combined with four tensile reinforcement arrangements (ρ_s = 0%, 0.7%, 1.4% and 2.2%) that leads to sixteen beam combinations, were tested. The tested beams had a clear span of 2500 mm, with a cross-section width and height of 200 and 220 mm, respectively. Two point-loads were applied on each span, 1.0 m apart from the intermediate support. In this regard, two beams were analysed: Beam A with V_f = 2.02% and ρ_s = 2.2% whilst Beam B had V_f = 1.01% and ρ_s = 1.4% (the beams are referred as 2B2.2 and 1B1.4, respectively in [35]). These beams were chosen since these had the highest and lowest V_f and fully developed the plastic mechanism and, hence, the full moment redistribution capacity. The mean compressive concrete strength (f_{cm}) was 80 MPa and the authors provided the σ–ε tensile constitutive curves. The σ–ε data of the steel reinforcement was also provided with f_y and f_u being equal to 537 and 610 MPa, respectively, with ε_{su} equal to 0.08.

The load–deflection curves for both experimental and numerical tests along with the key points are plotted in Figure 7 and in Table 4 the data for key points are gathered.

Table 4 – Key points loads for Küsel and Kearsley [35] *beams: experimental and numerical tests*

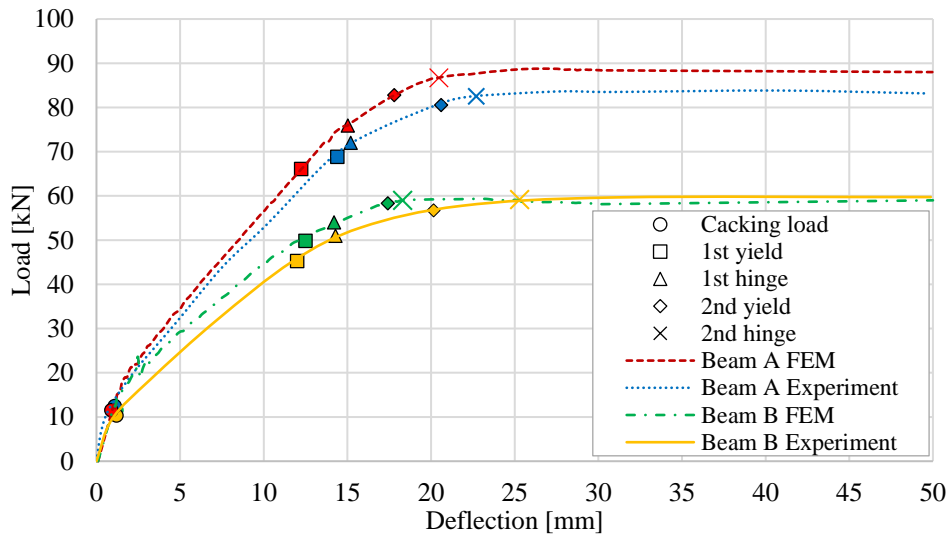|		Cracking load [kN]	First yield [kN]	First hinge [kN]	Second yield [kN]	Second hinge [kN]	Ultimate load [kN]
Beam A	Experiment	12.5	68.8	72.0	80.5	83.0	83.0
	FEM	11.5	66.0	75.9	82.7	86.7	88.0
Beam B	Experiment	10.3	45.0	50.0	56.0	59.0	60.0
	FEM	11.5	49.8	54.0	58.3	59.0	59.0

Figure 7 – Experimental and numerical load-deflection curves for Küsel and Kearsley [35]

beams A and B.

Both models exhibited a behaviour similar to that observed experimentally. The first crack and yielding were produced at the intermediate support and subsequently at the midspans. The key points (Table 3) show that the key points predicted by the model were in good agreement with the experimental ones, being slightly higher compared with the actual test. For Beam A, the ultimate load for the numerical was the same obtained in the experimental test whereas in Model B the numerical test exhibited major moment redistribution from the critical section to the midspan and therefore this reached higher loads.

Figure 8 plots the load–moment curve for the experimental test and the numerical simulations. In Figure 8a, it can be observed that model is able to capture the moment redistribution from the intermediate support, where the first hinge is produced, to the midspan (defined as "positive moment redistribution"). The hinges in the numerical moment were generated for higher load levels and, consequently, the redistribution started later. In case of Figure 8b, where it can be observed that the hinges appeared at the same load, the redistribution started simultaneously and slightly more redistribution is observed in the numerical curve.

| ━━━━━ Intermediate Support | ••••••••• Outer Support | ═══════ Elastic Theory |
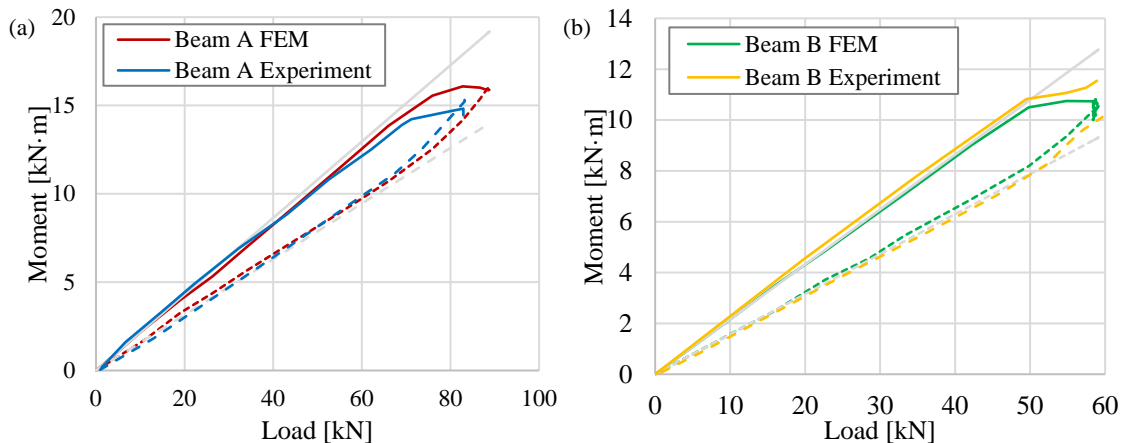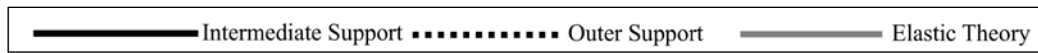
Figure 8 – Experimental and numerical Moment-Load curves for (a) Beam A and (b) Beam B.

The second experimental program on two-span continuous beams used for the model validation was that carried out by Visintin et al. [37]. The tensile reinforcement ratio ranged from 1.13% to 1.66% in the sagging region, and 0.9% to 1.66% in the hogging region and the fibre volume fraction was 2.08% for all beams. These beams had a total length of 5500 mm length, with cross-section width and height of 200 and 100 mm, respectively. Point loads were located at the mid-point of each span. Direct tensile tests were conducted to determine the tensile behaviour, providing the post-cracking constitutive curve ($\sigma_1 = 5.55$ MPa, $\sigma_2 = 5.27$ MPa, $\sigma_3 = 5.0$ MPa, $\sigma_4 = 3.80$ MPa and $w_1 = 0.00$ mm, $w_2 = 0.15$ mm, $w_3 = 0.40$ mm, $w_4 = 1.00$ mm), and the concrete compressive strength was 110 MPa. The σ–ε data of the steel reinforcement was also provided with f_y and f_u being equal to 580 and 610 MPa, respectively, with ε_{su} equal to 0.15.

For the model validation, three three-dimensional non-linear models of beams were generated: beam C ($\rho_s = 1.57\%$ at both midspan and intermediate support), beam D ($\rho_s = 1.13\%$ for the intermediate support and $\rho_s = 1.57\%$ for the midspan section) and beam E ($\rho_s = 1.57\%$ for the intermediate support and $\rho_s = 1.13\%$ for the midspan section) named as beam 1, 2 and 4 in [37], respectively. With regard to the reinforcement distribution, for beams C and D, positive moment redistribution was expected, whereas for beam E, the reinforcement distribution was meant to force moment redistribution from the midspan towards the intermediate support.

The load–deflection curves for both experimental and numerical tests along with the key points are plotted in Figure 9, and in Table 5 the data for key points are gathered. The results showed that the model results are in good agreement with those experimental, the positive (beams C and D) and negative moment redistribution (beam E) was well captured as well.

Table 5 – Key points loads for Visintin et al. [37] beams: experimental and numerical tests

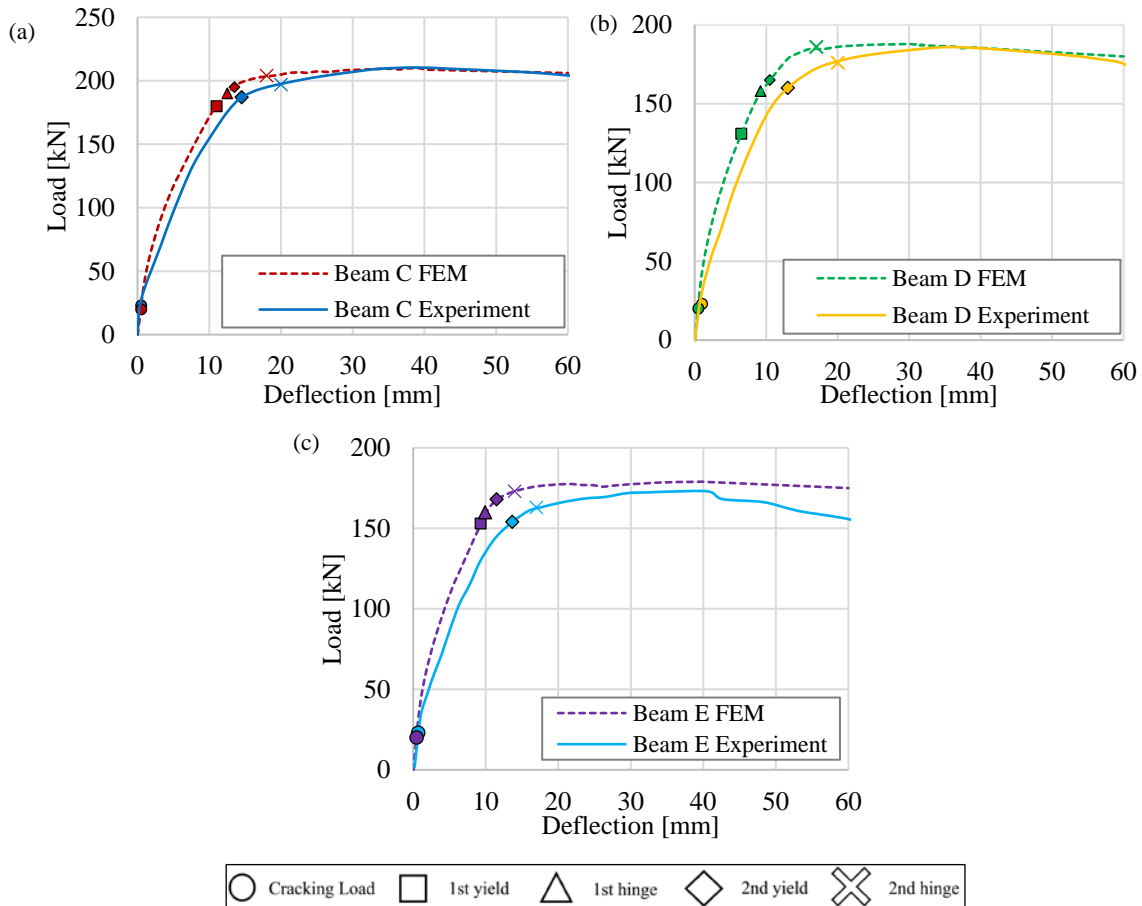|		Cracking load [kN]	First yield [kN]	First hinge [kN]	Second yield [kN]	Second hinge [kN]	Ultimate load [kN]
Beam C	Experiment	28	–	–	187	209	209
	FEM	19	180	190	195	208	208
Beam D	Experiment	29	-	-	160	183	183
	FEM	19	131	140	165	187	187
Beam E	Experiment	25	–	–	154	172	172
	FEM	19	153	168	176	177	177

Figure 9 – Experimental and numerical load-deflection curves for one span (a) beam C (b) beam D and (3) beam E from the study by Visintin et al. [37]

Figure 10a, 10b and 10c gathers the reaction-load graphs for Beam C, Beam D and Beam E, respectively. As it can be seen from Figure 10a and 10b, the redistribution from the intermediate support to midspan sections were well developed, the FEM model for Beam D captured properly the magnitude of the moment redistribution whereas for Beam C higher redistribution was seen for the experiment since early stages, probably this was caused by a greater loss of stiffness after cracking. With regard to Figure 10c, the model developed the negative moment redistribution as the experimental test, although less redistribution was achieved since the beginning, apparently due to stiffness difference.
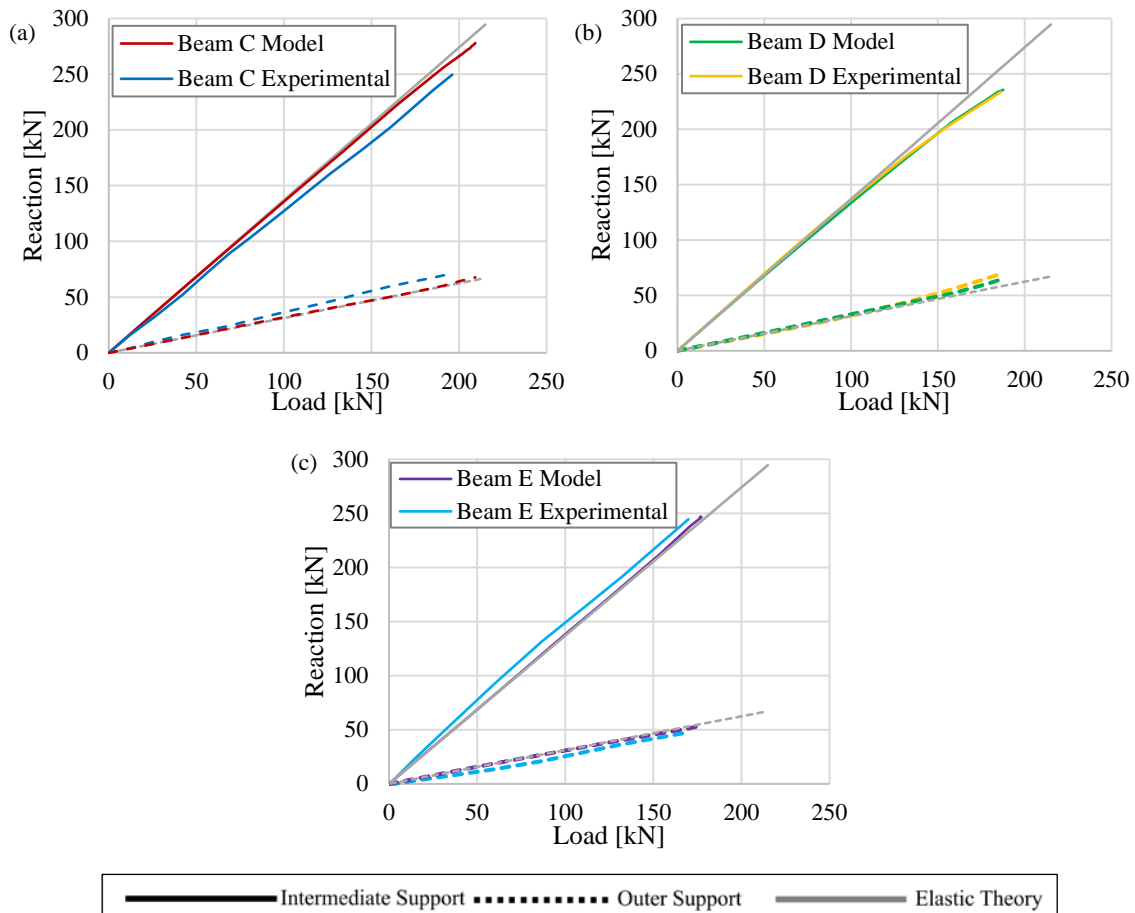
Figure 10 – Experimental and numerical reaction–load curves for (a) beam C (b) beam D and (c) beam E from the study by Visintin et al. [37]

2.3.2. VERIFICATION OF PLASTIC HINGE ROTATION CAPACITY

In this section, the experimental investigation carried out by Bosco and Debernardi [39] was used for the plastic rotation capacity verification of the model. The results from these tests were also considered for other model validations [46]. For assessing the plastic rotation capacity of RC beams, a total of 44 beams were used. Different configurations were taken into account: two grades of steel ductility normal steel (grade B 500 N) and high ductility steel (grade B 500 H); three cross-sectional area were used while maintaining the same span-to-depth ratio ($L/h = 10$) and the width to depth ratio ($b/h = 1/2$), with cross-sectional depths of 200, 400 and 600 mm; the reinforcing ratios (ρ_s) varied between 0.13% and 1.14% and finally two different loading conditions (point load at midspan and three symmetrically arranged loads).

For the rotation capacity verification, four beams with a length of 6000 mm, cross-section height and width of 600 and 300 mm, respectively, (with concrete cover of 35 mm) and ρ_s of 0.13%, 0.25%, 0.57% and 1.14% were modelled, along with Ø6 stirrups spaced every 150 mm. It is worth noticing that the rebar configuration for $\rho_s = 1.14\%$ was not provided and an equivalent

reinforcing area (6Ø20) configuration was used. All beams were reinforced with high ductility steel with f_y = 600 MPa, f_u = 578 MPa, ε_{su} = 0.1 and f_{max} = 672 MPa. Concrete had a compressive and tensile strength of 31.0 and 2.8 MPa, respectively. The analysed beams corresponded to T8A1, T9A1, T10A1 and T11A1 in [39]. Hereafter, the beams are labelled with a capital S or C (for simply supported or continuous beams, introduced later within the parametric analysis) followed by a percentage (indicating ρ_s) and either RC or FRC strength class according to MC2010 [32].

Figure 11a presents the meshed model adopted for the numerical analysis and its boundary conditions: the mesh comprised 8900 50-mm C3D8R finite elements for modelling concrete, whereas the reinforcement was modelled with linear 50-mm T3D2 elements embedded in the solid elements. One support was fixed in both x and y directions (u_x = u_y = 0) the other was fixed only in the vertical direction (u_y = 0). The analyses were performed by first applying self-weight and then an increasing load applied at the midspan by deflection control. Figure 11b shows the longitudinal reinforcement arrangement, in all cases the compressive reinforced consisted of 2Ø12.
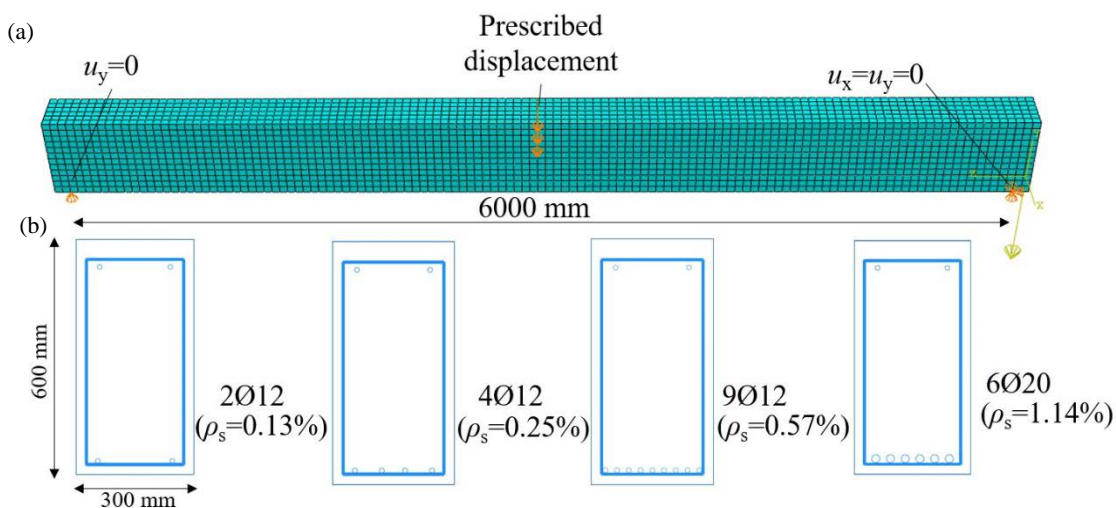
Figure 11 – FE model (a) mesh and boundary conditions and (b) reinforcement arrangement for beams S-0.13%-RC, S-0.25%-RC and S-0.57%-RC for study [39].

The comparison between the experimental and the numerical results are plotted in Figure 12a. The FEM results for the beams with $\rho_s \leq 0.57\%$ are in good agreement with the experimental in terms of load–deflection, with a slight difference in stiffness seen only in S-0.57%-RC, up to yielding loads (P_{yield}) which were well captured. These beams failed due to reinforcement failure (when the reinforcement reached ε_{su}). It was demonstrated that the model is able to simulate the plastic behaviour after yielding, although major deflections were registered for beams S-0.25%-RC and S-0.57%-RC. Beam S-1.14%-RC failed due to concrete crushing and in that case, there

is a difference in stiffness and in the peak load (8.2% higher) between the model and the actual test.

Figure 12b shows the moment–plastic rotation (θ_{plastic}) relationship, where the latter has been calculated by integration, along the plastic zone L_p (where the tension reinforcement had exceeded its yield limit), of the difference between the curvature (χ) and the curvature at steel yield limit (χ_y), as it is presented in Equation 3. In other words, θ_{plastic} was derived as the difference between the ultimate rotation and the rotation corresponding to the reinforcement yielding [14,39,46]. The ultimate rotation can be considered as the rotation beyond which the moment starts descending sharply according to [47,48].

$$\theta_{\text{plastic}} = \int_{L_p} (\chi - \chi_y)\, dz \qquad (3)$$

Although measuring θ_{plastic} in experimental tests can be of great difficulty due to the sudden deflection increases, the numerical results captured well the yielding moment load (M_{yield}) and the large plastic rotation, although larger rotations were registered in beams S-0.25%-RC and S-0.57%-RC. In case of concrete crushing (S-1.14%-RC) the failure mode was well captured by the model but the plastic rotational capacity was larger than in the test. These results were found to be acceptable for the numerical model verification of beam rotational capacity to perform a parametric analysis.
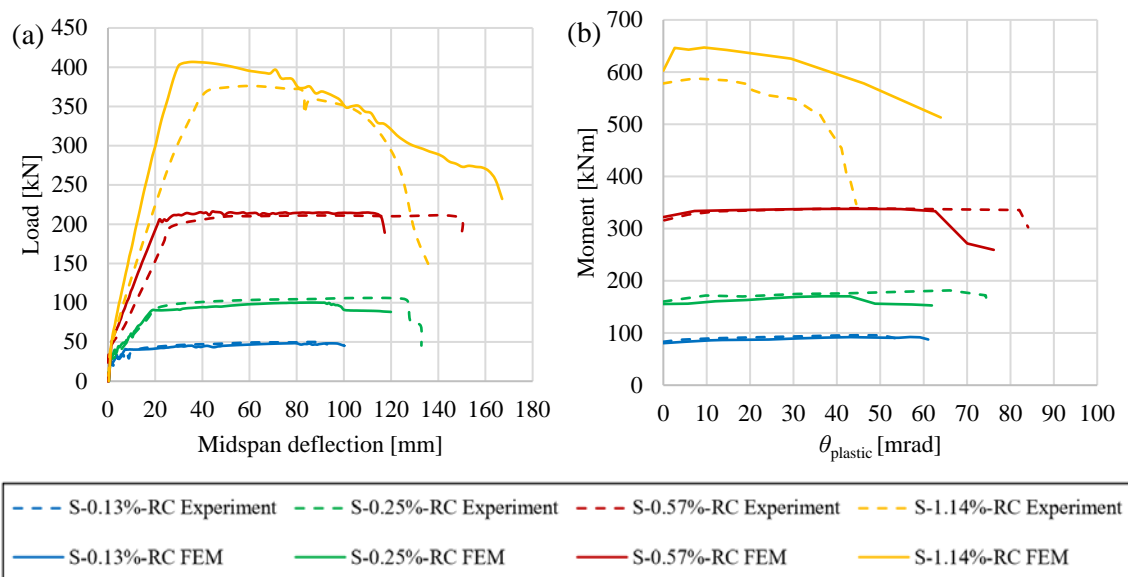
Figure 12 – Experimental and numerical comparison of Bosco and Debernardi [39] simply supported beams (a) load–midspan deflection and (b) moment–plastic rotation

3. PARAMETRIC ANALYSES

Using the model previously calibrated and validated in Section 2, two parametrical analysis, combining different FRC strength classes and varying reinforcement ratios, were carried out. The

object of this parametric analysis was to assess the influence of ρ and V_f on plastic rotation and moment redistribution capacities. The first step was to analyse the interaction between FRC flexural residual strength and HRC reinforcement ratio and its effect on plastic rotation capacity of simply supported beams. Such a choice was made as plastic rotation capacity is the prerequisite for moment redistribution in statically indeterminate structures. Then, in the second step, moment redistribution capacity was analysed on two-span continuous beams maintaining a geometry identical to the previously analysed simply supported beams. The beam's cross section and span length as well as the reinforcing ratio were based on the beams described in Section 2.5.

To this end, the reinforcement configurations of ρ_s = 0.13%, 0.25%, 0.57% and 1.14% from the study by Bosco and Debernardi [39] were used along with plain concrete and three FRC mixtures were taken into account. The FRC strength classes considered, represented by f_{R1m} (mean value), were 3, 5, and 7 MPa with ductility class f_{R3m}/f_{R1m} = 1.0 (i.e. class "c" according to MC2010 [32]). Such a ratio was chosen as being most representative of FRC structural applications (e.g.., precast concrete tunnel segments according to the *fib* Bulletin 83 [49]). The chosen values were considered to cover a wide range of f_R magnitudes (and indirectly, fibre contents). Furthermore, when determining the σ–w diagram according to MC2010, different post-cracking responses are obtained: FRC classes 3c and 5c exhibit a softening behaviour whereas 7c has a partially hardening behaviour, Figure 13.
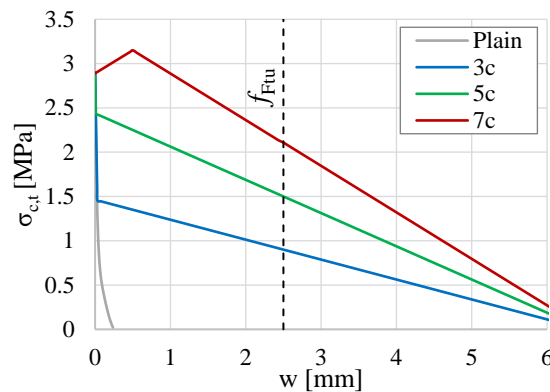
Figure 13 – Stress – crack post-cracking response of plain concrete and FRC class 3c, 5c and 7c

3.1. ANALYSIS OF PLASTIC ROTATION CAPACITY ON SIMPLY SUPPORTED BEAMS

The FEM presented in Figure 11 is used for carrying out the parametric analysis on simply supported beams. The results in terms of load–deflection and the normalized M/M_{yield}–$\theta_{plastic}/\theta_{elastic}$ relationship, up to failure, are plotted in Figure 14. In case of reinforcement failure, the failure was considered to occur at a steel deformation of ε_{su} = 0.1 according to MC2010 [32], and stablished as ultimate limit state criterion, in concrete crushing the graphs are plotted up to a sharp load decrease. Herein, $\theta_{elastic}$ stands for the rotation achieved at the yielding limit. The results

presented show that the addition of fibres affects differently to the performance of the beams depending on the reinforcing ratio. This justifying the need of carrying out this novelty parametrical analysis combining different V_f and varying reinforcing ratios.

As seen from the Figure 14, for low amounts of ρ_s (i.e. 0.13% and 0.25%) a considerable enhancement of maximum loading bearing capacity caused by the addition of fibres was achieved, with the enhancement being larger for higher residual strengths. Importantly, for these beams (S-0.13% and S-0.25%) a loss of ultimate deformation capacity with the increase of V_f was also found, up to 60% for 3c FRC strength classes and 50% for the rest. As Figures 14b and 14d show, a softening response was produced due to the increase of V_f after reaching the reinforcement yielding. The results obtained are aligned with the behaviour observed in actual beam tests conducted by and reported in [5,9–12].

For $\rho_s = 0.57\%$, the addition of fibres also led to an increase in load bearing capacity but did not produce a softening post-yielding response. In this case, a lower FRC residual strength (beam S-0.57%-3c) resulted in a slight increase of deformation capacity, 6%, although the onset of crack localisation was detected in the model. However, the influence of this crack localisation became more evident in the performance of beams S-0.57%-5c and S-0.57%-7c which suffered a reduction in deformation capacity, 42 and 30%, respectively, reaching a significantly lower ultimate deflection than beam S-0.57%-RC. Crack localisation was detected in the model since as the load progressively increased, a few cracks became wider and predominant over the rest. In beams with $\rho_s = 1.14\%$, only a slight increase of the ultimate load was found with the increment of f_{R1}, the governing mode of failure of the beams was concrete crushing for all cases. Crack localisation was also detected for high V_f resulting in a reduction of ultimate deflection capacity, 40% and 30% for S-1.14%-5c and S-1.14%-7c, respectively.

According to the presented results, to develop the full plastic rotation mechanism of HRC members, characterized by a plateau in the load-deflection relationship after yielding, reinforcement ratios of at least 0.3%–0.5% are required. The results of the study demonstrate that for $\rho_s = 0.57\%$ full rotation capacity is already achieved. However, since crack localization is detected for class 5c and 7c and not for 3c, it is probable that the "minimum reinforcement ratio" for ductility decreases with increasing residual strength class (i.e. it is ~0.5% for 3c but likely lower for 5c and lower still for 7c).

For higher amounts of reinforcement (i.e. $\rho_s = 1.14\%$), the failure mode turns from reinforcement failure to concrete crushing, disabling the development of such ductile failure mechanisms.

In order to quantitatively quantifying the ductility degree of the beams, a ductility index (μ) was adopted, defined by Equation 4, where δ_u stands for the ultimate deflection capacity and δ_y the deflection at rebar yielding.

$$\mu = \frac{\delta_u}{\delta_y} \tag{4}$$

For any reinforcement ratio, see Figure 15, there was a ductility reduction with the increase of V_f and the results were aligned with those obtained in previous studies [5,11]. However, whereas the authors of previous studies found that the lowest ductility was expected for low ρ_s and high V_f, the results presented in Figure 15 showed that the lowest values of μ are found for low ρ_s (0.13% and 0.25%) and low V_f (this being a direct proxy for residual strength), with μ increasing with increasing V_f. For beams S-0.57% and S-1.14%, μ is higher for low amounts of fibres; as explained earlier, this behaviour was caused by crack localisation.
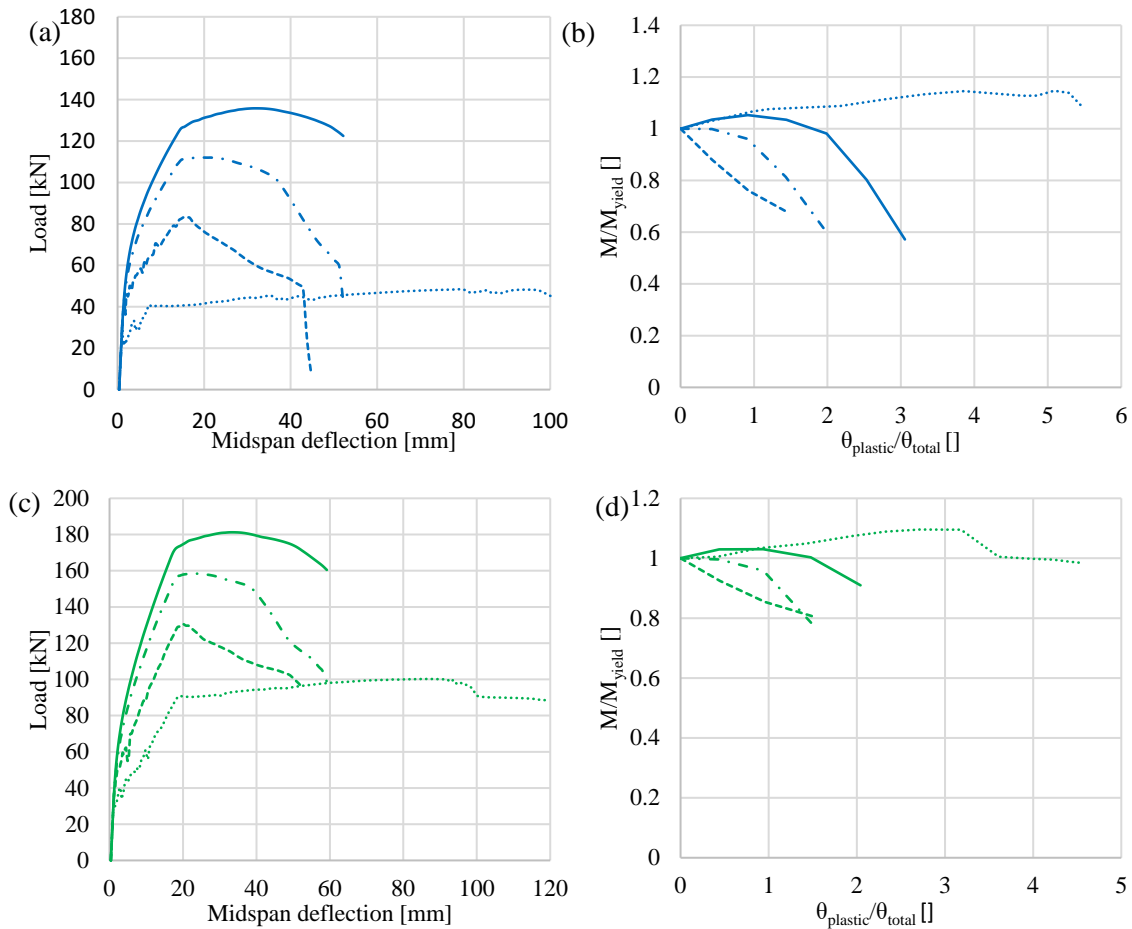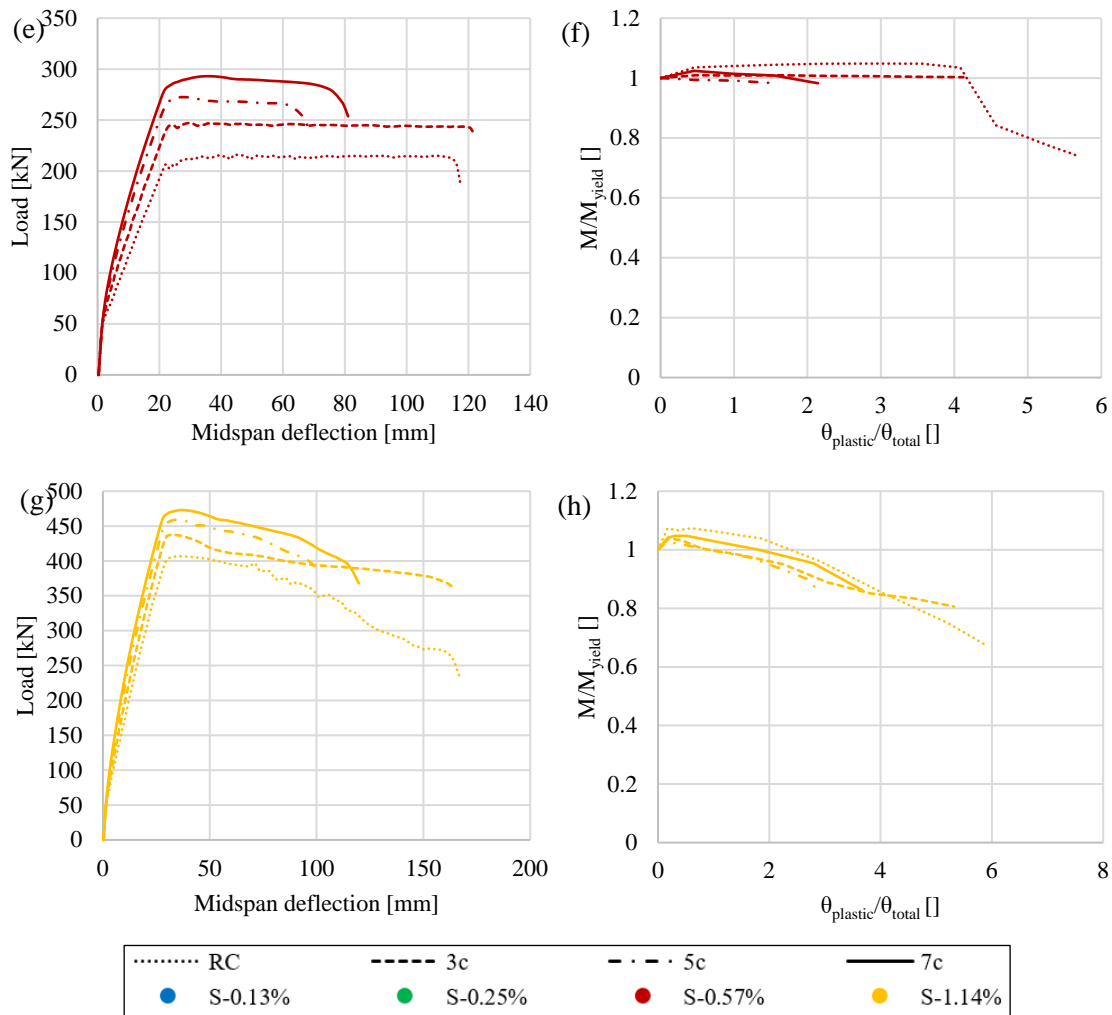
Figure 14 – Parametrical analysis on simply supported beams: Load-Deflection and M/M_{yield}– $\theta_{plastic}/\theta_{total}$
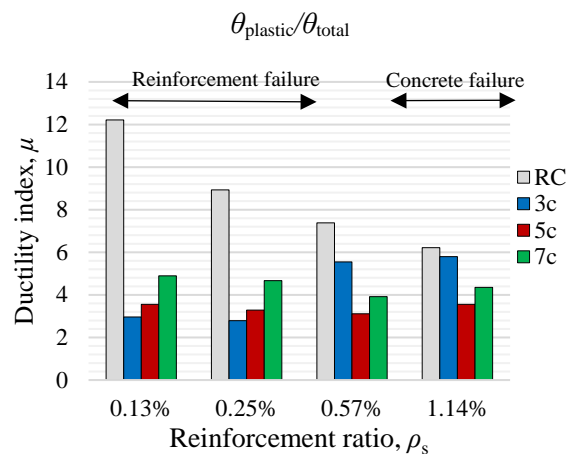
Figure 15 – Ductility of simply supported beams.

Finally, Figure 16a represents the ultimate plastic rotation $\theta_{plastic\_u}$–f_{R1} relationship. It can be seen that for higher residual strength classes (5c and 7c) $\theta_{plastic\_u}$ is less sensitive to ρ_s than for class 3c. Namely, for class 3c, $\theta_{plastic\_u}$ increases almost five times when increasing ρ_s from 0.13% and 0.25% to 1.14%, whereas for classes 5c and 7c this increase is only around 2.5 times, i.e. twice smaller. In other words, changes in longitudinal reinforcement have a much larger effect

(in terms of both load bearing capacity and ductility degree) for lower FRC residual strength classes. This is of particular importance when FRC is used as a way of reducing the longitudinal reinforcement ratio.

Figure 16b shows the relation between the plastic hinge length L_p (detected as the length along which the yield strain in steel is exceeded) and FRC residual strength. The figure demonstrates that L_p remained slightly affected by the increase of f_{Rm} for $\rho_s = 0.57\%$ and $\rho_s = 1.14\%$ but was remarkably affected for low ρ_s: for these beams, L_p decreases with decreasing FRC residual strength. These results are aligned with the conclusion obtained with regards to deformation capacity and post-yield response, discussed earlier.
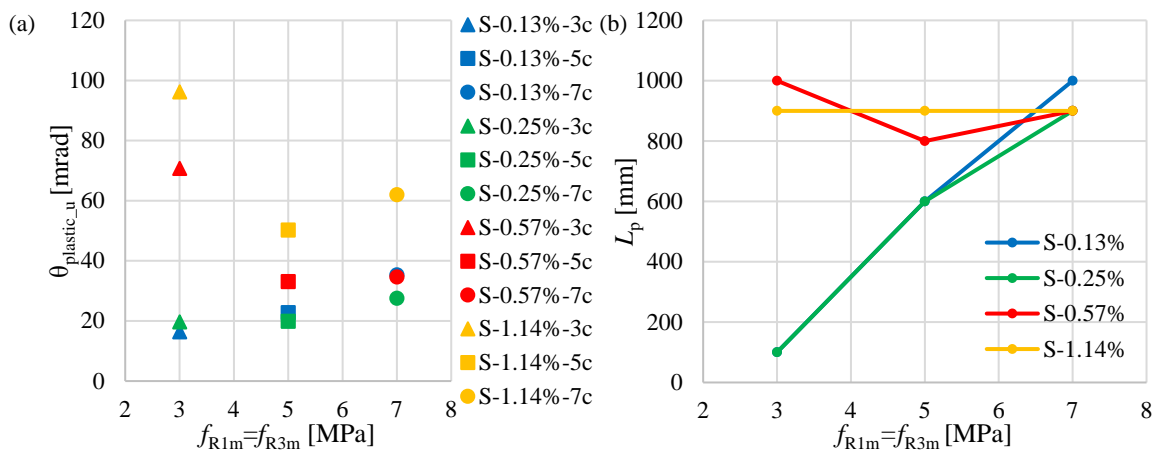
Figure 16 – Results based on residual strength (a) $\theta_{plastic\_u}$ (b) L_p

3.2. ANALYSIS OF MOMENT REDISTRIBUTION CAPACITY ON TWO-SPAN CONTINUOUS BEAMS

After analysing the plastic rotation capacity of HRC beams in the first parametric analysis, a second one was performed to assess the effects of changes in plastic rotation capacity on moment redistribution in statically indeterminate HRC beams. Based on the geometry of the beams presented in both Section 2.3.2 and 3.1 (clear span of 6000 mm, depth and width of 600 and 300 mm, respectively), two-span continuous beams were considered in the analysis. The reinforcement configurations were again ρ_s =0.13%, 0.25%, 0.57% and 1.14% along with plain concrete and three FRC mixtures ($f_{R1m} = f_{R3m}$ equal to 3, 5 and 7 MPa). Compressive longitudinal reinforcement consisted of 2Ø12 and transversal reinforcement consisted of Ø6 spaced at 150 mm, except for ρ_s =1.14% in which stirrups were Ø8 at a spacing of 150 mm, for reasons of shear.

Figure 17a presents the meshed model, its geometry and boundary conditions: one support was fixed in both *x* and *y* directions of translational degrees of freedom ($u_x = u_y = 0$) and the rest were fixed only in the vertical direction ($u_y = 0$). The mesh was comprised of 17600 50-mm C3D8R finite elements for concrete and the reinforcement was modelled with linear 50-mm T3D2 finite elements embedded in the solid elements. Figures 17b–e presents the reinforced models: the

length of tensile longitudinal reinforcement for sagging and hogging regions was 1.1 times the theoretical elastic length, which led to an overlap length of 0.8 m. The analysis was performed by first applying self-weight and subsequently two-point loads were applied at both midspans. Considering the applied longitudinal reinforcement arrangement, moment redistribution was expected from the hogging to sagging regions (from the intermediate support to the midspan section).
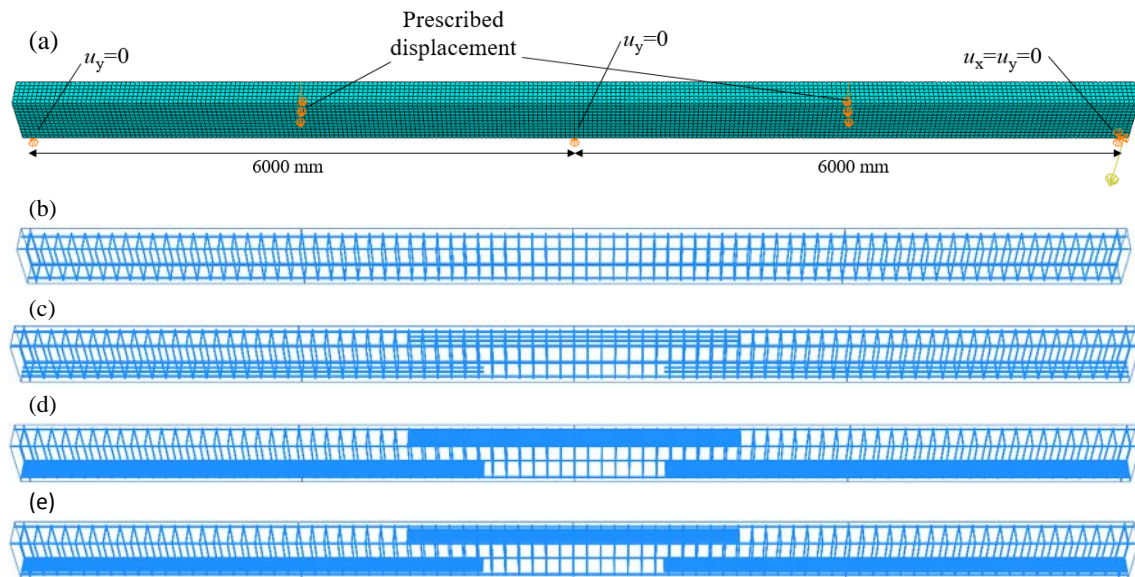

Figure 17 – FEM (a) mesh and boundary conditions and (b) reinforcement arrangement for beams C-0.13%, (c) reinforcement arrangement for beams C-0.25% (d) reinforcement arrangement for beams C-0.57% and (e) reinforcement arrangement for beams C-1.14%.

The results are presented in Figure 18 in terms of load–midspan deflection and M/M_{yield}–$\theta_{plastic}/\theta_{elastic}$ (at the intermediate support) relationships, up to reinforcement failure ($\varepsilon_s = 10‰$), with the plastic rotation calculated according to Equation 1. As expected, the first cracking occurred at the intermediate support and subsequently in the midspan section, in all cases studied. The increase of f_{R1} affected the overall response of the statically indeterminate members in different ways depending on ρ_s. For $\rho_s = 0.13\%$, the addition of fibres resulted in an increase of the load bearing capacity and enhancing the ultimate deflection capacity. Contrary to the results presented in Figure 14a for simply supported beams, the increase of f_{R1} did not reduce the deflection capacity of the beam but enhanced it. However, as it can be seen in Figure 18b, the use of HRC led to a softening response after yielding at the intermediate support (except for C-0.13%-7c where hardening was appreciated at the onset due to its post-cracking response, followed by softening) whilst C-0.13%-RC presented a hardening response.

In case of $\rho_s = 0.25\%$ (Figures 18c and 18d), the use of HRC enhanced the load bearing capacity and the overall stiffness. Similar to the response of simply supported beams with $\rho_s =$

0.25%, the enhancement of the load-bearing capacity for the solutions with fibres, was in detriment of the deformation capacity which was significantly reduced. As for C-0.13%, C-0.25%-3c and 5c presented a softening response after reinforcement yielding, for C-0.25%-7c a slight hardening was registered before softening and for C-0.25%-RC, deflection-hardening with associated ductility was detected.

For simply supported beams with $\rho_s = 0.57\%$, an increase of the load bearing capacity was found and even an enhanced deformation capacity in case of FRC concrete class 3c. In all cases, a ductile response was produced after yielding. In contrast, for continuous beams C-0.57% (Figures 18e and 18f) combining steel reinforcement and fibres only led to a load bearing capacity and stiffness enhancement and a clear loss of deformation capacity was observed along with a softening behaviour after reaching the reinforcement yield. For the highest amount of reinforcement studied of $\rho_s = 1.14\%$, Figures 18g and 18h, the failure of the beams was due to concrete crushing at the mid-support. In C-1.14%-RC the beam failed prior to reinforcement yield, the use of fibres enhanced the load-bearing capacity of the beams and significantly increased (100% in all cases) the deformation capacity of the conventional solution, improving the ductility before failure.
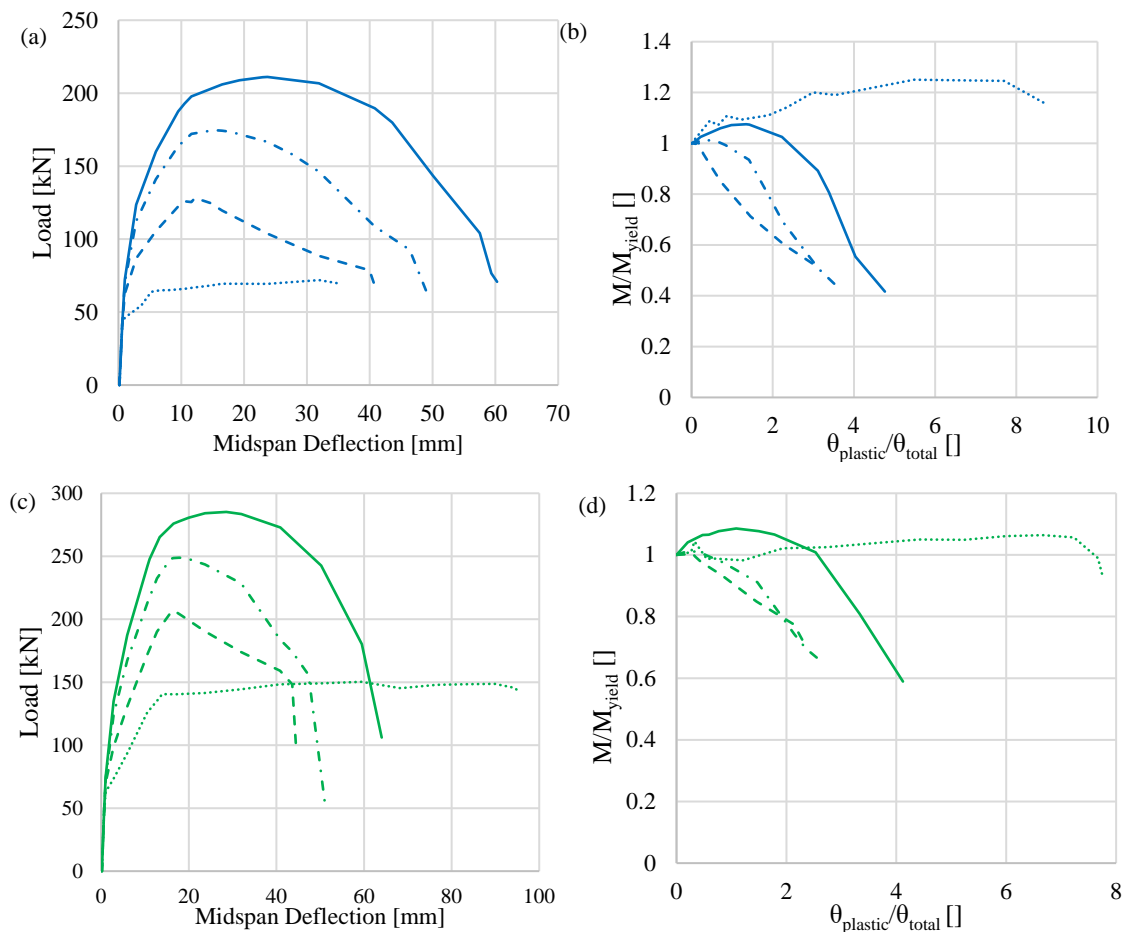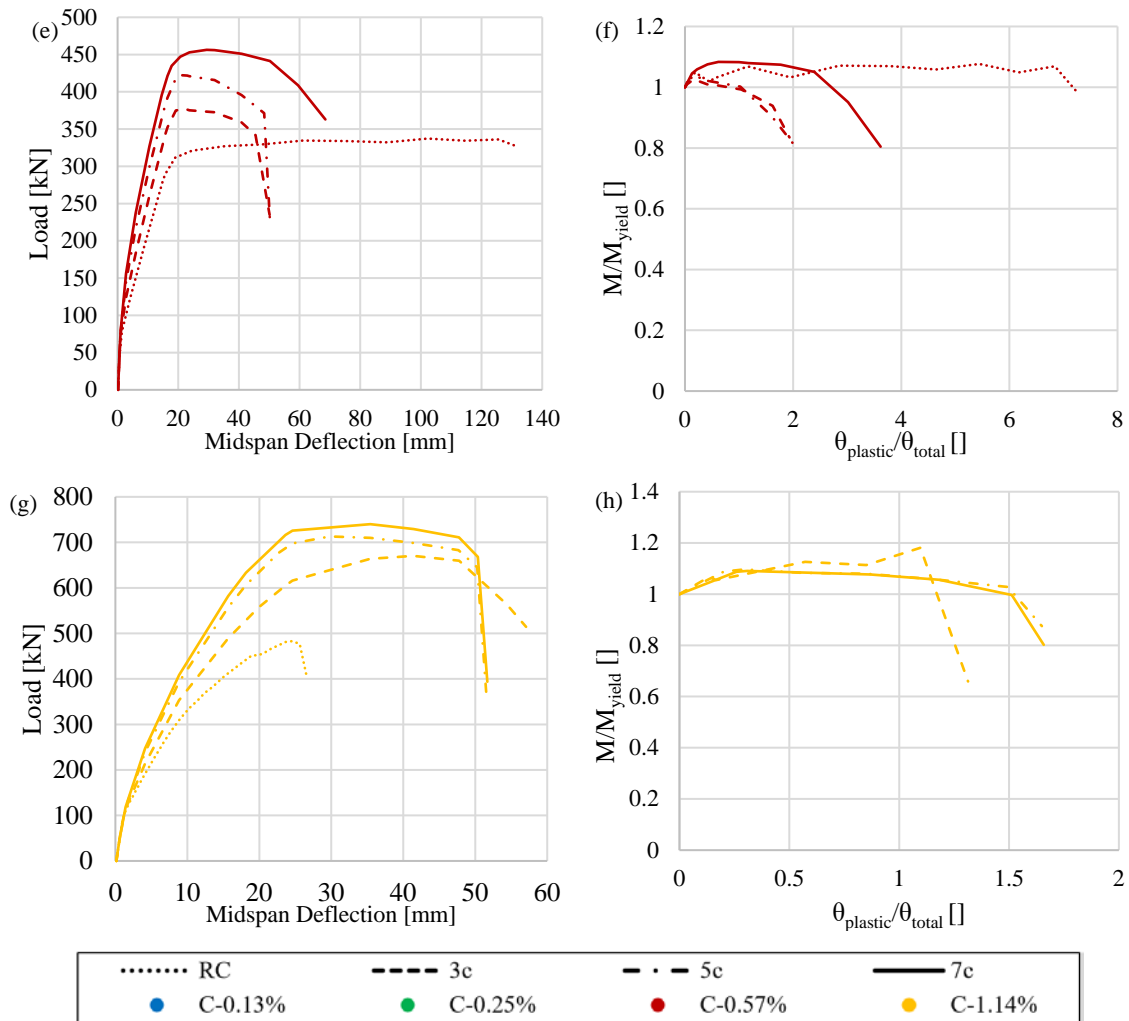
Figure 18 – Parametrical analysis on two-span continuous beams: Load-Deflection and

M/M_{yield}–$\theta_{plastic}/\theta_{total}$

The moment redistribution capacity was computed using the K_{MR} coefficient (see Equation 2). Then, the coefficient K_{MR} was plotted against $\theta_{plastic}$ and presented in Figure 19, with both K_{MR} and $\theta_{plastic}$ measured at the intermediate support. As the coefficient K_{MR} quantifies the capacity of transferring forces from critical sections towards those less demanded, the graphs depicted in Figure 19 are presented up to the point when loads started decreasing. For low amounts of reinforcement (0.13% and 0.25%) it can clearly be seen that at the onset of yielding a bigger redistribution of moments had already been produced for the RC configurations compared with those HRC beams, due to the loss of stiffness after the section cracking. This is aligned with the behaviour shown in Figures 18a and 18c. For C-0.13% beams, the solutions with fibres presented lower plastic rotations compared to C-0.13%-RC. In case of $\rho_s = 0.25\%$, the stiffness after yielding was similar meaning that the addition of fibres for this reinforcement configuration had less impact on the post-yielding stiffness. Again, the RC configuration achieved larger plastic deformations. For $\rho_s = 0.57\%$, K_{MR} at rebar yielding was similar in all cases, for this amount of longitudinal reinforcement the addition of fibres barely affected the loss of stiffness after

cracking. After yielding, the K_{MR}–$\theta_{plastic}$ curves had the same slope, C-0.52%-RC being the unique solution able to present high plastic rotation capacity. In case of $\rho_s = 1.14\%$, all beams had similar redistribution at the onset of rebar yielding, so the increase of f_{R1} unaltered the overall stiffness of the member, and the same range of moment redistribution was detected, ranging from 11% to 13%.
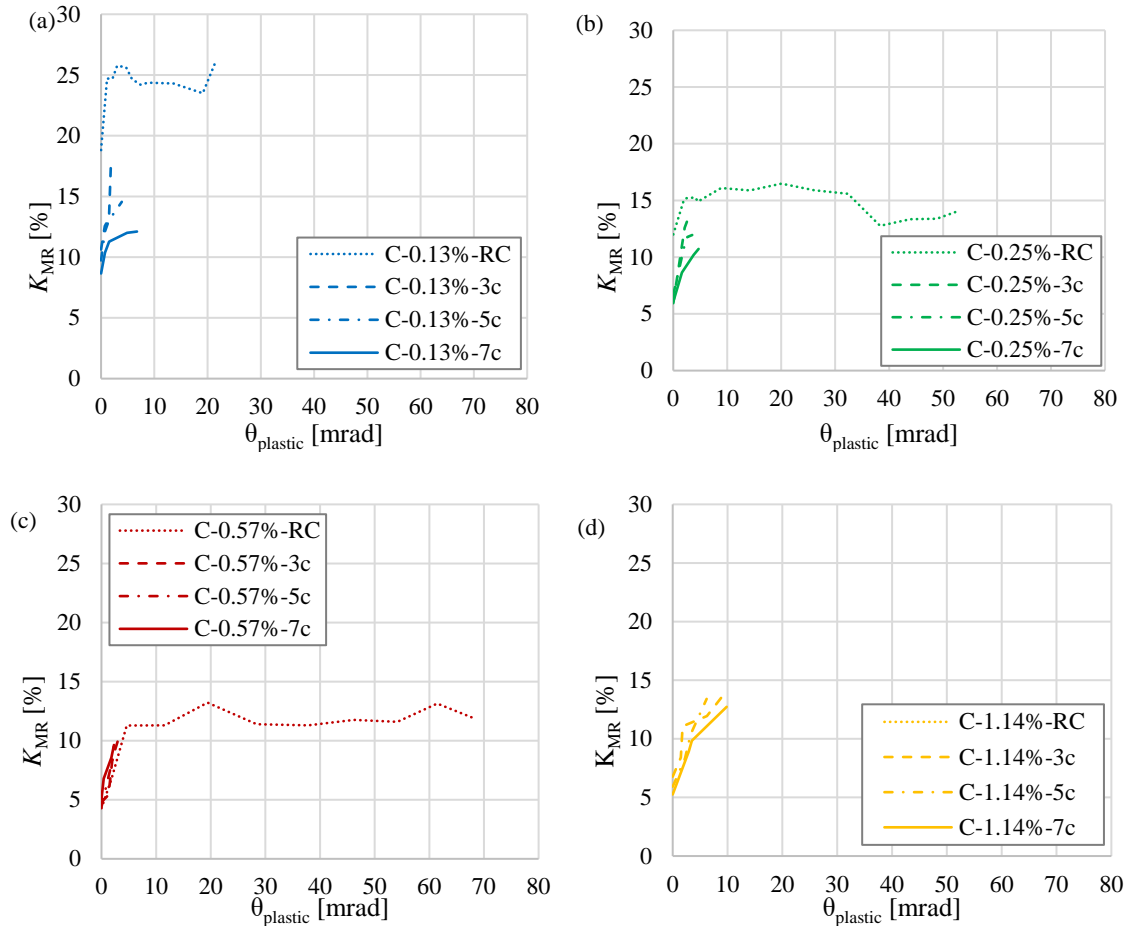

Figure 19 – Parametrical analysis on two-span continuous beams: K_{MR}*-* $\theta_{plastic}$ graphs for (a) C-0.13% (b) C-0.25% (c) C-0.57% and (d) C-0.1.14%

Finally, Figure 20 presents the K_{MR}–f_{R1m} relationship. Firstly, for reinforcement ratios higher than 0.57%, K_{MR} ranges between 10 and 14%, this being barely affected by FRC residual strength (although it remains significantly lower than for the RC solution). As reinforcement ratio decreases to 0.25% and 0.13%, K_{MR} becomes increasingly sensitive to f_{R1m}, particularly for a reinforcement ratio of 0.13% for which it linearly decreases with increasing f_{R1m}.
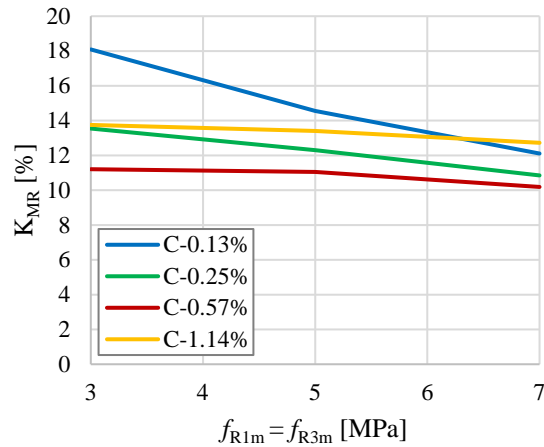
*Figure 20 –K*MR*- f*R1m *relationship for two-span continuous beams*

In the light of the previous results, it must be emphasized that the redistribution capacity of 20% accepted in the fib MC2010 (or even higher in other codes) for FRC structural members should be revised, especially in case of low longitudinal reinforcement ratios.

4. CONCLUSIONS

This paper has presented the results of a numerical parametric study on the plastic rotation and moment redistribution capacities in HRC members with different reinforcing ratios (from 0.13 % to 1.14%) and FRC residual strengths (classes 3c, 5c and 7c per MC2010 [32]). Plastic rotation capacity was assessed on simply supported beams, whereas two-span continuous beams were used to analyse the moment redistribution capacity. For this purpose, a numerical model was developed and validated on experimental data. The simulations were carried out using high ductility reinforcement (f_{max}/f_y=672/600), therefore the conclusions drawn in this paper only can be hold when this class of steel is used.

Based on the obtained results, the following conclusions can be drawn:

- The increase of the FRC strength class (represented by f_{R1}) in both simply supported and continuous beams led to increases in load-bearing capacity, especially for low values of ρ_s.

- The use of fibres in simply supported beams significantly affected the deformation capacity of those by reducing both deformation and rotation capacities for any FRC residual strength class in beams with $\rho_s \leq 0.25\%$.

- In simply supported beams with $\rho_s = 0.57\%$, there was an increase in deformation capacity due to the interaction of the softening response of FRC residual strength class 3c and the hardening of the steel reinforcement. For the remaining values of FRC residual strength classes (5c and 7c), crack localisation affected the deformation capacity leading to a clear reduction of this property. For HRC beams with $\rho_s = 1.14\%$

the beams failed due to concrete crushing, crack localisation was also detected, hence, a reduction of deformation capacity was found for all beams.

- In simply supported beams, changes in ρ_s have higher influence on the rotational capacity for lower FRC residual classes (3c) than for those with higher FRC classes. For $\rho_s \leq 0.57\%$ the plastic hinge length is not affected by the addition of fibres whereas for lower ratios the length decreases with the decrease of the FRC residual strength.

- In statically indeterminate members, prior to yielding, the increase of f_{R1} reduces the moment redistribution by enhancing the overall stiffness. As expected and in agreement with results from literature, the addition of fibres increased the load bearing capacity, with the contribution increasing when decreasing ρ_s.

- In HRC continuous beams, the deformation capacity only improved for beams with $\rho_s = 1.14\%$. For the rest of beams a reduction of the post-yield ductility response of the beam was observed.

- The moment redistribution capacity was not affected by the FRC residual strength for beams with $\rho_s \geq 0.57\%$. For low reinforcement ratios (i.e. 0.13% and 0.25%), the redistribution capacity became more sensitive, this increasing with decreasing f_{R1}.

- The latter conclusion is of paramount importance since the redistribution coefficient accepted in several design guidelines (including the *fib* MC2010) is superior to 20%. The results obtained numerically prove that lower redistribution coefficients are to be expected when the FRC strength class increases in HRC when those are compared with the equivalent (same reinforcement ratio) RC alternative.

The conclusions of this study are determined by the ranges of parameter values considered in the analyses and, therefore, cannot be directly extrapolated beyond these values. Although the numerical model was calibrated and validated on experiments using steel fibre reinforced concrete, it can be considered that, in general, the results are applicable also to FRC produced with macro-synthetic structural fibres as long as requirements of subclause 5.6.1 of the *fib* Model Code 2010 are fulfilled. Therefore, the results of this study can serve as an important first step towards defining moment redistribution and rotation capacity models and limits for HRC. Future studies should include more experimental tests, ranges of FRC residual strengths, as well as different static systems and load distributions.

REFERENCES

[1] Pfyl T, Marti P. Behaviour of reinforced steel fibre concrete members in bending and tensions. Proc. 3rd Int. PhD Symp. Civ. Eng., vol. 2, 2000, p. 47–55.

[2] Meda A, Minelli F, Plizzari GA. Flexural behaviour of RC beams in fibre reinforced concrete. Compos Part B Eng 2012;43:2930–7. https://doi.org/10.1016/j.compositesb.2012.06.003.

[3] Conforti A, Minelli F, Plizzari GA. Wide-shallow beams with and without steel fibres: A peculiar behaviour in shear and flexure. Compos Part B Eng 2013;51:282–90. https://doi.org/10.1016/j.compositesb.2013.03.033.

[4] Pujadas P, Blanco A, de la Fuente A, Aguado A. Cracking behavior of FRC slabs with traditional reinforcement. Mater Struct Constr 2012;45:707–25. https://doi.org/10.1617/s11527-011-9791-0.

[5] Yoo DY, Moon DY. Effect of steel fibers on the flexural behavior of RC beams with very low reinforcement ratios. Constr Build Mater 2018;188:237–54. https://doi.org/10.1016/j.conbuildmat.2018.08.099.

[6] Markić T, Amin A, Kaufmann W, Pfyl T. Strength and Deformation Capacity of Tension and Flexural RC Members Containing Steel Fibers. J Struct Eng (United States) 2020;146:1–17. https://doi.org/10.1061/(ASCE)ST.1943-541X.0002614.

[7] Fantilli AP, Chiaia B, Gorino A. Unified approach for minimum reinforcement of concrete beams. ACI Struct J 2016;113:1107–16. https://doi.org/10.14359/51688927.

[8] Fantilli AP, Gorino A, Chiaia B. Fiber volume fraction and ductility index in fiber-reinforced concrete round determined panels. Procedia Struct Integr 2016;2:2857–64. https://doi.org/10.1016/j.prostr.2016.06.357.

[9] Espion B. Discussion of 'Flexural analysis of reinforced concrete beams containing steel fibers' by Byung Hwan Oh (October, 1992, Vol. 118, No. 10). Struct Eng 1994;120:1932–4. https://doi.org/10 .1061/(ASCE)0733-9445(1994)120:6(1932).

[10] Dancygier AN, Savir Z. Flexural behavior of HSFRC with low reinforcement ratios. Eng Struct 2006;28:1503–12. https://doi.org/10.1016/j.engstruct.2006.02.005.

[11] Dancygier AN, Berkover E. Cracking localization and reduced ductility in fiber-reinforced concrete beams with low reinforcement ratios. Eng Struct 2016;111:411–24. https://doi.org/10.1016/j.engstruct.2015.11.046.

[12] Mertol HC, Baran E, Bello HJ. Flexural behavior of lightly and heavily reinforced steel fiber concrete beams. Constr Build Mater 2015;98:185–93. https://doi.org/10.1016/j.conbuildmat.2015.08.032.

[13] Conforti A, Zerbino R, Plizzari G. Assessing the influence of fibers on the flexural behavior of reinforced concrete beams with different longitudinal reinforcement ratios. Struct Concr 2020;22:1–14. https://doi.org/10.1002/suco.201900575.

[14] Pokhrel M, Shao Y, Billington S, Bandelt MJ. Effect of Fiber Content Variation in Plastic Hinge Region of Reinforced UHPC Flexural Members. BEFIB 2020, vol. 30, 2020, p. 1042–55. https://doi.org/10.1007/978-3-030-58482-5_92.

[15] Meda A, Plizzari GA, Riva P. Fracture behavior of SFRC slabs on grade. Mater Struct Constr 2004;37:405–11. https://doi.org/10.1617/14093.

[16] Meda A, Plizzari G. New design approach for steel fiber-reinforced concrete slabs-on-ground based on fracture mechanics. ACI Struct J 2004;101 (3):298–303.

[17] de la Fuente A, Pujadas P, Blanco A, Aguado A. Experiences in Barcelona with the use of fibres in segmental linings. Tunn Undergr Sp Technol 2012;27:60–71. https://doi.org/10.1016/j.tust.2011.07.001.

[18] de la Fuente A, Escariz RC, de Figueiredo AD, Molins C, Aguado A. A new design method for steel fibre reinforced concrete pipes. Constr Build Mater 2012;30:547–55. https://doi.org/10.1016/j.conbuildmat.2011.12.015.

[19] de la Fuente A, Escariz RC, de Figueiredo AD, Aguado A. Design of macro-synthetic fibre reinforced concrete pipes. Constr Build Mater 2013;43:523–32. https://doi.org/10.1016/j.conbuildmat.2013.02.036.

[20] Paulay T. Moment redistribution in continuous beam of earthquake resistan multistory reinforced concrete frames. Bull New Zeal Soc Earthq Eng 1976;9:205–12.

[21] Visintin P, Oehlers DJ. Mechanics-based closed-form solutions for moment redistribution in RC beams. Struct Concr 2016;17:377–89. https://doi.org/10.1002/suco.201500085.

[22] Scott RH, Whittle RT. Moment redistribution effects in beams. Mag Concr Res 2005;57:9–20.

[23] Nethercot DA, Li TQ, Choo BS. Required rotations and moment redistribution for composite frames and continuous beams. J Constr Steel Res 1995;35:121–63.

[24] Oehlers DJ, Haskett M, Mohamad Ali MS, Griffith MC. Moment redistribution in reinforced concrete beams. Struct Build 2010;163:165–76.

[25] Oehlers DJ, Ju G, Liu IST, Seracino R. Moment redistribution in continuous plated RC flexural members. Part1: netral axis depth approach and tests. Eng Struct 2004;26:2197–207.

[26] Oehlers DJ, Liu IST, Ju G, Seracino R. Moment redistribution in continuous plated RC flexural members. Part2: flexural rigidity approach. Eng Struct 2004;26:2209–18.

[27] Scott RH, Whittle RT. Serviceability influences on moment redistribution in beams. Struct Concr 2005;6:135–40. https://doi.org/10.1680/stco.2005.6.4.135.

[28] Sturm AB, Visintin P, Oehlers DJ. Closed-form expressions for predicting moment redistribution in reinforced concrete beams with application to conventional concrete and ultrahigh performance fiber reinforced concrete. Struct Concr 2020;21:1577–96. https://doi.org/10.1002/suco.201900498.

[29] Lou T, Lopes SMR, Lopes A V. Effect of relative stiffness on moment redistribution in reinforced high-strength concrete beams. Mag Concr Res 2017;69:716–27. https://doi.org/10.1680/jmacr.15.00499.

[30] EN 1992-1-1:2011-01. Eurocode 2. Brussels: CEN; 2014. https://doi.org/10.2788/35386.

[31] EHE-08. Instrucción de Hormigón Estructrural (EHE-08). Madrid: Ministerio de Fomento; 2008.

[32] International Federation for Structural Concrete (fib). fib-Model Code for Concrete Structures 2010. Lausanne: 2010. https://doi.org/10.1002/9783433604090.

[33] American Concrete Institut and International Organization for Standaritzation Building Code Requirements for Structural Concrete. ACI 318-08. Farmington Hills: ACI; 2008.

[34] AS 360 - 2009. AS 3600-2009 Concrete Structures. Australian Standards; 2009.

[35] Küsel F, Kearsley E. Effect of steel fibres in combination with different reinforcing ratios on the performance of continuous beams. Constr Build Mater 2019;227. https://doi.org/10.1016/j.conbuildmat.2019.07.279.

[36] Mahmood SMF, Agarwal A, Foster SJ, Valipour H. Flexural performance of steel fibre reinforced concrete beams designed for moment redistribution. Eng Struct 2018;177:695–706. https://doi.org/10.1016/j.engstruct.2018.10.007.

[37] Visintin P, Mohamad Ali MS, Xie T, Sturm AB. Experimental investigation of moment redistribution in ultra-high performance fibre reinforced concrete beams. Constr Build Mater 2018;166:433–44. https://doi.org/10.1016/j.conbuildmat.2018.01.156.

[38] Markić T, Amin A, Kaufmann W, Pfyl T. Discussion on " Assessing the influence of fibers on the flexural behavior of reinforced concrete beams with different longitudinal reinforcement ratios " by Conforti et al. [structural concrete, 2020]. Struct Concr 2021;22 (5). https://doi.org/10.1002/suco.202000488.

[39] Bosco C, Debernardi P. Influence of some basic parameters on the plastic rotation of reinforced concrete elements. CEB-Fib Bull d'Information No 218 1993;248:25–44.

[40] European Commitee for Standardization. Precast concrete products - test method for metallic fibre concrete- Measuring the flexural tensile strength. Br Stand Inst 2005. https://doi.org/9780580610523.

[41] Dassault Systèmes Simulia. Abaqus CAE User's Manual (6.12). Providence: Dassault Systèmes; 2012.

[42] Qin R, Zhou A, Lau D. Effect of reinforcement ratio on the flexural performance of hybrid FRP reinforced concrete beams. Compos Part B Eng 2017;108:200–9. https://doi.org/10.1016/j.compositesb.2016.09.054.

[43] Nana WSA, Bui TT, Limam A, Abouri S. Experimental and Numerical Modelling of Shear Behaviour of Full-scale RC Slabs Under Concentrated Loads. Structures 2017;10:96–116. https://doi.org/10.1016/j.istruc.2017.02.004.

[44] Jamshidi M, Hoseini A, Vahdani S, de la Fuente A. Numerical-aided design of fiber reinforced concrete tunnel segment joints subjected to seismic loads. Constr Build Matreials 2018;170:40–54.

[45] Nogales A, de la Fuente A. Numerical-aided flexural-based design of fibre reinforced concrete column-supported flat slabs. Eng Struct 2021;232:1–24. https://doi.org/10.1016/j.engstruct.2020.111745.

[46] Carpinteri A, Corrado M, Mancini G, Paggi M. Size-scale effects on plastic rotational capacity of reinforced concrete beams. ACI Struct J 2009;106:887–96. https://doi.org/10.14359/51663190.

[47] Hillerborg A. Fracture mechanics concepts applied to moment capacity and rotational capacity of reinforced concrete beams. Eng Fract Mech 1990;35:233.

[48] Pecce M. Experimental Evaluation of Rotational Capacity of HPC Beams. CEB Bull d'Information No 242, Com Euro-International Du Béton, Laussane 1997:197–210.

[49] FIB - Working party 1.4.1. Precast Tunnel Segments in Fibre-Reinforced Concrete. Lausanne: Federation internationale du béton; 2

3. PUBLICATIONS: RESEARCH CONTRIBUTIONS

This chapter reproduces the research contributions derived from this thesis. Each paper follows its own numbering of sections, figures, equations and references.

3.1. RESEARCH CONTRIBUTION I: TBM THRUST ON FIBRE REINFORCED CONCRETE PRECAST SEGMENT SIMULATION

Alejandro Nogales[a,b,*] and Albert de la Fuente[b]

[a]Smart Engineering Ltd., UPC Spin-Off, Jordi Girona 1-3, 08034 Barcelona, Spain

[b]Civil and Environmental Engineering Deparment, Universitat Politècnica de Catalunya (UPC), Jordi Girona 1-3, 08034 Barcelona, Spain

*Corresponding author

ABSTRACT

Fibre reinforced concrete (FRC) is gaining acceptance as a structural material for casting precast segments as this has proven to lead to various advantages respect to the traditional reinforced concrete, especially for improving the crack control during transient loading situations. Concentrated loads induced during the excavation stage by Tunnel Boring Machines (TBMs) is still a matter of discussion into the tunnelling construction field, this having a strong impact from both technical and economic perspectives. In this regard, although specific codes and guidelines have been published and intense research has been carried out, this pointing out the benefits of using FRC as partial or total substitution of conventional reinforcement; however, there is still not a thorough research on the effectiveness of the FRC strength class (as defined into the *fib* Model Code 2010) to control crack widths in tunnel linings during the TBM thrust phase. To this end, the objective of this research contribution consists in carrying out a parametric analysis, considering different FRC strength classes (including hybrid reinforcements), related with the crack patterns due to the TBM-thrust on FRC segments. This was performed by means of a comprehensive non-linear finite element (FE) numerical simulation. The results derived from this research are meant to be useful for those stakeholders involved in the design of precast tunnel linings.

KEYWORDS: Fibre reinforced concrete, non-linear analysis, precast segments, TBM, tunnelling, concentrated load.

1.   INTRODUCTION

Over the last decades, the use of structural fibres as partial/total replacement of the traditional steel bars has grown [1,2]. Among the structural applications where FRC is used is tunnelling, precast tunnel segments being suitable elements for this replacement [3]. The use of fibres has been proven as a potential solution and many tunnels were made up with this material in the recent years, among other examples: the "Barcelona metro line 9" [4,5], "Monte Lirio" in Panamá [6,7] and the "Prague Metro Line" [8,9]. Indeed, the recently *fib* Bulletin 83 [10] gather more than 70 experiences of the use of fibres in tunnel linings and provides design provisions for FRC tunnel segments.

During excavation, TBM hydraulic jacks take support against the previously place ring in order to advance forward, these jacks induce high concentrated loads in the segments. Experiences on tunnel design and research have confirmed that in terms of loading and concrete cracking, the most demanding scenario can be during the thrust stage [11,12].

In this sense, actions in tunnels can be classified in: (1) Primary loads due to soil-structure interactions and water pressure and (2) Secondary loads, which occur during construction called transient phases, which include demoulding, storage, transportation, handling, placing and TBM jack's thrust. Primary loads induce compressive forces combined with low shear forces and bending moments on the ring can be resisted by the concrete matrix and a combination of fibre and conventional reinforcement in linings with large diameters [13] (larger than 6 m). However, tunnels with smaller diameters (metro and hydraulic tunnels) might be subjected to compression in service stage, and it is during transient phases where tensile stresses appear either due to bending or thrust loads. The latter can lead to high concentrated loads and to tensile stresses, which result in splitting and spalling.

These stress patterns caused by concentrated loads are complex and its magnitude and distribution (within a D-region) are both difficult to be assessed. Leonhardt [14] and Iyengar [15] were the first who carried out research in this topic of transfer zones in pre-stressed structures. These studies concluded that concentrated loads induce a tri-axial state of stresses where a principal tensile component of stresses (splitting stresses) acts orthogonally to the paths of compressions. In addition, as a result of compatibility demands with respect to deformed cross section, tensile stresses (spalling stresses) appear in segments.

This state of stresses and the curved shape of the segments makes necessary a complex detailed reinforcement, which may leave uncovered areas where spalling and splitting take place. Alternatively (or complimentary), FRC can deal with this matter due to the randomly distribution nature of the fibres within the whole segment.

FRC for structural applications can be produced with different types of fibres (mainly metallic and synthetic), providing to the concrete matrix an improvement of: ductility; post-crack tensile

strength (residual strength); impact resistance and a more convenient crack pattern for serviceability purposes. Due to the growing use of FRC, many guidelines have included design recommendations for its mechanical characterization and design [16–19] and specific documents for FRC precast segments have also been published recently [10,20].

This topic is of great interest since it influences the design of precast tunnel segments (segment geometry, reinforcement amount and distribution) and cracking during this stage can jeopardise costs, structural durability and the serviceability of the tunnel leading to repairs and maintenance actions. The complex state of stresses generated by the concentrated loads is difficult to predict and this is only possible by means of experimental test and/or non-linear FE analysis [10].

The aim of this contribution is to assess the structural performance of precast FRC tunnel linings subjected to thrust jack forces. To this purpose, different classes of FRC according to *fib* MC-2010 were considered as constituent material of segments and both the bearing and crack control capacities were identified and quantified numerically by means of a model implemented with ABAQUS [21]. The model was previously validated with results derived from experimental tests available in the literature. Both the results and conclusions achieved are found to be of interest in terms of structural and economic optimization in those cases for which the TBM thrust is the design governing phase.

2.   NUMERICAL MODELLING OF FRC

According to *fib* MC-2010 FRC classes can be classified by its characteristic residual strength values (f_{Rk}) obtained from 3 point bending test notched beams according to EN 14651:2005. Two parameters are used for its classification: f_{R1k}, which represents the residual strength for a crack opening displacement of 0.5 mm and a letter (a, b, c, d or e) that represents the f_{R3k}/f_{R1k} ratio, where f_{R3k} stands for a CMOD of 2.5 mm. In order to establish the stress-strain (σ-ε) or stress-crack width (w-ε) constitutive relations, the equations proposed by *fib* MC-2010 are adopted, using mean values of f_{LOP}, f_{R1} and f_{R3} for the simulations. The compressive behaviour was simulated according to the expression proposed by *fib* MC-2010. These equations were implemented in the "Concrete Damage Plasticity" model available in ABAQUS

3.   EXPERIMENTAL MODEL VALIDATION

3.1.   FRC BLOCKS SUBJECTED TO CONCENTRATED LOADS

Small-scale experimental tests carried out by Schnütgen and Erdem [22], which consisted of steel FRC anchor blocks subjected to concentrated loads oriented to assess the response against splitting, were used for the validation. To that end, two fibre mixes were used: 35 kg/m³ (FRC-A) and 60 kg/m³ (FRC-B). The concrete compressive strengths (f_{cm}) were 58.2 MPa and 50.2 MPa for FRC-A and FRC-B respectively. Residual strengths were derived from NBN-B-15-238:1992 [23] test: f_{R1} = 5.41 MPa and f_{R3}= 4.81 MPa for FRC-A and 6.49 and 5.96 MPa for FRC-B. The

blocks had a square base of 350 mm and 700 mm height and a surface load on top of 150 x 350 mm (Figure 1a). The FE model was composed by 16800 eight-noded hexahedral elements (C3D8R), no vertical displacement allowed at the base and the load was applied by displacement control (Figure 1b).
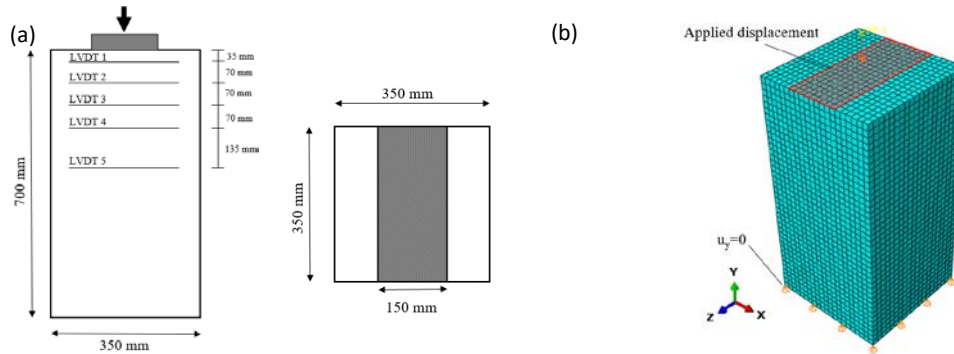

Figure 1 – Splitting test (a) Test set up (b) FE model adopted.

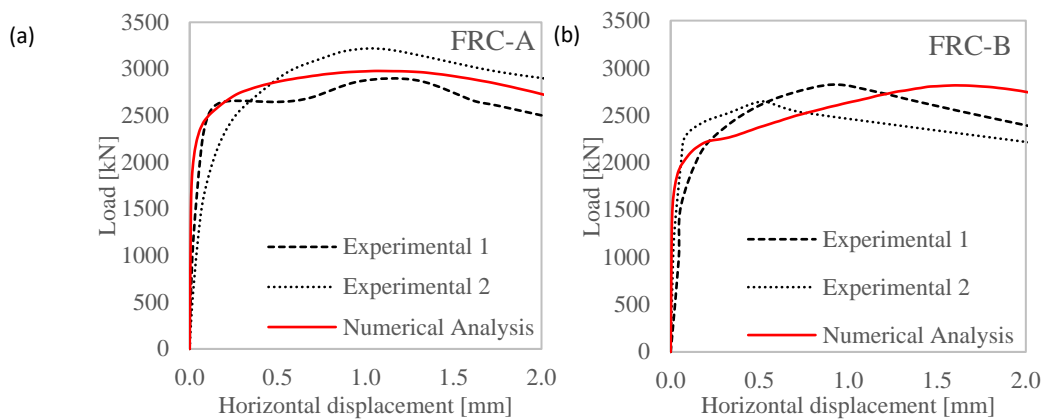The results of both experimental and numerical tests are presented in Figure 2.

Figure 2 – Load-Displacement chart for experimental and numerical test (a) FRC-A (b) FRC-B.

The horizontal displacement was measured at a distance of 175 mm from the top (LVDT 3) where the maximum tensile stresses appear. The load-displacement results of the numerical simulations are in good agreement with the experimental test, the block cast with FRC-A had a maximum load of 2880 kN, whereas those obtained experimentally were 3200 kN and 2870 kN. Regarding the FRC-B test, the numerical simulation reached 2815 kN whereas the experimental test were 2830 kN and 2650 kN.

3.2. PRECAST CURVED SEGMENT SUBJECTED TO CONCENTRATED LOADS

In order to check the suitability of the model for curved segments subjected to concentrated loads, the results of the experimental research carried out by Conforti [24] were considered. This experimental program was meant to analyse the suitability of polypropylene macrofibres for controlling crack width resulting from concentrated loads. To this end, tests on curved segments of 1810 mm length (internal diameter of 3200 mm), 1200 mm height and 250 thick subjected to

concentrated loads by means of two loading shoes (500 x 250 mm^2) (Figure 3a) were performed. The segment was cast with 10 kg/m^3 polypropylene fibres, had 49.9 N/mm^2 f_{cm} and 2.97 and 4.61 N/mm^2 for f_{R1m} and f_{R3m} respectively, according to EN-14651:2005. The FE model is composed by 8100 C3D8R elements, no vertical displacement allowed at the bottom face and the load was applied by displacement control (Figure 3b). The operational load (P_{nom}) and accidental load (P_{acc}, considered as the highest operational load) of the TBM were 785 and 1130 kN respectively.
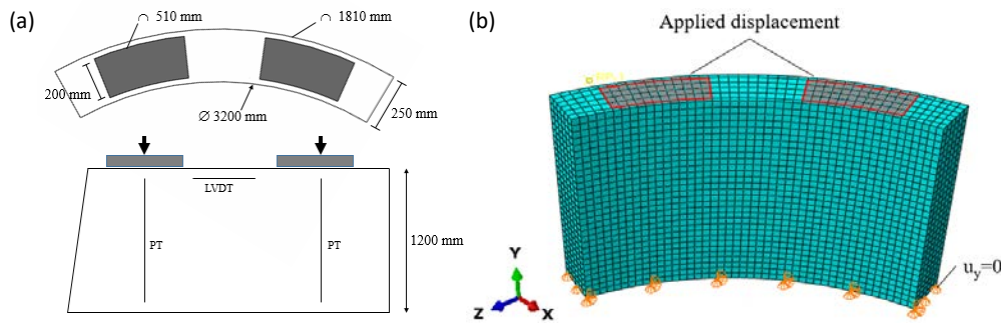
Figure 3 – Segment test (a) Test set up (b) meshed model and boundary conditions.

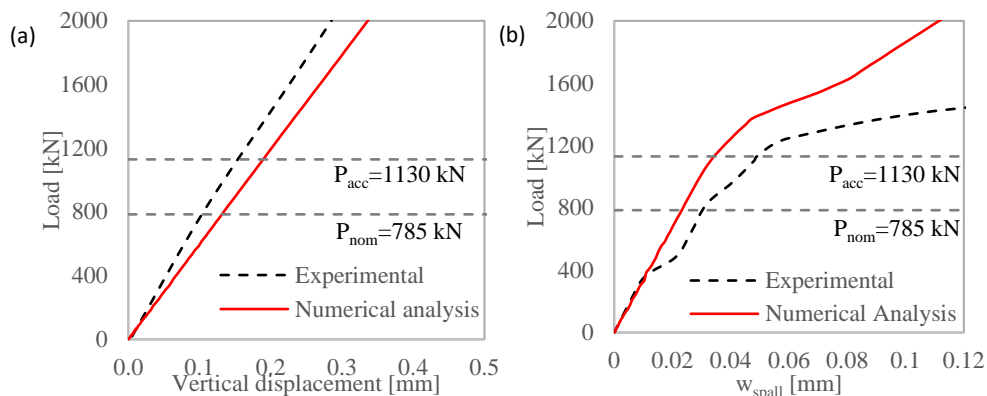In Figure 4a the load-vertical displacement is presented.

Figure 4 – Experimental and numerical comparison (a) Load-vertical displacement (b) Load-spalling crack opening.

It is worth noticing that the model performs similarly to the experimental test up to 1200 kN, but had a stiffer perfomance. The spalling load (load level that generates the spalling crack, P_{spall}) is 955 kN and 979 kN for both experimental and numerical (1.60%) and the splitting load (P_{sp}) was 1600 kN in the experimental test whereas 1585 kN is registered in the model (0.93%). The spalling crack (w_{spall}) is measured and depicted in Figure 4b, its location in both experimental and numerical test was between pads, the w_{spall} at P_{acc} is 0.050 mm for the experimental test and in the numerical model is 0.034 mm.

4. PARAMETRIC STUDY

The segment geometry and jack configuration are both taken from precast segment of an actual metro tunnel lining under construction. The inner diameter of the segment is 4075 mm, 1500 mm

height and 350 mm thickness (Figure 5). Four jacks for each segment, the loading surface being 222 x 500 mm² placed 42 mm from the inner edge of the segment.
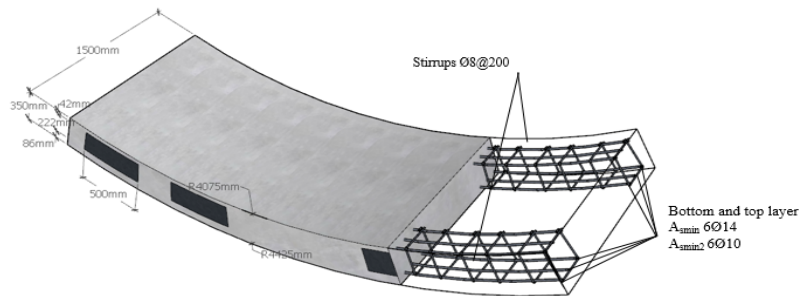

Figure 5 – Geometrical properties of the segment and rebar distribution.

4.1. MATERIALS

A C50/60 concrete has been used for the production of these segments; thus, according to the *fib* MC-2010, the values f_{ctm} = 4.07 N/mm², f_{cm} 58 N/mm² and E_{cm} = 32900 were assumed. The FRC strength classes 1, 3 and 5 (related to f_{R1k}) with f_{R3k}/f_{R1k} ratios a, b, c, d and e, these resulting in a total of 16 different concretes (15 FRC + 1 PC). The commonly accepted ratio f_{Rk}/f_{Rm} = 0.7 was used to estimate f_{Rm}. In this sense, it must be emphasized that this ratio might be greater as f_{Rm} increase, and viceversa. The constitutive equation according to *fib* MC-2010 is used for assessing the serviceability and ultimate residual strengths, f_{Fts} and f_{Ftu} respectively, calculation and are presented in Table 1.

Table 1 – Serviceability and ultimate residual strength for FRC adopted solutions.

	f_{R1k}					
	1		3		5	
f_{R3k}/f_{R1k}	f_{Fts} [MPa]	f_{Ftu} [MPa]	f_{Fts} [MPa]	f_{Ftu} [MPa]	f_{Fts} [MPa]	f_{Ftu} [MPa]
a		0.14		0.42		0.71
b		0.28		0.85		1.42
c	0.64	0.42	1.92	1.28	3.21	2.14
d		0.57		1.71		2.85
e		0.71		2.14		3.57

Furthermore, aiming at optimising the reinforcement configuration, hybrid reinforcements (RC+FRC) are also considered. Figure 5 shows the cage configuration, this being composed by two chords made by 2x3Ø14 curved rebar with Ø8@200mm stirrups, with a clear cover of 50mm. This amount (per face) corresponds to the minimum amount (As,min) required by fib MC-2010 to guarantee the ductile response in flexure. Additionally, As,min/2 (2x3Ø10 each face) a ratio of has also been included into the analysis.

Alejandro Nogales Arroyo

4.2. MODEL DESCRIPTION

In Figure 6 is presented a general view of the segment model, were is depicted the mesh and the boundary conditions. Simplifications must be taken in order to guarantee a robust model with a non-dependent mesh able to reduce computational calculation time while giving accurate results. To this end, only a single segment was modelled. The interactions with the surrounding segments at both longitudinal and radial joints were not taken into account, these interactions has negligible influence on local behaviour which do not affect the results of splitting and spalling phenomena that are produced under the loading zone and between pads, besides this assumption helps to avoid convergence problems and reduce computational time. For the same reason, in spite of setting a regular mesh, bolt and gasket holes were not modelled.
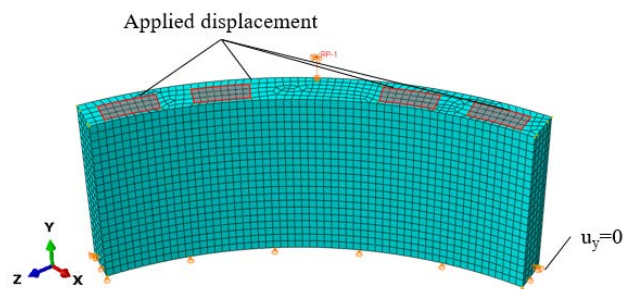

Figure 6 – Meshed model and boundary conditions.

The mesh is set by70 mm size C3D8R elements and the rebar are modelled using linear T3D2 elements embedded in the concrete section, adopting a perfect bond rebar-concrete.

5. RESULTS

5.1. CENTRED THRUST ON FRC SEGMENT

The first crack is produced due to spalling stresses, between centred pads, the cracking load ($P_{cr} = P_{spall}$) is 1975 kN for each jack. The TBM operational load (P_{nom}) must be lower than P_{cr}, taking this into account the assumption $P_{cr} = P_{nom}$ is adopted. Likewise, P_{acc} was considered as two times the cracking load ($2P_{cr}$). Figure 7 presents the non-dimensional load (P/P_{spall}) versus displacement of the jack.
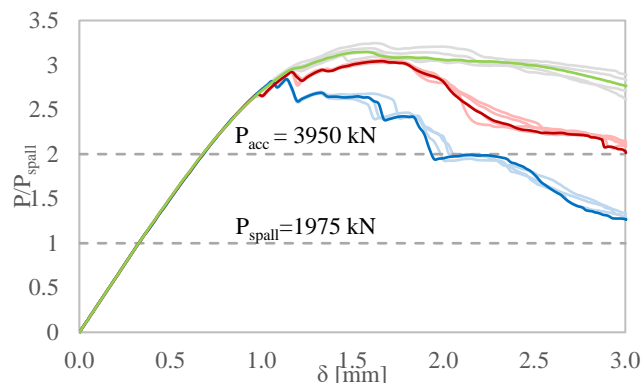

Figure 7 – Non-dimensional load-displacement curve for FRC. Stress pattern for P_{spall} and P_{acc}.

As it can be noticed, the mechanical response of the segments is the same in all cases up to $2.5P_{spall}$. Figure 8a depicts $P/P_{spall} - w_{spall}$ graph, in light colours are plotted "a, b, d and e" FRC classes and in dark colour "c" class. The results allow confirming that f_{R1} has great influence in cracking control whereas, the f_{R3}/f_{R1} ratio do not play a significant role (once f_{R1} is set). Figure 8b shows the non-dimensional load – w_{sp} (splitting crack), this being produced at 2173 kN ($P_{sp} = 1.1P_{spall}$), w_{sp} is minor than 0.05 mm for P_{acc} and no significant differences are noticed between solutions.
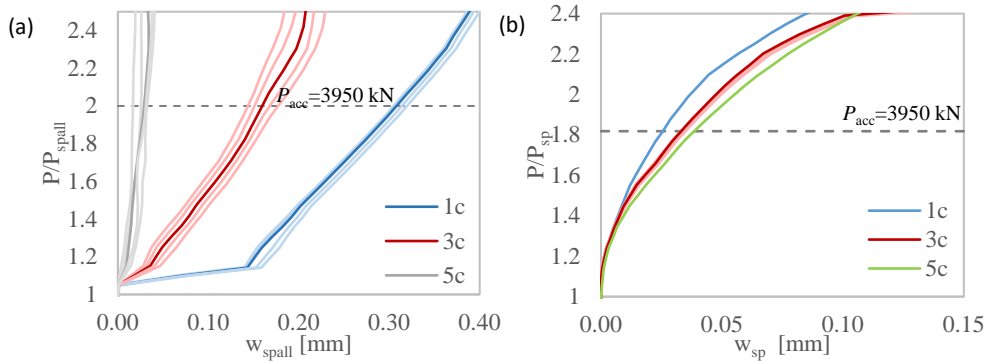

Figure 8 – Non-dimensional load – crack width (a) Spalling (b) Splitting.

5.2. ECCENTRIC THRUST ON FRC SEGMENT

During the excavation phase, there may be situations where the thrust exerted by the jacks is not centred and this can generate eccentricities. In order to study this phenomenon, simulations were carried out considering 30 mm eccentricity towards inside the tunnel (e^-) and outside the tunnel (e^+). The eccentric thrust does affect the cracking load as can be seen in Figure 9, where these loads are presented non-dimensional with respect to P_{spall} for centred thrust (1975 kN).

For e^+, P_{spall} reduces and P_{sp} increases. In the case of e^-, P_{spall} increases with respect to the centred thrust and P_{sp} reduces. These results have to be taken with precaution since the existence of the gasket could slightly modify these results; likewise, these tendencies are highly dependent on the load area and the curvature of the segment, hence, other results are expected for geometric configurations.

Figures 10a and 10b depict the non-dimensional load – crack width charts for the solution 1c, 3c and 5c. Based on the results presented in Figure 10a, it can be noticed that as the FRC strength class increases the spalling crack width is reduced drastically. The results shown in Figure 10b reveal that eccentric thrust has a relevant influence on splitting cracks width whilst the FRC strength class barely affects the response. The FRC 3c strength class seems to be the most suitable for controlling the crack width (while optimizing the amount of fibres) since the crack widths ranges between 0.12 mm ($e = -30$ mm) and 0.18 mm ($e = + 30$ mm), which is an acceptable range

($w < 0.20$ mm) for dealing with the posterior service conditions; this considering that the probability of reaching P_{acc} must be, by definition, very low.
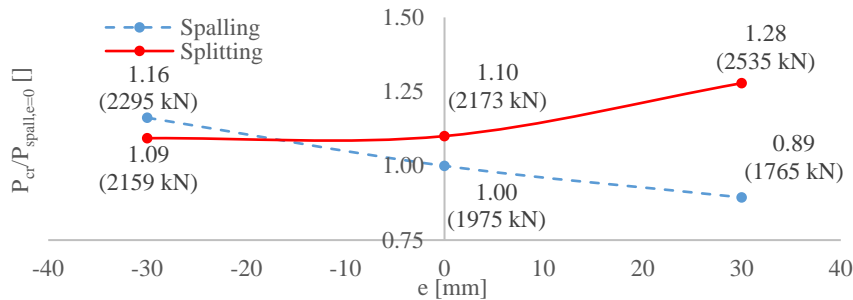

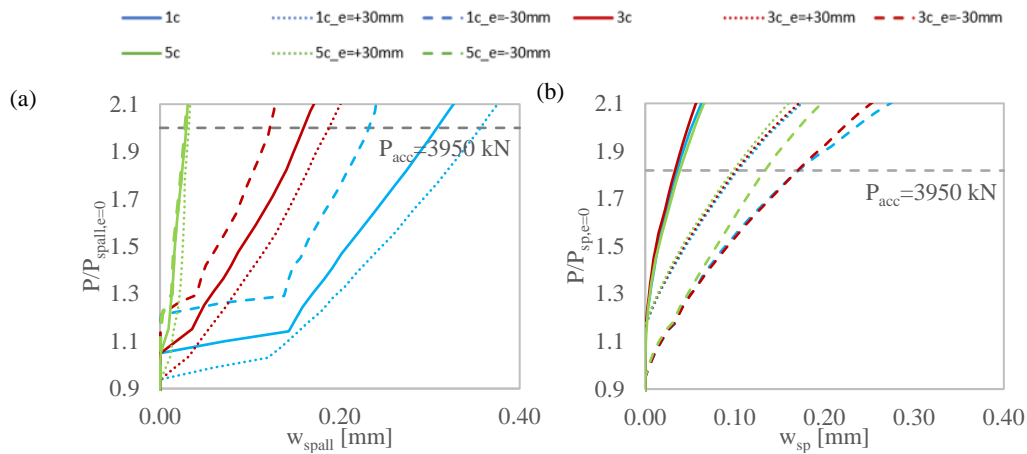*Figure 9 – Cracking load/P_{spall} for e=0 – eccentricity.*

Figure 10 – (a) Cracking load/P_{spall} for e=0 – spalling crack width (b) Cracking load/P_{sp} for e=0 – splitting crack width.

5.3. THRUST ON HYBRID REINFORCEMENT SEGMENT

For the studied geometry, the wider cracks are those due to spalling stresses. With the aim of reducing the crack width, a hybrid reinforcement (rebar + fibres) is proposed for the areas where spalling stresses appear. The rebar distribution is plotted in Figure 5. Simulations were carried out with two rebar configurations ($A_{s,min}$ and $A_{s,min2}$) combined with 1c, 3c and 5c for centred and eccentric thrust. Figure 11 plots ξ-eccentric thrust for P_{acc}. Where ξ stands for w_{spall}/w_{spall}=0.2 mm (assumed as a well-controlled crack opening, which can be considered different according other premises).

The results prove that the hybrid solutions help to reduce the crack width for low resistance classes (namely 1c), however, is less efficient for higher classes (3c and 5c) where the crack width is mainly controlled by the residual strength of FRC (ξ ≤ 1). Hybrid reinforcement is a suitable

solution when either very strict crack width limitations are imposed (e.g., $w \leq 0.15$ mm, $\xi \leq 0.75$) and/or when traditional steel reinforcement is also required to resist bending moments; for which the fibres as unique reinforcement are not a suitable solution from the economic point of view [13].
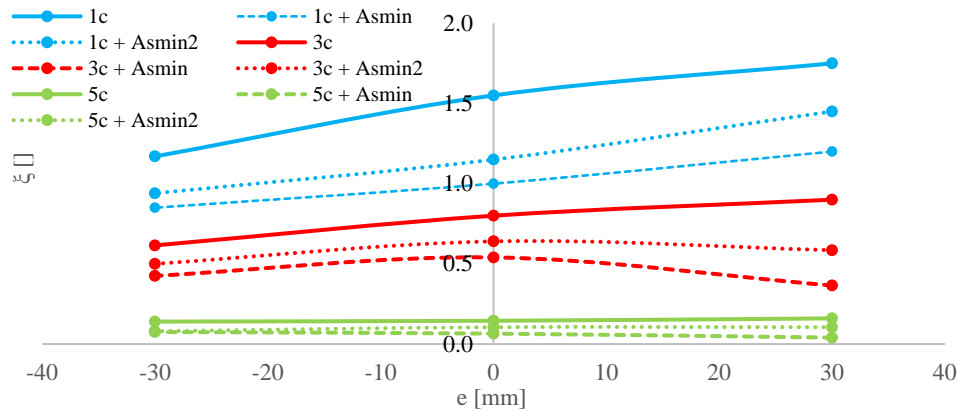

Figure 11 – $w_{spall,acc}$/0.2 versus eccentricity for accidental load (3950 kN)

6.   CONCLUSIONS

The effect of TBM thrust on precast segments was studied using a non-linear FE analysis and taking into account the residual strength of FRC and hybrid reinforcement. By using this model, spalling and splitting cracks for a range of thrust eccentricities are estimated and compared according to the different reinforcement configurations.

Based on the results presented in this research contribution, the following conclusions can be drawn:

-    The residual flexural strength for a crack width of 0.5 mm (f_{R1}) resulted to have a predominant influence in cracking control whilst the ratio f_{R3}/f_{R1} seems not play a significant role.

-    The spalling cracks appear to be those governing the FRC post-cracking tensile strength requirements. Eccentric thrust has a relevant influence on cracking performance; in this sense, attention must be paid for both cracking phenomena, specially, for splitting cracks for which cracks up to 6.0 times wider with respect to the centred thrust were measured.

-    Hybrid reinforcement leads to crack reduction and this can be considered as a suitable solution when severe crack width limitations are stablished. The combination of rebar and fibres has resulted to increase the efficiency in crack controlling when the FRC strength class decrease and viceversa.

Alejandro Nogales Arroyo

REFERENCES

[1] A. de la Fuente, A. Blanco, P. Pujadas, A. Aguado, Diseño óptimo de dovelas de hormigón reforzado con fibras para el revestimiento de túneles, Hormigón y Acero. 65 (2015) 267–279. https://doi.org/10.1016/j.hya.2014.11.002.

[2] M. di Prisco, G. Plizzari, L. Vandewalle, Fibre reinforced concrete : new design perspectives, Mater. Struct. (2009) 1261–1281. https://doi.org/10.1617/s11527-009-9529-4.

[3] R.G.A. de Waal, Steel fibres reinforced tunnel segments for the application in shield driven tunnel linings, Technische Universiteit Delft, 2000.

[4] R. Burgers, J. Walraven, G.A. Plizzari, G. Tiberti, Structural behaviour of SFRC tunnel segments during TBM operations, Undergr. Sp. - 4th Dimens. Metropolises. (2007) 1461–1468.

[5] R. Gettu, G. Ramos, A. Aguado, T. García, B. Barragán, Steel Fiber Reinforced Concrete for the Barcelona Metro Line 9 Tunnel Lining., BEFIB 2004, Proc 6th RILEM Symp. FRC. RILEM Symp (2004) 1–46.

[6] A. Caratelli, A. Meda, Z. Rinaldi, P. Romualdi, Structural behaviour of precast tunnel segments in fiber reinforced concrete, Tunn. Undergr. Sp. Technol. 26 (2011) 284–291. https://doi.org/10.1016/j.tust.2010.10.003.

[7] A. Caratelli, A. Meda, Z. Rinaldi, Design according to MC2010 of a fibre-reinforced concrete tunnel in Monte Lirio, Panama, Struct. Concr. 13 (2012) 166–173. https://doi.org/10.1002/suco.201100034.

[8] J. Beňo, M. Hilar, Steel fibre reinforced concrete for tunnel lining - Verification by extensive laboratory testing and numerical Modelling, Acta Polytech. 53 (2013) 329–337. https://doi.org/1049.

[9] M. Hilar, J. Vítek, P. Vítek, R. Pukl, Load testing and numerical modelling of SFRC segments, (2012).

[10] FIB Bulletin 83, Precast Tunnel Segments in Fibre-Reinforced Concrete, 2017.

[11] S. Cavalaro, C.B.. Blom, J. Walraven, A. Aguado, Structural analysis of contact deficiencies in segmented lining. Packer behaviour under simple and coupled stresses, Tunn. Undergr. Sp. Technol. 26 (2011) 734–749.

[12] M. Sugimoto, Causes of Shield Segment Damages During Construction, Int. Symp. Undergr. Excav. Tunn. (2006) 67–74.

[13] L. Liao, A. de la Fuente, S. Cavalaro, A. Aguado, Design of FRC tunnel segments considering the ductility requirements of the fib Model Code 2010: Application to the Barcelona Metro line 9, Tunn. Undergr. Sp. Technol. 47 (2015) 200–210.

[14] F. Leonhardt, E. Mönnig, Berlin: Springer-Verlag; 1973 (Italian version:1986) Casi speciali di dimensionamento nlle costruzioni in c.a. e c.a.pConcr. Struct. (1973) 66–66. https://doi.org/10.1201/9781439828410.ch37.

[15] K. Iyengar, Two-dimensional theories in anchorage zone stresses in Post- Tensioned prestressed beams., Heron. 32 (1962) 45–56.

[16] FIB, fib Model Code for Concrete Structures 2010, Lausanne: International Federation for Structural Concrete (fib), 2013. https://doi.org/10.1002/9783433604090.

[17] EHE-08, Instrucción de Hormigón Estructrural (EHE-08), (2008).

[18] RILEM TC 162-TDF, Test and design methods for steel fibre reinforced concrete. Design with σ-ε method, Mater. Struct. 35 (2003) 262–278. https://doi.org/10.1617/13837.

[19] ACI 544, Fibre-Reinforced Concrete: Design and Construction of Steel Fibre- Reinforced Precast Concrete Tunnel Segments., (2014).

[20] ACI 544.7R-16, Report on Design and Construction of Fiber-Reinforced Precast Concrete Tunnel Segments, ACI Comm. Rep. (2016) 1–36.

[21] C. Dassault systems Simulia, Abaqus Analysis user's manual 6.12-3, (2012) 1137.

[22] B. Schnütgen, E. Erdem, Sub-task 4.4 - Splitting of SFRC induced by local forces - Annex A, (2001).

[23] NBN-B-15-238:1992, Testing of fiber reinforced concrete. Bending test on prismatic specimens . Belgian Code - In French., (1992).

[24] A. Conforti, G. Tiberti, G. Plizzari, A. Caratelli, A. Meda, Precast tunnel segments reinforced by macro-synthetic fibers, Tunn. Undergr. Sp. Technol. 63 (2016) 1–11. https://doi.org/10.1016/j.tust.2016.12.005.

3.2. RESEARCH CONTRIBUTION II: ELEVATED FLAT SLAB OF FIBRE REINFORCED CONCRETE NON-LINEAR SIMULATION UP TO FAILURE

Alejandro Nogales[a,b,*] and Albert de la Fuente[b]

[a]Smart Engineering Ltd., UPC Spin-Off, Jordi Girona 1-3, 08034 Barcelona, Spain

[b]Civil and Environmental Engineering Deparment, Universitat Politècnica de Catalunya (UPC), Jordi Girona 1-3, 08034 Barcelona, Spain

*Corresponding author

ABSTRACT

The growing use of fibre reinforced concrete (FRC) on structural concrete has made that several codes and guidelines have included models for design in which the traditional reinforcement has been substituted partially or totally. Among the industrial applications, fibres as reinforcement of elevated flat slabs is gaining interest due the post-break bearing capacity of the material. This technology has already been used for real scale structures. This research contribution is focused on a parametrical analysis of FRC elevated flat slab by means of non-linear finite element simulation. The model is calibrated and compared with the real scale experimental test and with experimental slabs tested up to failure that can be found in the literature. The main goal of this paper is to carry out a parametrical analysis of the slab combining different types of reinforcement: FRC and hybrid reinforcement (fibres+conventional reinforcement) under design loads eventually choosing an amount of fibres for an actual test The results demonstrated that the combination of fibres and rebar improves the structure against failure, reduces deformation and presents a crack pattern better for cracking control.

KEYWORDS: Fibre reinforced concrete, non-linear analysis, elevated flat slabs, hybrid reinforcement.

1. INTRODUCTION

Over the last decades, the use of fibres for structural concrete reinforcement has noticeable grown. The growing use of FRC has made that several codes and guidelines such as DBV [1], RILEM [2], CNR-DT [3], EHE-08 [4], *fib* Model Code (*fib* MC-2010) [5] and ACI 544 [6] have included models for designing structural elements in which the traditional rebar reinforcement

has been partially or totally substituted. In this regard, *fib* MC-2010 has introduced FRC classes in order to classify the post cracking strengths of FRC. The codes are based on state limit methods and gather constitutive equations able to reproduce the post-break response of FRC valid for sectional analysis. The publication of design codes for FRC has boosted the use of this technique in building industry. In this sense, FRC is used for elevated slabs supported on piles or foundations [7,8], where failure and cracking behaviour has often been a troublesome concern for designers. These structures are likely to be under flexural and bending loading scenarios and allow exploiting the post-cracking tensile capacity and strength of FRC, bearing part of the total tensile forces, leading to a conventional reinforcement reduction. Apart from the technical point of view, buildings cast with FRC take profit from time and costs saving during the building process: fibres are added directly at the concrete plant and time needs reduces significantly compared to conventional reinforcement concrete where handing and placing of steel rebar operations are required. Besides, from sustainability point of view, indirect costs, social aspects and environmental issues are factors to take into account and therefore FRC is an attractive solution [9].

Nonetheless, despite of the existence of design codes and guidelines together with the experimental and numerical evidences that prove the suitability of using FRC in pile supported flat slabs, there is still controversy and barriers to its implementation [9]. FRC results are commonly compared with hybrid reinforced concrete or reinforced concrete (RC) and a lack of research is found when comparing between FRC classes. The reported experiences highlight the need of intensifying the research on: (1) the influence of the FRC strength class (flexural residual strength) on ultimate limit state (ULS), even with the combination of traditional reinforcement (hybrid reinforcement) and (2) the safety factors to be used for the design.

In view of this, the aim of this research contribution is focused on a parametrical analysis of an elevated flat slab by means of a non-linear finite element (FE) model capable of reproducing the post-cracking response of FRC and develop the stress redistribution mechanisms that are produced in the structures hyperstatically supported. The model was validated with actual elevated slabs tested up to failure found in the literature and the results are compared with the experimental test. The main goal of this paper is to carry out a parametric analysis of an elevated FRC slab considering design loads and different FRC classes. The analysis was also done from a safety point of view, taking into account the nominal resistance of the structure and the global safety factors.

2. NUMERICAL MODELLING OF FRC

According to *fib* MC-2010 FRC classes can be classified by its residual strength characteristic values ($f_{Ri,k}$ (i=1 to 4)) obtained form 3 point bending test notched beams according to EN

14651:2005. Two parameters are used for classifying: f_{R1k}, which represents the residual strength for a crack opening displacement (CMOD) of 0.5 mm and a letter (a, b, c, d or e) that represents the f_{R3k}/f_{R1k} ratio, where f_{R3k} stands for a CMOD of 2.5 mm. In order to stablish the stress-strain (σ-ε) or stress-crack width (σ-w) constitutive relations, the equations proposed by *fib* MC-2010 are adopted, using the variables' mean values for the simulations. The compressive behaviour has been characterised according to the expression proposed by *fib* MC-2010. The implementation of these equations have been done using the software ABAQUS [10] and the "Concrete Damage Plasticity" (CDP) model available. In this regard, the σ-w tensile and σ-ε compression curves proposed by the *fib* MC-2010 are used for the analysis, the characteristic length (L_{ch}), to turn crack opening into strain, implemented by default by the software is the size of the element.

The CDP parameters adopted in this analysis are the default ones proposed in ABAQUS User's Manual [10] for plain concrete and are reported in Table 1, where f_{b0}/f_{c0} and K represent the ratio of biaxial compressive strength to uniaxial compressive strength and the yield surface shape parameter, respectively. The analysis was performed using the ABAQUS explicit dynamic algorithm (quasi-static analysis) whose integration method is known as Forward Euler.

Table 1 – CDP parameters used for the analysis.

Dilation angle	Eccentricity	f_{b0}/f_{c0}	K	Viscosity
30	0.1	1.16	0.667	1e–5

3.   EXPERIMENTAL MODEL VALIDATION

A point load experimental test on a suspended elevated slab carried out by Gossla [11] is used for the model validation, this experimental test has previously been used for model validation by Facconi [12]. The slab composed by nine (9) 6.0 x 6.0 m^2 span, 0.2 m height resting on a grid of 16 0.3 x 0.3 m^2 square columns was tested applying a punctual load at the centre of the slab (Figure 1a). The fibre dosage was 100 kg/m^3 of an undulated commercial steel fibre (1.3 mm in diameter and 50 mm in length). In the actual test, anti-progressive collapse reinforcement was placed to guarantee safety during the test, this reinforcement has no contribution in the structural performance and therefore is not modelled. The average compressive concrete strength (f_{cm}) was 43.7 N/mm^2 and the post-cracking response properties used were obtained by means of an inverse analysis and reported by Soranakom et al. [13] (σ_1=2.5, σ_2=1.75, σ_3=1.06, σ_4=0 MPa and w_1=0, w_2=0.25, w_3=1.25, w_4=2 mm).

A non-linear 3D model was created (Figure 1b) to simulate both the geometry and loading conditions presented in Figure 1a. For the sake of simplicity due to the double-plane symmetry, in both geometry and loading conditions, only a quarter of the slab was modelled. In order to provide symmetry to the model no displacement nor rotations were allowed in both symmetry

planes (see Figure 1b); the columns were modelled as simple supports where vertical displacement is restricted ($U_y=0$), detailed in Figure 1c. The load was applied on a circular steel plate of 20 mm of diameter (Figure 1d) by means of displacement control in order to guarantee a proper convergence. The mesh consists of 8-noded solid linear hexahedral elements (C3D8R) used for modelling concrete, this leading to an amount of 44720 elements.
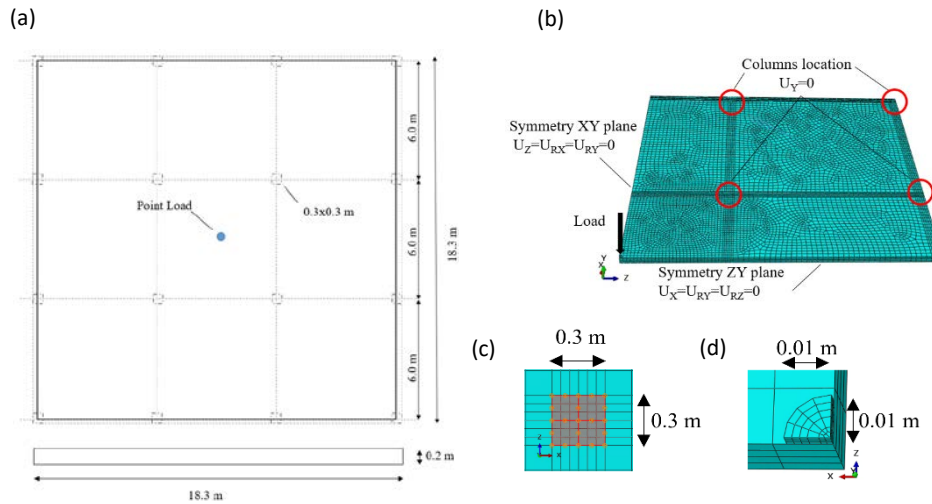

Figure 1 – Elevated slab test (a) Test set up (b) FE model (c) Columns detail (d) Loading plate.

Figure 2 presents the numerical and experimental load-deflection relationship. It can be noticed that the model presents a post-cracking response similar to that experimental in terms of load and deflection (with a maximum deviation of 40 kN). At first stages the stiffness are similar for both tests (up to 150 kN) then a ductile response is observed up to failure. The experimental cracking load ($P_{cr,exp}$) in the mid span bottom layer was 200 kN, whereas the numerical cracking load ($P_{cr,num}$) was 185 kN (-7.5%), from the safe side. The failure mode of the numerical model is unclear since the model is not able to reproduce the unloading curve; contrarily the load-deflection curve stabilizes and a constant load is found, even when the stress of the most demanded area (at the bottom face under where the point load is applied) has reached zero value. In this sense, as failure criteria the load level at which this area reach 0.02 strain (ultimate strain ε_{Fu}, according to *fib* MC-2010) is considered as the failure load, 466 kN (see Figure 2), <1% of difference with respect to the experimental test.
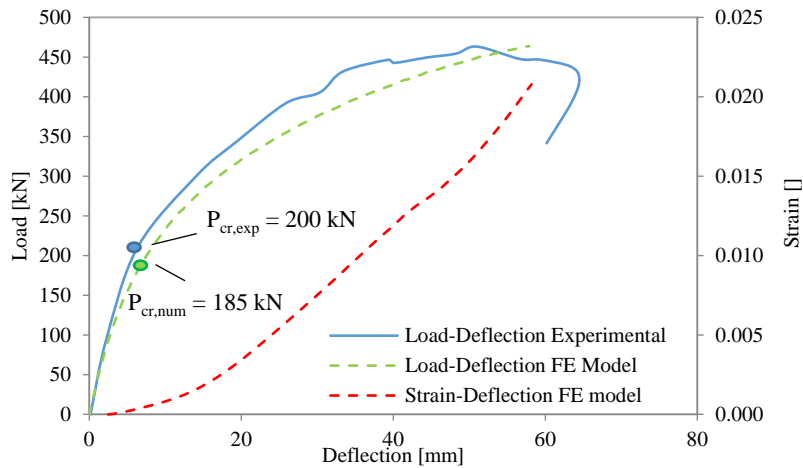
Figure 2 – Experimental and numerical load-displacement curves and strain-displacement.

The model does not provide the crack width directly, in this sense, the plastic strain (where tensile stresses have exceed tensile strength) is used instead to compare the crack pattern. The crack patterns measured after the test (up to failure) and those obtained numerically are included in Figure 3. The first cracks appeared on top centre columns and progressively grew towards the near columns (see Figure 3a). The second crack appeared on the bottom layer caused by postive bending moments and bifurqued into two directions paralel to the slab edges, plotted in Figure 3b.
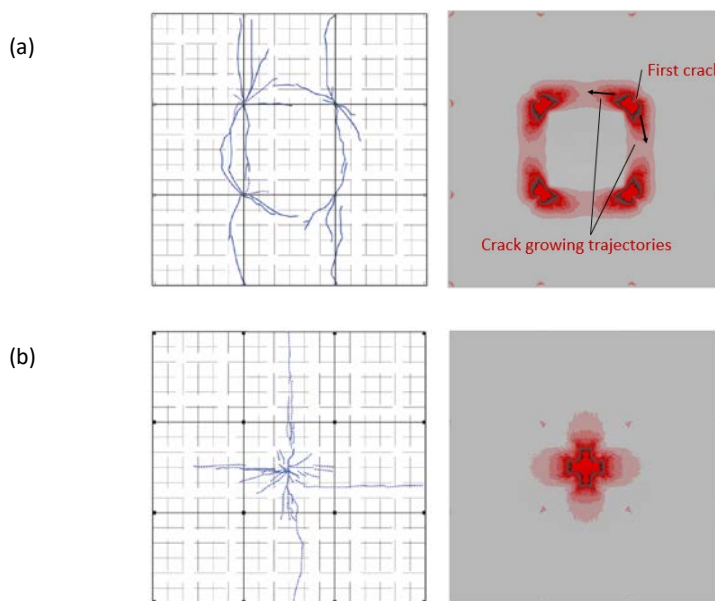

Figure 3 – Crack pattern at maximum load for experimental and numerical test. (a) Top layer and (b) bottom layer.

Therefore, according to the results presented in Figure 2 and Figure 3, it can be remarked that the model can reproduce properly the mechanical response of FRC elevated slabs subjected to point loads that generate flexural stresses and capture the ductile mechanism up to failure.

Alejandro Nogales Arroyo

4. CASE STUDY

An extensive experimental program on the characterization of self-compacting FRC composites and full-scale pile supported flat slabs was planned. A parametrical analysis was carried out to determine the fibre content which guaranteed the structural response higher than the design load (F_d). According to the Spanish code CTE [14], the flat slab was designed to resist, besides the self-weight (SW) of 4.8 kN/m^2, a Dead Load (DL) of 2.0 kN/m^2 and a live load (LL) of 3.0 kN/m^2 this leading to a F_d of 14 kN/m^2 taking into account partial safety factors from *fib* MC-2010. Besides using different FRC contents, three simulations combining FRC with conventional reinforcement (hybrid reinforcement) were done.

4.1. MODEL DESCRIPTION

The geometry of the elevated flat-slab consists in a rectangular slab of 12.00 m x 10.00 m in size and 0.2 m in thickness supported by a grid of 9 square columns (0.25 m), forming 4 bays 6.00 x 5.00 m meters each. The supporting columns were 3.00 m high. A quarter of the slab was modelled, due to symmetry, constraining displacements and rotations at the symmetry planes (see Figure 4a). The columns are modelled as simple supports where the vertical displacement is restricted (U_y=0) at the slab-column contact surface. The mesh is composed by 18000 elements and the concrete was modelled using C3D8R hexahedral solid elements.
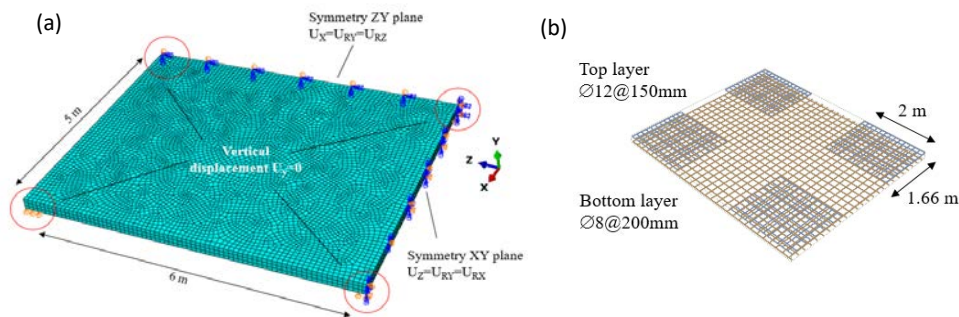

Figure 4 – Study case slab (a) geometry and boundary conditions (b) rebar configuration

Figure 5 depicts three types of FRC commonly used for these structural elements and used for the simulations: FRC class 4c (FRC4), FRC class 6c (FRC6) and FRC class 8c (FRC8) and the constitutive curves using mean values properties (FRC4$_m$, FRC6$_m$ and FRC8$_m$). f_{Fts} and f_{Ftu} stand for serviceability and ultimate residual strength respectively. A commonly used f_{R3m}/f_{R1m} ratio for structural application equal to 1 has been chosen since it has a flat Load-CMOD behaviour after cracking. f_{ctm}=4.07 N/mm^2, f_{cm}=58 N/mm^2 and E_{cm}=32900 N/mm^2 were assumed as concrete mechanical properties for all simulations.

Furthermore, a combination of fibres and steel rebar (hybrid reinforcement) was studied as the slab reinforcement configuration. The three FRC strength classes are combined with a rebar mesh of Ø8 every 200 mm, in both directions, at the bottom layer and Ø12 every 150 mm, in both

directions, on the top layer covering a surface equal to a third part of the bay length. A clear cover of 25 mm is considered. The rebar configuration is presented in Figure 4b. The nomenclature for hybrid solutions from now on is HYB followed by the fibre reinforced concrete strength (4, 6 or 8). A common value of steel yielding stress (f_y) equal to 600 MPa is adopted for the analysis. 2-noded 3D linear truss elements T3D2 are chosen for the rebar, embedded constraint is used for join linear and solid elements which leads to a perfect bond between concrete and steel. It must be highlighted that the reinforcement ratio adopted is considered for a hybrid solution (combining rebar and fibres) and not to withstand the design loads only with the rebar.
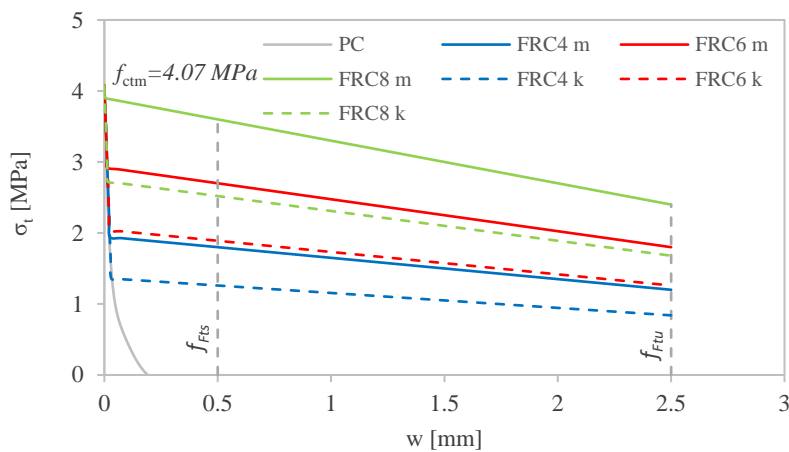

Figure 5 – Tensile constitutive equations of the concrete mixes used for the parametric analysis.

4.2. RESULTS

After being applied the self-weight (4.8 kN/m²) the slabs were tested up to failure. Figure 6 shows the load-deflection (δ) curve for all reinforcement configurations. In this sense, in order to evaluate the failure load of FRC and hybrid solutions for ULS, two failure criteria have been considered: (1) FRC reaching ε_{Fu} (20‰ of strain) and (2) rebar longitudinal strain (ε_s) equal to 10‰ (in hybrid solutions). In view of this, PC and RC configurations reached the lowest ultimate loads (q_u). These q_u, not including the self-weight, were 10.1 (FRC4), 14.0 (FRC6) and 18.0 (FRC8) kN/m² for FRC solutions and 14.9 (HYB4), 18.6 (HYB6) and 23.2 (HYB8) kN/m² for hybrid reinforcement. Figure 7 shows q_u versus the FRC residual strength ($f_{R1m}=f_{R3m}$). The results show that adopting a hybrid solution improves the slab strength against failure when compared to FRC and the efficiency decreases when FRC classes are adopted: 47%, 32% and 28 % of improvement for 4, 6 and 8 MPa hybrid solutions.

As Figure 6 shows, the maximum deflection (δ_{max}) for each simulations is reached at different load levels. In order to compare the deformations between different cases, the ductility index ξ is proposed. ξ is set as $\delta_{max}/\delta_{fr1m=fr3m=4}$, where $\delta_{fr1m=fr3m=4}$ stands for the maximum deflection reached by the configuration with less amount of fibres of each type of reinforcement (FRC4 and HYB4).

Figure 8 presents ξ – residual strength curve. The results showed that FRC solutions presented higher ductility as post-cracking strengths increased. In contrast, for hybrid reinforcement configurations, increasing the FRC residual strength turned into improving the structure against deflection and presented lower values of ξ, reaching less δ_{max} and increasing stiffness.
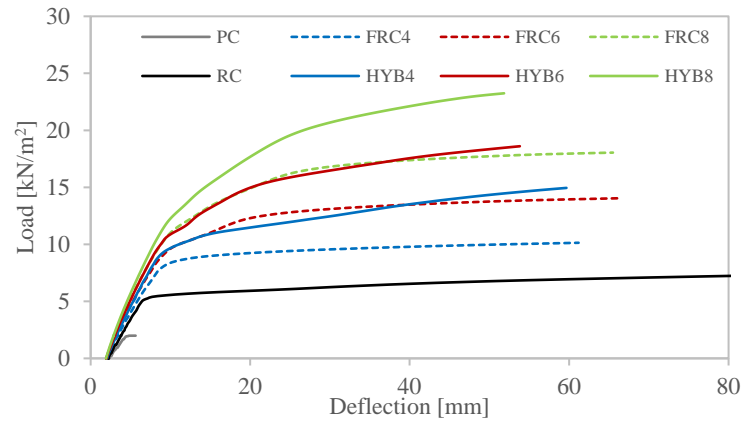

Figure 6 – Simulation results (a) Load – deflection (b) ultimate load – residual strength.
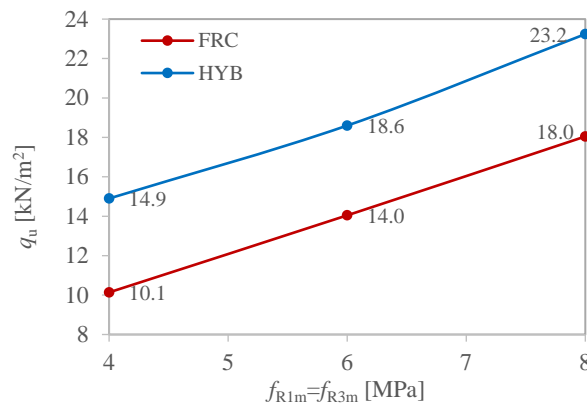
Figure 7 – Simulation results ultimate load – residual strength.
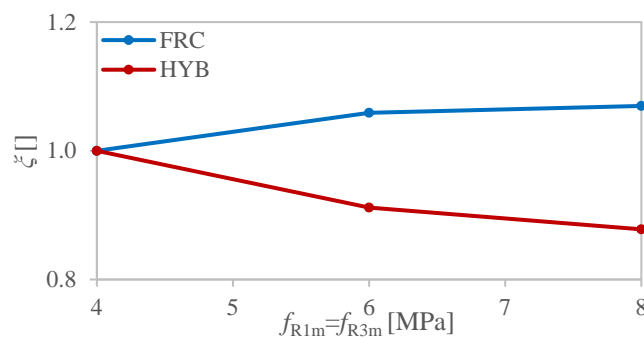

Figure 8 – Ductility index (ξ) – residual strength for FRC and hybrid solutions.

The crack pattern at the bottom layer at failure is shown in Figure 9a for FRC and in Figure 9b for hybrid solution, in this case FRC4 and HYB4 respectively. Due to positive bending moments, two crack crossed the bays perpendicular to the larger side of the slab. It is worth

noticing that in case of FRC the cracks were concentrated in the centred region where the damage is found, in contrast in hybrid solution the crack pattern showed a distributed shape, being this pattern more favourable in order to control the cracks and reduce the crack width.
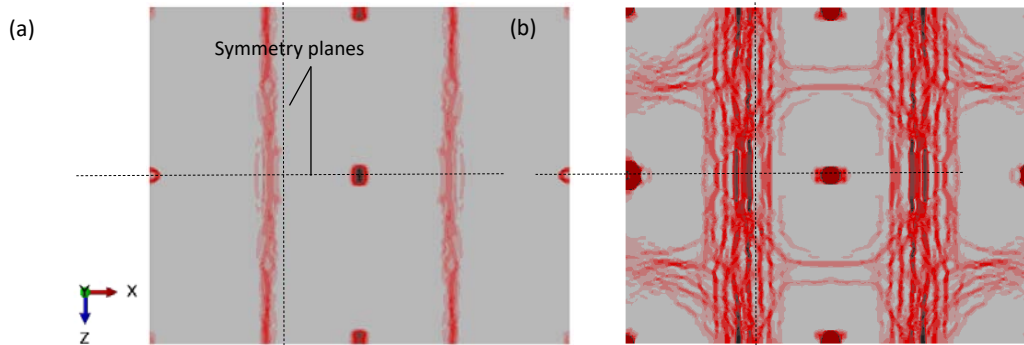

Figure 9 – Crack pattern at the bottom layer at failure for (a) FRC4 and (b) HYB4

4.3. STRUCTURAL SAFETY

Aiming to determine the FRC residual strength that would be used for the flat-slab experimental test [15], the structural safety analysis for the FRC solutions is presented in this section. In this sense, the Eurocode 2 [16] proposes a method to aid the assessment of the structural capacity by means of non-linear methods, the main challenge being the definition of the partial safety factor to be applied to both resistance and loading, since the partial safety factor gathered in the codes and guidelines are based on linear elastic methods. In order to fulfil this aspect, *fib* MC-2010 gathers a method that permits to obtain a resistance global safety factor for the whole structure by considering the variability of the mechanical and geometrical properties. The result of this reliability-based model is the safety coefficient to derive the design value of the structural bearing capacity, R_d (Eq. (1)); where R_m stands for the mean value of the structural bearing capacity (considering mean values for mechanical and geometrical properties) and γ_R is the global safety factor. The γ_R coefficient can be calculated as per Eurocode 2 (Eq. (2)), where V_R is the resistance coefficient of variation and α_R and β stands for the resistance sensitivity factor and reliability index respectively, taken as α_R=0.8 and β=3.8.

$$R_d = \frac{R_m}{\gamma_R} \tag{1}$$

$$\gamma_R = e^{(\alpha_R \cdot \beta \cdot V_R)} \tag{2}$$

The ECOV method proposed by Cervenka [17] allows estimating V_R by means of a logarithmic ratio between R_m and R_k, the latest being the characteristic resistance value obtained by implementing the non-linear solution with characteristic magnitudes of both mechanical and geometrical properties.

$$V_R = \frac{1}{1,65} \ln\left(\frac{R_m}{R_k}\right) \tag{3}$$

For this purpose, three additional FE simulations have been carried out using characteristic values of each of the involved mechanical variables. The σ-w curves for these simulations are plotted in Figure 5, the f_{Rk}/f_{Rm} ratio equal to 0.7 (CoV = 18.3% assuming a normal distribution) suggested by the *fib* MC-2010 is adopted. Regarding this aspect, the greater the f_{Rm} is, the lower the variability of f_{Rm} is expected (the amount of fibres is higher and the intrinsic scatter tends to be reduced [18]) and, thus, this relation f_{Rk}/f_{Rm} could be > 0.7 (CoV $< 18.3\%$). Table 1 gathers the ultimate loads obtained considering mean ($q_{u,m}$) and characteristic ($q_{u,k}$) resistance values as well as V_R, γ_R y R_d. R_m and R_k values are obtained by adding the self-weight (4.8 kN/m²) to $q_{u,m}$ and $q_{u,k}$ respectively.

Table 1. Mean, characteristic and design structural resistance, variation and global safety factor.

	$q_{u,m}$ [kN/m²]	R_m [kN/m²]	$q_{u,k}$ [kN/m²]	R_k [kN/m²]	V_R	γ_R	R_d
FRC4	10.1	14.9	7.3	12.1	0.12	**1.46**	**10.2**
FRC6	14.0	18.8	10.5	15.3	0.12	**1.47**	**12.8**
FRC8	18.0	22.8	13.1	17.9	0.14	**1.56**	**14.6**

The global safety factors gathered in Table 1 resulted to be 1.46 for FRC4, 1.47 for FRC6 and 1.56 for FRC8 (f_{Rm}=4, 6 and 8 MPa respectively). In this case study, the flat slab F_d was 14.0 kN/m², the *ultimate* limit state design condition ($R_d \geq F_d$) is therefore fulfilled for FRC solution of f_{Rm}=8 MPa. It must be remarked that, according to the abovementioned comment about the CoV of f_R, γ_R should decrease as f_R increases; hence, the γ_R obtained could be on the safe side for the higher values of f_R.

The FRC slab of the experimental test was cast with FRC of f_{R1m}=8 and f_{R3m}=7.5 N/mm² and was loaded up to 15 kN/m² without reaching structural collapse. The FRC8 (f_{R1m}= f_{R3m}=8 N/mm²) provided 14.6 kN/m² for R_d in the numerical simulation, this meaning that the model results using the global safety factors presented in this research contribution are in good agreement with the experimental test, even with a reasonable margin of safety.

5. CONCLUSIONS

Simulations of a FRC pile-supported flat slab were carried out by means of a non-linear FE model. Several FRC strengths classes were considered in order to quantify the effect of those on

the mechanical response and the structural safety of associated to each FRC strength class, the combination of rebars and fibres was also considered.

Based on the results presented in this research contribution, the following conclusions can be drawn:

- The results of the validation and the experimental real scale test allow confirming that the model is adequate to perform the analysis of this type of structures.

- The hybridization of structural fibres and rebars led to more efficient solutions in terms of bearing capacity. In this sense, the structural efficiency is more noticeable when low FRC strength classes are considered. Likewise, increasing the FRC strength resulted in an improvement of the deformation capacity at ultimate limit state (for the maximum load) while the hybrid solutions, although showing a remarkable ductility, a slight embrittlement respect to the FRC alternatives.

- Hybrid configurations presented a more distributed crack pattern favourable for cracking control and crack width reduction.

- The numerical model together with the safety format presented within the *fib* Model Code for non-linear analysis allowed safely design the real-scale slab constructed (see[15]). It must be highlighted that even the experimental results confirmed a reasonable safety margin respect the numerical results.

- These are preliminary conclusions of a research which is being currently carried out within the context of the PhD thesis of the first author.

ACKNOWLEDGMENTS

REFERENCES

[1] DBV, Guide to Good Practice: Steel Fibre Concrete, Ger. Soc. Concr. Constr. Technol. (DBV), Berlin, Ger. (2001).

[2]   RILEM TC 162-TDF, Test and design methods for steel fibre reinforced concrete. Design with σ-ε method, Mater. Struct. 35 (2003) 262–278. https://doi.org/10.1617/13837.

[3]   CNR-DT 204/2006, Guide for the Design and Construction of Fibre-Reinforced Concrete Structures, Ital. Natl. Res. Counc. (CNR), Rome, Italy. 75 (2007). https://doi.org/10.14359/10516.

[4]   EHE-08, Instrucción de Hormigón Estructrural (EHE-08), (2008).

[5]   FIB, fib Model Code for Concrete Structures 2010, Lausanne: International Federation for Structural Concrete (fib), 2013. https://doi.org/10.1002/9783433604090.

[6]   ACI 544, Fibre-Reinforced Concrete: Design and Construction of Steel Fibre- Reinforced Precast Concrete Tunnel Segments., (2014).

[7]   X. Destrée, J. Mandl, Steel fibre only reinforced concrete in free suspended elevated slabs: Case studies, design assisted by testing route, comparison to the latest SFRC standard documents, Tailor Made Concr. Struct. (2008) 437–443. https://doi.org/10.1016/j.jhydrol.2010.04.024.

[8]   M. di Prisco, P. Martinelli, B. Parmentier, On the reliability of the design approach for FRC structures according to fib Model Code 2010: the case of elevated slabs, Struct. Concr. 17 (2016) 588–602. https://doi.org/10.1002/suco.201500151.

[9]   A. de la Fuente, M.D.M. Casanovas-Rubio, O. Pons, J. Armengou, Sustainability of Column-Supported RC Slabs: Fiber Reinforcement as an Alternative, J. Constr. Eng. Manag. 145 (2019) 1–12. https://doi.org/10.1061/(ASCE)CO.1943-7862.0001667.

[10] C. Dassault systems Simulia, Abaqus Analysis user's manual 6.12-3, (2012) 1137. http://www.maths.cam.ac.uk/computing/software/abaqus_docs/docs/v6.12/pdf_books/BEN CHMARKS.pdf.

[11] U. Gossla, Development of SFRC Free Suspended Elevated Flat Slabs, research report for Arcelor Mittal, (2005).

[12] L. Facconi, G. Plizzari, F. Minelli, Elevated slabs made of hybrid reinforced concrete: Proposal of a new design approach in flexure, Struct. Concr. (2018) 1–16. https://doi.org/10.1002/suco.201700278.

[13] C. Soranakom, B. Mobasher, X. Destree, Numerical simulation of FRC round panel tests and full-scale elevated slabs, ACI Spec. Publ. 248 (2007) 31–40. http://www.concrete.org/Publications/GetArticle.aspx?m=icap&pubID=19008.

[14] Gobierno de España, DB SE- AE Seguridad Estructural, Acciones en la Edificación., Boletín Of. Del Estado. (2009) 1–42.

[15] S. Aidarov, F. Mena, A. de la Fuente, Self-compacting steel fibre reinforced concrete: material characterization and real scale test up to failure of a pile supported flat slab, BEFIB 2020. (2020).

[16] DIN EN 1992-1-1:2011-01, Eurocode 2, 2014. https://doi.org/10.2788/35386.

[17] V. Cervenka, Global safety formats in fib Model Code 2010 for design of concrete structures, 11th Int. Probabilistic Work. (2013) 31–40.

[18] S.H.P. Cavalaro, A. Aguado, Intrinsic scatter of FRC: an alternative philosophy to estimate characteristic values, Mater. Struct. Constr. 48 (2015) 3537–3555. https://doi.org/10.1617/s11527-014-0420-6.

3.3. RESEARCH CONTRIBUTION III: CHARACTERIZATION OF MACRO SYNTHETIC FIBRE REINFORCED CONCRETE CONSTITUTIVE EQUATION

Alejandro Nogales[a,b,*], Eduardo Galeote[a,b] and Albert de la Fuente[b]

[a]Smart Engineering Ltd., UPC Spin-Off, Jordi Girona 1-3, 08034 Barcelona, Spain

[b]Civil and Environmental Engineering Deparment, Universitat Politècnica de Catalunya (UPC), Jordi Girona 1-3, 08034 Barcelona, Spain

*Corresponding author

ABSTRACT

Over the last years, the use of fibre reinforced concrete (FRC) has increased for structural purposes. For the structural design of FRC elements, there was a need of a model that developed the behaviour of the post-cracking response of FRC. In this sense, national and international guidelines have included models to characterise the flexural behaviour of FRC (fib Model Code, EHE-08). These models gather the performance of FRC for serviceability limit state (SLS) and ultimate limit state (ULS) for either steel or macro synthetic polypropylene fibre reinforced concrete (SFRC and MSFRC, respectively). In this regard, the codes and guidelines do not distinguish between FRC comprised of steel or synthetic fibres and establish the FRC ultimate strain in 2.5%. This limitation represents the behaviour of SFRC but limits the full potential of MSFRC for large deformations. Owing to the aspects aforementioned, an extensive experimental programme has been carried out at the Universitat Politècnica de Catalunya (UPC) to characterise the behaviour of MSFRC. This research contribution is focused on an inverse analysis to derive the MSFRC constitutive equations by means of a non-linear finite element simulation. The main goal of this study is to compare the experimental results with those obtained through the simulation using the constitutive equations of the fib MC-2010. The results show a generalised underestimation of MSFRC at ultimate strain and the necessity of adjusting the constitutive equations for SFRC and MSFRC.

KEYWORDS: macro synthetic fibre reinforced concrete, non-linear analysis, constitutive equation.

1. INTRODUCTION

The addition of fibres into concrete, commonly known as fibre reinforced concrete (FRC), for structural purposes has experienced a huge growth in recent years. Fibres are either used for totally or partially replacing the traditional rebar reinforcement. In the FRC industry, there are different types of fibres such as organic, metallic or synthetic (i.e. glass fibre, steel fibres, polypropylene fibres, respectively) that are used to cover a wide range of structural typologies: industrial flooring [1,2], precast concrete segments for tunnel linings [3], elevated flat slabs [4,5], sewer pipes [6,7].

Due to the increasing use of this material, codes and guidelines [8–10] have been published as a demand for a reliable design tool for engineers and practitioners. These codes and guidelines developed material models that are able to reproduce the behaviour of FRC. The models consist of constitutive equations, in terms of uniaxial stress-strain (σ-ε) curves (or stress-crack width), that take into account the post-cracking residual strength of FRC given by the pull-out mechanism effect induced by fibres.

In the case of *fib* Model Code – 2010 (MC-2010) [8], the post-cracking strength of the material is obtained by carrying out the beam flexural strength test (EN:14651 [11]) from which the residual strength for crack mouth opening displacement (CMOD) 0.5 and 2.5 mm are extracted (f_{R1} and f_{R3}, respectively). This results in a bilinear post-cracking constitutive equation where the two main points are f_{Fts} and f_{Ftu}, which correspond to serviceability and ultimate residual strength, being the ultimate crack width (w_u) equal to 2.5. Figure 1 depicts the schematic representation of the stress-crack width curve for FRC according to MC-2010, the full curve is obtained as the combination of the post-cracking response of plain concrete (where f_{ctm} and G_F stand for mean tensile concrete strength and fracture energy, respectively) and the fibre contribution through the pull-out mechanism. Being the first point $\sigma_1 = f_{ctm}$ and $w_1 = 0$ mm, the second point σ_2 and w_2 (the intersection between the two curves) and the third one $\sigma_3 = f_{ctm}$ and $w_3 = 2.5$ mm.
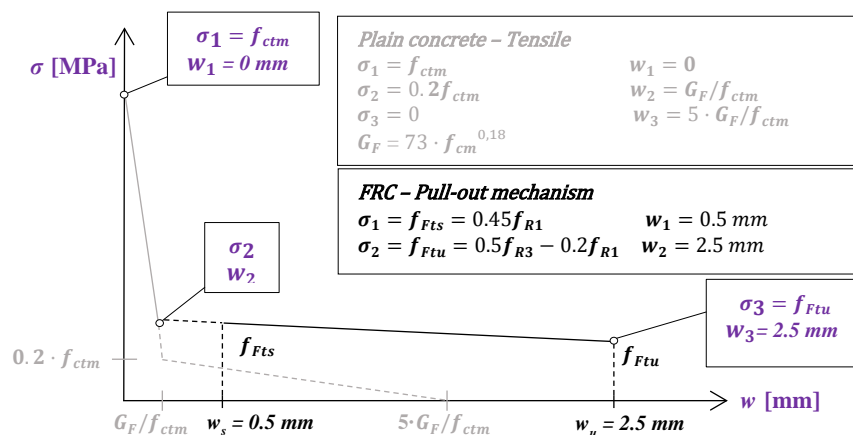

Fig.1 – MC-2010 FRC post-cracking curve

Alejandro Nogales Arroyo

However, the aforementioned guidelines do not distinguish between different types of fibres and w_u considered in terms of ductility or durability may not be adjusted for all type of fibres. This is especially important in beam flexural strength test of macro synthetic polypropylene fibre reinforced concrete (MSFRC) where, after the sudden drop due to cracking, a hardening response is observed up to failure and the peak of the residual strength is reached beyond 2.5 mm (w_u).

In view of this, in order to assess the behaviour of MSFRC, a wide experimental programme considering a broad range of compressive concrete strength along with a representative fibre dosage used for actual applications was performed at the Universitat Politècnica de Catalunya. The concrete mixes tested in this experimental research had strength classes of C30/37 (with fibre amount of 2.5, 3.5 and 5.0 kg/m^3), C40/50 (with 5.0, 7.5 and 10.0 kg/m^3) and C50/60 (with 5.0, 7.5 and 10 kg/m^3).

The results of this experimental research were used for deriving the constitutive equations (MC-2010) and were compared with the ones obtained performing back analysis (BA) by means of a FE software. The aim of this conference proceeding is twofold: (1) compare the equations derived using the MC-2010 equations with the ones obtained by the inverse analysis and (2) propose changes in the equation in order to take into account the full potential of the MSFRC concrete. The outcome of this research work proved that the current MC-2010 constitutive equation do not take into account the full potential of MSFRC.

2. EXPERIMENTAL RESULTS

In the experimental campaign, residual flexural strength and compressive tests were carried out. The mechanical and geometrical properties of macro synthetic fibres made of polypropylene (PPMSF) for structural purposes used are gathered in Table 1. In order to have sufficient representativeness of the MSFRC behaviour, nine beam tests were carried out per each concrete mix (a total amount of 81). The average curves of the beam flexural strength test of each concrete mix are depicted in Figure 2. In some cases the tests were carried out beyond the standard CMOD for research purposes, to see any possible fibre failure. As can be seen from Figure 2, the maximum post-cracking strength registered is beyond 2.5 mm for every individual mix, which is w_u for the constitutive equation of the MC-2010. These values are gathered in Table 2.

Table 1 – Characteristics of PPMSF fibre

Material	Anchorage	Length	Young's Modulus	Tensile strength	Number fibres/kg
Virgin Polypropylene	Continuous Embossing	48 mm	12 GPa	640 MPa	59500

Table 2 – CMOD at maximum post-cracking strength

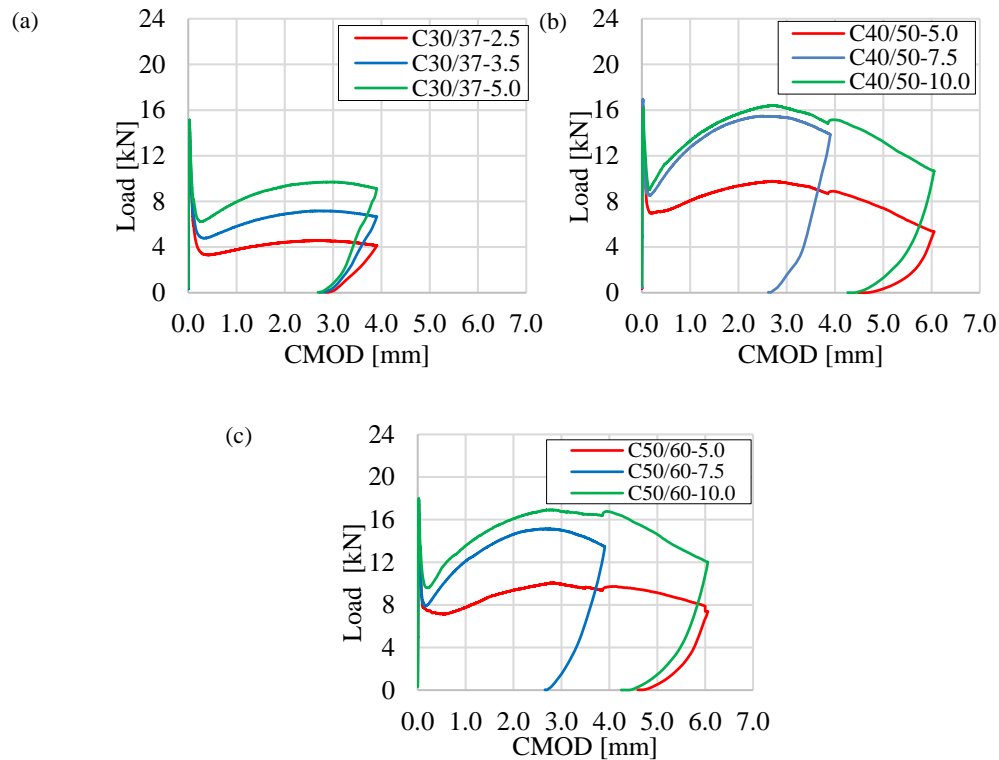|	C30/37	C40/50	C50/60
2.5 kg/m³	2.76 mm	-	-
3.5 kg/m³	2.69 mm	-	-
5.0 kg/m³	2.91 mm	2.70 mm	2.80 mm
7.5 kg/m³		2.51 mm	2.69 mm
10.0 kg/m³	-	2.71 mm	2.68 mm

Fig. 2 – Average curves of beam flexural strength test for (a) C30/37 (b) C40/50 and (c) C50/60.

In view of these results, it is highly unlikely that the σ–w constitutive curve is able to capture properly the late post-cracking behaviour of the MSFRC. In the following sections, a FE model is presented to carry out a back analysis (BA) and derive the constitutive curve suitable to reproduce the behaviour of MSFRC.

3.   FE ANALYSIS

In order to perform the BA, a non-linear 2D plain strain model was created in the FE software ABAQUS. The Concrete Damage Plasticity (CDP) model available in ABAQUS [12] was selected. This software presents a versatile tool to model a broad range of phenomena of structural concrete behaviour. The model assumes that the main two failure mechanisms for concrete are tensile cracking and compressive crushing. To model the concrete behaviour, the input data required are uniaxial σ–ε curves for compression and tension. In this study, to overcome mesh dependence due to different mesh size, the σ–w tensile curve was used instead of σ–ε.

In Fig. 3 are presented the geometry, boundary conditions and loading for the beam flexural strength test configuration. The boundary conditions were imposed so that in the vertical axis $u_y=0$ in both supports and $u_x=0$ in one of those. The load was applied by displacement control in order to guarantee proper convergence in case of flexural-softening response is detected. The mesh comprised of 1361 nodes and 2560 triangular linear elements (CPE3) with a mesh size of 10 mm, refined in the mid-section with 5 mm size elements. The post-cracking behaviour of FRC was captured by means of ABAQUS Explicit Dynamic algorithm (quasi-static analysis).
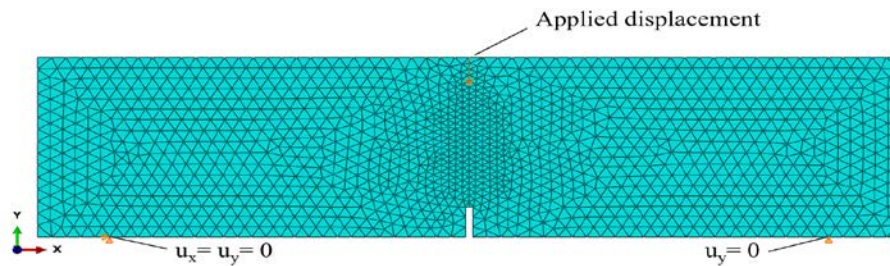

Fig. 3 – 2D FEM model adopted: mesh and boundary conditions considered

4.   RESULTS

To obtain the constitutive relationships, a generalised method of back analysis was used [13] considering an iterative trial and error to fit the experimental curves with the model results. The MC-2010 constitutive equations were obtained using the results presented in Figure 2.

From Figure 4 to Figure 12 are depicted the Load – CMOD curves for the experimental results and three FE model simulations (1) using the MC-2010 constitutive curves, (2) using the constitutive curve obtained by BA and (3) an obtained simplified trilinear curve (based on the back analysis results). Additionally, the figures with stress-crack width present the constitutive curves used for the FE simulations.

The results show how the MC-2010 constitutive equation overestimates the mechanical performance for CMOD <1.0 mm, i.e., the loss of strength is larger in the Experimental test than in the Model (MC-2010). This is of great importance, suggesting that the MC-2010 curve tends to show higher strength for serviceability limit state (f_{Fts}). Although the MC-2010 bilinear curve captures well the maximum post-cracking strength, it is reached at smaller CMOD as compared to the experimental results. Further, when the maximum post-cracking strength for MSFRC is expected (CMOD > 2.5 mm), the Load-CMOD curve starts decreasing, which does not correspond with the behaviour observed in the actual tests. This is even more evident in tests with high hardening behaviour (e.g. C40/50-10 and C50/60-10). In view of these results, two main issues can be highlighted with the MC-2010 approach: overestimates the residual strength for serviceability limit state (SLS) and it is not representative of the full potential of MSFRC reached at larger CMOD.

The constitutive curve obtained by means of BA fits well the behaviour of the actual test. In this regard, seven points (up to nine in the case of C30/37-3.5) were necessary to match the curve. The loss of strength and the mechanical performance for CMOD < 1.0 mm was well captured, which highlights the necessity of decreasing the value of σ_2 for the MC-2010 constitutive equation. For high values of CMOD (> 2.5 mm), an additional point was required to capture well the behaviour ($\sigma = 0$ MPa, $w = 5$ mm), decreasing the residual strength with a smooth slope down to zero.

Although the BA curve worked perfectly, in terms of structural design it is not a quick process due to tedious trial and error process. In view of this, a trilinear curve (four points) was proposed, so the MSFRC behaviour was better reproduced than using the MC-2010 constitutive curve. To this end, two changes in the MC-2010 are proposed to improve the results. First, a reduction in σ_2 was necessary so the loss of strength after cracking was similar to the experimental test. Moreover, the f_{Fts} was closer to the values of the experimental test being on the safe side for serviceability requirements. The second change regards the late post-cracking response (CMOD > 2.5 mm), which was sorted out adding an additional point with zero strength and $w = 5.0$ mm. In cases where a huge hardening behaviour was observed (i.e. C40/50-7.5, C40/50-10, C50/60-7.5 and C50/60-10), the third point of the trilinear equation was set for $w < 2.5$ mm to better fit the experimental behaviour.

The results using the trilinear constitutive curve showed a good agreement with the Experimental curve and a huge improvement compared to using the MC-2010 curves. However, implementing the trilinear curve there is a region (1.0 mm < CMOD < 3.0 mm) in which the Model does not fit the experimental curve (being this easily solved by setting an additional point in the σ–w curve) although the proposed trilinear approach is on the safe side for design purposes. The results evidenced that the trilinear curve proposed (based on the BA) considerably improved the results compared to adopting the MC-2010 curve.

Fig. 4 – C30/37 2.5 kg/m^3 (a) Load – CMOD curves (b) Constitutive equations.

Alejandro Nogales Arroyo

Fig. 5 – C30/37 3.5 kg/m³ (a) Load – CMOD curves (b) Constitutive equations.

Fig. 6 – C30/37 5.0 kg/m³ (a) Load – CMOD curves (b) Constitutive equations.

Fig. 7 – C40/50 5.0 kg/m³ (a) Load – CMOD curves (b) Constitutive equations.

Fig. 8 – C40/50 7.5 kg/m³ (a) Load – CMOD curves (b) Constitutive equations.

(b)

Fig. 9 – C40/50 10.0 kg/m³ (a) Load – CMOD curves (b) Constitutive equations.
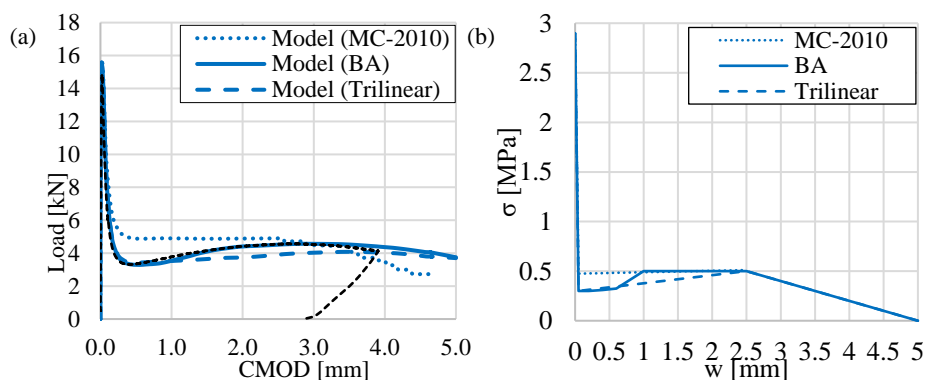

Fig. 10 – C50/60 5.0 kg/m³ (a) Load – CMOD curves (b) Constitutive equations.
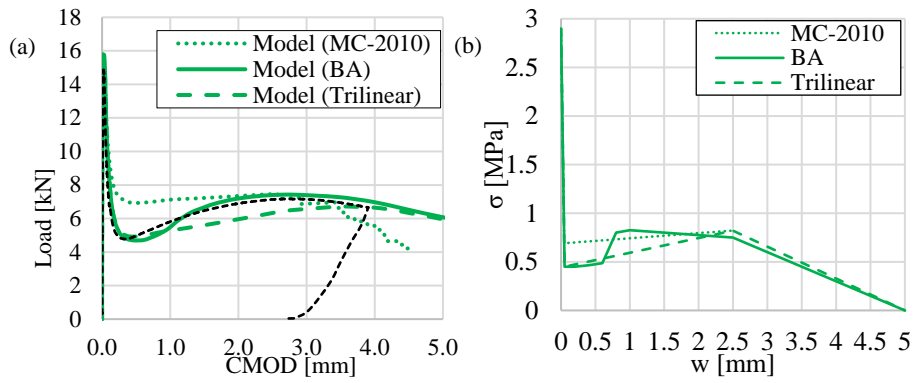

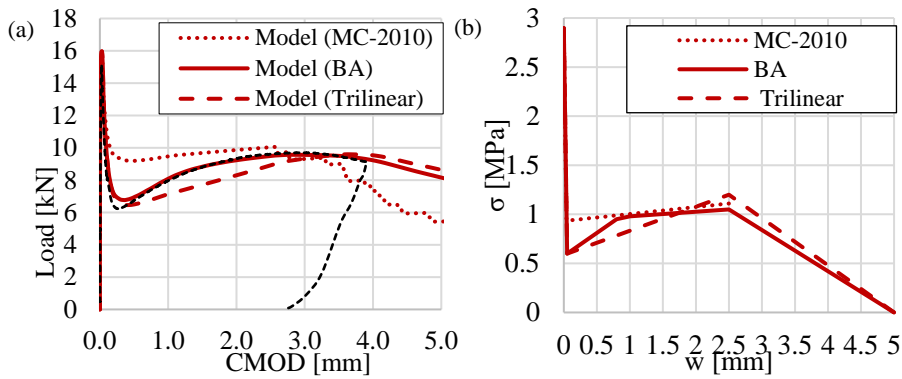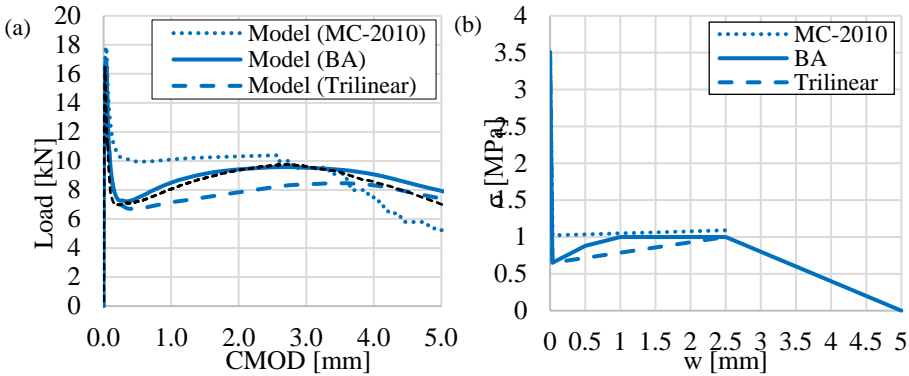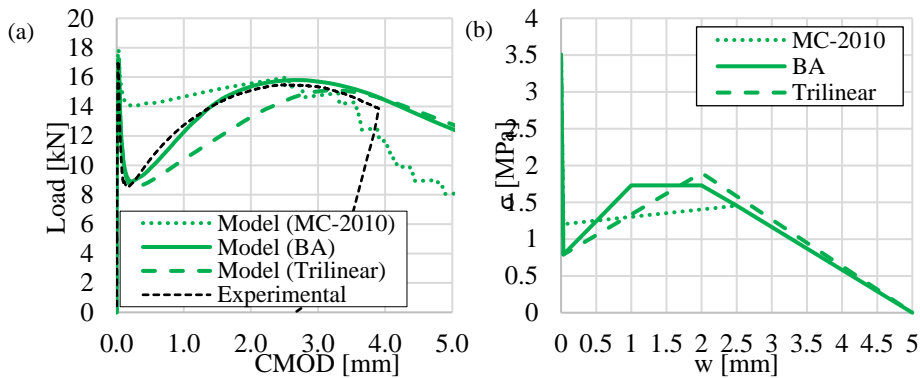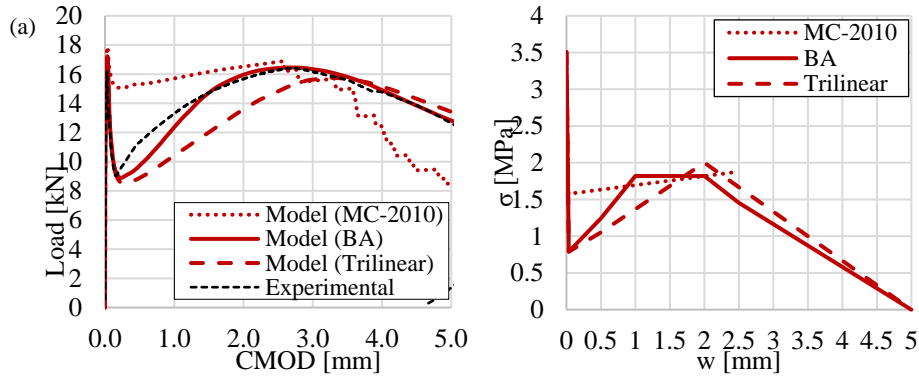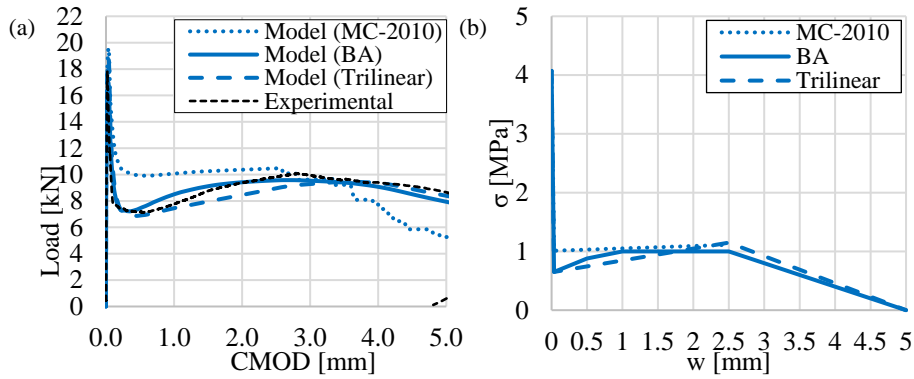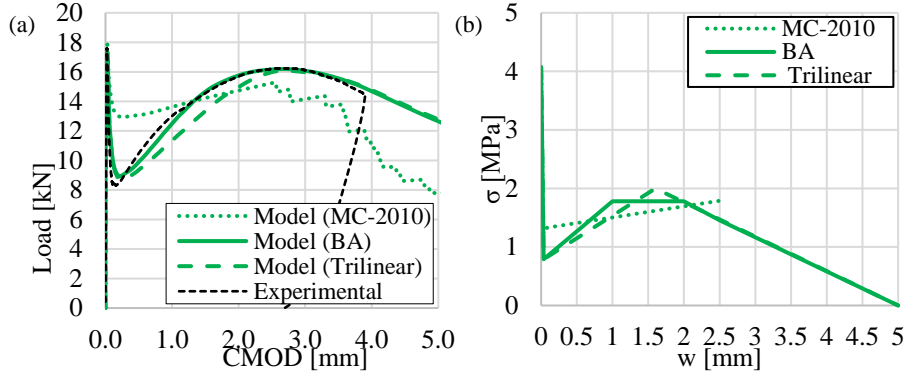*Fig. 11 – C50/60 7.5 kg/m³ (a) Load – CMOD curves (b) Constitutive equations.*
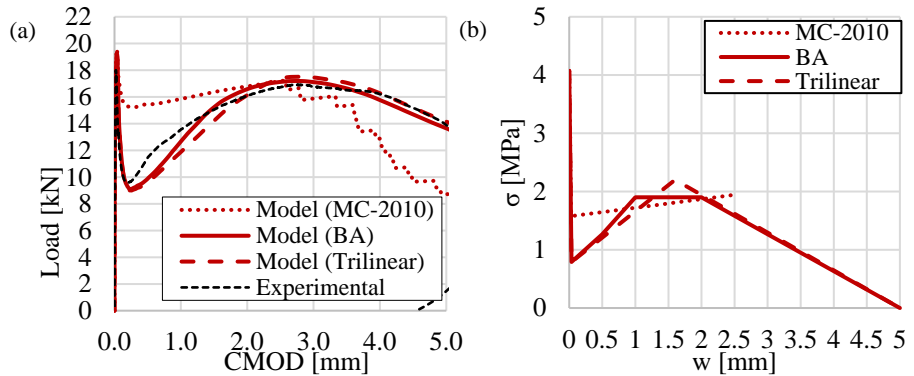
Fig. 12 – C50/60 10.0 kg/m³ (a) Load – CMOD curves (b) Constitutive equations.

5. CONCLUSIONS

Numerical simulations of beam flexural post-cracking strength tests have been carried out by means of a non-linear FE model. Based on the outcomes of an experimental research work, the model was used for assessing the MC-2010 FRC constitutive curve with macro synthetic fibres made of polypropylene. Moreover, a BA was performed and a trilinear curved was proposed to better fit the experimental behaviour observed.

Based on the results presented in this research contribution, the following conclusions can be drawn:

- The MC-2010 constitutive curve does not fully reproduce the potential of MSFRC. The maximum post-cracking strength for MSFRC appears for CMOD > 2.5 mm, and this is not captured for the MC-2010 constitutive curve since it is limited to $w_u = 2.5$ mm.
- The MC-2010 constitutive curve slightly overestimates the performance of MSFRC for CMOD < 1.0 mm as well as the loss of strength after cracking.
- Two modifications in the tri-linear constitutive curve induced a huge improvement in order to better represent the post-cracking behaviour of MSFRC: a reduction in σ_2, so the loss of strength after cracking reproduces the drop in strength in the actual behaviour, and progressively reducing the strength of the constitutive equation beyond $w_u = 2.5$ mm up to $w = 5.0$ mm and $\sigma = 0$ MPa.
- The non-corrosive behaviour of the PP fibres justifies an opening of the crack width limitations of MC-2010. The constitutive model developed and presented here accurately represents the flexural material behaviour of MSFRC used in this experimental research. Its deviation from the MC-2010 model enables a significantly better exploitation of the favourable material response, especially at larger CMOD.

ACKNOWLEDGEMENTS

REFERENCES

[1] Meda A, Plizzari GA, Riva P. Fracture behavior of SFRC slabs on grade. Mater Struct Constr 2004;37:405–11. https://doi.org/10.1617/14093.

[2] Meda A, Plizzari G. New design approach for steel fiber-reinforced concrete slabs-on-ground based on fracture mechanics. ACI Struct J 2004;101 (3):298–303.

[3] Nogales A, de la Fuente A. Crack width design approach for fibre reinforced concrete tunnel segments for TBM thrust loads. Tunn Undergr Sp Technol 2020;98. https://doi.org/10.1016/j.tust.2020.103342.

[4] Nogales A, de la Fuente A. Numerical-aided flexural-based design of fibre reinforced concrete column-supported flat slabs. Eng Struct 2021;232:1–24. https://doi.org/10.1016/j.engstruct.2020.111745.

[5] Aidarov S, Mena F, de la Fuente A. Structural response of a fibre reinforced concrete pile-supported flat slab: full-scale test. Eng Struct 2021;239:112292. https://doi.org/10.1016/j.engstruct.2021.112292.

[6] de la Fuente A, Escariz RC, de Figueiredo AD, Molins C, Aguado A. A new design method for steel fibre reinforced concrete pipes. Constr Build Mater 2012;30:547–55. https://doi.org/10.1016/j.conbuildmat.2011.12.015.

[7] de la Fuente A, Escariz RC, de Figueiredo AD, Aguado A. Design of macro-synthetic fibre reinforced concrete pipes. Constr Build Mater 2013;43:523–32. https://doi.org/10.1016/j.conbuildmat.2013.02.036.

[8] International Federation for Structural Concrete (fib). fib-Model Code for Concrete Structures 2010. Lausanne: 2010. https://doi.org/10.1002/9783433604090.

[9] EN1992-1-1. Eurocode 2: Design of concrete structures – Part 1-1: General rules, rules for buildings, bridges and civil engineering structures. Brussels: CEN; 2019.

[10] EHE-08. Instrucción de Hormigón Estructrural (EHE-08). Madrid: Ministerio de Fomento; 2008.

[11] European Commitee for Standardization. Precast concrete products - test method for metallic fibre concrete- Measuring the flexural tensile strength. Br Stand Inst 2005. https://doi.org/9780580610523.

[12] Dassault Systèmes Simulia. Abaqus CAE User's Manual (6.12). Providence: Dassault Systèmes; 2012.

[13] Roelfstra PE, Wittmann FH. Numerical method to link strain softening with failure of concrete. Fract Toughness Fract Energy, Elsevier 1986:163–75

4. GENERAL AND SPECIFIC CONCLUSIONS

The main purpose of this chapter is to discuss the relevance and limitations of the main contributions derived from the thesis based on a general perspective, which results from the combination of papers written. Additionally, opinions on future research lines are included. It is important to highlight that the present chapter does not aim to summarize the work done or replace the specific discussion of the results included in each paper.

4.1. GENERAL CONCLUSIONS

This thesis presents a research on FRC aided by means of non-linear FE simulations. The outcomes of this thesis revealed that the use of FE for different typologies of FRC structural elements, currently built in the industrial sector, allow optimizing geometry and the required mechanical properites. The results and the methodology described are meant to be used as a reference for engineers and practitioners for using fibres as partial or total substitution of conventional reinforcement, since the main barriers that prevented its use such as material characterisation or problems inherent to FE definition are overcome. In this sense, numerical simulations were shown to be a critical tool for illuminating limits of applicability of FRC and models for FRC design.

In terms of research, the constitutive material models along with its implementation with FE present a versatile tool to perform analysis with a broad range of parameters. Once the FE model is validated -accurately simulates the experimental test used as a reference- a comprehensive assessment of the structural element can be done by means of parametrical analyses. The ease of monitorization permits measuring a wide range of variables that might be difficult in actual tests due to different factors such as complexity or safety. This results in time and costs save and makes the numerical analysis, in combination with the experimental results, an attractive solution since its straightforward implementation allows to identify rapidly those parameters that play a significant role, disregarding others that might have less influence, and focus on those for future experimental programmes.

With regard to structural design, in this thesis it has been proven the adequacy of FE for carrying out proper design methods. By implementing FE models, the non-linear behaviour of FRC provided by its post-cracking strength, can be properly reproduce and, therefore, the design can take into account the full potential of the material. The models together with safety formats developed using global safety factors, rather than partial safety factor traditionally used for linear elastic and sectional analysis, allows evolving towards more optimised structures: taking more advantage of the material potential, reducing uncertainties that might eventually reduce the safety coefficients whilst maintaining, or even increasing, the safety level.

4.2. SPECIFIC CONCLUSIONS

A selection of the specific conclusions are listed below grouped within the main areas of contribution of the thesis.

1. Tunnel linings subjected to TBM thrust jack

- The residual flexural strength for a crack width of 0.5 mm (f_{R1}) has resulted to have a great influence in cracking control whilst the ratio f_{R3}/f_{R1} seems not play a significant role. This is of relevant importance when deciding the type of fibre (material and geometry) to be used since those that lead to higher f_{R1} would be more appropriate than those that perform better for larger crack widths.

- The spalling cracks appear to be those governing the FRC post-cracking tensile strength requirements. Eccentric thrust has a relevant influence on cracking performance; in this sense, attention must be paid to both cracking phenomena, especially, for splitting cracks for which cracks up to 6.0 times wider with respect to the perfectly centred thrust have registered.

- Hybrid reinforcement leads to crack reduction and this can be considered as a suitable solution when severe crack width limitations are stablished for service.

2.   Pile supported elevated flat slab

- The results derived from the validated numerical model allowed confirming that FRC and HRC solutions can lead to optimized amounts of steel reinforcement (for flexure) for column-supported flat slabs respect to the traditional RC alternatives. In the studied case, a reduction in 30% of the steel fibre amount was achieved respect the previous reported cases

- The HRC solutions analyzed proved to provide a better structural performance than those with only FRC. In this sense, the structural efficiency of the HRC alternatives is more noticeable when low FRC residual strength classes are considered. Nevertheless, precautions should be taken when low reinforcement ratios and strain-softening FRCs are combined since crack localization and reductions of the sectional ductility were reported by other researchers [1–8]. To avoid these phenomena, the minimum reinforcement ratio should be assessed considering the residual tensile strength performance of the FRC.

- Hybrid configurations led to global resistance reduction safety factors lower than those obtained for the FRC solutions analysed. However, a convergence of this safety factor to 1.25 was detected for HRC and FRC with $f_{Rm} \geq 8.0$ N/mm^2.

- The numerical model together with the safety format presented in the *fib* MC2010 for non-linear analysis proved to be a reliable tool for safely design of real-scale slab constructed, even from the safe side, according to the experimental results reported by Aidarov [9].

3.   Two-span continuous beams

- The increase of the FRC strength class (represented by f_{R1}) in both simply supported and continuous beams led to increases in load-bearing capacity, especially for low values of ρ_s.

- The use of fibres in simply supported beams significantly affected the deformation capacity of those by reducing both deformation and rotation capacities for any FRC residual strength class in beams with $\rho_s \leq 0.25\%$.

- In simply supported beams with $\rho_s = 0.57\%$, there was an increase in deformation capacity due to the interaction of the softening response of FRC residual strength class 3c and the hardening of the steel reinforcement. For the remaining values of FRC residual strength classes (5c and 7c), crack localisation affected the deformation capacity leading to a clear reduction of this property. For HRC beams with $\rho_s = 1.14\%$ the beams failed due to concrete crushing, crack localisation was also detected, hence, a reduction of deformation capacity was found for all beams.

- In simply supported beams, changes in ρ_s have higher influence on the rotational capacity for lower FRC residual classes (3c) than for those with higher FRC classes. For $\rho_s \leq 0.57\%$ the plastic hinge length is not affected by the addition of fibres whereas for lower ratios the length decreases with the decrease of the FRC residual strength.

- In statically indeterminate members, prior to yielding, the increase of f_{R1} reduces the moment redistribution by enhancing the overall stiffness. As expected and in agreement with results from literature, the addition of fibres increased the load bearing capacity, with the contribution increasing when decreasing ρ_s.

- In HRC continuous beams, the deformation capacity only improved for beams with $\rho_s = 1.14\%$. For the rest of beams a reduction of the post-yield ductility response of the beam was observed.

- The moment redistribution capacity was not affected by the FRC residual strength for beams with $\rho_s \geq 0.57\%$. For low reinforcement ratios (i.e. 0.13% and 0.25%), the redistribution capacity became more sensitive, this increasing with decreasing f_{R1}.

- The latter conclusion is of paramount importance since the redistribution coefficient accepted in several design guidelines (including the *fib* MC2010) is superior to 20%. The results obtained numerically prove that lower redistribution coefficients are to be expected when the FRC strength class increases in HRC when those are compared with the equivalent (same reinforcement ratio) RC alternative.

4. FRC characterization

- The *fib* MC2010 constitutive curve does not fully reproduce the potential of MSFRC. The maximum post-cracking strength for MSFRC appears for CMOD > 2.5 mm, and this is not captured for the MC-2010 constitutive curve since it is limited to $w_u = 2.5$ mm.

- The *fib* MC2010 constitutive curve slightly overestimates the performance of MSFRC for CMOD < 1.0 mm as well as the loss of strength after cracking.

- Two modifications in the tri-linear constitutive curve induced a huge improvement in order to better represent the post-cracking behaviour of MSFRC: a reduction in σ_2, so the

loss of strength after cracking reproduces the drop in strength in the actual behaviour, and progressively reducing the strength of the constitutive equation beyond $w_u = 2.5$ mm up to $w = 5.0$ mm and $\sigma = 0$ MPa.

- The non-corrosive behaviour of the PP fibres justifies an opening of the crack width limitations of *fib* MC2010. The constitutive model developed and presented here accurately represents the flexural material behaviour of MSFRC used in this experimental research. Its deviation from the MC-2010 model enables a significantly better exploitation of the favourable material response, especially at larger CMOD.

4.3.   FUTURE PERSPECTIVES

In view of the outcomes derived from this research, it can be stated that the non-linear simulation of concrete structures, and particularly for FRC, has a huge potential in both research and design.

The future research lines in this sense, should focus on new, or adjusted, constitutive models for FRC in order to reproduce more accurately the post-cracking behaviour of the material. There should be specific models for finite element analysis, rather than models for both sectional and numerical models, since the values of the latter give conservative values. Additionally, the models should discern between different types of fibres (steel or synthetic), which is of great importance in terms of durability and service life.

Furthermore, researchers and practitioners should co-operate in order to propose new design methods, with adjusted safety coefficients, that take into account the level of uncertainties of the non-linear analysis along with the ones inherent to the material. This will lead towards more reliable structures that could take more advantage of the material post-cracking strength potential that could drive towards more optimised structural elements whilst reducing the material consumption.

4.4. REFERENCES

[1] Meda A, Minelli F, Plizzari GA. Flexural behaviour of RC beams in fibre reinforced concrete. Compos Part B Eng 2012;43:2930–7. https://doi.org/10.1016/j.compositesb.2012.06.003.

[2] Conforti A, Zerbino R, Plizzari GA. Assessing the influence of fibres on the flexural behaviour of RC beams with different longitudinal reinforcement ratios. Struct Concr 2020. https://doi.org/10.1093/comnet/xxx000.

[3] Markić T, Amin A, Kaufmann W, Pfyl T. Strength and Deformation Capacity of Tension and Flexural RC Members Containing Steel Fibers. J Struct Eng (United States) 2020;146:1–17. https://doi.org/10.1061/(ASCE)ST.1943-541X.0002614.

[4] Dancygier AN. Effect of cracking localization on the structural ductility of normal strength and high strength reinforced concrete beams with steel fibers. Int J Prot Struct 2019;10:457.

[5] Yoo DY, Moon DY. Effect of steel fibers on the flexural behavior of RC beams with very low reinforcement ratios. Constr Build Mater 2018;188:237–54. https://doi.org/10.1016/j.conbuildmat.2018.08.099.

[6] Dancygier AN, Berkover E. Cracking localization and reduced ductility in fiber-reinforced concrete beams with low reinforcement ratios. Eng Struct 2016;111:411–24. https://doi.org/10.1016/j.engstruct.2015.11.046.

[7] Dancygier AN, Savir Z. Flexural behavior of HSFRC with low reinforcement ratios. Eng Struct 2006;28:1503–12. https://doi.org/10.1016/j.engstruct.2006.02.005.

[8] Mertol HC, Baran E, Bello HJ. Flexural behavior of lightly and heavily reinforced steel fiber concrete beams. Constr Build Mater 2015;98:185–93. https://doi.org/10.1016/j.conbuildmat.2015.08.032.

[9] Aidarov S, Mena F, de la Fuente A. Structural response of a fibre reinforced concrete pile-supported flat slab: full-scale test. Eng Struct 2021;239:112292. https://doi.org/10.1016/j.engstruct.2021.112292.

ANNEX I – NUMERICAL MODELLING OF FRC

This annex reproduces a brief overview of the different methods to model concrete and FRC by means of numerical analysis through finite elements.

A1.1. NUMERICAL MODELLING OF FRC

Concrete is one of those materials that, beyond a certain point, behaves non-linearly in both tension and compression and has been traditionally analysed by means of a linear elastic sectional analysis. Nowadays, many structures cannot be assessed by analytical procedures because of their complex geometry or material non-linearities. The use of powerful computational tools allows the non-linear analysis of the material behaviour. This is of great importance since it can take full advantage of the mechanical capacity of the materials through complex constitutive models to simulate and analyse the behaviour for both compressive and tensile behaviour. For quasi-brittle materials such as concrete, this is a topic that has been thoroughly investigated in the literature [1–9] and more recently, national and international codes have included models for the tensile post-cracking response of FRC [10–13].

In this regard, concrete is a composite material comprised of cement, water and aggregates that is considered homogeneous for continuum mechanics. Since the 1950s, an increasingly growing way to assess continuum mechanics is by means of finite element analysis (FEA), which discretises the whole space into smaller parts (discrete elements) and solves the partial differential equations particularly for each domain.

The stress-strain behaviour of concrete after a certain point is inherently non-linear for both tensile and compressive behaviour; the two main failure modes are crushing due to compression and cracking due to tension. When the principal tensile stress exceeds the tensile strength, cracking occurs orthogonal to the principal stress' direction. Once the cracking is set, it generates a geometrical discontinuity in the material and the stiffness in that directions reduces since it is not able to withstand tensile stresses (softening behaviour) [14]. Since the early use of FEA, there are two most extended ways to model concrete, namely, discrete crack approach and smeared crack approach.

The discrete crack concept is the approach that reproduces this phenomenon most closely since it models the crack as a displacement discontinuity between elements; in other words, the bond between two adjacent elements (interface elements) brakes and they separate (see Figure 2.1a). This was first introduced by Ngo and Scordelis [15] and Nilson [16]. This approach does not fit the nature of the finite element displacement method since it implies a continuous change in nodal connectivity and thus it is not computationally recommended [17]. Although this method is more suitable to capture the failure localisation, the main drawback resides in the need of a constant re-meshing in areas where progressive failure takes places since the crack is constrained to follow a predefined path along the element edges [17,18].
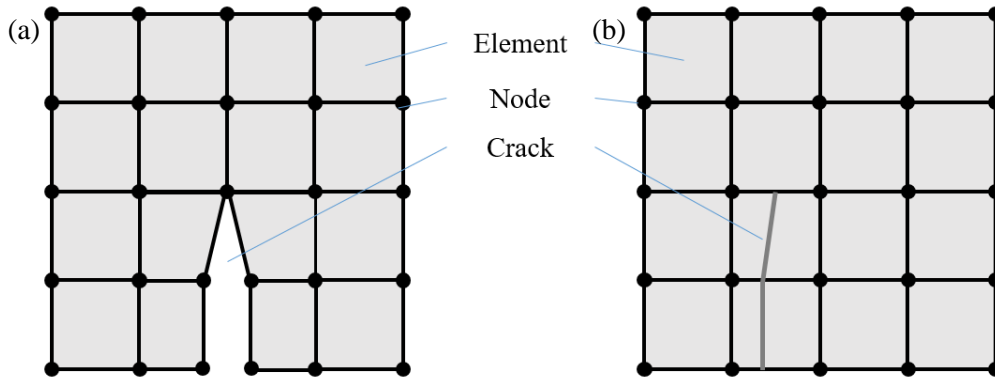
Figure 2.1 – Model representation (a) Discrete crack model and (b) Smeared crack model

In smeared crack models, introduced by Rashid [19] in 1968 for the first time, the crack are smeared over the finite element and the cracked solid remains continuum, conversely to discrete crack model, and allows the description in terms of uniaxial stress-strain (or crack width) relationships. When crack occurs, the mesh remains unaltered, maintaining the original mesh geometry and not imposing constrains to the crack orientation (see Figure 2.1 b). The main drawback is that the crack might propagate aligned to the mesh direction, which can lead to mesh sensitivity. Smeared crack models are categorised in fixed, multi-directional and rotating crack models.
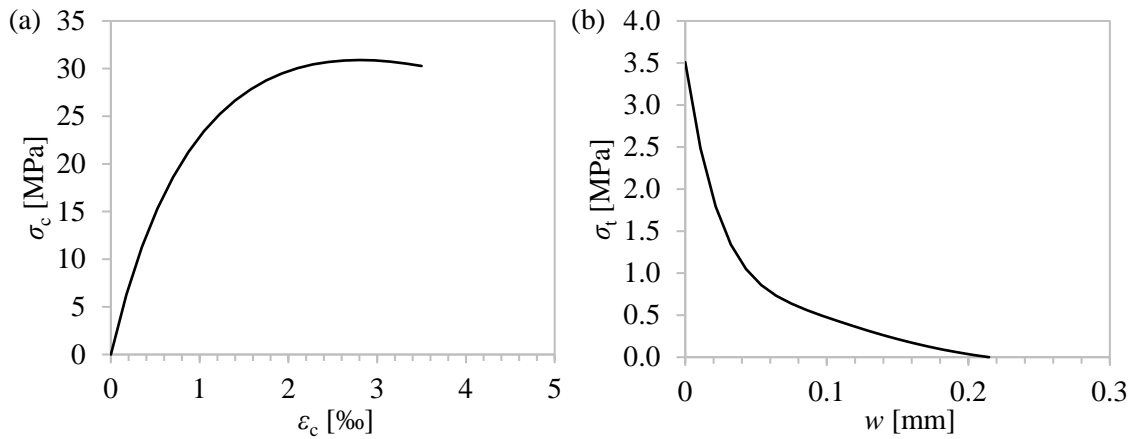
Figure 2.2 – Example of commonly adopted curves for uniaxial relationships for Smeared Crack models (a) compression in terms of stress-strain and (b) tension in terms of stress-crack width

As an example, discrete crack models would be more accurate for specimens in which the potential cracking areas can clearly be expected in advanced (e.g. when undertaking a numerical analysis on a specimen previously experimentally tested). However, in those engineering problems where it is not clear where cracking may occur, may occur in two separated areas

(distributed fracture), or there is crushing and reinforcement yielding, the discrete crack method it is not recommended [17,18] and a smeared approach it is used instead.

Based on the features aforementioned, the smeared crack models are the most widespread approach among researchers and engineering practitioners. Discrete approaches are more demanding in terms of computational costs and need more specialised software, whereas there are many commercial software that include the smeared crack approach [20–22].

In this research, the ABAQUS CAE software [22] was used for undertaking the FEA of FRC. The software presents a versatile tool to successfully model a wide range phenomena of concrete structural behaviour, as evidenced by numerous published studies [23–28]. The software has three material models for concrete modelling: (1) concrete smeared cracking (in ABAQUS/Standard) which is intended for the analysis of reinforced concrete structures (2) cracking model for concrete (in ABAQUS/Explicit) designed for applications in which the behaviour is dominated by tensile cracking and no concrete crushing is expected and (3) concrete damaged plasticity (ABAQUS/Standard and ABAQUS/Explicit) to properly represent the inelastic behaviour of concrete. The latter was chosen because of its capacity to properly reproduce the inelastic tensile behaviour of concrete, of great importance in FRC elements for its post-cracking residual strength. The CDP model is a continuum, smeared crack, plasticity-based model that assumes that the main two failure mechanisms for concrete are tensile cracking and compressive crushing. To model the concrete behaviour, the input data required are uniaxial stress-strain (σ–ε) curves for compression and tension. However, to try to overcome mesh size dependence inherent in smeared models, the (σ–w) tensile curve was used instead. The CDP magnitude of the parameters adopted for all the simulations were those proposed in ABAQUS User's Manual [22] for plain concrete, except those for the dilation angle, which was determined by means of a sensitivity analysis for each case study.

A1.2. REFERENCES

[1] Willam KJ, Warnke EP. Constitutive model for the triaxial behaviour of concrete, International association of bridge and structural engineers. In: IABSE Proc.19, editor. Semin. Concr. Struct. Subj. to triaxial Stress. Pap. III-1, Bergamo, Italy: 1974.

[2] Mazars J, Pijaudier-Cabot G. Continuum damage theory - Application to concrete. J Eng Mech 1989;115:345–65.

[3] Yazdani S, Schreyer HL. Combined plasticity and damage mechanics model for plain concrete. ASCE J Eng Mech 1990;116:1435–50.

[4] Borst R, Feenstra PH. A composite plasticity model for concrete. Int J Solids Struct 1996;33:707–30.

[5] Grassl P, Jirásek M. Damage-plastic model for concrete failure. Int J Solids Struct 2006;43:7166–96.

[6] Addessi D, Marfia S, Sacco E. A plastic nonlocal damage model. Comput Methods Appl Mech Eng 2002;191:1291–310.

[7] Salari MR, Saeb S, Willam KJ, Patchet SJ, Carrasco RC. A coupled elastoplastic damage model for geomaterials. Comput Methods Appl Mech Eng 2004;193:2625–43.

[8] Hsu LS, Hsu TCC. Complete stress - strain behaviour of high-strength concrete under compression 1994:46:301-3012.

[9] Grassl P, Lundgren K, Gylltoft K. Concrete in compression: a plasticity theory with a novel hardening law. Int J Solids Struct 2002;39:5205–23.

[10] International Federation for Structural Concrete (fib). fib-Model Code for Concrete Structures 2010. Lausanne: 2010. https://doi.org/10.1002/9783433604090.

[11] EN1992-1-1. Eurocode 2: Design of concrete structures – Part 1-1: General rules, rules for buildings, bridges and civil engineering structures. Brussels: CEN; 2019.

[12] EHE-08. Instrucción de Hormigón Estructrural (EHE-08). Madrid: Ministerio de Fomento; 2008.

[13] American Concrete Institut and International Organization for Standaritzation Building Code Requirements for Structural Concrete. ACI 318-08. Farmington Hills: ACI; 2008.

[14] Genikomsou A. Nonlinear Finite Element Analysis of Punching Shear of Reinforced Concrete Slab-Column Connections. 2016.

[15] Ngo D, Scordelis AC. Finite element analysis of reinforced concrete beams. J Am Concr Inst 1967;64:152–63.

[16] Nilson AH. Nonlinear analysis of reinforced concrete by the finite element method. J Am Concr Institute1 1968;65:757–66.

[17] Rots JG, Blaauwendraad J. Crack models for concrete: Discrete or Smeared? Fixed, Multi-directional or rotating? Heron 1989;34:1–59.

[18] Jendele L, Cervenka J, Saouma V, Pukl R. On the choice between discrete or smeared approach in practical structural FE analyses of concrete structures. Int Conf Anal Discontinuous Deform 2001;1:18.

[19] Rashid YR. Analysis of prestressed concrete pressure vessels. Nucl Eng Des 1968;7:334–44.

[20] Červenka Consulting Ltd. ATENA Program Documentation. Prague: 2013.

[21] TNO - DIANA FEA BV. Analysis procedures DIANA - Finite Element Analysis. User's Manual 2008.

[22] Dassault Systèmes Simulia. Abaqus CAE User's Manual (6.12). Providence: Dassault Systèmes; 2012.

[23] Qin R, Zhou A, Lau D. Effect of reinforcement ratio on the flexural performance of hybrid FRP reinforced concrete beams. Compos Part B Eng 2017;108:200–9. https://doi.org/10.1016/j.compositesb.2016.09.054.

[24] Nana WSA, Bui TT, Limam A, Abouri S. Experimental and Numerical Modelling of Shear Behaviour of Full-scale RC Slabs Under Concentrated Loads. Structures 2017;10:96–116. https://doi.org/10.1016/j.istruc.2017.02.004.

[25] Jamshidi M, Hoseini A, Vahdani S, de la Fuente A. Numerical-aided design of fiber reinforced concrete tunnel segment joints subjected to seismic loads. Constr Build Matreials 2018;170:40–54.

[26] Nogales A, de la Fuente A. Numerical-aided flexural-based design of fibre reinforced concrete column-supported flat slabs. Eng Struct 2021;232:1–24. https://doi.org/10.1016/j.engstruct.2020.111745.

[27] Genikomsou AS, Polak MA. Finite element analysis of punching shear of concrete slabs using damaged plasticity model in ABAQUS. Eng Struct 2015;98:38–48. https://doi.org/10.1016/j.engstruct.2015.04.016.

[28] Oikonomou-Mpegetis S. Behavior and Design of steel fibres reinforced concrete slabs. 2012.

ANNEX II – COMPLEMENTARY RESEARCH DERIVED FROM THE THESIS

This chapter reproduces co-authored journal papers and research contributions derived from the research in this thesis and are excluded from the official compendium of publications.

A2.1. RESEARCH CONTRIBUTION IV: ANALYSIS OF DESIGN CONSTITUTIVE MODEL FOR PLASTIC FIBRE REINFORCED CONCRETE THROUGH INVERSE ANALYSIS

Eduardo Galeote[1*], Alejandro Nogales[1,2] and Albert de la Fuente[1]

[1] Department of Civil and Environmental Engineering, Universitat Politècnica de Catalunya (UPC), Jordi Girona 1-3, 08034 Barcelona, Spain

[2] Smart Engineering Ltd., UPC Spin-Off, Jordi Girona 1-3, 08034 Barcelona, Spain

*Corresponding author

ABSTRACT

The increasing use of fibre reinforced concrete (FRC) as a structural material requires a constant development of new tools for design purposes. In this line, different codes and guidelines include constitutive models for FRC in their specifications. However, these constitutive models are usually based on the behaviour of steel fibre reinforced concrete (SFRC) and present several limitations on representing the full behaviour of plastic fibre reinforced concrete (PFRC). With the aim of analysing the suitability of the constitutive models when applied on plastic fibres, an experimental program to determine the performance of PFRC using different fibre contents and concrete mixes was performed. The study of the constitutive models was conducted through an inverse analysis using a two-dimensional analytical model to verify and compare the FRC constitutive equations of the MC2010 with the experimental results. The constitutive model of MC2010 was selected given that it is able to capture both the softening and hardening behaviour of FRC through a three-point constitutive equation. The results show that the original constitutive model of the MC2010 tends to overestimate the performance of PFRC. Moreover, it could be necessary to include an additional point on the post-cracking branch of the constitutive model to represent more accurately the full residual strength of PFRC. The results also show that the ultimate strain of the constitutive model should be extended to fully capture the performance of PFRC, especially for large deformations. This study suggests that it should be necessary to redefine the constitutive models through a new approach distinguishing between FRC blended with steel or plastic fibres.

KEYWORDS: First Keyword, Second Keyword, Third Keyword, Forth Keyword, Sixth Keyword.

Alejandro Nogales Arroyo

1. INTRODUCTION

The use of synthetic polypropylene fibres for fibre reinforced concrete (FRC) has been attracting the attention of designers and engineers during the last years. In this line, previous studies [1,2] have analysed the use of plastic fibres in FRC for structural purposes. This has also been motivated by the presence of design constitutive equations for FRC in different codes and guidelines [3], which has led to an increasing use of fibres as reinforcement for structural elements. However, most of these constitutive models are based on studies conducted on concretes reinforced with steel fibres, this leading to certain uncertainty in case of using fibres made of other materials.

For this reason, it is necessary to develop modelling strategies that take into consideration the singularities of synthetic fibres so these can be used for designing safe and sustainable structures. Based on these principles, the present study aims at evaluating the suitability of these constitutive equations for its application on synthetic fibres. Accordingly, the constitutive equation for FRC of the Model Code 2010 [4] was selected given that is based on a performance-based approach and is able to identify a softening or hardening post-cracking behavior.

To analyse the suitability of the constitutive equation of the MC2010 for its use with polypropylene fibres, an experimental program including three different types of concretes with three polypropylene fibre contents each was conducted. Numerical simulations based on an inverse analysis were also conducted to analytically determine the post-cracking behavior of polypropylene FRC. The experimental results of flexural three-point bending tests have been compared to analytical Strength-CMOD curves obtained through inverse analyses to assess the accuracy of the constitutive model.

The results showed the necessity of modifying the parameters of the constitutive equation of the MC2010 for its use with plastic fibres. Through an iterative procedure, these parameters were modified until the analytical curves fit the experimental results, also revealing that the incorporation of an additional point for the definition of the constitutive equation would lead to improved analytical results. This study shows that constitutive models should reflect the singularities of each type of reinforcement given their different behavior and properties

2. EXPERIMENTAL PROGRAM

An experimental program based on nine mixes of polypropylene fibre reinforced concrete (PFRC) was conducted. The concrete mixes (Table 1) had strength classes of C30/37 (with contents of fibres 2.5, 3.5 and 5.0 kg/m^3), C40/50 (with fibres in contents of 5.0, 7.5 and 10.0 kg/m^3) and C50/60 (fibres in contents of 5.0, 7.5 and 10.0 kg/m^3). For each concrete class, the content of superplasticizer was modified for workability purposes. The characteristics of the polypropylene fibres used as reinforcement are shown in Table 2.

Table 1 – Mix compositions.

Material	C30/37	C40/50	C50/60
CEM II/A-L 42,5R	309	400	500
0-2 Sand	205	154	-
0-4 Sand	873	918	945
10-20 Gravel	757	760	750
Polypropylene fibre	2.5 – 3.5 – 5.0	5.0 – 7.5 – 10.0	5.0 – 7.5 – 10.0
Water	165	175	185
Plasticizer (% o.c.w)	0.50	0.84	0.80
Superplasticizer (% o.c.w)	0.83 – 1.03 – 1.05	0.81 – 0.98 – 1.05	0.62 – 0.68 – 0.82

Table 2 – Characteristics of the polypropylene fibres.

Property	Characteristics
Material	Polypropylene
Fibre shape	Continuous embossing
Length [mm]	48
Tensile strength [MPa]	640
Elastic modulus [GPa]	12

The flexural strength was determined by means of three-point bending tests (3PBT) conducted on casted specimens of 150x150x600 mm [5]. The average flexural strength-CMOD curves for each concrete mix, gathered by concrete class, and for the different fibre contents are presented in Figure 1.
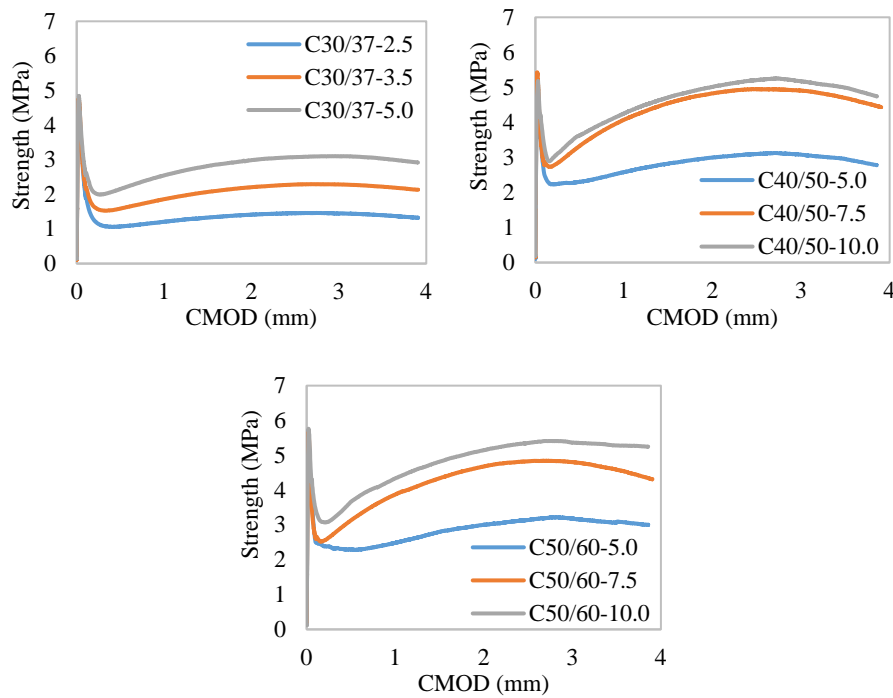
Fig. 1 – Average Strength-CMOD curves for PFRC.

As expected, the results exhibit that flexural strength f_{LOP} slightly increased with concrete strength class, while increasing the content of fibres also increased the residual strengths. However, it should be highlighted that, for concrete classes C40/50 and C50/60, increasing the content of fibres from 7.5 to 10 kg/m^3 did not significantly improve the residual strength.

3.   INVERSE ANALYSIS

An inverse analysis based on an analysis of evolutionary sections (AES) [6] with a multi-layer approach was conducted to simulate the Strength-CMOD curves to analytically obtain the experimental results of the beams tested under three-point bending tests. For this, it is assumed that (i) sections remain plane after loading or imposed strains, (ii) there is strain compatibility, in which there is a perfect bond between concrete and fibres, (iii) shear stress strains are negligible and not considered and (iv) the internal forces are applied on the symmetrical axis of the section.

To conduct the analytical model, the constitutive law for FRC of the MC2010 was taken as reference. This constitutive model (Figure 2) is able to represent both the hardening and softening behavior of FRC, and is based on a stress-strain (σ-ε) relationship, in which stresses σ are determined through residual strengths (f_{R1} and f_{R3}) obtained and strains (ε_{SLS} and ε_{ULS}) from crack openings of 0.5 and 2.5 mm, with all parameters obtained from three-point bending tests. The characteristic length, which is the parameter that relates the crack opening and the strain ($w = \varepsilon \cdot l_{cs}$), was defined to be equal to the depth of the beam ($l_{cs} = h$), despite several authors proposing different values for this parameter [8].
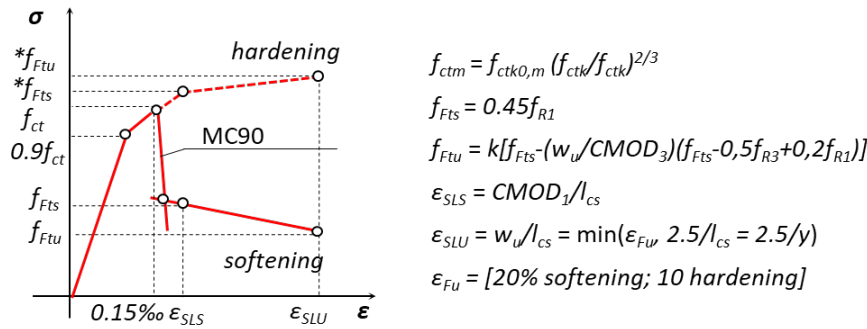
Fig. 2 – Average Strength-CMOD curves for PFRC.

The inverse analysis is based on a discretization of the element into layers along its height. Considering that tensile stresses are located at the bottom and compression stresses are placed at the top part of the section, a tensile strain ε_{bot} value is imposed for the initial stage, while a compressive strain at the top (ε_{top}) is iterated so the curvature χ and the strain at any layer may be calculated until the equilibrium condition between the internal and the external forces and momentums are satisfied.

Each time the iterative process to determine ε_{top} is completed, ε_{bot} is progressively increased until the iterated result of ε_{top} achieves the ultimate compressive strain ε_{cu}. While increasing the value ε_{bot}, so does the crack width at the section. When the strain of the concrete at the top layer of the section achieves the ultimate strain ($\varepsilon_c = \varepsilon_{cu}$), the area under compression collapses by crushing. At this stage, the iterative process stops and the Strength-CMOD curve for all the iterated results are determined.

4. ANALYSIS OF THE RESULTS

The parameters of the constitutive model of the MC2010 were calibrated through an iterative process so the analytical results fit the experimental curves, obtaining two modified constitutive models based on 3- and 4-point equations. A comparison between the constitutive equation of the MC2010 and the 3- and 4-point adjusted equations are shown from Figures 3 to 5. The results also show the Strength-CMOD curves of the experimental results and the analytical curves obtained through the MC2010 and the 3- and 4-point calibrated equations.

In line with previous studies [3][9], the results indicate that the constitutive model of the MC2010 overestimates the residual strength for crack openings below 1.5 mm. Such overestimation might be attributed to the use of polypropylene fibres, given that the proposed constitutive equation of the MC2010 is mainly based on data and studies made of FRC with steel fibres.

The results also indicate that the residual strength of FRC with polypropylene fibres exhibit a sudden load drop after cracking, although after fibre activation the strength increases reaching in

all cases a maximum residual strength at CMODs between 2.5 and 3 mm. This means that polypropylene fibres can still provide residual strength beyond such crack openings. However, the constitutive equation of the MC2010 is defined to reach a maximum strain of 20‰, which makes this constitutive law able to represent the residual strength in a Strength-CMOD curve only up to crack openings of 2.5 mm for standard specimens 150x150x600 mm considering $l_{cs} = 125$ mm. This makes such constitutive law unable to represent larger crack openings, lacking information about the residual strength behaviour beyond 2.5 mm.

The calibration of the parameters of the proposed 3- and 4-point constitutive equations leads to a greater similarity of the analytical Strength-CMOD curves with the experimental ones. For both 3- and 4-point equations, the ultimate strain was increased to 40‰, this entailing that the Strength-CMOD curve can be analytically modelled up to a crack opening of 5 mm.

The calibration of the 3-point equation with respect to the one of the MC2010 mainly consisted in increasing the strain ε_{SLS} from 4‰ to 15‰, so the maximum residual strength could be reached at a wider crack opening, as exhibited in the experimental results. Stresses f_{Fts} were also calibrated by increasing their value between 25% and 43%, being greater the increment for greater contents of fibres. Considering these modifications, the trilinear curve presents greater accuracy for contents of fibres below 5 kg/m^3 (C30/37-2.5, C30/37-3.5, C30/37-5.0, C40/50-5.0 and C60/70-5.0), whereas for contents over 5 kg/m^3 (C40/50-7.5, C40/50-10.0, C60/70-7.5 and C60/70-10.0) the analytical results underestimate the experimental values especially up to 2.5 mm. The results obtained reveal that this underestimation may reach a maximum 17% at a crack opening of 1 mm in C40/50-7.5.

With the aim of reaching to a solution for such underestimation, an additional point was included at the constitutive equation, this leading to a 4-point approach. Adjusting the equation with a 4-point alternative leads to obtain an improved approximation of the analytical results to the experimental values, thus mitigating the differences exhibited by the 3-point constitutive calibrated equation. This 4-point proposed constitutive equation establishes its new intermediate points at strains 10‰ and 25‰. If compared to the 3-point constitutive equation, the 4-point approach provides a greater accuracy especially at the range between 1mm and 2.5 mm of the Strength-CMOD curve. Despite this, the 4-point approach still presents a slight underestimation of the experimental results for contents of fibres over 5 kg/m^3 (C40/50-7.5, C40/50-10.0, C60/70-7.5 and C60/70-10.0), this reaching a maximum value of 11% although only up to a crack opening of 1.5 mm.
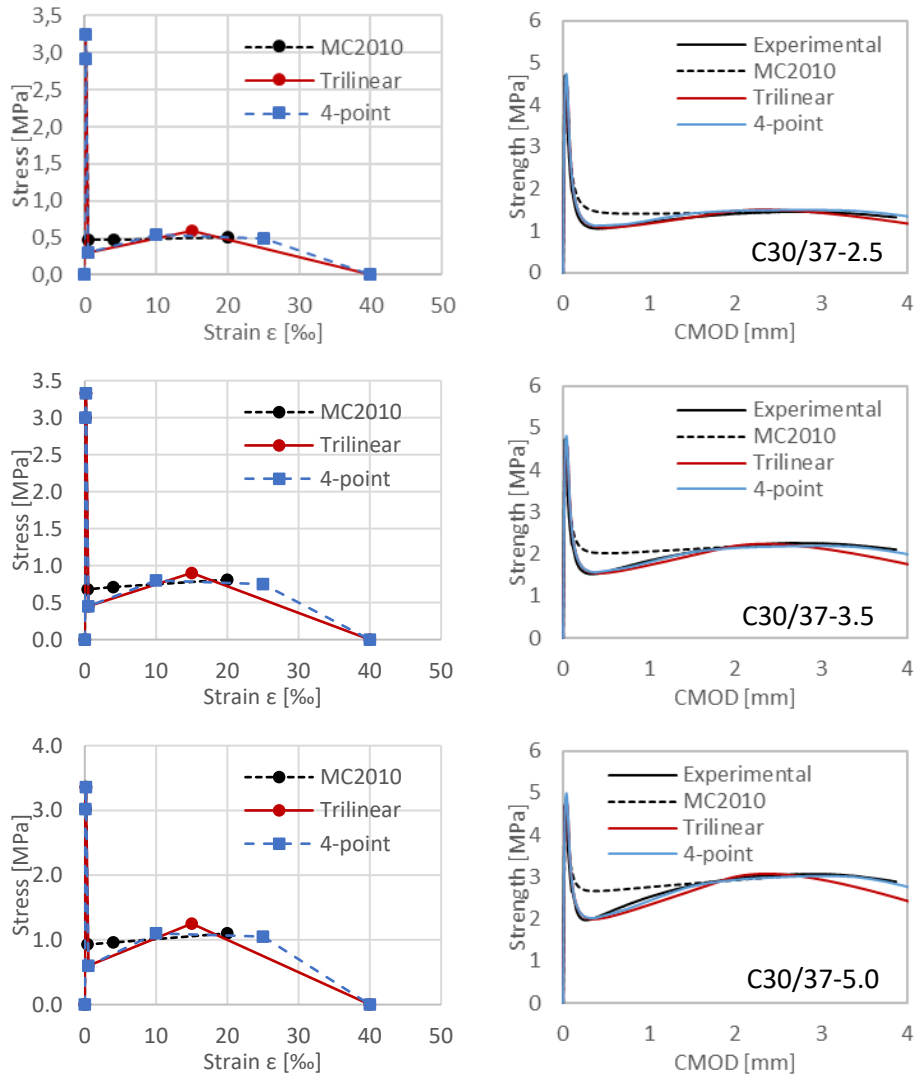
Fig. 3.– Strength-CMOD curves for C30/37-2.5, C30/37-3.5 and C30/37-5.0.
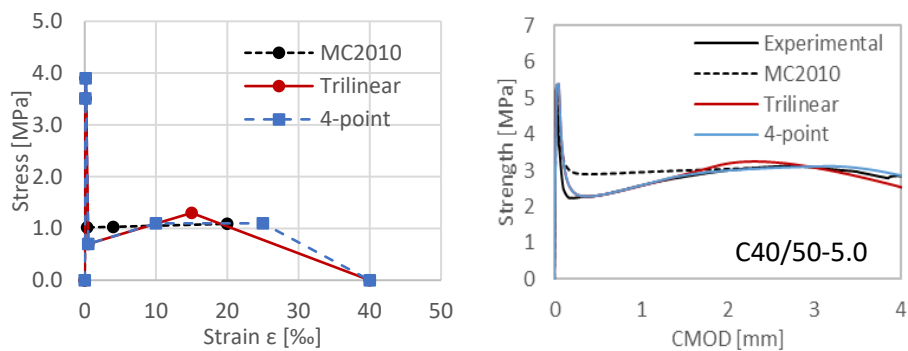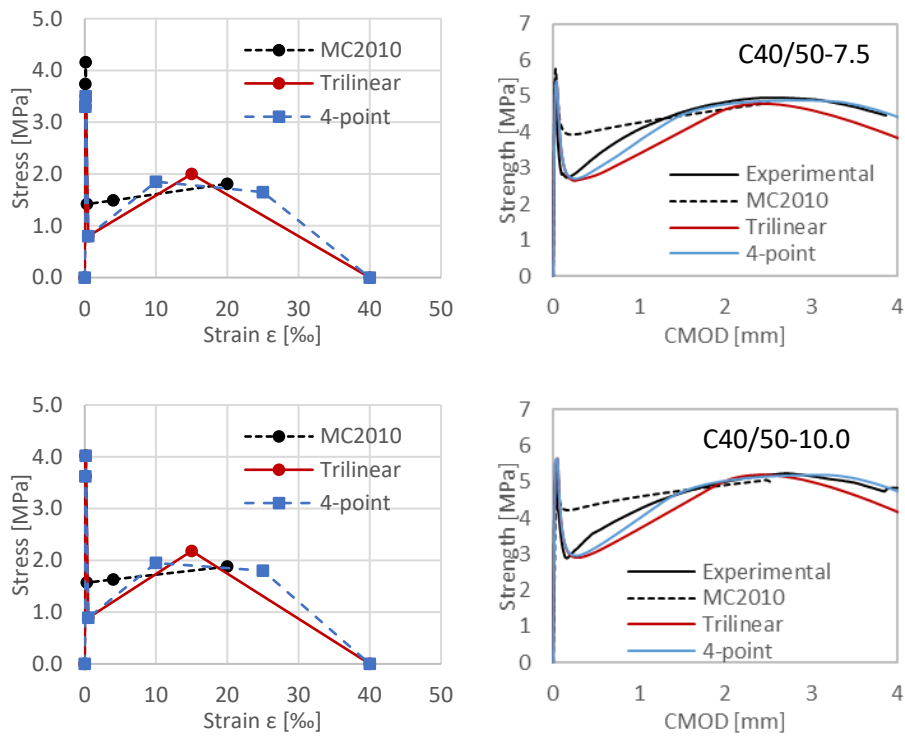
Fig. 4 – Strength-CMOD curves for C40/50-5.0, C40/50-7.5 and C40/50-10.0.
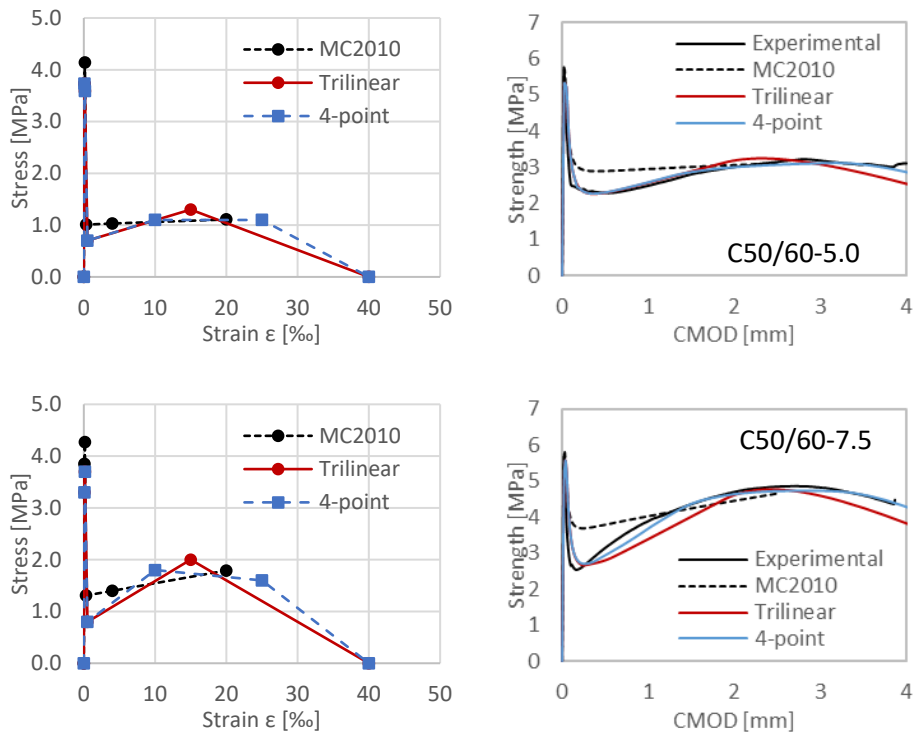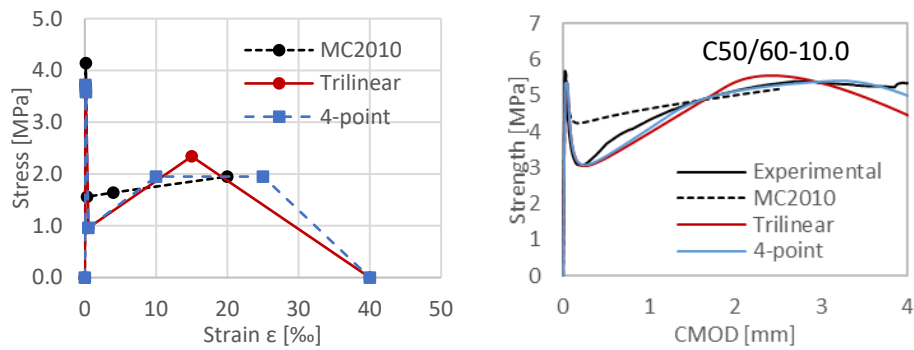
Fig. 5.– Strength-CMOD curves for C50/60-5.0, C50/60-7.5 and C50/60-10.0.

5. CONCLUSIONS

An inverse analysis based on the constitutive equation for FRC of the MC2010 was conducted to determine its suitability when using polypropylene fibres as reinforcement. Based on the results of an experimental program conducted on concretes of different strength classes and contents of polypropylene fibres, the following conclusions can be drawn:

- The MC2010 overestimates the residual strength of polypropylene fibres at small crack openings (SLS), this leading to potential unsafe designs.
- The constitutive model is able to reproduce the Strength-CMOD curves only up to 2.5 mm, this leading to the necessity of extending the ultimate strain ε_{ULS} up to 40‰.
- The calibrated 3-point constitutive model is able to represent accurately the post-cracking results when fibres are used in contents below 5 kg/m^3. For contents of 7.5 and 10.0 kg/m^3, the analytical curves underestimate the experimental results at crack openings under 2.5 mm.
- The proposed 4-point equation presents an improved accuracy of the analytical results. This approach also underestimates the experimental results, although at a less extent than the 3-point equation.

REFERENCES

[1] Pujadas P, Blanco A, Cavalaro S, Aguado A. Plastic fibres as the only reinforcement for flat suspended slabs: Experimental investigation and numerical simulation. Constr Build Mater 2014;57:92–104. https://doi.org/10.1016/j.conbuildmat.2014.01.082.

Alejandro Nogales Arroyo

[2] Pujadas P, Blanco A, Cavalaro S, de la Fuente A, Aguado A. Fibre distribution in macro-plastic fibre reinforced concrete slab-panels. Constr Build Mater 2014;64:496–503. https://doi.org/10.1016/j.conbuildmat.2014.04.067.

[3] Blanco A, Pujadas P, de la Fuente A, Cavalaro S, Aguado A. Application of constitutive models in European codes to RC–FRC. Constr Build Mater 2013;40:246–59. https://doi.org/10.1016/j.conbuildmat.2012.09.096.

[4] International Federation for Structural Concrete. fib Model Code for Concrete Structures 2010. 2010.

[5] EN 14651:2007. Test method for metallic fibre concrete. Measuring the flexural tensile strength (limit of proportionality (LOP), residual). 2007.

[6] de la Fuente A, Aguado A, Molins C, Armengou J. Numerical model for the analysis up to failure of precast concrete sections. Comput Struct 2012;106–107:105–14. https://doi.org/10.1016/j.compstruc.2012.04.007.

[7] Galeote E, Blanco A, de la Fuente A. Design-oriented approach to determine FRC constitutive law parameters considering the size effect. Compos Struct 2020;239:112036. https://doi.org/10.1016/j.compstruct.2020.112036.

[8] de Montaignac R, Massicotte B, Charron J-P. Design of SFRC structural elements: flexural behaviour prediction. Mater Struct 2012;45:623–36. https://doi.org/10.1617/s11527-011-9785-y.

[9] Blanco A, Cavalaro S, de la Fuente A, Grünewald S, Blom CBM, Walraven JC. Application of FRC constitutive models to modelling of slabs. Mater Struct 2015;48:2943–59. https://doi.org/10.1617/s11527-014-0369-5.

A2.2. JOURNAL PAPER IV: EFFECTS OF LOW TEMPERATURES ON FLEXURAL STRENGTH OF MACRO-SYNTHETIC FIBER REINFORCED CONCRETE: EXPERIMENTAL AND NUMERICAL INVESTIGATION

Stanislav Aidarov [a]*, Alejandro Nogales [a], Igor Reynvart [a], Nikola Tošić [b] and Albert de la Fuente [b]

[a]Smart Engineering Ltd., UPC Spin-Off, Jordi Girona 1-3, 08034 Barcelona, Spain

[b]Civil and Environmental Engineering Deparment, Universitat Politècnica de Catalunya (UPC), Jordi Girona 1-3, 08034 Barcelona, Spain

*Corresponding author

ABSTRACT

Fiber reinforced concrete (FRC) is an attractive alternative to traditional steel-bars reinforced concrete structures, as evidenced by a constantly increasing market consumption of structural fibers for this purpose. In spite of significant research dedicated to FRC, less attention has been given to the effects of low temperatures on the mechanical properties of FRC, which can be critical for a variety of structural typologies and regions. With this in mind, an experimental program was carried out to assess the flexural behavior of macro-synthetic fiber reinforced concrete (MSFRC, hereinafter) at different temperatures (from 20°C to –30°C) by means of three-point bending notched beams tests. The tested MSFRCs were produced varying the content of polypropylene fibers (4 and 8 kg/m^3). The results allowed proving that the flexural strength capacity of all MSFRCs improved with decreasing temperature. Finite element analyses were then used to calibrate constitutive models following *fib* Model Code 2010 guidelines and to formulate empirical adjustments for taking into account the effects of low temperatures. The outcomes of this research are the basis for future experimental and numerical efforts meant to improve the design of MSFRCs to be subjected to low temperatures during service conditions.

KEYWORDS: polymeric fiber reinforced concrete, experimental program, temperature variation, residual tensile strength, one-way element, beam, non-linear analysis, modeling

1.   INTRODUCTION

Alejandro Nogales Arroyo

Fiber reinforced concrete (FRC) is one of several new types of innovative concretes that can be used for structural purposes in accordance with a number of national and international codes, guidelines, and design recommendations [1–6]. The incorporation of fibers in cement-based composites allows the partial or even total substitution of traditional reinforcement (reinforcing steel bars) with a positive effect on fracture energy of the matrix [7], cracking control [8–10], fire resistance [11], fatigue [12,13], redistribution capacity [14], and impact resistance [15,16]. As a result, the application of FRC is already observed in a multitude of structural elements, such as precast tunnel segments [17–19], elevated flat slabs [20–22], reinforced earth-retaining walls [23], and ground-supported flats slabs for industrial applications [24,25].

Moreover, numerous research programs are focused on the material characterization of FRC [26–30] and further elaboration of design approaches [31–35] to suitably evaluate the response of FRC elements under diverse load/boundary conditions. However, the majority of research studies tend to evaluate the mechanical performance of FRC subjected to normal temperature conditions or high/extremely high (fire) temperatures. In contrast, the behavior of FRC at low temperatures is scarcely analyzed, although there are a number of possible scenarios in which it would be essential to adequately predict its structural response under relatively adverse conditions, e.g. (1) storage (Figure 1), handling and transportation of precast tunnel segments in cold regions or (2) service life of industrial floors for cold-storage warehouses.

Figure 1 – Precast concrete elements subjected to low temperatures (reproduced with permission from [36])

Drawing an analogy with plain or traditionally reinforced concrete under these conditions, an increase in compressive and tensile strength can be expected [53,54] along with the embrittlement of a concrete matrix [55]. Taking into account the increased tensile strength of the material, sufficient ductility to the structural element must be provided by the reinforcement once cracking occurs. In the case of FRC, residual tensile strength is mainly responsible for the post-cracking behavior of the material—this property should also be improved as the matrix–fiber interaction

enhances with decreasing temperatures as long as the mechanical properties of the fibers are not negatively affected by external conditions.

However, to the authors' best knowledge, only a few experimental investigations were dedicated to examining the influence of low temperatures on the post-cracking response of FRC with moderate values of compressive strength (up to 60 MPa). Pigeon and Cantin [56] highlighted the slight and significant increase in steel fiber reinforced concrete (SFRC) toughness at −10 °C and −30 °C, respectively. Caballero-Jorna et al. [57] emphasized a minor enhancement of the post-cracking flexural strength of SFRC and MSFRC at −15 °C, whereas Richardson and Ovington [58], on the contrary, stressed a considerably greater flexural strength of both SFRC and MSFRC at −20 °C. Despite the obtained results, there is still a lack of information for modeling possible "temperature–post-cracking flexural strength" relationships for different types of FRC and, more importantly, the adjusted designed procedures to suitably predict the structural response of FRC at low temperatures have still not been analyzed.

With this in mind, the presented research study was conducted, this being comprised of two main parts. Primarily, an experimental program was carried out in order to characterize pre- and post-cracking flexural behavior of FRC at different temperatures (from 20 °C to −30 °C): the standardized three-point bending test (3PBT) on a notched beam ($150 \times 150 \times 600$ mm^3) according to EN 14651 [59]. For the sake of more detailed analysis, two types of FRC were characterized: MSFRC with fiber contents of 4 kg/m^3 (MSFRC-4) and 8 kg/m^3 (MSFRC-8).

Thereafter, multi-linear constitutive models were derived pursuant to the *fib* Model Code 2010 [1] in order to simulate experimentally obtained "load–displacement" curves at 20 °C, 0 °C, −10 °C, and −30 °C. Moreover, correction factors to the elaborated constitutive diagrams were identified with the aim of fitting the numerical prediction to the real behavior of the tested beams.

2.   EXPERIMENTAL PROGRAM

2.1.   CONCRETE MIX

The adopted mix (Table 1) corresponded to the normal strength concrete and S3 consistency class, i.e. the measured slump was between 100 and 150 mm [44]. A Portland cement type CEM II-A/L was used for producing the MSFRC mixes. The concrete matrix consisted of three aggregate sizes: sand 0/4, gravel 4/10, and gravel 10/20 from crushed calcareous stone. A lignosulphonate-based plasticizer (POZZOLITH 7003) and a polycarboxylate-based superplasticizer (MASTERASE 3850) were also added during the material elaboration in order to provide the required workability of the mix.

Table 1 – Composition of studied MSFRC

Alejandro Nogales Arroyo

Materials	MSFRC-4	MSFRC-8
CEM II-A/L 42.5R (kg/m³)	310	310
Coarse aggregate 10/20 (kg/m³)	690	680
Coarse aggregate 4/10 (kg/m³)	127	125
Fine aggregate 0/4 (kg/m³)	1025	1025
Water-cement ratio	0.58	0.58
Additives (% on cement content)	1.2	1.5
Synthetic fibers (kg/m³)	4	8

Based on the described concrete composition, two types of FRC were produced: polypropylene fiber-reinforced concrete with a fiber content of (1) 4 kg/m^3 (volume fraction 0.425%) and (2) 8 kg/m^3 (volume fraction 0.850%); Table 2 gathers the essential properties of the used polypropylene fiber (PPF). MSFRC-4 was oriented to industrial floors in which only the minimum reinforcement is required to control cracking due to thermal–hydrometric (temperature and shrinkage gradients) phenomena. In turn, MSFRC-8 was selected to reproduce medium-heavy duty pavements, which, apart from the previously mentioned indirect loads, could be subjected to external loads of notable magnitude.

Table 2 – Properties of the implemented fiber

Property	PPF	Representation
Material	Transparent polypropylene	
Shape	Embossed monofilament	
Diameter (mm)	0.85	
Length (mm)	48	
Aspect ratio	56.5	
Number of fibers per kg	41200	
Tensile strength (MPa)	>400	

2.2. TEST SETUP AND TESTING PROCEDURE

The structural response of the elaborated MSFRC mixes in terms of flexural pre- and post-cracking strengths was analyzed at 20 °C (reference temperature), 0 °C, −10 °C, and −30 °C. This mechanical property of the studied MSFRC was assessed in compliance with EN 14651 [59] (Figure 2a) by testing six notched prismatic beams (150 × 150 × 600 mm) for each temperature magnitude, resulting in 48 tested samples. The casting and demolding (in 24 h) of the prismatic beams in question were followed by the curing of these specimens in a temperature (20 °C) and humidity (95%) controlled chamber for 28 days.

Thereafter, three-quarters of all beams were placed in a laboratory freezer, and each quarter was cooled to 0 °C, −10 °C, and −30 °C, respectively. Importantly, the prismatic samples were equipped with a thermocouple in order to guarantee the target test temperature and, additionally, to monitor its evolution (Figure 2b). Once the required temperature was reached, the specimens were placed in an INSTRON 8505 testing machine (Figure 2c) equipped with a load cell of 100 kN in order to estimate the flexural behavior. The parameters of major concern within the testing procedure were the limits of proportionality (f_{LOP}), f_{R1}, and f_{R3}; f_{LOP} represented the pre-cracking flexural behavior, whereas the residual tensile strengths f_{R1} and f_{R3} were used to derive the constitutive models of the MSFRC for design purposes, being related with serviceability and ultimate limit states, respectively.

Figure 2 – a) 3PBT at 20°C; b) Freezing procedure and temperature monitoring; c) 3PBT at –30°C

3. EXPERIMENTAL RESULTS AND DISCUSSIONS

Figure 3 gathers responses obtained by means of the 3PBT in terms of pre- and post-cracking strength and crack mouth opening displacement (CMOD); average values are highlighted by red lines (based on six tested specimens for each case), whereas result scatter (envelope) is represented by a shaded area. Primarily, pre-cracking behavior was assessed for both MSFRC-4 and MSFRC-8. Taking into consideration that this mechanical property is mainly dependent on the material matrix [61,62] (amount of cement paste and granular skeleton), similar results were expected regardless of the fiber content.

This expectation was proven accurate, as seen in Figure 4—the limit of the proportionality of MSFRC-4 and MSFRC-8 at the reference temperature was almost identical. Decreasing the temperature to the threshold value for water to start freezing (0°C), f_{LOP} started increasing by 15.8% and 47.0% for MSFRC-4 and MSFRC-8, respectively. Further reduction in the temperature led to a significant enhancement of f_{LOP}: a total increment of 67.7% and 66.5% was detected for the above listed materials at –10°C, whereas the temperature magnitude of –30°C entailed an increment of 68.5% and 73.2% for MSFRC-4 and MSFRC-8, respectively (comparing with f_{LOP} at 20°C).

Thereafter, the effect of the temperature variation on the residual tensile strengths (f_{R1}, f_{R3}) was estimated. This mechanical parameter, apart from the characteristics of the concrete matrix, depends on a certain number of factors, such as the mechanical properties of the implemented fibers, fiber geometry (having a main effect on anchorage and bond capacity), and fiber distribution and orientation within the critical section. Therefore, the analysis of post-cracking behavior of FRC at low temperatures is a challenging aspect to be investigated.
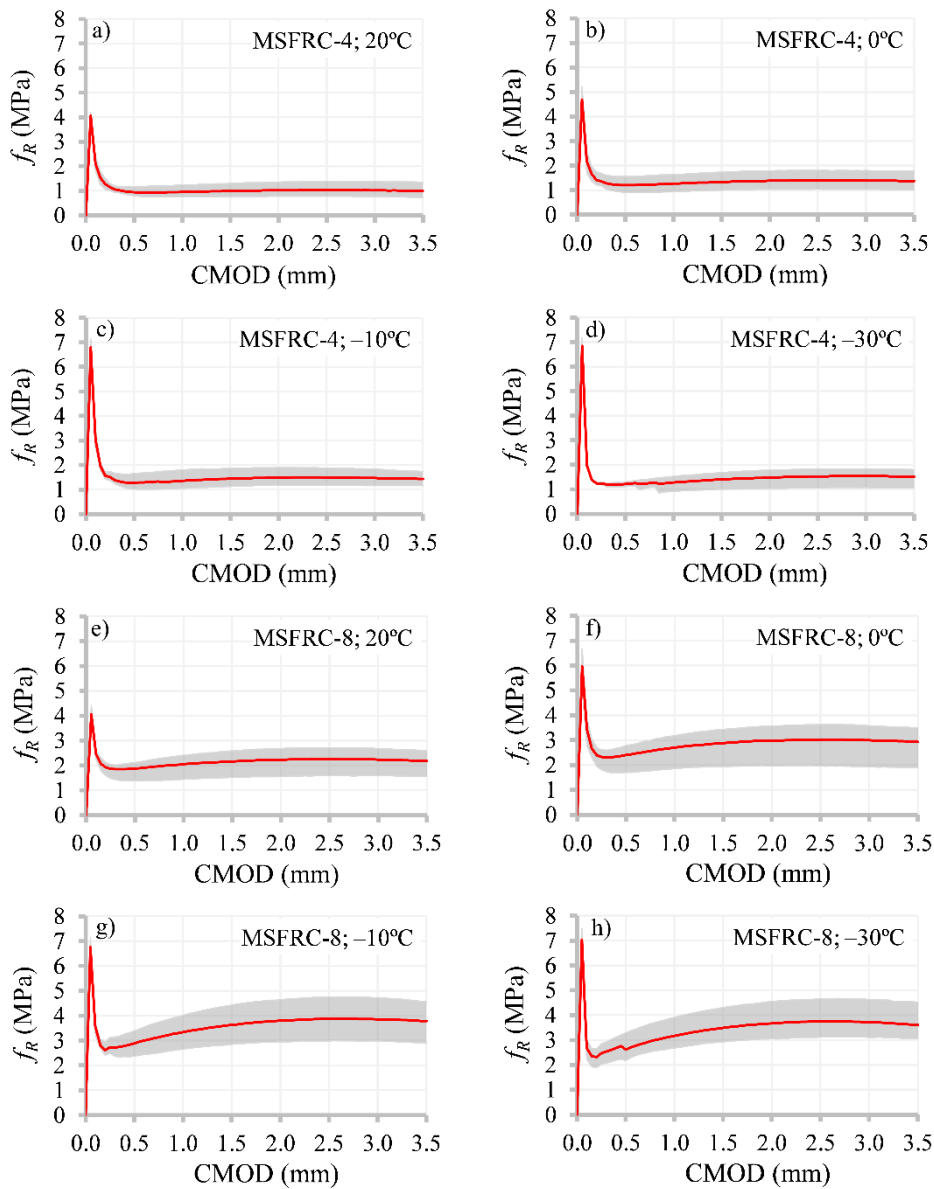
Figure 3 – Flexural pre- and post-cracking strength at different temperatures of: a-d) MSFRC-4; e-f) MSFRC-8
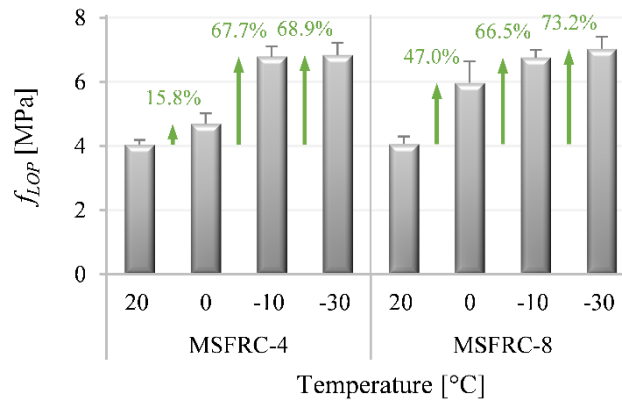
Figure 4 – Mean values of f$_{LOP}$ with corresponding standard deviations of the studied MSFRCs at different temperatures

The results that can serve as a base for further investigations are presented in Figure 5. Analyzing the observed structural response of the tested FRC beams, the positive effect of the low temperatures on the required energy to produce fiber pull-out can be emphasized, i.e. the concrete matrix that embeds the fibers shrinks with the decrease of the temperature, provoking an increase of the confinement pressure along the fibers and, thus, enhancing the anchorage capacity of fibers. This phenomenon, in turn, improves the post-cracking flexural behavior as it was depicted in [47,48]. Importantly, the studied range of temperatures had no negative influence (detectable) on the mechanical properties of the implemented fibers and, thereby, on the overall performance of the studied FRC beams.
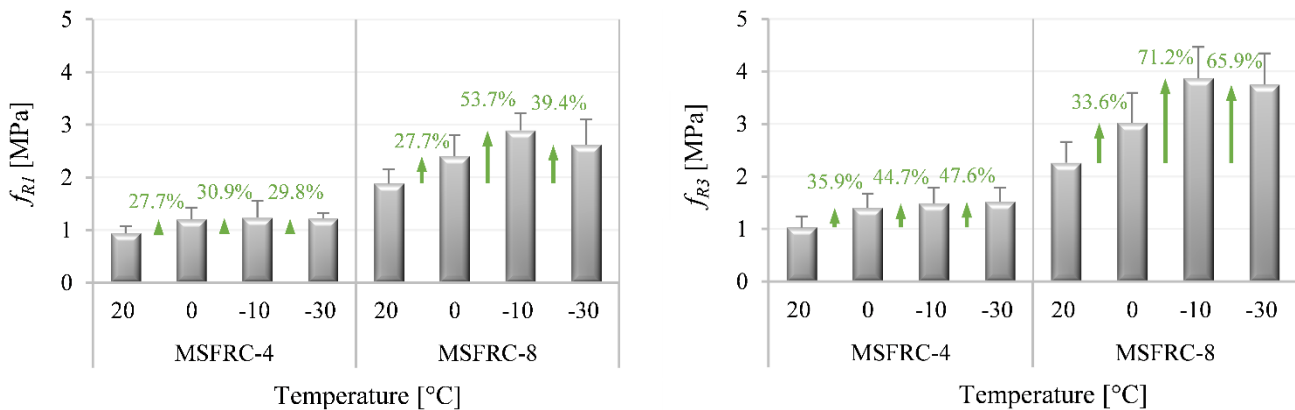
Figure 5 – Mean values of f$_{R1}$ and f$_{R3}$ with corresponding standard deviations of the studied MSFRCs at different temperatures

Additionally, Additionally, the effect of the higher fiber content on the enhancement rate of the residual tensile strength (due to temperature reduction) can be stressed: the relatively moderate values of residual tensile strengths in the case of MSFRC-4 did not ensure the continuous increment of post-cracking strength, i.e., both *f$_{R1}$* and *f$_{R3}$* presented similar enhancements of this parameter in the range between 0 °C and −30 °C. Contrarily, MSFRC-8 evidenced a significant

increment of residual tensile strengths once temperatures surpassed the threshold temperature magnitude of 0°C—up to 71.2% in comparison with the reference values (at 20 °C). Moreover, the greater increase in f_{R3} should be highlighted, opposing the enhancement rate due to low temperatures to the increase in f_{R1}—this phenomenon results from the improvement of the bond capacity in the matrix–fiber interaction that is generally a governing failure mechanism (fiber debonding).

Although the obtained experimental outcome clearly evidenced the increase in pre- and post-cracking flexural strength of the given FRCs, further studies are required to extend the database related to the effect of low temperatures on flexural capacity of the material in question, varying temperature magnitudes, concrete mixes, and fiber type/contents. This will allow to propose a relationship between temperature variation and the flexural strength of FRCs; this relationship, in turn, will allow to characterize the materials at ambient conditions with a subsequent estimation of their potential behavior at more severe conditions.

4. NUMERICAL ANALYSIS

In In previous sections, experimental tests have proven the positive effect of low temperatures on FRC by increasing post-cracking strength. Based on the authors' experience, the FRC constitutive equation proposed in the *fib* Model Code 2010 [1], which was set as a reference for design engineers and practitioners to take into account the post-cracking behavior of FRC, needs to be adjusted in order to properly reproduce the latter. The adjustments usually adopted in MSFRC are to reduce residual strength at early stages (for CMOD < 0.5 mm) since the constitutive equation tends to overestimate the flexural post-cracking capacity after cracking, whereas the behavior at larger crack openings tends to be underestimated, and the residual strength needs to be increased [65,66]

With that in mind, this section presents a non-linear finite element (FE) simulation to obtain and assess the ratio of residual strength (obtained by means of a numerical simulation) to experimental residual strength ($f_{R,NL}/f_{R,EXP}$) for the FRC mixes (MSFRC-4 and MSFRC-8) tested at different temperatures. In order to derive these $f_{R,NL}/f_{R,EXP}$ ratios, the strategy adopted is the following: first, non-linear simulations of a beam flexural post-cracking strength test were carried out implementing an FRC-constitutive relationship according to *fib* Model Code 2010 [1]. Figure 6 depicts the schematic representation of the stress-crack width curve for FRC according to the *fib* Model Code 2010 [1]. A full curve is obtained as the combination of the post-cracking response of plain concrete (where f_{ctm} and G_F stand for mean tensile concrete strength and fracture energy, respectively) and the fiber contribution through the pull-out mechanism, the first point being $\sigma_1 = f_{ctm}$ and $w_1 = 0$ mm, the second point σ_2 and w_2 (the intersection between the two curves), and the third one $\sigma_3 = f_{ctm}$ and $w_3 = 2.5$ mm. Moreover, since the results did not fit the

experimental ones well, the f_{R1} and f_{R3} coefficients (to derive constitutive curves according to the *fib* Model Code 2010 constitutive equations) were modified so that the resulting curves fit the values at CMOD of 0.5 and 2.5 mm, which are the crack openings for serviceability and ultimate limit states, respectively. The latter task was undertaken by implementing a back analysis by an iterative trial and error process.
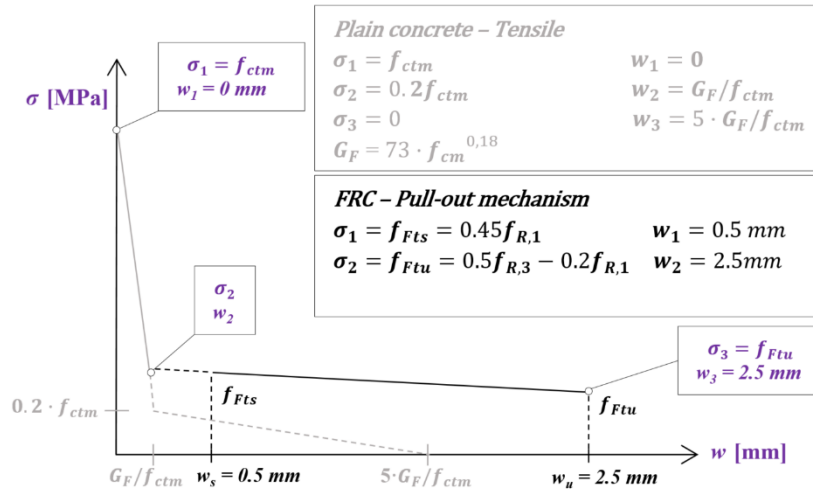
Figure 6 – fib MC-2010 [1] FRC tensile constitutive equation.

In order In order to carry out the numerical analysis, non-linear simulations were implemented by means of the commercial finite element (FE) software ABAQUS CAE 2016 [67], as its adequacy in properly reproducing the post-cracking flexural performance of FRC has been successfully proven through an available Concrete Damaged Plasticity (CDP) numerical model [20,66]. CDP is a smeared crack plasticity-based numerical model, which assumes that the main two failure mechanisms are tensile cracking and concrete crushing. Input data are required in terms of uniaxial stress-strain (σ–ε) curves for both tensile and compressive behavior. In this study, in order to minimize mesh dependence due to different mesh size, the stress-crack width (σ–w) tensile curve was used instead of σ–ε [67]. The compressive constitutive curve adopted was proposed in the *fib* Model Code 2010 [1], and the CDP magnitude of the parameters adopted for all the simulations were those proposed in ABAQUS Users' Manual [67] for plain concrete, which can be found elsewhere [68].

The adopted 2D model considering plain strain conditions is depicted in Figure 7, which shows the loading and boundary conditions along with the mesh. In agreement with the experimental test, the boundary conditions were imposed so that vertical displacement was restrained ($U_y = 0$) at both supports and horizontal displacement ($U_x = 0$) in one of them. The loading was applied by means of displacement control using an explicit dynamic algorithm (quasi-static analysis) in order to properly capture the post-cracking performance of FRC. The mesh comprised 485 nodes and 886 triangular linear elements (CPE3) with a mesh size of 20 mm, refined in the mid-section with

5 mm size elements, wherein the mesh size was determined after carrying out a mesh sensitivity analysis.
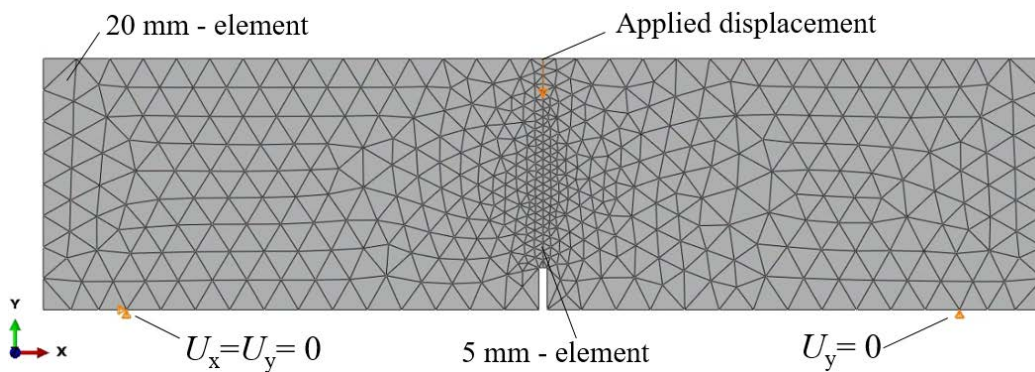
Figure 7 – 2D FEM model adopted: mesh and boundary conditions considered

The results of the non-linear simulations for MSFRC-4 and MSFRC-8 for all temperatures are plotted in Figure 8. The load–CMOD graphs include three curves: experimental results and two from non-linear simulations (1) implementing the *fib* Model Code [1] constitutive equation (FE MC-2010, derived using f_{R1} and f_{R3} obtained from the experimental tests presented in Section 3) and (2) using the constitutive curve (FE MC-2010 Modified), adjusted so that the results fit the experimental curve at 0.5 and 2.5 mm. As can be seen, the simulations with FE MC-2010 Modified only fit the experimental data at these points, and hardening is produced in a linear way. Based on the authors' experience, in those cases where the hardening is produced in a curved way, more points would be necessary in the constitutive equation in order to better adjust the experimental outcome [65,66].

It is worth noticing that the ultimate displacement in the *fib* Model Code [1] constitutive curve is 2.5 mm (set as the stress for ultimate limit state analysis). However, in this research study, after 2.5 mm, the constitutive curve smoothly decreases to zero stress, set at $w = 5$ mm, in order to better capture the flexural bearing capacity of MSFRC at latter stages. Without the last branch of the curve, the maximum post-cracking load of the tests, after the drop due to cracking, cannot be captured since it is produced for crack openings higher than 2.5 mm [65,66].

Table 3 gathers more detailed information regarding f_{R1} and f_{R3} parameters for MSFRC-4 and MSFRC-8, respectively. These parameters were used for deriving the constitutive curves obtained from the experimental data and by means of the back analysis. In addition, the table also presents the $f_{R,NL}/f_{R,EXP}$ ratios for each MSFRC mix and temperature.

Based on the outcome presented in the table, it can clearly be seen that the ranges of the $f_{R,NL}/f_{R,EXP}$ ratios for either f_{R1} or f_{R3} are quite narrow, particularly for f_{R1}. In this sense, it could be stated that the $f_{R,NL}/f_{R,EXP}$ ratios are constant despite the increasing post-cracking strength with

decreasing temperature. In view of this, in cases where no data are available for low temperatures, and the structure is expected to be subjected to large temperature variations, the same $f_{R,NL}/f_{R,EXP}$ ratio (for either f_{R1} and f_{R3}) at reference temperature could be taken for the MSFRC design.
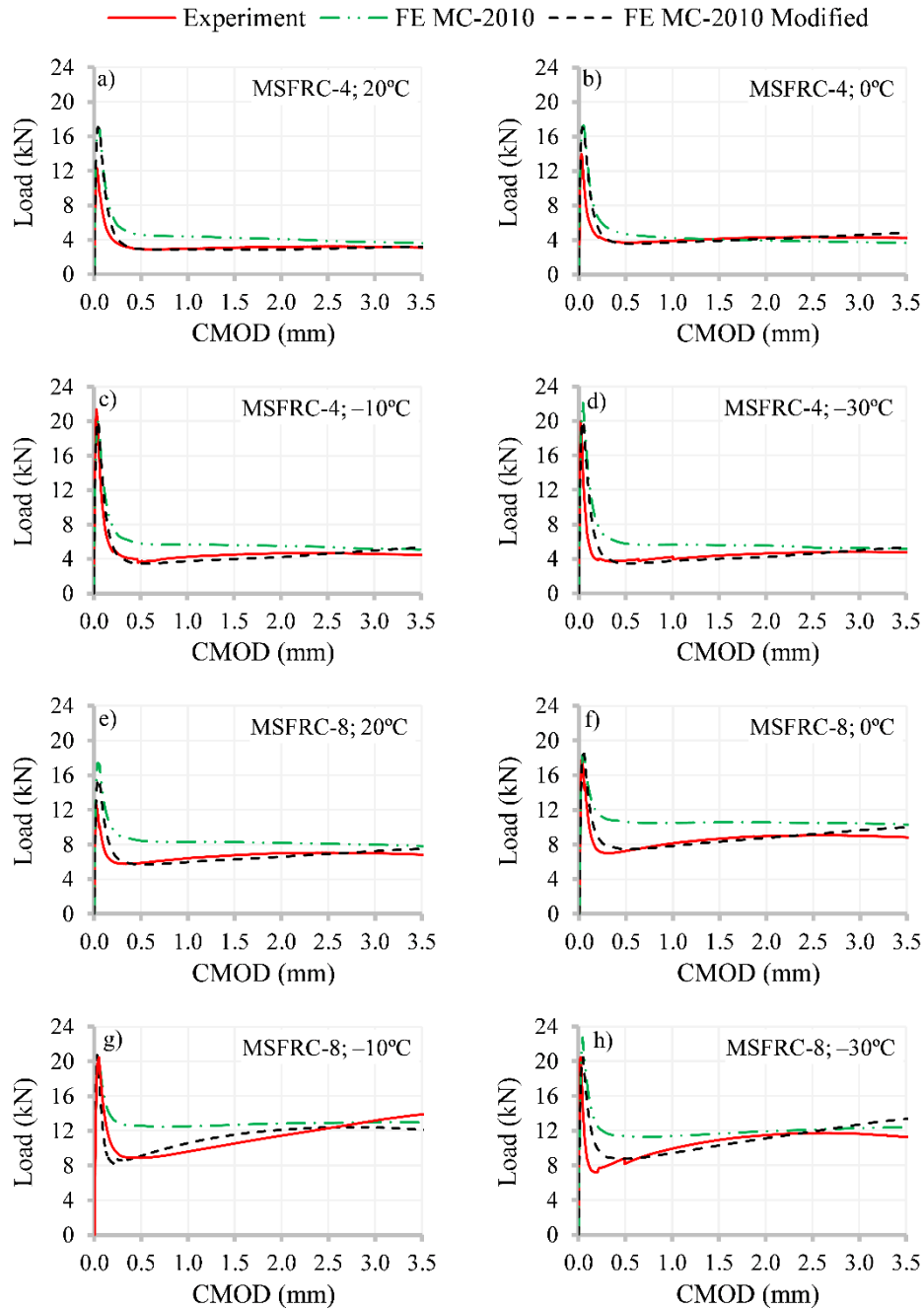
Figure 8 – Results for MSFRC-4 and MSFRC-8 at studied temperatures in terms of "Load – CMOD"

Table 3 – f_{RNL}/f_{REXP} ratio for MSFRC-4 and MSFRC-8 at studied temperatures

Temperature	MSFRC-4	MSFRC-8

	(°C)	$f_{R,EXP}$ (MPa)	$f_{R,NL}$ (MPa)	$f_{R,NL}/f_{R,EXP}$	$f_{R,EXP}$ (MPa)	$f_{R,NL}$ (MPa)	$f_{R,NL}/f_{R,EXP}$
f_{R1}	20	0.94	0.60	**0.64**	1.88	1.35	**0.72**
	0	1.20	0.80	**0.67**	2.4	1.80	**0.75**
	−10	1.23	0.80	**0.65**	2.89	2.25	**0.78**
	−30	1.22	0.80	**0.66**	2.83	2.25	**0.80**
f_{R3}	20	1.03	1.03	**1.00**	2.26	2.40	**1.06**
	0	1.40	1.60	**1.14**	3.02	3.20	**1.06**
	−10	1.49	1.80	**1.21**	3.87	4.60	**1.19**
	−30	1.52	1.80	**1.18**	3.75	4.60	**1.23**

In order to verify this assumption, in Figure 9 were plotted the FE simulations using the residual strengths from the tests at each temperature and multiplied by the $f_{R,NL}/f_{R,EXP}$ ratio (for either f_{R1} and f_{R3}) at 20 °C (i.e., $f_{R1,NL}/f_{R1,EXP}$ = 0.65 and 0.75 for MSFRC-4 and MSFRC-8, respectively, and $f_{R3,NL}/f_{R3,EXP}$ = 1.10 for both solutions). As can be seen, the differences at CMOD 0.5 and 2.5 mm have a deviation lower than 10% in all cases (Figure 9) which is assumed to be acceptable for engineering design. Moreover, taking into consideration the scatter in the experimental tests of MSFRC post-cracking performance, these new simulations are inside the envelope, which means that this approach is representative of the mechanical performance of each solution of MSFRC.

It It is worth noticing that, in a hypothetical situation in which no tests were performed at low temperatures, f_{R1} and f_{R3} at different temperatures could be obtained based on the established relationship "temperature variation–flexural strength" that is to be elaborated once the broader database of the experimental results is developed, as proposed in Section 3.
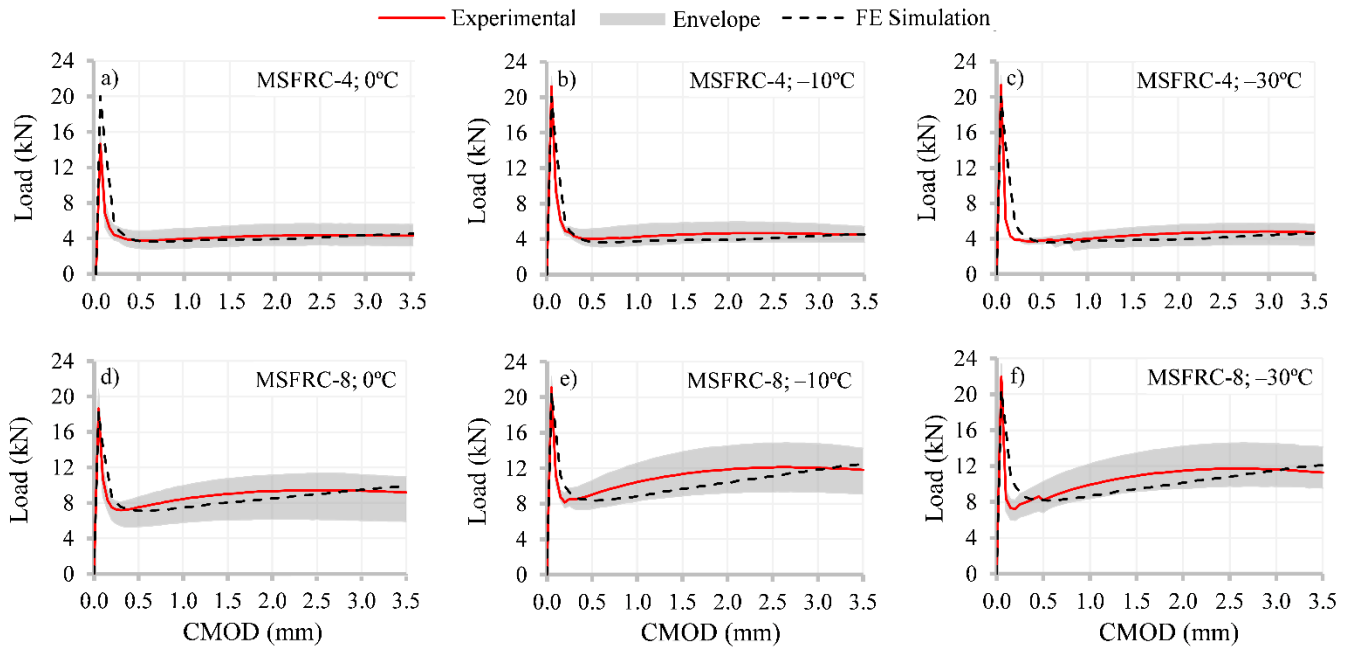
Figure 8 – Results in terms of Load – CMOD for MSFRC-4 and MSFRC-8 using $f_{R,NL}/f_{R,EXP}$ at reference temperature to derive the constitutive curves.

5. CONCLUSIONS

In this paper, an experimental program was described with a following analysis of low temperature effects on the pre- and post-cracking flexural behavior of macro-synthetic fiber reinforced concrete (MSFRC). In total, 48 prismatic notched beams were tested under a three-point bending configuration, varying temperatures from 20°C to –30°C. Moreover, numerical analyses were performed to verify the suitability of the current constitutive models suggested by the *fib* Model Code 2010 for simulating the pre- and post-cracking response of the MSFRCs tested at low temperatures. The following conclusions may be derived from the obtained results:

- Low temperatures led to an increase of the required energy to produce fiber pull-out and, therefore, post-cracking flexural behavior was enhanced: f_{R1} and f_{R3} increased up to 54% and 71%, respectively, for temperatures below 0°C.

- A higher increase of f_{R3} at low temperatures (in comparison with the observed values of f_{R1}) was appreciated for all studied cases due to the confinement effect caused by the shrinkage of the matrix embedding the fibers. This effect seemed to lead to a higher fiber bond (higher matrix-fiber friction). This outcome is of paramount importance for design procedures at ultimate conditions.

- The numerical analysis conducted adopting the multi-linear constitutive model that is suggested by the *fib* Model Code 2010 evidenced a certain overestimation of the real flexural behavior in case of studied MSFRC prismatic beams. This phenomenon led to the requirement of introducing correction factors to properly simulate the structural

response of the elements in question. Importantly, the imposed correction factors (for both f_{R1} and f_{R3}) were almost identical despite the temperature variation, although the fiber content did have an effect on these values.

The outcome of the described research program reveals the enhanced performance of the given FRCs in terms of pre- and post-cracking flexural strengths – therefore, these phenomena should be taken into account during the design procedures of the elements that are to be subjected to low temperatures during transient or in-service conditions. However, further investigation is required to expand the experimental database related to the behavior of FRCs at low temperatures. This will allow to evaluate the "temperature – pre- and post- flexural strength" relationships so the designers and practitioners will only need to carry out the characterization of the required material at ambient conditions (20°C) in order to adequately predict the structural behavior at low temperatures.

REFERENCES

[1] Fib. fib Model Code for Concrete Structures 2010; International Federation for Structural Concrete (FIB): Lausanne, Switzerland, 2013; ISBN 9783433030615.

[2] Spanish Ministry of Public Works. Code on Structural Concrete, EHE-08, Permanent Commission of the Concrete; Spanish Ministry of Public Works: Madrid, Spain, 2008

[3] RILEM. Bending Test: Final Recommendations; RILEM TC-162-TDF. Mater. Struct. 2002, 35, 579–582.

[4] Italian National Research Council CNR. CNR-DT 204/2006 Guide for the Design and Construction of Fiber-Reinforced Concrete Structures; Consiglio Nazionale Delle Riserche Rome, Italy, 2006.

[5] DBV. Guide to Good Practice Steel Fibre Concrete; German Society for Concrete and Construction Technology: Berlin, Germany, 2001.

[6] ACI Committee 544. Report on Design and Construction of Steel Fiber-Reinforced Concrete Elevated Slabs; American Concrete Institute: Farmington Hills, MI, USA, 2004. ISBN 9781942727323.

[7] Zollo, R.F. Fiber-reinforced Concrete : an Overview after 30 Years of Development. Cem. Concr. Compos. 1997, 19, 107–122.

[8] Groli, G.; Pérez, A.; Marchetto, F.; Aríñez, F. Serviceability performance of FRC columns under imposed displacements : An experimental study. Eng. Struct. 2015, 101, 450–464, doi:10.1016/j.engstruct.2015.07.035.

[9] Pujadas, P.; Blanco, A.; de la Fuente, A.; Aguado, A. Cracking behavior of FRC slabs with traditional reinforcement. Mater. Struct. Constr. 2012, 45, 707–725, doi:10.1617/s11527-011-9791-0.

[10] Tiberti, G.; Minelli, F.; Plizzari, G.A.; Vecchio, F.J. Influence of concrete strength on crack development in SFRC members. Cem. Concr. Compos. 2014, 45, 176–185, doi:10.1016/j.cemconcomp.2013.10.004.

[11] Conforti, A.; Zerbino, R.; Plizzari, G.A. Influence of steel, glass and polymer fibers on the cracking behavior of reinforced concrete beams under flexure. Struct. Concr. 2018, 20, 133–143, doi:10.1002/suco.201800079.

[12] McMahon, J.A.; Birely, A.C. Service performance of steel fiber reinforced concrete (SFRC) slabs. Eng. Struct. 2018, 168, 58–68, doi:10.1016/j.engstruct.2018.04.067.

[13] Serrano, R.; Cobo, A.; Prieto, M.I.; de las Nieves González, M. Analysis of fire resistance of concrete with polypropylene or steel fibers. Constr. Build. Mater. 2016, 122, 302–309. https://doi.org/10.1016/j.conbuildmat.2016.06.055.

[14] Jin, L.; Zhang, R.; Dou, G.; Du, X. Fire resistance of steel fiber reinforced concrete beams after low-velocity impact loading. Fire Saf. J. 2018, 98, 24–37, doi:10.1016/j.firesaf.2018.04.003.

[15] Khaliq, W.; Kodur, V.; Asce, F. Effectiveness of Polypropylene and Steel Fibers in Enhancing Fire Resistance of High-Strength Concrete Columns. J. Struct. Eng. 2018, 144, 1–12, doi:10.1061/(ASCE)ST.1943-541X.0001981.

[16] Carlesso, D.M.; de la Fuente, A.; Cavalaro, S.H.P. Fatigue of cracked high performance fiber reinforced concrete subjected to bending. Constr. Build. Mater. 2019, 220, 444–455, doi:10.1016/j.conbuildmat.2019.06.038.

[17] Germano, F.; Tiberti, G. Post-peak fatigue performance of steel fiber reinforced concrete under flexure. Mater. Struct. 2015, 49(10), 4229–4245, doi:10.1617/s11527-015-0783-3.

[18] Fall, D.; Shu, J.; Rempling, R.; Lundgren, K.; Zandi, K. Two-way slabs: Experimental investigation of load redistributions in steel fibre reinforced concrete. Eng. Struct. 2014, 80, 61–74.

[19] Mahmood, S.M.F.; Foster, S.J.; Valipour, H. Moment redistribution and post-peak behaviour of lightly reinforced-SFRC continuous slabs. Eng. Struct. 2021, 232, 111834, doi:10.1016/j.engstruct.2020.111834.

[20] Nogales, A.; Tošić, N.; de la Fuente, A. Rotation and moment redistribution capacity of fibre reinforced concrete beams: Parametric analysis and code compliance. Struct. Concr. 2021 (Online version before inclusion in an issue). https://doi.org/10.1002/suco.202100350.

[21] Venkateshwaran, A.; Tan, K.H. Moment redistribution in continuous steel-fibre-reinforced concrete slabs. Struct. Build. 2020, 173, 161–174, doi:https://doi.org/10.1680/jstbu.17.00152.

[22] Nia, A.A.; Hedayatian, M.; Nili, M.; Sabet, V.A. An experimental and numerical study on how steel and polypropylene fibers affect the impact resistance in fiber-reinforced concrete. Int. J. Impact Eng. 2012, 46, 62–73, doi:10.1016/j.ijimpeng.2012.01.009.

[23] Teng, T.; Chu, Y.-A.; Chang, F.-A.; Shen, B.-C.; Cheng, D.-S. Development and validation of numerical model of steel fiber reinforced concrete for high-velocity impact. Comput. Mater. Sci. 2008, 42, 90–99, doi:10.1016/j.commatsci.2007.06.013.

[24] Rai, B.; Singh, N.K. Statistical and experimental study to evaluate the variability and reliability of impact strength of steel-polypropylene hybrid fiber reinforced concrete. J. Build. Eng. 2021, 44, 102937, doi:10.1016/j.jobe.2021.102937.

[25] Vivas, J.C.; Zerbino, R.; Torrijos, M.; Giaccio, G. A test procedure for evaluating the impact behaviour of fibre reinforced concrete. Mater. Struct. 2021, 54, 208. doi:10.1617/s11527-021-01804-9.

[26] Liu, X.; Sun, Q.; Yuan, Y.; Taerwe, L. Comparison of the structural behavior of reinforced concrete tunnel segments with steel fiber and synthetic fiber addition. Tunn. Undergr. Space Technol. 2020, 103, 103506. https://doi.org/10.1016/j.tust.2020.103506.

[27] Conforti, A.; Trabucchi, I.; Tiberti, G.; Plizzari, G.A.; Caratelli, A.; Meda, A. Precast tunnel segments for metro tunnel lining : A hybrid reinforcement solution using macro-synthetic fi bers. Eng. Struct. 2019, 199, 109628, doi:10.1016/j.engstruct.2019.109628.

[28] de la Fuente, A.; Pujadas, P.; Blanco, A.; Aguado, A. Experiences in Barcelona with the use of fibres in segmental linings. Tunn. Undergr. Sp. Technol. 2012, 27, 60–71, doi:10.1016/j.tust.2011.07.001.

[29] Aidarov, S.; Mena, F.; de la Fuente, A. Structural response of a fibre reinforced concrete pile-supported flat slab: Full-scale test. Eng. Struct. 2021, 239, 112292. https://doi.org/10.1016/J.ENGSTRUCT.2021.112292.

[30] Leporace-Guimil, B.; Mudadu, A.; Conforti, A.; Plizzari, G.A. Influence of fiber orientation and structural-integrity reinforcement on the flexural behavior of elevated slabs. Eng. Struct. 2021, 113583. https://doi.org/10.1016/j.engstruct.2021.113583.

[31] di Prisco, M.; Colombo, M.; Pourzarabi, A. Biaxial bending of SFRC slabs: Is conventional reinforcement necessary? Mater. Struct. Constr. 2019, 52, 1–15, doi:10.1617/s11527-018-1302-0.

[32] de la Fuente, A.; Aguado, A.; Molins, C.; Armengou, J. Innovations on components and testing for precast panels to be used in reinforced earth retaining walls. Constr. Build. Mater. 2011, 25, 2198–2205, doi:10.1016/j.conbuildmat.2010.11.003.

[33] Meda, A.; Plizzari, G.A.; Riva, P. Fracture behavior of SFRC slabs on grade. Mater. Struct. Constr. 2004, 37, 405–411, doi:10.1617/14093.

[34] Meda, A.; Plizzari, G.A. New design approach for steel fiber-reinforced concrete slabs-on-ground based on fracture mechanics. ACI Struct. J. 2004, 101, 298–303, doi:10.14359/13089.

[35] Aidarov, S.; Mena, F.; de la Fuente, A. Self-compacting Steel Fibre Reinforced Concrete: Material Characterization and Real Scale Test up to Failure of a Pile Supported Flat Slab. In Proceedings of the RILEM-fib International Symposium on Fibre Reinforced Concrete, Valencia, Spain, 20–22 September 2021; Springer, Cham, Switzerland, 2021; pp. 702–713.

[36] Alberti, M.G.; Enfedaque, A.; Gálvez, J.C. The effect of fibres in the rheology of self-compacting concrete. Constr. Build. Mater. 2019, 219, 144–153, doi:10.1016/j.conbuildmat.2019.05.173.

[37] Cavalaro, S.H.P.; Aguado, A. Intrinsic scatter of FRC: an alternative philosophy to estimate characteristic values. Mater. Struct. Constr. 2015, 48, 3537–3555, doi:10.1617/s11527-014-0420-6.

[38] Tiberti, G.; Germano, F.; Mudadu, A.; Plizzari, G.A. An overview of the flexural post-cracking behavior of steel fiber reinforced concrete. Struct. Concr. 2018, 19(3), 695–718. https://doi.org/10.1002/suco.201700068.

[39] Parmentier, B., De Grove, E., Vandewalle, L. and Van Rickstal, F., 2008. Dispersion of the mechanical properties of FRC investigated by different bending tests. Tailor made concrete structures, pp.507-512.

[40] Amin, A.; Gilbert, R.I. Instantaneous crack width calculation for steel fiber-reinforced concrete flexural members. ACI Struct. J. 2018, 115, 535–543, doi:10.14359/51701116.

[41] Colombo, M.; Martinelli, P.; di Prisco, M. On the evaluation of the structural redistribution factor in FRC design: a yield line approach. Mater. Struct. 2017, 50, 1–18, doi:10.1617/s11527-016-0969-3.

[42] de la Fuente, A.; Escariz, R.C.; de Figueiredo, A.D.; Aguado, A. Design of macro-synthetic fibre reinforced concrete pipes. Constr. Build. Mater. 2013, 43, 523–532, doi:10.1016/j.conbuildmat.2013.02.036.

[43] di Prisco, M.; Martinelli, P.; Parmentier, B. On the reliability of the design approach for FRC structures according to fib Model Code 2010: the case of elevated slabs. Struct. Concr. 2016, 17, 588–602, doi:10.1002/suco.201500151.

[44] di Prisco, M.; Plizzari, G.; Vandewalle, L. Fibre reinforced concrete: New design perspectives. Mater. Struct. Constr. 2009, 42, 1261–1281, doi:10.1617/s11527-009-9529-4.

[45] Facconi, L.; Minelli, F. Verification of structural elements made of FRC only: A critical discussion and proposal of a novel analytical method. Eng. Struct. 2017, 131, 530–541, doi:10.1016/j.engstruct.2016.10.034.

[46] Facconi, L.; Plizzari, G.; Minelli, F. Elevated slabs made of hybrid reinforced concrete: Proposal of a new design approach in flexure. Struct. Concr. 2019, 20, 52–67, doi:10.1002/suco.201700278.

[47] Enfedaque, A.; Alberti, M.G.; Gálvez, J.C.; Domingo, J. Numerical simulation of the fracture behaviour of glass fibre reinforced cement. Constr. Build. Mater. 2017, 136, 108–117, doi:10.1016/j.conbuildmat.2016.12.130.

[48] Enfedaque, A.; Alberti, M.G.; Galvez, J. Analysis of the Versatility of Multi-Linear Softening Functions Applied in the Simulation of Fracture Behaviour of Fibre-Reinforced Cementitious Materials. Materials 2019, 12, 3656. https://doi.org/10.3390/ma12223656.

[49] Enfedaque, A.; Alberti, M.G.; Galvez, J.; Cabanas, P. Numerical Simulation of the Fracture Behavior of High-Performance Fiber-Reinforced Concrete by Using a Cohesive Crack-Based Inverse Analysis. Materials 2022, 15, 71. https://doi.org/10.3390/ma15010071.

[50] de Maio, U.; Fantuzzi, N.; Greco, F.; Leonetti, L.; Pranno, A. Failure Analysis of Ultra High-Performance Fiber-Reinforced Concrete Structures Enhanced with Nanomaterials by Using a Diffuse Cohesive Interface Approach. Nanomaterials 2020, 10, 1792. https://doi.org/10.3390/nano10091792.

[51] di Prisco, M.; Martinelli, P.; Dozio, D. The structural redistribution coefficient KRd: A numerical approach to its evaluation. Struct. Concr. 2016, 17, 390–407. https://doi.org/10.1002/suco.201500118.

[52] Фотограф Сергей Филинин Available online: https://sergeyfilinin.ru/#portfolio (accessed on Dec 25, 2021).

[53] Lee, G.C.; Shih, S.; Chang, K.C. Mechanical Properties of Concrete at Low Temperature. J. Cold Reg. Eng. 1988, 2, 13–24.

[54] Xie, J.; Yan, J.B. Experimental studies and analysis on compressive strength of normal-weight concrete at low temperatures. Struct. Concr. 2018, 19, 1235–1244, doi:10.1002/suco.201700009.

[55] Montejo, L.A.; Sloan, J.E.; Kowalsky, M.J.; Hassan, T. Cyclic Response of Reinforced Concrete Members at Low Temperatures. J. Cold Reg. Eng. 2008, 22, 79–102, doi:10.1061/(asce)0887-381x(2008)22:3(79).

[56] Pigeon, M.; Cantin, R. Flexural properties of steel fiber-reinforced concretes at low temperatures. Cem. Concr. Compos. 1998, 20, 365–375, doi:10.1016/S0958-9465(98)00017-1.

[57] Caballero-Jorna, M.; Roig-Flores, M.; Serna, P. Short-term effects of moderate temperatures on the mechanical properties of steel and macrosynthetic fiber reinforced concretes. In Proceedings of the RILEM-Fib X International Symposium on Fibre Reinforced Concrete BEFIB 2021, Valencia, Spain, 20–22 September 2021; Springer: Berlin/Heidelberg, Germany, 2021.

[58] Richardson, A.; Ovington, R. Temperature related steel and synthetic fibre concrete performance. Constr. Build. Mater. 2017, 153, 616–621, doi:10.1016/j.conbuildmat.2017.07.101.

[59] CEN. EN 14651. Test Method for Metallic Fibre Concrete. Measuring the Flexural Tensile Strength (Limit of Proportionality (LOP), Residual); European Committee for Standardization: Bruxelles, Belgium, 2007. ISBN 9780580610523.

[60] CEN. EN 12350-2:2019. Testing Fresh Concrete. Slump Test; European Committee for Standardization: Bruxelles, Belgium, 2019.

[61] König, G.; Kützing, L. Modelling the increase of ductility of HPC under compressive forces—A fracture mechanical approach. In Proceedings of the Third International RILEM Workshop on High Performance Fiber Reinforced Cement Composites, Mainz, Germany, 16-19 May 1999; RILEM Publications SARL: Bagneux, France, 1999; pp. 251–260.

[62] Mena, F.; Aidarov, S.; de la Fuente, A. Hormigones autocompactantes reforzados con fibras para aplicaciones con alta responsabilidad estructural. Campaña experimental en laboratorio. In Proceedings of the III Congreso de Consultores de Estructuras; Barcelona, Spain, 3–5 April 2019; pp. 1–10.

[63] Bentur, A.; Mindess, S. Fibre Reinforced Cementitious Composites; Taylor & Francis: Abingdon, UK, 2007.

[64] Kim, J.K.; Mai, Y.-W. High strength, high fracture toughness fibre composites with interface control-A review. Compos. Sci. Technol. 1991, 41, 333–378, doi:10.1016/0266-3538(91)90072-W.

[65] Galeote, E.; Nogales, A.; de la Fuente, A. Analysis of design constitutive model for plastic fibre reinforced concrete through inverse analysis. In Proceedings of the 75th RILEM Week, Merida, Mexico, 29 August–3 September 2021; Springer: Berlin/Heidelberg, Germany, 2021.

[66] Nogales, A.; Galeote, E.; de la Fuente, A. Finite element analysis characterization of macro synthetic fibre reinforced concrete constitutive equation. In Proceedings of the 75th RILEM Week, Merida, Mexico, 29 August–3 September 2021; Springer: Berlin/Heidelberg, Germany, 2021.

[67] Dassault Systèmes Simulia Abaqus CAE User's Manual (6.12); Dassault Systèmes, Providence, 2012;

[68] Nogales, A.; de la Fuente, A. Elevated Flat Slab of Fibre Reinforced Concrete Non-Linear Simulation Up to Failure; Springer International Publishing: Berlin/Heidelberg, Germany, 2022; Volume 36. ISBN 9783030837198.

A2.3. JOURNAL PAPER SUBMITTED FOR PUBLICATION: EFFECTIVE MOMENT OF INERTIA AND SLENDERNESS LIMITS OF RC AND FRC SLABS

Nikola Tošić, Marc Sanabra-Loewe, Alejandro Nogales, Albert de la Fuente

Nikola Tošić is a Marie Skłodowska-Curie Individual Fellow at the Polytechnic University of Catalonia, Barcelona, Spain. He received his BS, MS, and PhD in civil engineering from the University of Belgrade, Belgrade, Serbia in 2010, 2011, and 2018, respectively. In 2019 he was a Fulbright Visiting Scholar at the University of Notre Dame, Indiana. His research interests include concretes with recycled and waste materials, serviceability of concrete structures, and fiber reinforced concrete.

ACI member Marc Sanabra-Loewe is Lecturer at the Polytechnic University of Catalonia (Barcelona Tech), Barcelona, Spain. He received his Architect's License, MS and PhD in Architecture Technology specializing in Structures Analysis and Design from the Barcelona Tech in 2005, 2011 and 2014 respectively. In 2018-2019, he was full time lecturer at the University of Illinois at Urbana-Champaign, as Hilfinger Fellow. His research interests include concrete floors optimization and precast and prestressed concrete floors.

Alejandro Nogales is a PhD student at the Polytechnic University of Catalonia, Barcelona, Spain. He received his BC and MSc in civil engineering from the Polytechnic University of Catalonia in 2014 and 2017, respectively. His research interests include design of fiber reinforced concrete structures and finite element numerical simulations.

Albert de la Fuente is an Associate Professor at the Civil and Environmental Engineering Department of the Universitat Politècnica de Catalunya (UPC Barcelona Tech.) since 2015. His research interests include design and optimization of concrete structures, FRC technology and sustainability assessment by means of multi-criteria decision-making approaches. He is *fib* member active in tasks groups belonging to Commission 6 and TG 10.1 Model Code 2020.

ABSTRACT:

Following the trend of updating methods that establish minimum slenderness of concrete members based on work by Rangan and Scanlon, this paper elaborates new formulations of the stiffness factor (α), which expresses the ratio of the equivalent moment of inertia to the gross moment of inertia. For this purpose, closed-form solutions for α in reinforced concrete (RC) and fiber reinforced concrete (FRC) one-way members are derived. Further, a parametric study is carried out to evaluate the relationship of the neutral axis position in RC and FRC members with

equal longitudinal reinforcement ratios. Additionally, a simplified equation is proposed for the neutral axis position in FRC members. Based on experimental and numerical data on deflections of FRC members, the expression for the effective moment of inertia is adjusted. Finally, a comparison between α factors for RC and FRC members is presented and implications for minimum thicknesses of members are discussed.

KEYWORDS: deflection, serviceability, design code, stiffness, reinforced concrete, fibre reinforced concrete.

INTRODUCTION

The design of the great majority of reinforced concrete flexural members for floors (beams, slabs) is governed by deflection control rather than by flexural or shear strength. That is why, once the span of a member is established, typically, the next step is establishing the depth that allows an effective deflection control. Since the mid-twentieth century, constant slenderness ratios, such as L/n and L_n/n, have been the most common method recommended by codes to guarantee proper deflection control in reinforced concrete flexural members. However, several authors have proved [1,2] that these approaches may eventually lead to either excessively heavy and resource-inefficient slabs, or to excessively slender and deformable slabs. That is why, in previous decades, several authors have been suggesting updates to codes [1,3,4]. In fact, several codes [5–7] have started to update their minimum slenderness provisions, replacing those constant slenderness ratios by more refined approaches.

Despite this trend, Sanabra-Loewe and Scanlon [4] showed that constant slenderness ratios may still be appropriate to control the deflection of reinforced concrete beams. This was found to be true mainly for narrow beams, but also to a certain extent for wide beams. However, for slabs, constant slenderness ratios are not sensitive to variations of the main influencing variables controlling deflection control: boundary conditions, span, load, and allowable deflection [2]. However, a method that was originally formulated by Rangan [8], and was subsequently complemented by Scanlon and Choi [9] and Scanlon and Lee [10], has proved to be sensitive to all these factors as well as to the modulus of elasticity of concrete [2]. So far, this method has been the basis for the update of the Australian code [6] and it has inspired the Israeli code [7], and may well become the basis for the updates of other national and international codes. As it will be shown below, this is a very rational method, directly derived from basic statics formulae for deflections. This enables its adaptation to a wide number of design situations for slabs; as well as its adaptation to the developments of future research. Indeed, despite the original formulations of Scanlon being based on criteria included in the American concrete standard [11], the rationality of the method makes it relatively easy to adapt the formulas to other standards.

Taking advantage of this advantage, hereinafter referred to as the Rangan–Scanlon method, the purpose of this research paper is to present the derivation of a closed-form solution for the stiffness factor (α) that the method requires to be found in order to establish the slenderness of reinforced concrete (RC) members. This factor is essential for simplified computations of deflection, as it relates the effective moment of inertia I_e to the gross cross-section moment of inertia I_g. The derivation is also expanded to cover fiber reinforced concrete (FRC) members and hybrid-reinforced FRC members (HFRC), as a material and solution that is increasingly used for structural applications such as flat slabs [12–14] but is still lacking full coverage by design codes. The basis for the derivation of the closed-form solution are the studies by Scanlon and Choi [9] and Scanlon and Lee [10], and Sanabra-Loewe and Scanlon [4]. The derivations for FRC members are based on the ACI 544.4-18 Guide to Design with Fiber-Reinforced Concrete [15], the *fib* Model Code 2010 [16] and the study by Amin et al. [17].

The paper proceeds by firstly summarizing the two variants of the method, the so called 'long method of Rangan-Scanlon' and the 'short method of Rangan-Scanlon'. Then, closed-form solutions of the stiffness factor (α) for RC and FRC members are derived. Subsequently, the relationship between neutral axis positions in RC and FRC sections with equal longitudinal reinforcement ratios is established through a parametric study and regression analysis, and the exponent in the expression for effective moment of inertia is calibrated based on experimental and numerical data. Subsequently, a summary of the method for finding the stiffness factors (α) for RC and FRC members with equal longitudinal steel reinforcement ratios is presented and implications of the results are discussed.

RESEARCH SIGNIFICANCE

Establishing appropriate slenderness limits of one-way slabs is an important step towards their more material-efficient design and construction. As the deflection behavior of those is governing in design, rational and easy-to-use methods that consider critical factors such as load, boundary conditions and reinforcing ratio, are needed. The authors consider that the Rangan–Scanlon method provides an excellent basis for further development. Furthermore, the increasing use of FRC brings with it the need for expanding methods to this material as well. The closed-form solutions of the stiffness factor α presented in this study offer a possible answer to these challenges.

THE RANGAN–SCANLON METHOD

The starting point for deriving a unified span-to-depth equation for Rangan [8] and Scanlon and Choi [9] is the incremental deflection Δ_{inc}. This can be considered as the deflection after the attachment to the structure of damageable constructive elements, i.e., the part of the total

deflection occurring after the attachment of non-structural elements , including the time-dependent portion of deflection caused by all sustained loads and the immediate deflection due to any additional live load [11]. In many cases this deflection is governing in design as it can lead to damage of partitions and other non-structural members or malfunction of installed equipment. In the ACI Building code ACI 318-19 [11], the incremental deflection is limited to $L/480$ (where L is the clear span) when floors are attached to non-structural elements that are likely to be damaged by large deflections. As a comparison, the *fib* Model Code 2010 [16] and Eurocode 2 [5] limit is $L/500$.

$$\Delta_{inc} = \frac{\lambda_\Delta \kappa W_s L^4}{384 E_c I_e} + \frac{\kappa W_L(add) L^4}{384 E_c I_e} \tag{1}$$

The long-term deflection multiplier for sustained loads taking into account shrinkage, creep and compressive reinforcement per ACI 318-19 [11] is

$$\lambda_\Delta = \frac{\xi}{1 + 50\rho'} \tag{2}$$

As will be shown later, one of the most important aspects of the method is the effective moment of inertia I_e that is calculated as

$$I_e = \begin{cases} I_g & \text{for } M_a \leq (2/3)M_{cr} \\ \dfrac{I_{cr}}{1 - \left(\dfrac{(2/3)M_{cr}}{M_a}\right)^2 \left(1 - \dfrac{I_{cr}}{I_g}\right)} & \text{for } M_a > (2/3)M_{cr} \end{cases} \tag{3}$$

The cracking moment M_{cr} is calculated as

$$M_{cr} = \frac{I_g}{y_t} f_r \tag{4}$$

For a rectangular cross-section, the cracking moment is

$$M_{cr} = W_g f_r = \frac{bh^2}{6} f_r \tag{5}$$

The modulus of rupture f_r is defined by ACI 318-19 [11] as

$$f_r = 0.625\sqrt{f_c'} \text{ (MPa)} \tag{6}$$

The formulation in Equation (3) is a novelty introduced in the latest edition of the code ACI 318-19 [11]. It was based on studies like those of Scanlon and Murray [18] and Scanlon and Bischoff [19] that demonstrated the previous formulation's underestimation of deflections for

members loaded close to cracking load in service. In effect, the new formulation amounts to a 33% reduction of the cracking moment, taking into account the effects of restrained shrinkage – this is equivalent to the approaches of the *fib* Model Code 2010 and Eurocode 2 [5,16].

To obtain an expression in terms of span-to-depth ratio based on Equation (1), the following is assumed:

1) Δ_{inc} is equated with the maximum allowable value of the incremental deflection $(\Delta_{inc})_{allow}$,
2) I_g is taken as $bh^3/12$, assuming a rectangular cross-section, and
3) I_e is taken as αI_g

Then:

$$(\Delta_{inc})_{allow} = \frac{12\lambda_\Delta \kappa W_s L^4}{384 E_c \alpha bh^3} + \frac{12 W_L(add) L^4}{384 E_c \alpha bh^3} \tag{7}$$

$$= \frac{\kappa}{32} \frac{\left(\lambda_\Delta W_s + W_L(add)\right)L}{\alpha E_c b} \left(\frac{L}{h}\right)^3$$

$$\frac{L}{h} = \left[\left(\frac{\Delta_{inc}}{L}\right)_{allow} \frac{32\alpha E_c b}{\kappa\left(\lambda_\Delta W_s + W_L(add)\right)}\right]^{\frac{1}{3}} \tag{8}$$

In cases where the incremental deflection does not govern the design (e.g. when there are no partitions that can be damaged by incremental deflection), other variants of allowable deflection may be more restrictive, and the formulas of the Rangan-Scanlon method may be adapted accordingly, by simply replacing $\left(\frac{\Delta_{inc}}{L}\right)_{allow}$ by a more general term $\left(\frac{\Delta}{L}\right)_{allow}$ and adjusting the rest of the equation to consider the loads causing the according deflection.

Subsequently, Scanlon and Lee [10] presented the modifications necessary to expand the method to two-way members: edge-supported slabs, flat slabs, and slabs with drop panels; the resulting equation being Equation (9).

$$\frac{L}{h} = \beta_{ES} \left[\left(\frac{\Delta_{inc}}{L}\right)_{allow} \frac{32 k_{DP} \alpha E_c b}{\kappa k_{AR} k_{SS} L_{trib}\left(\lambda_\Delta W_s + W_L(add)\right)}\right]^{\frac{1}{3}} \tag{9}$$

One way of using the Equation (8) is by taking a fixed value for α, e.g., 0.40 as it was suggested for the first time by Scanlon and Choi (1999). This method is referred here as the "short method of Rangan-Scanlon" and can be used as very expedite and quite accurate method to establish the span-to-depth ratio of reinforced concrete members, and among its main advantages stands the fact that it is independent of knowing the reinforcement ratio, as pointed out by Sanabra-Loewe et al. [2]. However, this method is insufficiently functional. This can be seen by the fact that,

Scanlon and Lee [10] suggested 0.52 a new 'constant' value for α; but then Sanabra-Loewe and Scanlon [4] and Sanabra-Loewe et al. [2] suggested that further study was necessary in order to establish a set of values of α depending on a number of usual factors that influence deflection. That is why, to the date, the so-called "long method of Rangan-Scanlon" has been used as the most reliable method to find the value of α, that is subsequently used in the "short method of Rangan-Scanlon".

The "long method of Rangan-Scanlon" consists of the following steps [4]:

1) Initial choice of *h* to account for self-weight (e.g., from current code-recommended *L/h* ratios)

2) Calculation of required steel area for strength requirements

3) Calculation of I_e to determine α

4) Use of computed α in Equation (8), or Equation (9), to find *h*

5) Check for convergence between obtained and assumed *h*

6) Iteration until convergence

It is obvious that this method requires knowing the reinforcement ratio of the slab. As pointed out by Sanabra-Loewe et al. [2] this making the method unsuitable to establish the depth of slabs at early stages of design.

Aiming at reducing the computational efforts in using the 'long method of Rangan-Scanlon', and at expanding the method for the use of fiber-reinforced concrete, the current study presents a rational method based on a closed-form equation to expedite finding the stiffness factor α, and avoid using the "the long method of Rangan-Scanlon".

The closed-form equation presented in the next section is based on: the properties of concrete and steel (f'_c, E_c, f_y, E_s), the tensile reinforcement concrete cover expressed as *d/h*, the maximum expected service moment expressed as M_a/M_n, and the longitudinal reinforcement ratio (ρ). The method is also expanded to cover hybrid reinforced members, including both conventional longitudinal reinforcement and structural fibers in the concrete mix (HFRC).

Despite the method presented here is still dependent on knowing the reinforcement ratio (ρ), which makes it unsuitable to be used at early stages of design, it can be considered in the last step before reaching a set of α depending exclusively on those factors known at early stages of design that influence deflection.

These factors known at early stages are: span, load, boundary conditions, tension reinforcement cover (*d/h*), expected service moment (M_a/M_n), allowable deflection ((Δ/L)$_{allow}$),

long-term deflection multiplier (λ_Δ), properties of concrete and steel (f'_c, E_c, f_y, E_s), and residual tensile strength (f_{R1}, f_{R3}), when fibers are included in the concrete mix.

Regarding the ratio of reinforcement of one-way slabs, it generally ranges from 0.20% to 0.60%, and unlikely to be beyond 0.80%, as it is reported in Bischoff and Scanlon [20] and Sanabra-Loewe et al. [2]. Accordingly, the parametric analyses carried out were limited to ratios of reinforcement under 1.00%.

CLOSED-FORM SOLUTIONS FOR THE STIFFNESS FACTOR α
RC Members

The starting point for a closed-form solution for α is Equation (3) that can be rewritten as follows by taking $\mu = M_{cr}/M_a$ and $\delta = I_{cr}/I_g$:

$$I_e = \begin{cases} I_g & \text{for } \mu \geq 1.5 \\ \dfrac{\delta I_g}{1 - \left(\dfrac{2}{3}\mu\right)^2 (1 - \delta)} & \text{for } \mu < 1.5 \end{cases} \qquad (10)$$

from where it follows that

$$\frac{I_e}{I_g} = \alpha = \begin{cases} 1 & \text{for } \mu \geq 1.5 \\ \dfrac{\delta}{1 - \left(\dfrac{2}{3}\mu\right)^2 (1 - \delta)} & \text{for } \mu < 1.5 \end{cases} \qquad (11)$$

Now it is a matter of expressing μ and δ in the least possible number of variables. For this purpose, the following assumptions were made:

- A rectangular cross-section b/h is considered,

- Only tensile reinforcement is present in the cross-section ($\rho' = 0$),

The relation between effective depth and height d/h is maintained as an input parameter, while its value can be safely assumed as 0.85 [20]. Deflections are generally calculated for a maximum moment due to service load which is typically equal to 2/3 of the flexural strength of the slab (M_n), $M_a = (2/3)M_n$ [20]. However, some authors such as Granham and Scanlon [21], report that slabs may be exposed to loads as high as their flexural strength during the erection due to the shoring procedure. Therefore, in this study, the ratio of M_a to M_n is left as an input variable, i.e. $M_a = \eta M_n$.

Now, the cracking moment can be determined as

$$M_{cr} = \frac{bh^2}{6} f_r = \frac{bh^2}{6} \left(0.625 \sqrt{f_c'} \right) = \frac{0.625}{6} bh^2 \sqrt{f_c'} \text{ (Nmm)} \qquad (12)$$

Considering an assumed value of ρ, the applied moment $M_a = \eta M_n$ can be determined as

$$M_a = \eta M_n = \eta \left[A_s f_y \left(d - 0.5 \frac{A_s f_y}{0.85 f_c' b} \right) \right] = \eta \left[\rho b d f_y \left(d - 0.5 \frac{\rho b d f_y}{0.85 f_c' b} \right) \right] \tag{13}$$

$$=$$

$$= \eta \left(\frac{d}{h} \right)^2 b h^2 \rho f_y \left(1 - \frac{\rho f_y}{1.7 f_c'} \right) \text{ (Nmm)}$$

Then, μ is obtained as

$$\mu = \frac{M_{cr}}{M_a} = \frac{\dfrac{0.625}{6} b h^2 \sqrt{f_c'}}{\eta \left(\dfrac{d}{h} \right)^2 b h^2 \rho f_y \left(1 - \dfrac{\rho f_y}{1.7 f_c'} \right)} = \frac{0.625 \sqrt{f_c'}}{6 \eta \left(\dfrac{d}{h} \right)^2 \rho f_y \left(1 - \dfrac{\rho f_y}{1.7 f_c'} \right)} \tag{14}$$

As for $\delta = I_{cr}/I_g$, it is calculated from the following

$$I_g = \frac{b h^3}{12} \tag{15}$$

For an RC cross-section under bending moments (without an axial force), the position of the neutral axis is independent of the applied load (thus, of M) and can be expressed through the neutral axis coefficient $\xi = c/d$, where c is the depth of the compressed zone:

$$I_{cr} = b d^3 n \rho (1 - \xi) \left(1 - \frac{\xi}{3} \right) = 0.729 b h^3 n \rho (1 - \xi) \left(1 - \frac{\xi}{3} \right) = \tag{16}$$

$$= \frac{b h^3}{12} \left[8.75 n \rho (1 - \xi) \left(1 - \frac{\xi}{3} \right) \right] \text{ (mm}^4\text{)}$$

Then, δ can be obtained as

$$\delta = \frac{I_{cr}}{I_g} = 8.75 n \rho (1 - \xi) \left(1 - \frac{\xi}{3} \right) \tag{17}$$

For reinforced concrete sections under bending with only tensile reinforcement and under service load, the neutral axis coefficient ξ can be directly calculated as

$$\xi = -n\rho + \sqrt{(n\rho)^2 + 2n\rho} = n\rho \left(-1 + \sqrt{1 + \frac{2}{n\rho}} \right) \tag{18}$$

Using Equations (14), (17) and (18), α can be calculated as a function of the specified concrete strength (from which E_c is determined), steel grade (from which f_y and E_s are determined), and an assumed reinforcement ratio ρ.

The dependence of α on ρ for the case of concrete with $f_c' = 30$ MPa (4,351 psi), $d/h = 0.85$ and $M_a = (2/3)M_n$, is shown in Figure 1, for $\rho > 0.1\%$ (which is actually below the minimum reinforcement limit of 0.14%—valid for steels with f_y higher than 413 MPa (60,000 psi)—prescribed by ACI 318-19 [11]). Good agreement with the results by Bischoff and Scanlon [20] and Scanlon and Choi [4] confirms the correctness of the obtained closed-form solution.

It can be seen that α reaches its minimum value precisely in the area of $\rho \leq 0.5\%$, i.e., for reinforcement ratios typical of RC slabs. In this region, an average value of $\alpha \approx 0.25$ can be adopted.

Hybrid-Reinforced FRC Members

In practice, in FRC slabs (i.e., pile-supported flat-slabs) longitudinal steel reinforcement is added in those zones where maximum bending moments are expected so that the combination of both reinforcement types leads to an optimized hybrid-reinforced (HFRC) solution [12,22–25], while guaranteeing $M_{n\text{-}HFRC} \approx M_{n\text{-}RC}$. Thus, the ratio $\eta = M_a/M_n$ remains the same for both RC and HFRC alternatives (the load magnitudes and combinations are independent to the reinforcement configuration).

The ACI 544.4-18 Guide to Design with Fiber-Reinforced Concrete [15] allows the calculation of the flexural strength of HFRC members by straightforwardly assuming the superposition of the flexural strength of both RC and the FRC section, i.e., $M_{n\text{-}HFRC} = M_{n\text{-}RC} + M_{n\text{-}FRC}$. Although this approach deviates from the exact solution (non-linear) for higher reinforcement ratios, for lower reinforcement ratios, such as those of slabs, this assumption is found reasonable. Alternatively, the ACI 544.4-18 [15] suggest the use of the *fib* Model Code 2010 (MC2010) [16] for constitutive modeling of FRC.

The flexural strength of FRC can be calculated using the rigid-plastic model of MC2010 [16] according to which

$$M_{n-FRC} = 0.5bh^2 f_{Ftu} \,(\text{Nmm}) \tag{19}$$

Therefore, the flexural strength of HFRC can be computed with Equation (21).

$$M_{n-HFRC} = \left(\frac{d}{h}\right)^2 bh^2 \rho f_y \left(1 - \frac{\rho f_y}{1.7 f_c'}\right) + 0.5 bh^2 f_{Ftu} = \tag{20}$$

$$= bh^2 \left[\left(\frac{d}{h}\right)^2 \rho f_y \left(1 - \frac{\rho f_y}{1.7 f_c'}\right) + 0.5 f_{Ftu}\right] \,(\text{Nmm})$$

As seen from Equation (20), the increase of flexural strength of HFRC relative to RC has a magnitude of $0.5 f_{Ftu}$. Consequently, μ changes to μ_{HFRC}:

$$\mu_{HFRC} = \frac{\dfrac{0.625}{6}bh^2\sqrt{f_c'}}{\eta bh^2\left[\left(\dfrac{d}{h}\right)^2\rho f_y\left(1-\dfrac{\rho f_y}{1.7f_c'}\right)+0.5f_{Ftu}\right]}$$

$$= \frac{0.625\sqrt{f_c'}}{6\eta\left[\left(\dfrac{d}{h}\right)^2\rho f_y\left(1-\dfrac{\rho f_y}{1.7f_c'}\right)+0.5f_{Ftu}\right]}$$

(21)

As for δ, it changes as well because of the different value of I_{cr} for HFRC members. For this purpose, the expression proposed by Amin et al. [17] is considered (in a slightly different form, the expression is also presented in studies by Tan et al. [26,27]):

$$I_{cr,HFRC} = \left[\frac{bc^3}{3}+nA_s(d-c)^2\right]+nA_F\frac{(h-c)^2}{3}\ (\text{mm}^4)$$

(22)

In Equation (22), the first two terms in brackets "[]" are equivalent to Equation (16), and may be replaced by the term in brackets of Equation (16). Therefore, the only addition is the third term where n is assumed equal for steel reinforcement and fibers (i.e. $E_f = E_s$). The term A_F represents "the cumulative area of fibres in the cracked portion of the cross-section" [17]. It is expressed by Amin et al. [17] as

$$A_F = 0.82\frac{V_f}{2k_t}(h-c)b\ (\text{mm}^2)$$

(23)

However, fiber volume and fiber length are a matter of mix design and are rarely known in advance by the designer. Therefore, an assumption must be adopted at this point. For a typical steel fiber length of 60 mm (2.36 in) and a considered strip of slab width of 1000 mm (3.28 ft), $k_t = 1$ is obtained and adopted herein.

As for fiber volume, it can be correlated with FRC residual strengths f_{R3} and f_{R1}, corresponding to CMOD of 0.5 and 2.5 mm (0.02 and 0.10 in), respectively. Namely, using a statistical analysis of an extensive database consisting of EN 14651 [28] tests of SFRC notched-beams ($150 \times 150 \times 600$ mm/$5.9 \times 5.9 \times 23.6$ in) reported by Venkateshwaran et al. [29], Tiberti et al. [30], Galeote et al. [31], as well as other experimental programs conducted at the Structural and Material Technology Laboratory (LATEM) of the Polytechnic University of Catalonia (UPC). This database includes a large variety of concrete mixes, covering a range of compressive strength (f_c') of 15–117 MPa (2,175–16,970 psi), V_f of 0.33–2.52%, fiber aspect ratios (λ_f) 35–110, fiber tensile strength (f_{uf}) 1000–3000 MPa (145–435 ksi) and fiber modulus of elasticity (E_s) 190,000–210,000 MPa (27,557–30,458 ksi). Figure 2 shows the obtained correlation, and a suitable fit with a coefficient of determination R^2 of 0.75 and 0.93 is found for f_{R3} and f_{R1}, respectively.

Alejandro Nogales Arroyo

Using Figure 2, V_f can inversely be predicted from f_{R3}:

$$\frac{f_{R3}}{\sqrt{f_c'}} = 0.103 V_f \lambda_f f_{uf} \sqrt{E_s} \Rightarrow V_f = \frac{f_{R3}}{0.103 \cdot \sqrt{f_c'}} \frac{1}{\lambda_f f_{uf} \sqrt{E_s}} \tag{24}$$

Adopting typical values of λ_f, f_{uf}, and E_s as 65, 1.25 GPa and 200 MPa (9427, 181 and 29 ksi), respectively, the following is obtained:

$$V_f = 8.45 \frac{f_{R3}}{\sqrt{f_c'}} 10^{-3} \tag{25}$$

Now, Equation (23) can be rewritten as

$$A_F = \frac{0.82}{2} 8.45 \frac{f_{R3}}{\sqrt{f_c'}} h \left(1 - \frac{c}{h}\right) b 10^{-3} = 3.46 bh \frac{f_{R3}}{\sqrt{f_c'}} (1 - 0.9\xi_{HFRC}) 10^{-3} \tag{26}$$

Finally, Equation (22) can be reformulated as

$$I_{cr,HFRC} = \frac{bh^3}{12} \left[8.75 n\rho(1 - \xi_{HFRC}) \left(1 - \frac{\xi_{HFRC}}{3}\right) \right]$$

$$+ nA_F \frac{h^2(1 - 0.9\xi_{HFRC})^2}{3} = $$

$$= \frac{bh^3}{12} n \left[8.75\rho(1 - \xi_{HFRC}) \left(1 - \frac{\xi_{HFRC}}{3}\right) \right.$$

$$\left. + 0.014 \frac{f_{R3}}{\sqrt{f_c'}} (1 - 0.9\xi_{HFRC}) \right] (\text{mm}^4) \tag{27}$$

Therefore, the coefficient δ for HFRC (δ_{HFRC}) is

$$\delta_{HFRC} = \frac{I_{cr,HFRC}}{I_g} \tag{28}$$

$$= n \left[8.75\rho(1 - \xi_{HFRC}) \left(1 - \frac{\xi_{HFRC}}{3}\right) \right.$$

$$\left. + 0.014 \frac{f_{R3}}{\sqrt{f_c'}} (1 - 0.9\xi_{HFRC}) \right]$$

Once μ_{HFRC} is found using equation (22) and δ_{HFRC} is found using equation (29), the stiffness factor for HFRC members using steel fibers (α_{HFRC}) can be computed.

However, it is not evident that Equation (11), defining α, should be equal for RC and HFRC, specifically in terms of the exponent (=2 for RC). The formulation was proposed by Bischoff and

Scanlon [20] who found that the value of 2 corresponds well with an exponent value of 3 in the previously used Branson's formulation for I_e [32,33].

As α provides the ratio of I_e/I_g averaged over the entire member length, it depends not only on the neutral axis position in individual cracked sections but also on the extent of cracking and contribution of uncracked sections (tension stiffening). In general, the cracking pattern of HFRC members will be significantly different from that of RC members with the same ratio of longitudinal reinforcement. Therefore, a calibration of the exponent m_{HFRC} in the following formulation is needed:

$$\alpha_{HFRC} = \begin{cases} 1 & \text{for } \mu_{HFRC} \geq 1.5 \quad (29) \\ \dfrac{\delta_{HFRC}}{1 - \left(\frac{2}{3}\mu_{HFRC}\right)^{m_{HFRC}}(1 - \delta_{HFRC})} & \text{for } \mu_{HFRC} < 1.5 \end{cases}$$

Hence, in the following sections, two analyses are performed:

1. The position of the neutral axis in HFRC sections is determined, as compared to the neutral axis position in RC sections with the same longitudinal reinforcement. This is done through a regression, thus avoiding the need for iterative calculations.
2. The exponent m_{HFRC} in Equation (29) is calibrated for HFRC members based on experimental results and numerical simulations.

SIMPLIFIED ASSUMPTIONS FOR THE DESIGN OF HFRC MEMBERS

Neutral Axis Position in HFRC Members

For RC sections under bending and without an axial force, the position of the neutral axis ξ_{RC} is independent of the moment acting on the cross-section. The external moment M is resisted by the compressive force C_c in concrete and a tensile force T_s in tensile steel (no compressed steel is assumed), Figure 3 (left). The position of the neutral axis for such a section is directly calculated using Equation (18). However, for a HFRC section, this is not possible if the contribution of the fibers is considered. According to MC2010 [16], below the neutral axis, a constant tensile stress f_{Fts} can be assumed, equal to $0.45f_{R1}$, where f_{R1} is the residual tensile strength corresponding to a CMOD of 0.5 mm (0.02 in) in the EN 14651 test [28].

Next, a relation that allows the calculation of ξ_{RC} and its subsequent transformation into ξ_{HFRC} is searched for. It is assumed that both the RC and HFRC members have the same longitudinal reinforcement (ρ) and that both members are under the same bending moment M_a. For that moment M_a, the presence of an additional tensile force in the cracked part of an HFRC section,

T_f, causes a reduction in T_s but also an increase in C_c and a lowering of the neutral axis position ξ_{HFRC} such that $\xi_{HFRC} > \xi_{RC}$.

The fact that the tensile stress in cracked HFRC is independent of strain (i.e., constant magnitude of f_{Fts}), means that the neutral axis position needs to be calculated iteratively. Such an approach would make the process of estimating an L/d ratio hardly operative. In order to facilitate this procedure, a parametric analysis was performed to establish a relationship between ξ_{HFRC} and ξ_{RC}.

The following parameters were considered:

- $b; h; d = 1000$ mm (3.28 ft); 300 mm (11.81 in); 270 mm (10.63 in) (1 m/3.28 ft strip of a slab was considered with $d/h = 0.85$)
- $f_c' = 30$ and 50 MPa (4,351 and 7,252 psi)
- $f_{R3} = f_{R1} = 3, 5,$ and 7 MPa (435, 725 and 1,015 psi), covering the typical range of FRC with 0–2% of fibers by volume
- $\rho = 0.1$–3.0% (covering the range from minimum to high reinforcement ratios in beams)
- $f_y = 500$ MPa (72,519 psi)

Considering the correlations established in Figure 2, it is adopted that $f_{R3} = f_{R1}$, meaning that the FRC is classified as type "c" per MC2010 [16]. A type "c" is representative of the FRC degree of ductility required for slabs.

The process consisted of the following. First, the serviceability bending moment M_a was established for HFRC according to Equation (20) as $(2/3)M_{n\text{-}HFRC}$. The neutral axis position of an RC section with the same longitudinal reinforcement ratio as the HFRC section was then calculated using Equation (18). Then, for the HFRC section, ξ_{HFRC} was determined by considering the following:

$$C_{c2} = 0.5\xi_{HFRC}bd\sigma_{c2}; \quad T_{s2} = \rho bd\sigma_{s2}; \quad T_f = f_{Fts}b(h - \xi_{HFRC}d) \tag{30}$$

where the stress in the longitudinal reinforcement is expressed in terms of σ_{c2} (Equation (31)) following the Navier-Bernoulli assumption.

$$\sigma_{s2} = n\sigma_{c2}\frac{1 - \xi_{HFRC}}{\xi_{HFRC}} \tag{31}$$

The moment equilibrium can be expressed as

$$C_{c2}d\left(1 - \frac{\xi_{HFRC}}{3}\right) - T_f\left(\frac{h - \xi_{HFRC}d}{2} - d_1\right) - M_a = 0 \tag{32}$$

Herein, $d = 0.85h$ and $d_1 = 0.15h$. The modulus of elasticity of concrete necessary for calculating n was following the ACI 318-19 [11] expression as $E_c = 4700\sqrt{f_c'}$ (MPa).

The neutral axis position ξ_{HFRC} was determined by solving Equation (32) by varying σ_{c2}. This was done for a total of 120 cases ($f_c' \times f_{R1} \times \rho = 2 \times 3 \times 20$). The results are shown in Figure 4.

The results show major differences in neutral axis position for reinforcement ratios <0.5–1.0%, while the ξ_{HFRC}/ξ_{RC} ratio quickly converging to 1.0 for reinforcement ratios above 1%. This is as expected from considerations of Figure 3. For lower reinforcement ratios, the position of the neutral axis is fairly high in RC sections (c_1 is small). By adding structural fibers, the cracked portion of the section starts carrying a relatively large tensile force which needs to be equilibrated by a significant increase in the compressive force in concrete—which can only be achieved by a lowering of the neutral axis. The effect is more pronounced with increasing f_{R1} values (as T_f increases accordingly). The differences also slightly grow when increasing the concrete strength. As a consequence of a slightly higher modulus of elasticity of concrete and lower n, ξ_{RC} is smaller for higher concrete strengths, but the effect of fibers is the same, so the relative increase is larger.

Considering the results in Figure 4, a regression analysis was performed to determine the ξ_{HFRC}/ξ_{RC} ratio. For this purpose, only one variable was selected, the reinforcement ratio ρ. The regression was separated into a power function in the form $a\rho^b$ for $\rho \leq 1.0\%$ and a linear function for $\rho > 1.0\%$. The expression is given in Equation (33) and shown in Figure 4. A conservative approach was selected for the power function, formulating it as an upper boundary of the curves in Figure 4. Since HFRC members, and especially slabs, are still a relatively novel solution in practice, this conservative approach was considered appropriate.

$$\xi_{HFRC}/\xi_{RC} = \begin{Bmatrix} 1.14\rho^{-0.62}, & \rho \leq 1.0\% \\ -0.065\rho + 1.24, & \rho > 1.0\% \end{Bmatrix} \geq 1.0 \tag{33}$$

Exponent m_{HFRC} for determining $I_{e,HFRC}$

The results of the previous section confirm that the neutral axis position always lowers in a section when fibers are added, and the higher f_{R1} is the larger the lowering of the neutral axis is. This implies that the moment of inertia of the cross-section at cracked regime (I_{cr}) is smaller for HFRC than for RC with the same longitudinal reinforcement ratio (although the HFRC member will be subjected to a higher bending moment in absolute value). This is due to the fact that, for an equal reinforcement ratio, the neutral axis will be lower in the HFRC section, thereby reducing the contribution of tension reinforcement to the moment of inertia. Basing an analysis of HFRC deflections only on the sectional level would lead to the wrong conclusion that stiffness of HFRC members is always smaller than that of an RC member with the same longitudinal reinforcement. This would be the result if in Equation (29) if the exponent m was maintained as 2. Therefore, the aim of this section is to present a calibration of the exponent m_{HFRC} for HFRC members.

Because of the lack of experimental results, numerical simulations were performed with ABAQUS [34]. First, results obtained by Bosco and Debernardi [35] on simply supported beams tested until failure were modelled. From this experimental program, simply supported beams *L; b; h; d* = 6000 mm (19.68 ft); 300 mm (11.81 in); 600 mm (23.62 in); 565 mm (22.24 in) were modeled with longitudinal reinforcement ratios of 0.13%, 0.25%, and 0.57% (covering the range of reinforcement ratios of slabs). The concrete had a mean compressive strength of 30 MPa (4,351 psi), and the longitudinal reinforcement had a mean yield strength of 600 MPa (87,022 psi). In the experimental program, only RC beams were tested.

The beams were tested in short-term until failure in a three-point bending configuration. Such an analysis is also beneficial for the purposes of this study as it leaves out possible compounding effects of shrinkage and creep. The short-term service-load deflection was selected as corresponding to the load equal to 2/3 of yielding load for each beam. After fitting the numerical models to RC beams, HFRC beams of the same geometry and mechanical properties were modelled but with residual strengths $f_{R1} = f_{R3}$ (i.e. class "c" FRC) of 3, 5, and 7 MPa (435, 725 and 1,015 psi).

The service loads and deflections are shown in Table 1. From the table, a decrease in deflections can be seen with the addition of fibers. The decrease is larger with increasing values of f_{R1} and this is more pronounced for lower values of ρ (such as in slabs).

As a next step, deflections were calculated using the methods outlined in the previous sections. Since the goal was to compare differences in the values of the exponent *m* for RC and HFRC, its value was fitted for each case so that a suitable match with numerically obtained deflections was achieved – doing this fitting is justifiable considering the scatter associated with deflection control models using "default" parameter values. The obtained values of the exponent m_{HFRC} and the m_{HFRC}/m_{RC} ratio are shown in Table 2.

First, it can be seen that even for RC members, the "perfect fit" of the exponent *m* deviates significantly from the proposed value of 2 in Eq. (3). However, this is expectable and acceptable, considering the high intrinsic scatter and uncertainties associated with deflection prediction models [36]. Second, it can be seen that the values of the m_{HFRC}/m_{RC} ratio generally follow the trends of Table 1, i.e., the m_{HFRC}/m_{RC} ratios decrease with increasing f_{R1} and are lower for lower values of ρ.

The results of Table 2 are presented graphically in Figure 5 in relation to the ratio of f_{R1} and the modulus of rupture f_r. An important observation can be made from these results. Namely, for the considered concrete, with $f_c' = 30$ MPa (4,351 psi), the modulus of rupture f_r is 2.93 MPa (425 psi). Therefore, it is evidenced that as the ratio f_{R1}/f_r becomes greater than 1.0, the ratio m_{HFRC}/m_{RC} "stabilizes".

Therefore, for the general case of the method when $m = 2$ for RC members, the following correction is proposed for HFRC members:

$$m_{HFRC} = \begin{cases} 2\left(1 - \dfrac{f_{R1}}{f_r} \cdot (1 - 1.1\rho^*)\right); & \text{for } \dfrac{f_{R1}}{f_r} \leq 1.0 \\[4mm] 2\rho^* \leq 1; & \text{for } \dfrac{f_{R1}}{f_r} > 1.0 \end{cases} \qquad (34)$$

where $\rho^* = \min(0.5\%, \rho)$ and is entered in [%].

COMPARISON OF α STIFFNESS FACTOR VALUES FOR RC AND HFRC MEMBERS

Based on the previous sections, the α stiffness factor can be computed based on a reduced number of initial parameters both for RC and for HFRC sections.

Namely, the calculation process for RC sections consists of:

a. assuming an initial section height h (based, for example, in existing constant L/h ratios in codes),

b. assuming (or calculating from strength requirements) the reinforcement ratio ρ,

c. calculating ξ, μ and δ using Equations (18), (14), and (17), respectively, based on properties of materials (f_y, E_s, f'_c, E_c), the reinforcement ratio ρ, the reinforcement concrete cover in terms of d/h, and the relation of service moments to nominal strength $\eta = M_a/M_n$ considering the shoring process,

d. calculating the stiffness factor α using Equation (11), based on μ and δ, and

e. using Equation (8) to find h for one-way members or Equation (9) to find h for two-way slabs, based on span (L), the stiffness factor α, allowable deflection $(\varDelta/L)_{allow}$, boundary conditions (expressed through factor κ), modulus of elasticity of concrete (E_c), long-term deflection multiplier ($\lambda_\varDelta$), and loads causing deflections; plus, some other geometric parameters defining the structural layout in the case of two-way slabs.

f. checking the value of h found with the initially assumed value and repeating until convergence.

For HFRC sections, the calculation process consists of:

a. assuming a section height h (based, for example, in existing constant L/h ratios for RC members in codes),

b. assuming (or calculating from strength requirements) the reinforcement ratio of longitudinal reinforcement ρ, considering the contribution of steel fibers, through f_{R3},

c. calculating ξ_{HFRC} using Equations (18) and (33), based on properties of materials (E_s, f'_c, E_c), the reinforcement ratio of longitudinal reinforcement ρ, and the residual tensile strength of fibers (f_{R3}),

d. calculating μ_{HFRC} and δ_{HFRC} using Equations (21), and (28), respectively, based on properties of materials (f'_y, E_s, f'_c, E_c), the reinforcement ratio of longitudinal reinforcement ρ, and the ultimate residual tensile strength of FRC (f_{Ftu}), the reinforcement cover in terms of d/h, and the relation of service moments to nominal strength $\eta = M_a/M_n$ considering the shoring process

e. calculating m_{HFRC} using Equation (34), based on properties of materials (f'_c, f_r), the reinforcement ratio of longitudinal reinforcement ρ, and the ultimate residual tensile strength of FRC (f_{Ftu}),

f. calculating α_{HFRC} using Equation (29), based on μ_{HFRC}, δ_{HFRC} and m_{HFRC}, and

g. using Equation (8) to find h for one-way members or Equation (9) to find h for two-way slabs, based on the same parameters as RC members,

h. checking the value of h found with the initially assumed value, and repeating until convergence.

It should be noted that the long-term deflection multiplier λ_Δ may differ between HFRC and RC members. However, its proper assessment would require sufficient long-term deflection data on HFRC members, which is scarce. Nonetheless, current literature shows that, in case using fibers that do not display significant sensitivity to sustained load effects, the time-dependent increase of deflections of HFRC members is comparable (or even smaller) than that of RC members [37].

In order to facilitate the use of the method and its understanding, worked examples are provided in Annexes A and B of this paper.

Using the described processes, α and α_{HFRC} were calculated for the cases used in the parametric study, i.e., f_c' equal to 30 and 50 MPa (4,351 and 7,252 psi), and f_{R1} equal to 0, 3, 5, and 7 MPa (435, 725 and 1,015 psi), where $f_{R1} = 0$ corresponds to RC. The results are shown in Figures 6 and 7.

The figures evidence the contribution of SFRC residual strength to the effective moment of inertia over most of the reinforcement ratios range. The first aspect to note is a significant increase in I_e relative to RC for HFRCs with $f_{R1} > f_r$, as implied by Equation (34) (in this case, for concretes with $f_{R1} = 5$ and 7 MPa (725 and 1,015 psi), i.e. FRCs that exhibit deflection-hardening behavior).

Looking at the close-ups of the graphs for reinforcement ratios up to 1.0%, it is noticeable that for very low reinforcement ratios, α is lower for HFRC members in comparison to RC members with the same ρ. However, it should be kept in mind that when HFRC and RC members have the same ρ, the HFRC member will be loaded to a higher M_a due its higher design strength. Additionally, this occurs within the range of very low reinforcement ratios ($\rho < 0.2\%$ for $f_c' = 30$ MPa/4,351 psi, and $\rho < 0.3\%$ for $f_c' = 50$ MPa/7,252 psi) and this coincides with the range for

which previous research reported losses of performance, i.e. ductility, deformation and rotation capacity of HFRC (especially for lower values of FRC residual strength) [38]. Furthermore, these are reinforcement ratios that would rarely be used in practice as maximum reinforcement ratios of a member. Therefore, using fibers to eliminate steel reinforcement down to very low reinforcement ratios should be carefully analyzed.

CONCLUSIONS

This study presents the results of further development of the method originally proposed by Rangan and Scanlon for determining minimum slenderness limits of RC slabs and beams. This paper presents in detail the formulation of a closed-form solution for the stiffness factor (α) that relates the effective moment of inertia to the gross moment of inertia of a cross-section ($\alpha = I_e/I_g$). Furthermore, the method has been extended to cover HFRC members. Based on the results of the study, the following conclusions can be drawn:

- The proposed method considers all of the variables involved in the formula (i.e. boundary conditions, loads, span, f'_y, E_s, f'_c, E_c, d/h, M_a/M_n, $(\Delta/L)_{allow}$, λ_Δ) except one—the reinforcement ratio (ρ)—i.e., basic data that the designer can establish at early stages of design. Hence, with the current proposal the method gets very close to becoming useable by practitioners to find the depth of slabs at early stages of design.
- The proposal for HFRC members allows an easy and sufficiently accurate estimation of the contribution of fiber reinforcement to the effective moment of inertia (I_e), thereby opening the way for easier design of HFRC members, and in particular, slabs.
- The results of the study facilitate the identification of main factors influencing the minimum slenderness limits and demonstrate that, in general, HFRC members lead to more slender members, highlighting the potential benefits of these structural solutions.

The results of this study of course depend on the range of properties and cases considered in the parametric analyses. Hence, further research is needed for a wider validation of the proposed method. Nonetheless, the results of this study open the way towards obtaining simple and practicable tools for practitioners designing RC and HFRC members, and in particular, slabs.

ACKNOWLEDGEMENTS

Alejandro Nogales Arroyo

LIST OF NOTATIONS

E_c – modulus of elasticity of concrete

I_{cr} – moment of inertia of the fully cracked cross-section

I_e – effective moment of inertia

I_g – moment of inertia of the gross concrete cross-section

L – span length

L_{trib} – tributary width for surface load (for slabs should be equal to b)

M_a – maximum moment in member due to service loads at the stage deflection is calculated [11]

M_{cr} – cracking moment

V_f – volumetric ratio of steel fibers in SFRC

W_L – live load

$W_l(add)$– additional live load ($W_L – W_l(sus)$)

$W_l(sus)$– sustained portion of live load

W_s – sustained load ($W_{sw} + W_{sd} + W_l(sus)$)

W_{sd} – superimposed dead load

W_{sw} – self-weight

b – cross-section width

d – distance from extreme compression fiber to centroid of longitudinal tension reinforcement

f_c' – specified compressive strength of concrete

f_{Ftu} – ultimate residual tensile strength, $=f_{R3}/3$

f_r – modulus of rupture

f_{R3} – residual flexural tensile strength corresponding to a crack mouth opening displacement (CMOD) value of 2.5 mm in the EN 14651 [28] three-point bending characterization test

f_y – specified yield strength of reinforcement

h – cross-section height

k_{AR} – correction factor for edge-supported slabs (= 1 otherwise), explained in [10]

k_{DP} – correction factor for drop panels (= 1 otherwise), explained in [10]

k_{SS} – correction factor for flat slabs (= 1 otherwise), explained in [10]

k_t – orientation factor for steel fibers (=$1/(0.94 + l_f/b)$, where l_f is the fiber length)

n – ratio of steel-to-concrete moduli of elasticity (E_s/E_c)

y_t – distance from centroidal axis of gross section to tension face

α – stiffness factor (I_e/I_g)

β_{ES} – span correction factor for edge-supported slabs (= 1 otherwise), explained in [10]

δ – ratio of cracked to gross moment of inertia (I_{cr}/I_g)

κ — deflection coefficient depending on support conditions (5, 1.4, 2, 48 for simply supported, both ends continuous, one end continuous, and fixed end cantilever conditions, respectively)

λ_{Δ} — long-term deflection multiplier for sustained loads

μ — ratio of cracking moment to maximum moment in member due to service loads (M_{cr}/M_a)

ξ — time-dependent factor (1.0, 1.2, 1.4, and 2.0 for 3, 6, 12, and >60 months, respectively)

ξ_{RC} — neutral axis coefficient for an RC member

ξ_{HFRC} — neutral axis coefficient for an HFRC member

ρ — tensile reinforcement ratio (at midspan for simply supported and continuous members and at the support for cantilevers)

ρ' — compressive reinforcement ratio (at midspan for simply supported and continuous members and at the support for cantilevers)

REFERENCES

[1] Bondy, K.B. Code deflection requirements - time for a change? In Serviceability of Concrete; Barth, F., Frosch, R., Nassif, H., Scanlon, A., Eds.; American Concrete Institute: Farmington Hills, MI, 2005; pp. 133–145.

[2] Sanabra-Loewe, M.; Capellà-Llovera, J.; Ramírez-Anaya, S.; Pujadas-Gispert, E. A path to more versatile code provisions for slab deflection control. Proc. Inst. Civ. Eng. - Struct. Build. 2021, 1–15, doi:10.1680/jstbu.20.00205.

[3] Pérez Caldentey, A.; Corres Peiretti, H. EN 1992. Problems in its application and suggestions for improvement. Hormigón y Acero 2014, 65, 113–122, doi:10.1016/s0439-5689(14)70003-8.

[4] Sanabra, M.; Scanlon, A. Reinforced concrete predimensioning to enhance optimization. In Proceedings of the Engineering for Progress, Nature and People; 2014; pp. 1626–1633.

[5] EN 1992-1-1 Eurocode 2: Design of concrete structures - Part 1-1: General rules and rules for buildings; CEN: Brussels, 2004; ISBN 978 0 580 62664 7.

[6] SA Committee BD-002: Concrete Structures; Sydney, 2001;

[7] SII SII 466: Concrete Code: General principles; Tel Aviv, 2003;

[8] Rangan, B.V. Control of Beam Deflections by Allowable Span-to-Depth Ratios. ACI J. Proc. 1982, 79, 372–377, doi:10.14359/10914.

[9] Scanlon, A.; Choi, B.S. Evaulation of ACI 318 minimum thickness requirements for one-way slabs. ACI Struct. J. 1999, 96, 616–622, doi:10.14359/699.

[10] Scanlon, A.; Lee, Y.H. Unified span-to-depth ratio equation for nonprestressed concrete beams and slabs. ACI Struct. J. 2006, 103, 142–148, doi:10.14359/15095.

[11] ACI 318-19 Building code requirements for structural concrete (ACI 318-19) and commentary; Farmington Hills, MI, 2019;

[12] Aidarov, S.; de la Fuente, A.; Mena, F.; Ángel, S. Campaña experimental de un forjado de hormigón reforzado con fibras a escala real. In Proceedings of the ACE; 2019; pp. 1–10.

[13] Gossla, U. Development of SFRC free suspended elevated flat slabs, Aachen University of Applied Sciences, 2005.

[14] Destrée, X.; Mandl, J. Steel fibre only reinforced concrete in free suspended elevated slabs: Case studies, design assisted by testing route, comparison to the latest SFRC standard

documents. In Proceedings of the Proceedings of the International FIB Symposium 2008 - Tailor Made Concrete Structures: New Solutions for our Society; 2008; pp. 437–443.

[15] ACI 544.4-18 Guide to Design with Fiber-Reinforced Concrete; Farmington Hills, MI, 2018;

[16] FIB fib Model Code for Concrete Structures 2010; International Federation for Structural Concrete (fib): Lausanne, 2013; ISBN 9783433604090.

[17] Amin, A.; Foster, S.J.; Kaufmann, W. Instantaneous deflection calculation for steel fibre reinforced concrete one way members. Eng. Struct. 2017, 131, 438–445, doi:10.1016/j.engstruct.2016.10.041.

[18] Scanlon, A.; Murray, D.W. Practical Calculation of Two-way Slab Deflection. Concr. Int. 1982, 4, 43–50.

[19] Scanlon, A.; Bischoff, P.H. Shrinkage restraint and loading history effects on deflections of flexural members. ACI Struct. J. 2008, 105, 498–506.

[20] Bischoff, P.H.; Scanlon, A. Effective moment of inertia for calculating deflections of concrete members containing steel reinforcement and fiber-reinforced polymer reinforcement. ACI Struct. J. 2007, 104, 68–75, doi:10.14359/18434.

[21] Graham, C.J.; Scanlon, A. Long-time multipliers for estimating two-way slab deflections. J. Am. Concr. Inst. 1986, 83, 899–908, doi:10.14359/2626.

[22] Pujadas, P.; Blanco, A.; De La Fuente, A.; Aguado, A. Cracking behavior of FRC slabs with traditional reinforcement. Mater. Struct. Constr. 2012, 45, 707–725, doi:10.1617/s11527-011-9791-0.

[23] Michels, J.; Waldmann, D.; Maas, S.; Zürbes, A. Steel fibers as only reinforcement for flat slab construction - Experimental investigation and design. Constr. Build. Mater. 2012, 26, 145–155, doi:10.1016/j.conbuildmat.2011.06.004.

[24] Hedebratt, J.; Silfwerbrand, J. Full-scale test of a pile supported steel fibre concrete slab. Mater. Struct. Constr. 2014, 47, 647–666, doi:10.1617/s11527-013-0086-5.

[25] di Prisco, M.; Colombo, M.; Pourzarabi, A. Biaxial bending of SFRC slabs: Is conventional reinforcement necessary? Mater. Struct. Constr. 2019, 52, 1–15, doi:10.1617/s11527-018-1302-0.

[26] Tan, K.H.; Paramasivam, P.; Tan, K.C. Creep and shrinkage deflections of RC beams with steel fibers. J. Mater. Civ. Eng. 1994, 6, 474–494.

[27] Tan, K.H.; Paramasivam, P.; Tan, K.C. Instantaneous and long-term deflections of steel fiber reinforced concrete beams. ACI Struct. J. 1994, 91, 384–393.

[28] EN 14651 Test method for metallic fibred concrete — Measuring the flexural tensile strength (limit of proportionality (LOP), residual). Br. Stand. Inst. 2005, doi:9780580610523.

[29] Venkateshwaran, A.; Tan, K.H.; Li, Y. Residual flexural strengths of steel fiber reinforced concrete with multiple hooked-end fibers. Struct. Concr. 2018, 19, 352–365, doi:10.1002/suco.201700030.

[30] Tiberti, G.; Germano, F.; Mudadu, A.; Plizzari, G.A. An overview of the flexural post-cracking behavior of steel fiber reinforced concrete. Struct. Concr. 2018, 19, 695–718, doi:10.1002/suco.201700068.

[31] Galeote, E.; Blanco, A.; Cavalaro, S.H.P.; de la Fuente, A. Correlation between the Barcelona test and the bending test in fibre reinforced concrete. Constr. Build. Mater. 2017, 152, 529–538, doi:10.1016/j.conbuildmat.2017.07.028.

[32] Branson, D.E.; Metz, G.A. Instantaneous and time-dependent deflections of simple and continuous reinforced concrete beams - Alabama Highway Research Report; 1963;

[33] Branson, D.E.; Kripanarayanan, K.M. Loss of prestress, camber and deflection of non-composite and composite prestressed concrete structures. J Prestress. Concr Inst 1971.

[34] Simulia Abaqus 6.14; Vélizy-Villacoublay, Ed.; Dassault Systèmes, 2018;

[35] Bosco, C.; Debernardi, P.G. Influence of some basic parameters on the plastic rotation of reinforced concrete elements. In CEB Bulletin d'Information 218; 1993; p. 276.

[36] Beeby, A.W.; Narayanan, S. Designer's guide to Eurocode 2: Design of concrete structures; Thomas Telford: London, 2005;

[37] Tošić, N.; Aidarov, S.; de la Fuente, A. Systematic Review on the Creep of Fiber-Reinforced Concrete. Materials (Basel). 2020, 13, 5098.

[38] Markić, T.; Amin, A.; Kaufmann, W.; Pfyl, T. Discussion on "Assessing the influence of fibers on the flexural behavior of reinforced concrete beams with different longitudinal reinforcement ratios" by Conforti et al. [structural concrete, 2020]. Struct. Concr. 2021, doi:10.1002/suco.202000488.

APPENDIX A

In this appendix, a calculation example is provided showcasing the use of the developed method described in the paper. Appendix A and B present the analysis of the same cases with the only difference being the total superimposed load, thus highlighting its effect and importance in proper deflection control.

A continuous one-way slab is selected with 8-m (26.25 ft) spans and a service load-to-nominal load is $\eta = 2/3$. Specifically, the slab is exposed to self-weight (W_{sw}) and a total superimposed load ($W_{sd} + W_l$) of 5 kN/m^2 (104 lb/ft^2), of which 2 kN/m^2 (42 lb/ft^2) are the additional live load portion ($W_l(add)$).

The specified compressive strength of concrete is chosen as 35 MPa (5,076 psi) and the specified yield strength of reinforcement is chosen as 500 MPa (72,519 psi).

The one-way slab is considered as a floor supporting non-structural elements likely to be damaged by large deflections. Therefore, the deflection limitation related to the incremental deflection after attachment of nonstructural elements is $L/480$ [11].

<u>RC slab</u>

a. First, an initial height h is assumed considering code recommended minimum heights for simply supported slabs of $L/28$ [11], corrected for reinforcement strength by a factor of 1.125, leading to a recommendation of $L/25$.

$$h_{RC,1} = \frac{8000}{25} = 320 \text{ mm (12.6 in)}$$

From the assumed height of the slab, the self-weight can be calculated. The service load is then

$$W_s = 13.0 \text{ kN/m (9,588 lb/ft)}$$

The maximum bending moment due to service loads as well as the nominal bending moment at mid-span (considering a strip of 1-m/3.28-ft width) can be determined for the mid-span (+) and support (−) sections

$$M_a^+ = 34.7 \text{ kNm (25.59 kip} - \text{ft)}; \quad M_n^+ = \frac{3}{2} \cdot M_a^+ = 52.0 \text{ kNm (38.35 kip} - \text{ft)};$$

$$M_a^- = 69.3 \text{ kNm (51.11 kip} - \text{ft)}; \quad M_n^- = \frac{3}{2} \cdot M_a^- = 104.0 \text{ kNm (76.71 kip} - \text{ft)};$$

b. Secondly, the necessary reinforcement ratios ρ^+ and ρ^- can be calculated considering code provisions [11]. Considering the illustrative purpose of the calculation example, minimum reinforcement requirements were deliberately not considered.

$$A_{s,1}^+ = 366 \text{ mm}^2 \ (0.57 \text{ in}^2); \ \rho_1^+ = 0.127\%$$
$$A_{s,1}^- = 741 \text{ mm}^2 \ (1.15 \text{ in}^2); \ \rho_1^- = 0.257\%$$

Alejandro Nogales Arroyo

c. Next, ξ, μ and δ are calculated using Equations (18), (14), and (17) for both the mid-span and support sections, considering E_s = 200000 MPa (29,007 ksi) and E_c = 4700·(35)$^{0.5}$ = 27805 MPa (4,033 ksi) (n = 200000/27805 = 7.19)

$$\xi_1^+ = n\rho\left(-1 + \sqrt{1 + \frac{2}{n\rho}}\right) = 7.19 \cdot 0.00127 \cdot \left(-1 + \sqrt{1 + \frac{2}{7.19 \cdot 0.00127}}\right) = 0.126$$

$$\mu_1^+ = \frac{0.625 \cdot \sqrt{35}}{6 \cdot \frac{2}{3} \cdot (0.9)^2 \cdot 0.00127 \cdot 500 \cdot \left(1 - \frac{0.00127 \cdot 500}{1.7 \cdot 35}\right)} = 1.818 \geq 1.5$$

$$\delta_1^+ = 8.75 \cdot 7.19 \cdot 0.00127 \cdot (1 - 0.126)\left(1 - \frac{0.126}{3}\right) = 0.067$$

$$\xi_1^- = n\rho\left(-1 + \sqrt{1 + \frac{2}{n\rho}}\right) = 7.19 \cdot 0.00257 \cdot \left(-1 + \sqrt{1 + \frac{2}{7.19 \cdot 0.00257}}\right) = 0.175$$

$$\mu_1^- = \frac{0.625 \cdot \sqrt{35}}{6 \cdot \frac{2}{3} \cdot (0.9)^2 \cdot 0.00257 \cdot 500 \cdot \left(1 - \frac{0.00257 \cdot 400}{1.7 \cdot 35}\right)} = 0.907 < 1.5$$

$$\delta_1^- = 8.75 \cdot 7.19 \cdot 0.00257 \cdot (1 - 0.175)\left(1 - \frac{0.175}{3}\right) = 0.126$$

d. Subsequently, α can be calculated using Equation (11) for the mid-span and support cross-section, based on μ and δ, and then interpolated into the overall α factor considering an assumed linear elastic distribution of sagging and hogging moments (sagging length of $L \cdot \sqrt{3}/3$ and hogging length of $L \cdot (1 - \sqrt{3}/3)$:

$$\alpha_1^+ = 1.0$$

$$\alpha_1^- = \frac{0.126}{1 - \left(\frac{2}{3} \cdot 0.907\right)^2 (1 - 0.126)} = 0.185$$

$$\alpha = \frac{\sqrt{3}}{3} \cdot \alpha_1^+ + \left(1 - \frac{\sqrt{3}}{3}\right) \cdot \alpha_1^- = 0.656$$

e. Finally, using Equation (8), the necessary height h (i.e. h^2) can be determined:

$$\frac{L}{h} = \left[\frac{1}{480} \frac{32 \cdot 0.656 \cdot 27805 \cdot 1000}{5(2 \cdot (13 - 2) + 2)}\right]^{\frac{1}{3}} = 33.0$$

$$h_{RC,2} = \frac{8000}{33} = 242 \text{ mm (9.53 in)}$$

The process is then reinitiated with the new value of slab height 242 mm (9.53 in) and repeated until convergence is achieved.

In this case, the converged solution is obtained as

h_{RC} = 273 mm (10.75 in)

This value should be rounded up to the nearest 5 mm to 275 mm (10.83 in). It can be seen that the code-recommended slenderness of $L/25$ ($h = 320$ mm/12.6 in), provides a slightly conservative first approximation for this superimposed load value.

HFRC slab

For this case, it is considered that the concrete is an SFRC with residual strengths $f_{R1} = f_{R3} = 4$ MPa (580 psi) ($f_{Ftu} = f_{R3}/3 = 1.33$ MPa/192.9 psi). The process begins similarly to the case of RC.

a. First, an initial height h is assumed considering code recommended minimum heights for simply supported slabs of $L/28$ [11], corrected for reinforcement strength by a factor of 1.125, leading to a recommendation of $L/25$.

$$h_{HFRC,1} = \frac{8000}{25} = 320 \text{ mm (12.6 in)}$$

Therefore, in this first iteration, the service load and therefore service and nominal bending moments are the same as for the first iteration in the RC slab case

$$W_s = 13.0 \text{ kN/m (9,588 lb/ft)}$$

$$M_a^+ = 34.7 \text{ kNm (25.59 kip} - \text{ft)}; \quad M_n^+ = \frac{3}{2} \cdot M_a^+ = 52.0 \text{ kNm (38.35 kip} - \text{ft)};$$

$$M_a^- = 69.3 \text{ kNm (51.11 kip} - \text{ft)}; \quad M_n^- = \frac{3}{2} \cdot M_a^- = 104.0 \text{ kNm (76.71 kip} - \text{ft)};$$

b. Secondly, the necessary reinforcement ratios ρ^+ and ρ^- can be calculated considering the contribution of the fibers, see Equations (19) and (20):

$A_{s,1}^+ = 0$ mm²; $\rho_1^+ = 0\%$, i.e. complete substitution of steel reinforcement with FRC is possible

$A_{s,1}^- = 250$ mm² (0.39 in²); $\rho_1^- = 0.087\%$

c. Next, ξ_{HFRC} can be calculated based on Equations (18) and (33)

$\xi_{HFRC,1}^+ = 1$, i.e. assuming the rigid-plastic FRC model, a concentration of compressive stresses at the extreme fiber in compression can be assumed [15]

$$\xi_1^- = 7.19 \cdot 0.00087 \cdot \left(-1 + \sqrt{1 + \frac{2}{7.19 \cdot 0.00087}} \right) = 0.106$$

$$\xi_{HFRC,1}^- = 0.106 \cdot 1.14 \cdot 0.087^{-0.62} = 0.548 > 0.106$$

d. In the next step, μ_{HFRC} and δ_{HFRC} are calculated for the mid-span and support sections using Equations (21), and (28),

$$\mu_{HFRC,1}^+ = \frac{0.625 \cdot \sqrt{35}}{6 \cdot \frac{2}{3} \cdot \left[(0.9)^2 \cdot 0 \cdot 500 \cdot \left(1 - \frac{0 \cdot 500}{1.7 \cdot 35}\right) + 0.5 \cdot 1.33 \right]} = 1.387 < 1.5$$

$$\delta_{HFRC,1}^+ = 7.19 \cdot \left[8.75 \cdot 0 \cdot (1-1) \cdot \left(1 - \frac{1}{3}\right) + 0.014 \cdot \frac{4}{\sqrt{35}} \cdot (1 - 0.9 \cdot 1) \right] = 0.007$$

$$\mu_{HFRC,1}^- = \frac{0.625 \cdot \sqrt{35}}{6 \cdot \frac{2}{3} \cdot \left[(0.9)^2 \cdot 0.00087 \cdot 500 \cdot \left(1 - \frac{0.00087 \cdot 500}{1.7 \cdot 35}\right) + 0.5 \cdot 1.33\right]} = 0.910 < 1.5$$

$$\delta_{HFRC,1}^- = 7.19 \cdot \left[8.75 \cdot 0.00087 \cdot (1 - 0.548) \cdot \left(1 - \frac{0.548}{3}\right) + 0.014 \cdot \frac{4}{\sqrt{35}}\right.$$
$$\left. \cdot (1 - 0.9 \cdot 0.548)\right] = 0.055$$

e.   Next, the exponent m_{HFRC} is calculated for the mid-span and support sections using Equation (34) considering that $f_{R1}/f_r > 1.0$:

$$m_{HFRC,1}^+ = 2 \cdot 0 = 0$$

$$m_{HFRC,1}^- = 2 \cdot 0.087 = 0.174$$

f.   Then, α_{HFRC} can be calculated using Equation (29) for the mid-span and support cross-section, based on μ and δ, and then interpolated into the overall α factor considering an assumed linear elastic distribution of sagging and hogging moments (sagging length of $L \cdot \sqrt{3}/3$ and hogging length of $L \cdot (1 - \sqrt{3}/3)$:

$$\alpha_1^+ = \frac{0.007}{1 - \left(\frac{2}{3} \cdot 1.387\right)^0 (1 - 0.007)} = 1.0$$

$$\alpha_1^- = \frac{0.055}{1 - \left(\frac{2}{3} \cdot 0.910\right)^{0.174} (1 - 0.055)} = 0.410$$

$$\alpha = \frac{\sqrt{3}}{3} \cdot \alpha_1^+ + \left(1 - \frac{\sqrt{3}}{3}\right) \cdot \alpha_1^- = 0.751$$

g.   Finally, using Equation (8), the necessary height h (i.e. h^2) can be determined:

$$\frac{L}{h} = \left[\frac{1}{480} \frac{32 \cdot 0.751 \cdot 27805 \cdot 1000}{5(2 \cdot (13 - 2) + 2)}\right]^{\frac{1}{3}} = 34.5$$

$$h_{HFRC,1} = \frac{8000}{34.5} = 232 \text{ mm (9.13 in)}$$

The process is then reinitiated with the new value of slab height 232 mm (9.13 in) and repeated until convergence is achieved. In this case, the converged solution is obtained as

$h_{HFRC} = 242$ mm (9.53 in)

This value should be rounded up to the nearest 5 mm to 245 mm (9.64 in). It can be seen that the code-recommended slenderness of $L/25$ ($h = 320$ mm/12.6 in) provides a significant overestimation of the necessary slab height under the considered superimposed load and selected FRC residual strength. In fact, in this case, the HFRC solution offers a possible reduction of slab height of $(275 - 245)/275 = 0.011$, i.e. 11% when compared to the conventional reinforced concrete slab.

APPENDIX B

In this appendix, the same continuous slab is considered as in Appendix A, both in the RC and HFRC variants, with the only difference in this case being the superimposed load.

In other words, the same continuous one-way slab is selected with 8-m (26.25 ft) spans and a service load-to-nominal load is $\eta = 2/3$. However, in this case, the slab is exposed to self-weight (W_{sw}) and a total superimposed load ($W_{sd} + W_l$) of 15 kN/m² (313 lb/ft²), of which 6 kN/m² (125 lb/ft²) are the additional live load portion ($W_l(add)$). Therefore, the ratio of $W_l(add)$ to total superimposed load is maintained at 0.4 in both appendices.

The specified compressive strength of concrete is chosen as 35 MPa (5,076 psi) and the specified yield strength of reinforcement is chosen as 500 MPa (72,519 psi).

The one-way slab is considered as a floor supporting non-structural elements likely to be damaged by large deflections. Therefore, the deflection limitation related to the incremental deflection after attachment of nonstructural elements is $L/480$ [11].

<u>RC slab</u>

a. First, an initial height h is assumed considering code recommended minimum heights for simply supported slabs of $L/28$ [11], corrected for reinforcement strength by a factor of 1.125, leading to a recommendation of $L/25$.

$$h_{RC,1} = \frac{8000}{25} = 320 \text{ mm (12.6 in)}$$

From the assumed height of the slab, the self-weight can be calculated. The service load is then

$$W_s = 23.0 \text{ kN/m (16,964 lb/ft)}$$

The maximum bending moment due to service loads as well as the nominal bending moment at mid-span (considering a strip of 1-m/3.28-ft width) can be determined for the mid-span (+) and support (−) sections

$$M_a^+ = 61.3 \text{ kNm (45.21 kip} - \text{ft)}; \; M_n^+ = \frac{3}{2} \cdot M_a^+ = 92.0 \text{ kNm (67.86 kip} - \text{ft)};$$

$$M_a^- = 122.7 \text{ kNm (90.50 kip} - \text{ft)}; \; M_n^- = \frac{3}{2} \cdot M_a^- = 184.0 \text{ kNm (135.71 kip} - \text{ft)};$$

b. Secondly, the necessary reinforcement ratios ρ^+ and ρ^- can be calculated considering code provisions [11]. Considering the illustrative purpose of the calculation example, minimum reinforcement requirements were deliberately not considered.

$A_{s,1}^+ = 653 \text{ mm}^2 \text{ (1.01 in}^2\text{)}; \; \rho_1^+ = 0.227\%$

$A_{s,1}^- = 1339 \text{ mm}^2 \text{ (2.08 in}^2\text{)}; \; \rho_1^- = 0.465\%$

c. Next, ξ, μ and δ are calculated using Equations (18), (14), and (17) for both the mid-span and support sections, considering E_s = 200000 MPa (29,007 ksi) and E_c = 4700·(35)$^{0.5}$ = 27805 MPa (4,033 ksi) (n = 200000/27805 = 7.19)

$$\xi_1^+ = 7.19 \cdot 0.00227 \cdot \left(-1 + \sqrt{1 + \frac{2}{7.19 \cdot 0.00227}} \right) = 0.165$$

$$\mu_1^+ = \frac{0.625 \cdot \sqrt{35}}{6 \cdot \frac{2}{3} \cdot (0.9)^2 \cdot 0.00227 \cdot 500 \cdot \left(1 - \frac{0.00227 \cdot 500}{1.7 \cdot 35}\right)} = 1.026 < 1.5$$

$$\delta_1^+ = 8.75 \cdot 7.19 \cdot 0.00227 \cdot (1 - 0.165)\left(1 - \frac{0.165}{3}\right) = 0.113$$

$$\xi_1^- = 7.19 \cdot 0.00465 \cdot \left(-1 + \sqrt{1 + \frac{2}{7.19 \cdot 0.00465}} \right) = 0.227$$

$$\mu_1^- = \frac{0.625 \cdot \sqrt{35}}{6 \cdot \frac{2}{3} \cdot (0.9)^2 \cdot 0.00465 \cdot 500 \cdot \left(1 - \frac{0.00465 \cdot 400}{1.7 \cdot 35}\right)} = 0.511 < 1.5$$

$$\delta_1^- = 8.75 \cdot 7.19 \cdot 0.00465 \cdot (1 - 0.227)\left(1 - \frac{0.227}{3}\right) = 0.209$$

d. Subsequently, α can be calculated using Equation (11) for the mid-span and support cross-section, based on μ and δ, and then interpolated into the overall α factor considering an assumed linear elastic distribution of sagging and hogging moments (sagging length of $L \cdot \sqrt{3}/3$ and hogging length of $L \cdot (1 - \sqrt{3}/3)$:

$$\alpha_1^+ = \frac{0.113}{1 - \left(\frac{2}{3} \cdot 1.026\right)^2 (1 - 0.113)} = 0.193$$

$$\alpha_1^- = \frac{0.209}{1 - \left(\frac{2}{3} \cdot 0.511\right)^2 (1 - 0.209)} = 0.230$$

$$\alpha = \frac{\sqrt{3}}{3} \cdot \alpha_1^+ + \left(1 - \frac{\sqrt{3}}{3}\right) \cdot \alpha_1^- = 0.208$$

e. Finally, using Equation (8), the necessary height h (i.e. h^2) can be determined:

$$\frac{L}{h} = \left[\frac{1}{480} \frac{32 \cdot 0.208 \cdot 27805 \cdot 1000}{5(2 \cdot (23 - 6) + 6)}\right]^{\frac{1}{3}} = 19.0$$

$$h_{RC,2} = \frac{8000}{19} = 421 \text{ mm (16.57 in)}$$

The process is then reinitiated with the new value of slab height 421 mm (16.57 in) and repeated until convergence is achieved.

In this case, the converged solution is obtained as

$$h_{RC} = 383 \text{ mm (15.08 in)}$$

This value should be rounded up to the nearest 5 mm to 385 mm (15.16 in). It can be seen that the code-recommended slenderness of $L/25$ ($h = 320$ mm/12.60 in) does not provide an adequate first approximation for this superimposed load value, which is three times the superimposed load discussed in Appendix A. In this case, the code provision is unconservative, rather than conservative (as it was found in Appendix A). Hence, considering the results of both appendix, it is put forward the importance of having a model that explicitly considers the magnitude of applied loads.

<u>HFRC slab</u>

For this case, it is considered that the concrete is an SFRC with residual strengths $f_{R1} = f_{R3} = 4$ MPa (580 psi) ($f_{Ftu} = f_{R3}/3 = 1.33$ MPa/192.9 psi). The process begins similarly to the case of RC.

a. First, an initial height h is assumed considering code recommended minimum heights for simply supported slabs of $L/28$ [11], corrected for reinforcement strength by a factor of 1.125, leading to a recommendation of $L/25$.

$$h_{HFRC,1} = \frac{8000}{25} = 320 \text{ mm (12.6 in)}$$

Therefore, in this first iteration, the service load and therefore service and nominal bending moments are the same as for the first iteration in the RC slab case

$$W_s = 23.0 \text{ kN/m (16,964 lb/ft)}$$

$$M_a^+ = 61.3 \text{ kNm (45.21 kip} - \text{ft); } M_n^+ = \frac{3}{2} \cdot M_a^+ = 92.0 \text{ kNm (67.86 kip} - \text{ft);}$$

$$M_a^- = 122.7 \text{ kNm (90.50 kip} - \text{ft); } M_n^- = \frac{3}{2} \cdot M_a^- = 184.0 \text{ kNm (135.71 kip} - \text{ft);}$$

b. Secondly, the necessary reinforcement ratios ρ^+ and ρ^- can be calculated considering the contribution of the fibers, see Equations (19) and (20):

$A_{s,1}^+ = 166 \text{ mm}^2 (0.26 \text{ in}^2); \ \rho_1^+ = 0.058\%$

$A_{s,1}^- = 827 \text{ mm}^2 (1.28 \text{ in}^2); \ \rho_1^- = 0.287\%$

c. Next, ξ_{HFRC} can be calculated based on Equations (18) and (33)

$$\xi_1^+ = 7.19 \cdot 0.00058 \cdot \left(-1 + \sqrt{1 + \frac{2}{7.19 \cdot 0.00058}} \right) = 0.087$$

$$\xi_{HFRC,1}^- = 0.087 \cdot 1.14 \cdot 0.058^{-0.62} = 0.582 > 0.087$$

$$\xi_1^- = 7.19 \cdot 0.00287 \cdot \left(-1 + \sqrt{1 + \frac{2}{7.19 \cdot 0.00287}} \right) = 0.184$$

$$\xi_{HFRC,1}^- = 0.184 \cdot 1.14 \cdot 0.287^{-0.62} = 0.454 > 0.184$$

d. In the next step, μ_{HFRC} and δ_{HFRC} are calculated for the mid-span and support sections using Equations (21), and (28),

$$\mu_{HFRC,1}^+ = \frac{0.625 \cdot \sqrt{35}}{6 \cdot \frac{2}{3} \cdot \left[(0.9)^2 \cdot 0.00058 \cdot 500 \cdot \left(1 - \frac{0.00058 \cdot 500}{1.7 \cdot 35}\right) + 0.5 \cdot 1.33\right]} = 1.029 < 1.5$$

$$\delta_{HFRC,1}^+ = 7.19 \cdot \left[8.75 \cdot 0.00058 \cdot (1 - 0.582) \cdot \left(1 - \frac{0.582}{3}\right) + 0.014 \cdot \frac{4}{\sqrt{35}}\right.$$

$$\left. \cdot (1 - 0.9 \cdot 0.582)\right] = 0.045$$

$$\mu_{HFRC,1}^- = \frac{0.625 \cdot \sqrt{35}}{6 \cdot \frac{2}{3} \cdot \left[(0.9)^2 \cdot 0.00287 \cdot 500 \cdot \left(1 - \frac{0.00287 \cdot 500}{1.7 \cdot 35}\right) + 0.5 \cdot 1.33\right]} = 0.513 < 1.5$$

$$\delta_{HFRC,1}^- = 7.19 \cdot \left[8.75 \cdot 0.00287 \cdot (1 - 0.454) \cdot \left(1 - \frac{0.454}{3}\right) + 0.014 \cdot \frac{4}{\sqrt{35}}\right.$$

$$\left. \cdot (1 - 0.9 \cdot 0.454)\right] = 0.124$$

e. Next, the exponent m_{HFRC} is calculated for the mid-span and support sections using Equation (34) considering that $f_{RI}/f_r > 1.0$:

$$m_{HFRC,1}^+ = 2 \cdot 0.058 = 0.116$$

$$m_{HFRC,1}^- = 2 \cdot 0.287 = 0.574$$

f. Then, α_{HFRC} can be calculated using Equation (29) for the mid-span and support cross-section, based on μ and δ, and then interpolated into the overall α factor considering an assumed linear elastic distribution of sagging and hogging moments (sagging length of $L \cdot \sqrt{3}/3$ and hogging length of $L \cdot (1 - \sqrt{3}/3)$:

$$\alpha_1^+ = \frac{0.045}{1 - \left(\frac{2}{3} \cdot 1.029\right)^{0.115} (1 - 0.045)} = 0.524$$

$$\alpha_1^- = \frac{0.124}{1 - \left(\frac{2}{3} \cdot 0.513\right)^{0.574} (1 - 0.124)} = 0.235$$

$$\alpha = \frac{\sqrt{3}}{3} \cdot \alpha_1^+ + \left(1 - \frac{\sqrt{3}}{3}\right) \cdot \alpha_1^- = 0.402$$

g. Finally, using Equation (8), the necessary height h (i.e. h^2) can be determined:

$$\frac{L}{h} = \left[\frac{1}{480} \frac{32 \cdot 0.402 \cdot 27805 \cdot 1000}{5(2 \cdot (23 - 6) + 6)}\right]^{\frac{1}{3}} = 23.7$$

$$h_{HFRC,2} = \frac{8000}{23.7} = 338 \text{ mm (13.31 in)}$$

The process is then reinitiated with the new value of slab height 338 mm (13.31 in) and repeated until convergence is achieved. In this case, the converged solution is obtained as

$h_{HFRC} = 330$ mm (12.99 in)

It can be seen that the code-recommended slenderness of *L*/25 (*h* = 320 mm/12.60 in) provides only a slight underestimation of the necessary slab height under the considered superimposed load and selected FRC residual strength. However, this should be a considered a coincidence, as the code provision is not meant for this kind or reinforced concrete members.

Besides, in this case, the HFRC solution offers a significant potential reduction of slab height of (385 – 330)/385 = 0.166, i.e. 16.6%, when compared to the depth for the conventional reinforced concrete slab.

LIST OF TABLES

Table 1. Short-term deflections of numerically simulated simply supported RC and HFRC beams.

Table 2. Ratio of exponent m for short-term deflections of HFRC and RC simply supported beams.

LIST OF FIGURES

Figure 1. Dependence of α on ρ = 0–3% (left) and 0–1% (right), for f_c' = 30 MPa (4,351 psi).

Figure 2. Correlation used to assess f_{R3} and f_{R1} for SFRC.

Figure 3. Internal forces in RC and HFRC sections under the same bending moment (M_a).

Figure 4. Ratio of ξ_{HFRC} to ξ_{RC} for sections with equal M_a and ρ.

Figure 5. Dependence of the m_{HFRC}/m_{RC} ratio on the ratio f_{R1}/f_r.

Figure 6. Values of α stiffness factors for RC and HFRC members with f_c' = 30 MPa (4,351 psi). (Note: 1 MPa = 0.145 ksi)

Figure 7 Values of α stiffness factors for RC and HFRC members with f_c' = 50 MPa (7,252 psi). (Note: 1 MPa = 0.145 ksi)

TABLES

Table 1.

ρ (%)	f_{R1} (MPa)	M_y (kNm)	(2/3)M_y (kNm)	Δ_0 (mm)	($\Delta_{HFRC}-\Delta_{RC}$)/$\Delta_{RC}$ (%)
	0	61.5	41.0	2.79	0.0
0.13	3	122.6	81.7	4.112	47.3
	5	164.4	109.6	4.73	69.5
	7	186.9	124.6	4.82	72.8
	0	120.0	80.0	6.86	0.0
0.25	3	192.9	128.6	8.77	27.8
	5	232.2	154.8	7.78	13.4
	7	252.6	168.4	7.42	8.2

	0	242.7	161.8	9.04	0.0
0.57	3	358.1	238.7	12.35	36.5
	5	396.2	264.1	11.5	27.2
	7	413.0	275.3	11.1	22.9

Note: 1 MPa = 0.145 ksi, 1 kNm = 0.738 kip-ft, 1 mm = 0.039 in

Table 2.

ρ (%)	f_{R1} (MPa)	m_{HFRC}	m_{HFRC}/m_{RC}
	0	1.122	1.000
0.13	3	0.164	0.146
	5	0.128	0.114
	7	0.111	0.099
	0	0.784	1.000
0.25	3	0.312	0.398
	5	0.207	0.264
	7	0.179	0.229
	0	0.601	1.000
0.57	3	0.379	0.632
	5	0.293	0.488
	7	0.274	0.456

Note: 1 MPa = 0.145 ksi

FIGURES

Figure 1.

$$f_{R3}/\sqrt{f_c'} = 0.103 \cdot V_f\, \lambda_f\, f_{uf}\, \sqrt{E_s}$$
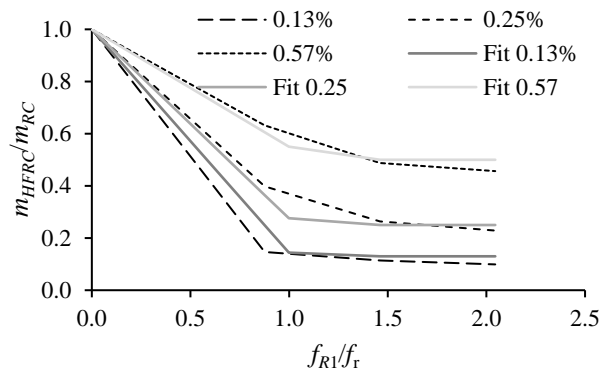$$R^2 = 0.75$$

$$f_{R3} = 0.93 f_{R1}$$
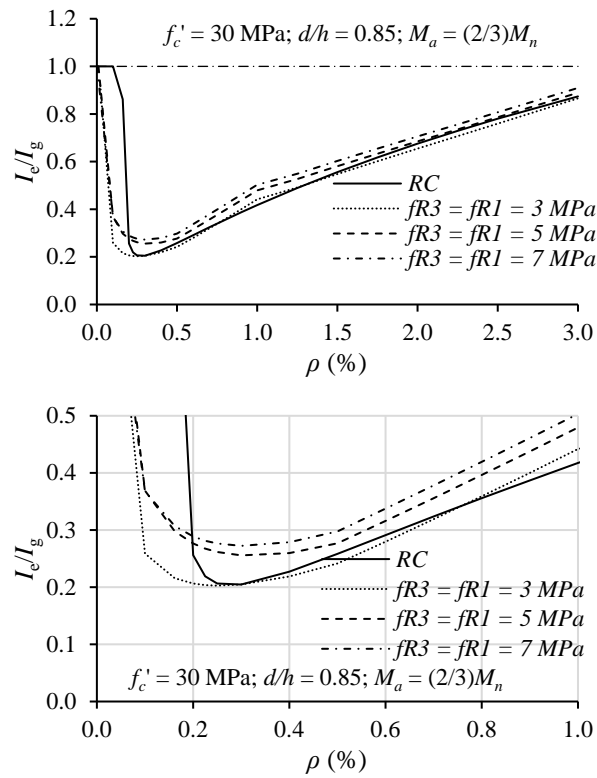$$R^2 = 0.93$$
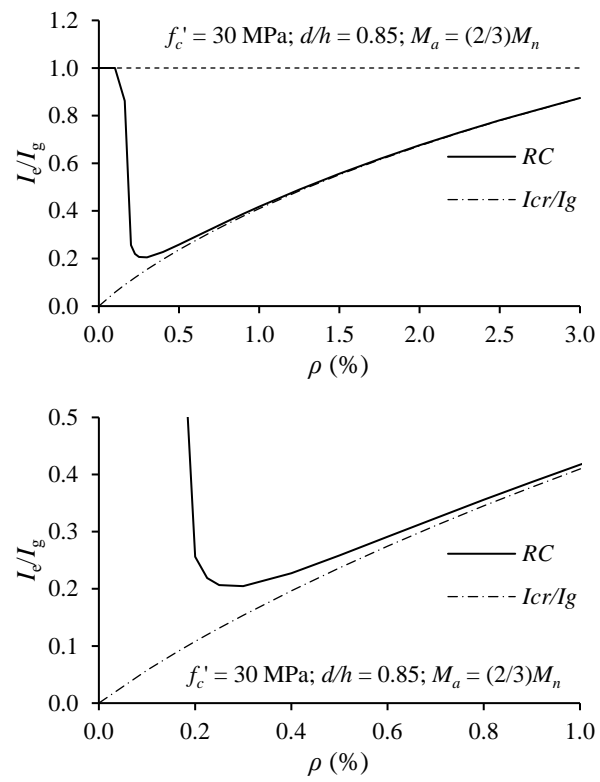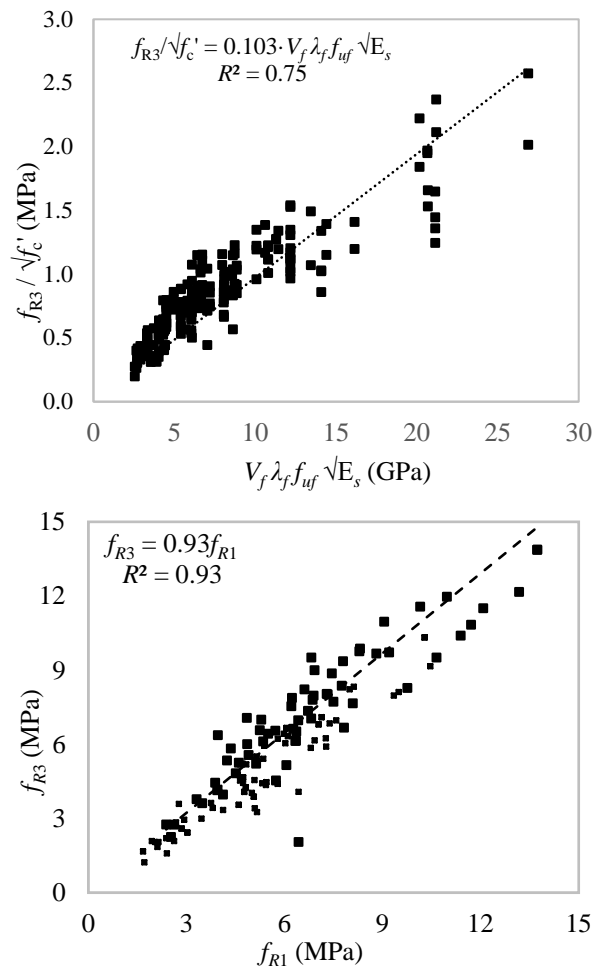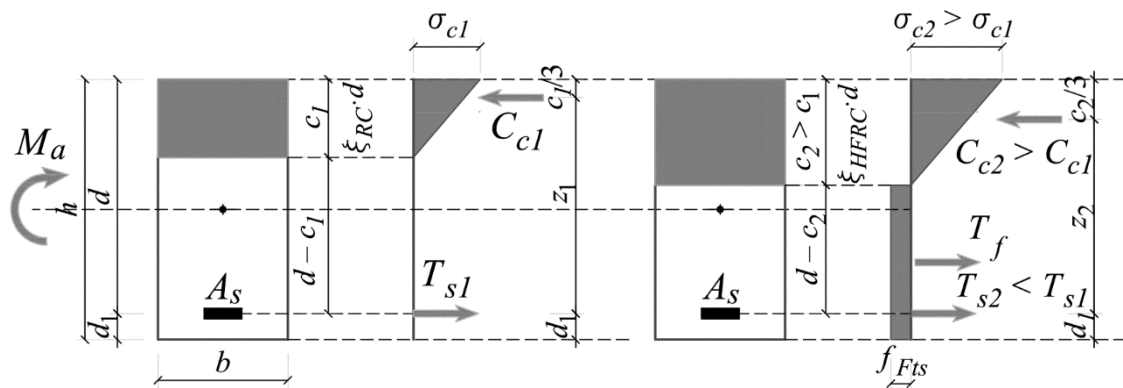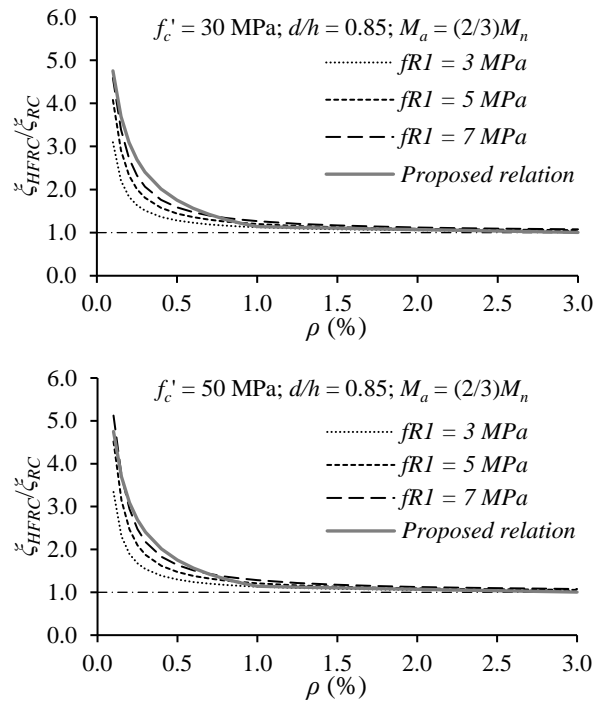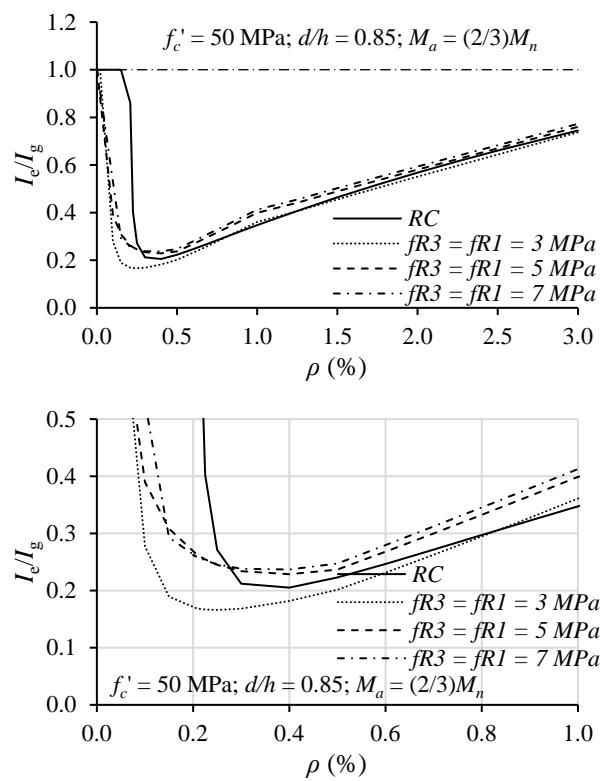
Figure 2.

Figure 3.

Figure 4.

Figure 5.

Figure 6.

Figure 7.